Tesi Doctoral

Ph.D. Dissertation

Assessment of a Micro-grid Ionization-chamber (EOS) for Low-Dose Chest Radiography

Joaquim Piqueras Pardellans

Departament de Medicina (Medicine Department)
Universitat Autònoma de Barcelona
Bellaterra (Cerdanyola del Vallès), 2015

under the direction of
Prof. Dr. Rafael Salvador Tarrasón

Universitat Autònoma de Barcelona

(Left blank)

Ph.D. Dissertation Technical Record

Ph.D Dissertation Director

Family Name: **Salvador Tarrasón**
First Name: **Rafael**
Title: **Ph.D. in Medicine**
Position: Clinical Chief in Radiology, Department of Diagnostic Imaging, Breast Imaging Unit.
Institution: **University Hospital Vall d'Hebron**. Barcelona (Catalonia, Spain). Institut Català de la Salut (ICS).
Academic Position: **Associated Professor in Radiology,** Department of Medicine of the Autonomous University of Barcelona (Catalonia, Spain)

Doctorate candidate in Medicine

Family Name: **Piqueras Pardellans**
First Name (given): **Joaquim**
Title: **Ph.D. in Medicine**
Postal Address: 08208 Sabadell (Spain)
E-mail: joaquim@piqueras.org

Department of Medicine
Autonomous University of Barcelona (UAB)
08193 Bellaterra (Cerdanyola del Vallès, Barcelona, Spain
www.uab.cat – Medicina

(blank page)

Dedications:

To my wife Neus and to my sons Adrià and Marcel. Their support has allowed me to devote uncountable hours to my profession, research, and to complete this work.

To my dear 'professor', Dr. Xavier Lucaya, radiologist and teacher, to whom three generations of pediatric radiologists should be grateful.

To my Parents, Jesús and Carme. They have encouraged me to study and work hard, but also to enjoy family and friends.

Acknowledgments:

To Dr. Rafael Salvador for his comments, help, and patience, directing this work.

To EOS development team and EOS GROWTH project GRD1-2001-40084 members: Biospace - EOS Imaging (France) for the concept development and manufacture of the EOS prototype and its detectors: Prof. Georges Charpak, Ms. Marie Meynadier, Ms. Irène Dorion and Mr. Georges Le Bras, and the rest of the EOS team.

To Mr. Gillberto Contento and Mr. Carlo Maccia, from Cyberqual (Italy) for their radiation measurements, calibration and quality assessment contributions and expertize.

To Prof. Dr. Gabriel Kalifa (H.. St. Vicent Paul, Paris, FR), Dr. Pierre Scillia (Hôpital U. Erasme, BE), and Dr. Paulino Sousa (HU Vall d'Hebron, Institut de Recerca, ES) who contributed as readers in the image assessment.

To Prof. Dr. Fred Avni (H. Erasme Brussels, Belgium) and their medical and radiographers teams.

Grants:

The development of the EOS device and the research experiments have been funded by the Competitive and Sustainable Growth (GROWTH) Programme of the European Union (EU): **GROWTH Project GRD1-2001 – 40084 EOS** (1998-2002)**.** EOS. Low dose X-ray diagnostic imaging: a new modality for planar and three dimensional applications in rheumatology, orthopaedics and chest radiography (2002-2006). The author was the scientific partner at the Hospital Vall d'Hebron, Inst. Català de la Salut, Barcelona (ES) contributing to spine assessment and leading chest assessment. (1)

Disclosure:

The author has no financial or contractual relations with EOS Imaging or Biospace Imaging or affiliated companies excluding the research done under the original research grant of the EU intended to asses the EOS imaging prototype between 2003 and 2006.

(blank page)

Abstract

Introduction: **In this study, the prototype unit of the EOS imaging device was applied to chest imaging to assess its feasibility in a clinical setting**.

The EOS is a new 2D/3D radio-imaging technology that uses a gaseous radiation detector and micro-grid ionization chamber derived from Micromegas, the micro-grid developed by the Nobel Prize winner Georges Charpak and extensively used in high-energy research (eg, CERN, Geneva, Switzerland). The detectors are very efficient and enable low-dose medical imaging by stringent collimation, which avoids the undesired scattered radiation that increases dose and degrades image quality. The EOS prototype uses very thin (500 µm) fan-like x-ray beams and was planned for low-dose standing radiography of the human skeleton. It has two x-ray tubes and two detectors that allow synchronous biplanar linear acquisition of two 90-degree images of the body. The biplanar method was designed for automatic extraction of anatomic reference points that can be mathematically projected as a 3D model of a patient's skeleton. EOS software can build 3D models using lower radiation doses (1/10 to 1/100) than existing systems (computed radiography [CR], digital radiography [DR], or low-dose CT). The main application of the prototype, spine imaging, has been validated, and the subsequent, re-designed industrial EOS (EOS Imaging, Paris, France) has attained certification for skeletal studies.

While preparing the experimental phase of EOS for spine imaging, a second objective was considered: to assess applicability of the EOS prototype to another field of imaging, the chest x-ray, the most common radiologic exam. Chest x-rays could pose several difficulties for a large, linear-scanning, biplanar, low-dose and low-spatial-resolution technique, in this case micro-grid detectors, which would have to be investigated.

Material and methods: A prospective study was designed to assess the clinical feasibility, technical problems, dose and image quality of EOS as compared to a state-of-the-art DR system, the aSi-Csi flat panel detector. Forty adult patients undergoing scheduled chest x-ray examinations at the Erasme University Hospital (Brussels, BE) were recruited for paired examinations using EOS (at 50% dose) and DR. Paired data and images were compiled. Image data sets were independently scored by 4 radiologists according to the European Quality Criteria in Diagnostic Imaging, with additional challenges, such as scoring of thin anatomical structures. The dosimetry data obtained were also compared to those of CR, and experimental laboratory data were compiled on collimation and detector performance.

Results: 37 of 40 cases were available for complete analysis. EOS chest examinations were acquired with a 13,5% repeat rate. Radiation dose (PA) was higher for EOS (0.22 mGy) than with DX (0.05), but less than CR or reference doses (0.3 mGy). Noise and ripple artifacts lowered the MTF (Modulation Transfer Function) to 1-1.5 pl/mm. Image quality scores between EOS and DX were comparable, but with better scores for EOS in several items as air-ways, mediastinum or anatomic coverage.

Conclusion: EOS is feasible for chest imaging and is compliant with the chest reference doses. Radiation dose was higher than with DR, but lower than with CR, achieved by suppressing scatter. EOS image quality scores were not significantly inferior from those of DR, even for thin structures, as the extended density resolution and absence of scatter of EOS compensated for the inferior spatial resolution. Further development is needed to reach better dose containment and improve resolution, with validation in patients having various clinical conditions.

Resum

Introducció: Aquest treball presenta una valoració del primer prototip de l'equip d'imatge mèdica EOS aplicat a la radiografia del tòrax.

EOS és una nova tecnologia d'imatge que fa servir un detector de radiació gasós, una cambra d'ionització de micro-reixeta, derivada del Micromegas desenvolupat per Georges Charpak (Premi Nobel 1992) per recerca en física d'altes energies al CERN (Ginebra, CH). Aquests detectors poden obtenir imatges mèdiques a baixa dosi, permetent col·limacions estrictes que eviten la radiació difusa que degrada dosi i qualitat. El prototip EOS, fent servir feixos de raigs-X molt fins (500 µm), va ser pensat per fer radiografia a baixa dosi de l'esquelet en bipedestació. Dissenyat amb dos tubs de raigs-X i dos detectors, realitza una adquisició per escanejat lineal biplanar sincrònica, de dues imatges (a 90º) del cos. Aquest mètode biplanar permet l'extracció automàtica de punts de referència anatòmics que poden ser matemàticament projectats com un model 3D de l'esquelet real del pacient. El programari EOS pot generar models 3D amb baixa dosi, entre 1/10 i 1/100, de les modalitats existents (radiografia computada (CR), radiografia digital (DR), o TC a baixa-dosi). L'objectiu principal de la recerca d'aquest prototip, la imatge de columna, va ser validat, i el seu subseqüent re-disseny industrial ha acabat com un dispositiu mèdic certificat per a estudis de l'esquelet: EOS ('EOS Imaging, Paris, France)'.

Preparant la fase experimental de EOS en columna, un segon objectiu va ser considerat: valorar l'aplicabilitat del prototip EOS a l'exploració radiogràfica més freqüent: radiografia de tòrax. Si EOS fos validat, permetria aplicar-lo a un altre camp del radiodiagnòstic. La radiografia del tòrax és una prova que pot comportar algunes dificultats en un dispositiu voluminós, d'escanejat lineal, biplanar, amb baixa dosi i baixa resolució espacial, com són els detectors de micro-reixeta, a investigar.

Material i mètodes: Es va preparar un estudi prospectiu comparant exploracions repetides entre EOS i un equip radiogràfic estat-de-l'art (DR, detector pla de aSi-Csi), per valorar l'aplicabilitat clínica, problemes tècnics, dosi i qualitat d'imatge. Un grup de 40 adults, amb radiografia de tòrax programada al Hôpital Univ. Erasme (Brussel·les, BE), van ser enrolats per a fer un estudi repetit amb EOS (amb 50% dosi de CR). Les imatges recollides van ser puntuades independentment per quatre radiòlegs seguint els 'European quality criteria in diagnostic imaging', incorporant reptes com valorar estructures anatòmiques fines. Es recolliren dades tècniques, estudis dosimètrics addicionals, comparatius amb CR, i mesura de dades de dosi i de rendiment del detector.

Resultats: 37 dels 40 casos van ser analitzats. La radiografia va ser correcta amb EOS, amb 13,5% d'estudis repetits. La dosi de radiació es superior amb EOS (0.22 mGy) que amb DR (0.05) però menys que la DRL o dosi per CR. Artefactes de soroll i 'arrissat' redueixen la FTM (funció de transferència de la modulació) mesurada a 1-1.5 pl/mm. La puntuació en qualitat d'imatge entre EOS i DR va ser comparable, amb millor puntuació per a EOS en via aèria, mediastí o en cobertura anatòmica.

Conclusió: EOS és una modalitat funcional que compleix les dosis de referència. La dosi és més alta que per DR i més baixa que per CR, per supressió de la radiació difusa. En qualitat d'imatge, EOS no mostra valoracions inferiors significants a la DR, fins i tot en estructures fines; pot atribuir-se a la resolució més gran de densitats i a l'absència de difusa que compensen la seva inferior resolució espacial. Caldrà fer desenvolupaments addicionals per millorar el control de la dosi i per millorar resolució, i caldrà fer recerca dirigida a validar resultats en sèries amb patologies clíniques.

Chapter Index

(Left Blank)

1 Introduction

The subject of this work is the assessment of the EOS imaging prototype, a novel imaging technology, for chest radiography, still the most common radiographic examination, This imaging device belongs to the family of linear scanning radiography devices. It is based in a new an unusual detector in imaging: a Micromegas, a micro-grid ionization gas chamber detector, developed by Georges Charpak (Charpak's detector) (2–6). This detector can be used as a linear scanning modality allowing the acquisition of a large bi-planar scanned image of the body by concatenation of very thin (0.5 mm) linear x-ray samples exposed to a very thin fan-shaped X-ray beam. The detector derived from multi-wire ionization chambers allowing, by its single photon detection capability, to use a very small radiation dose, but at the same time providing a wider energy resolution than current detectors. EOS applies for its acquisition thin fan shaped x-ray beam conveying much less scattered radiation than current radiographic full-field systems, reducing absorbed dose and improving the effective image resolution by improving signal to noise ratio.

Two of these detectors were combined with their corresponding X-ray tubes in a first prototype, with a sliding vertical frame that allows scanning the body by two simultaneous perpendicular very thin X-ray beams: the EOS prototype. This device was built and assessed by a team lead by Biospace Imaging (Paris, FR), company now renamed EOS imaging), who designed and built the system, and several European partners that helped in dosimetry and clinical assessment. The EOS project was partially financed by the European Community programme GROWTH 2001 as the project Project GRD1-2001 – 40084 EOS**.** **(***EOS*. *Low dose X-ray diagnostic imaging: a new modality for planar and three dimensional applications in rheumatology, orthopaedics and chest radiography)*, between 2001-2005. (1)

EOS technology offered ex-ante advantages in terms of dose reduction, at both patient and operator level, image quality (contrast resolution and dynamic range), image size, which is not limited along the vertical axis and can provide eventually full body exams. The maximum image width is defined by the size of the linear array detector, and the pixel pitch defines the image sampling in this direction. Vertical resolution is defined by the scanning speed and related sampling.

From its initial design EOS was found particularly suited for bone system analysis, both in terms of dose reduction and native image resolution (< 2k pixels wide). The original experimental and pre-clinical target of the EOS device was the acquisition of standing images of

the spine, simultaneous in two orthogonal planes, allowing synchronized bi-plane images of the whole spine. Following this registered bi-dimensional acquisition, a three-dimensional (3D) model of the spine can be calculated by software using the coordinates of the anatomical landmarks automatically extracted from each element of the patient spine. Combining the low-dose, the bi-plane standing acquisition, and the anatomic landmarks with 3D reconstruction software, the EOS device allows displaying patients' skeleton as complete 3D models. EOS only exposes patients to a fraction of current digital radiographic images (1/3rd-1/10th the basal dose of computed radiography or screen-film) while generating planar images. EOS is able to obtain 3D images as computed tomography, but the former will be associated to a dose 10 to 100 folds that of EOS, besides that the CT acquisition would be in horizontal position without bearing weight.

The EOS project had the target to complete, and asses, the development of an operative clinical prototype targeted for low-dose spine applications (planar imaging and 3D reconstruction) previous to its launching as a commercial product. The first clinical evaluations allowed the consortium to successfully evaluate EOS with respect to X-ray film for scoliotic patients (children and young adults). In this first phase of the clinical trials it was only possible to compare film to EOS on scoliotic children and teenagers. 3D information was not fully evaluated. Shortly after, the 3D software reconstruction was completed and assessed, and dose and images comparison of EOS against different digital modalities before the end of the project.

As scoliosis is a 3D complex pathology of the spine, with rotation and tilting of multiple vertebral bodies, the access to a low-dose, weight-bearing, 3D imaging modality, was required (vertical MRI gantries are the alternative for these studies (7–9). The device has been installed in several hospitals in different countries in Europe and America, mostly orthopedic centers, as an imaging product since 2007 (EOS Imaging, Paris, FR). The imaging capabilities of the already installed EOS systems are becoming reported in orthopedics and bone surgery journals for spine, hip or lower limbs pathologies. This modality is being able to provide advantages in diagnosis, prognosis, or surgery planning thanks to its 2D and 3D images, preceding or following orthopedic or surgical interventions in the spine, pelvis or lower limbs.

EOS devices are expensive low dose imaging devices, that can be best financed if they can be concurrently used in other fields than skeletal radiography. Besides spine or pelvic bone imaging, chest imaging, the most common explored by radiography, was an area with a potential for investigation that was added to the initial experimentation of the EOS

prototype. The advantages of the EOS detector contrast/density resolution, and dose reduction over conventional film, computed radiography or digital flat panel detectors, should confront the fact that EOS detectors have less resolution than accepted chest imaging modalities (2 lp/mm), raising questions about the feasibility of using EOS for general planar thorax radiography.

This PhD dissertation presents an assessment of the EOS-1 prototype as an imaging device for clinical chest radiography.

Disclaimer

Clinical thorax imaging (chest imaging) should be considered still considered an off-label clinical application of the EOS device.

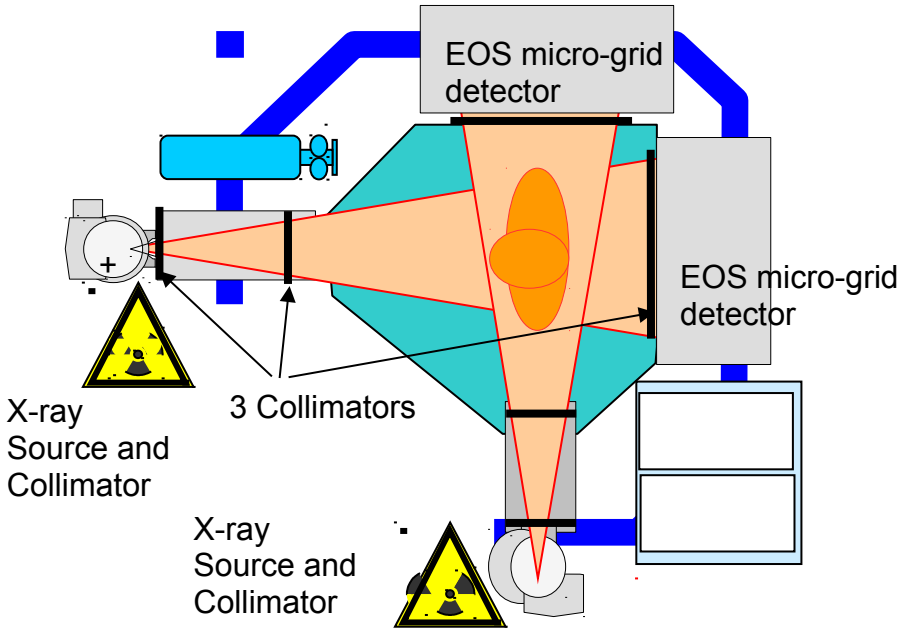

Figure 1. EOS device configuration. Floor view.

Two orthogonal paired x-ray sources and detectors may scan simultaneously the studied upright subject. This modality was designed for spine imaging with 3D reconstruction.

1.1 Radiation Dose, Physics and Health Risks

1.1.1 The discovery of X-rays

Wilhelm Röntgen (1845-1923), a German physicist, discovered a new form electromagnetic radiation the 8th November 1895, while doing essays with high voltage electrical discharges in vacuum tubes. He was studying the behavior of cathode rays (electrons) under different conditions when he started to notice a fluorescent effect on a cardboard screen painted with barium platinocyanide when it was exposed to the radiation of a modified Lenard's tube with a thin aluminum window. Because electrons or light cannot escape from the black opaque cardboard and glass enclosures, he concluded that an unknown type of ray that cross solid materials can be produced if a vacuum tube is energized. He noticed that the new rays generate fluorescent shadows of his own bones, and where able to impress shadows on photographic plates. Two weeks after the discovery he took the first radiography of his wife hand. As he investigated the properties of the new rays he temporarily termed “X-rays”, for something unknown. The news of this discovery were first published in the Viennese newspaper *Neue Freie Presse* (January 5, 1896), but the discovery was promptly praised around world, as the newspaper *New York Sun* (January 8, 1896), adding emphasis in their future utility in medicine. Just one moth later, The Boston Medical and Surgical Journal published the potential for medical application for X-rays (February 13, 1896), and along the next months, several medical imaging applications of x-ray in chest diseases, using fluoroscopy devices, where already published: Tuberculosis, pneumonia, and the first observations of the air-bronchogram (postmortem). The Nobel Prize in Physics 1901 was awarded to Wilhelm Conrad Röntgen “in recognition of the extraordinary services he has rendered by the discovery of the remarkable rays subsequently named after him”. Note. Röntgen is commonly phonetically written as 'Roentgen'. (10–13)

1.1.2 The nature of Ionization radiation and its interactions

X-rays belong to a group of radiations called **electromagnetic radiation**. Electromagnetic radiation is the transport of energy through the space as a combination of electric and magnetic fields Electromagnetic radiation is generated by a charge (usually a charged particle) being accelerated. The converse is also true; a charge being accelerated will emit electromagnetic radiation. Electromagnetic radiation is propagated through the space in the form of waves, with associated wavelength (as meters, symbol **λ**) and frequency (as cycles per second, symbol ***v***), always traveling at the same velocity in a vacuum (3 x10^8 meters per second, symbol **c**). The relationship between velocity, wavelength and fre-

quency may be expressed as:

$$\mathbf{c = \lambda}\ \boldsymbol{v}$$

As the speed **c** is a constant for all electromagnetic radiation, the frequency of the radiation must be inversely proportional to its wavelength. The wavelength of diagnostic X-rays is extremely short, and it is usually expressed in Angstrom units (**Å**). One Å is $1x10^{10}$m. Most X-radiation have a wavelength between 1 and 0,1 Å. Below 0,1 Å the electromagnetic radiation spectrum is considered gamma radiation.

Those such short electromagnetic waves, which are discrete bundles of energy, quantum or photons, that may interact with other particles following the **Planck constant** (denoted ***h)***, that has been determined experimentally to be **4.13×10^{-18} keV sec**

$$E = hc/\lambda$$

The product constant *hc* of the velocity of light *(c)* and Planck's constant *(*h*) is 12.4, and the relationship between energy (E) to wavelength (λ) is inversely related following this formula:*

$$E(keV) = \frac{12{,}4}{\lambda(Å)}$$

Electromagnetic radiation with more than 15 keV of energy, as most X-ray photons, are capable to liberate electrons from atoms, ionizing atoms and molecules, and it is called ionizing radiation. Gamma rays, X-rays and part of the spectrum of ultraviolet rays are all types of ionizing radiation. Gamma rays have wavelength shorter than 0.1 Å. (10,14,15).

1.1.3 Units measuring radiation, and dose

Nowadays, the applied measurement system in radiology physics is the **SI** (Système Internationale d'Unités) compiled by ISO, the International Organization for Standardization. We will use this standard unit system along this work (16–18).

The **unit of ionizing radiation absorbed dose**, as the energy deposited, is the **Gray** (unit Gray, J•$kg^{-1,}$ symbol **Gy**), which refers to the quantity of ionizing radiation absorbed per unit of mass.

The unit to account for the **biological effect of radiation**, so-called dosimetry and **equivalent dose** is the **Sievert** (unit Sievert, J•$kg^{-1,}$ symbol **Sv**). As it is a quite large unit for diagnostic radiology decimal as mSv, cSv are commonly used for examination dose assessment.

The quantity **dose equivalent** (***H***) is the product of the **absorbed dose** (***D***) of ionizing radiation and the dimensionless quality factor (***Q***) defined as a function of linear

energy transfer:

$$H = Q \cdot D$$

*For most of the radiation used in medicine, as X-rays, **Q** = 1, so the absorbed dose and the equivalent dose are numerically equal.*

*In order to avoid any risk of confusion between the absorbed dose **D** and the dose equivalent **H**, the special names for the respective units are be used, that is, the name Gray (Gy) is used instead of joules per kilogram for the unit of absorbed dose D and the name sievert (Sv) instead of joules per kilogram for the unit of dose equivalent H.*

Kerma is the ionizing effect of the radiation field, and absorbed dose is the amount of radiation energy deposited per unit mass (unit Gray, Gy, symbol **K**).

Radiation fluence is the number of radiation particles impinging per unit area per unit time (unit m^{-2}, symbol **Φ**) .

International System (SI) units of use in external radiological protection and dosimetry, and their relationship are presented in figures 2 and 3:

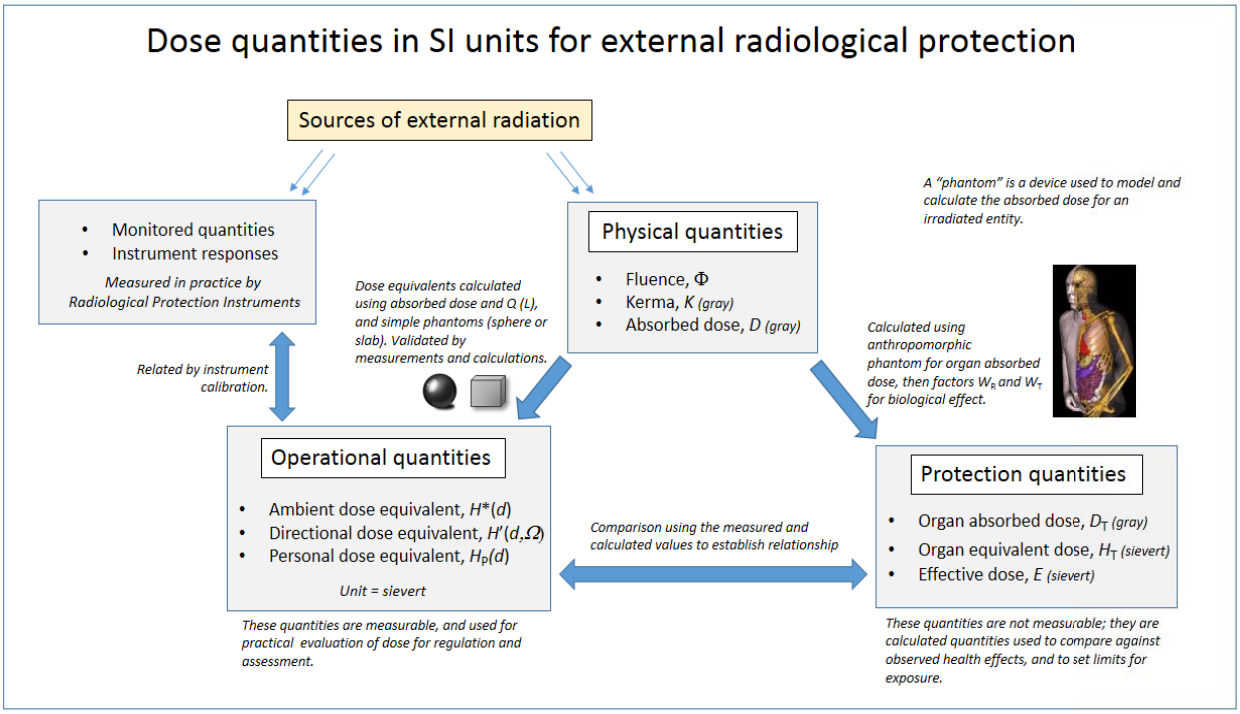

Figure 2. Dose quantities in SI Units for external radiological protection

Original graphic by Doug Sim, CC-BY-SA-3.0 Original from here: http://commons.wikimedia.org/wiki/File:Dose_quantities_and_units.png

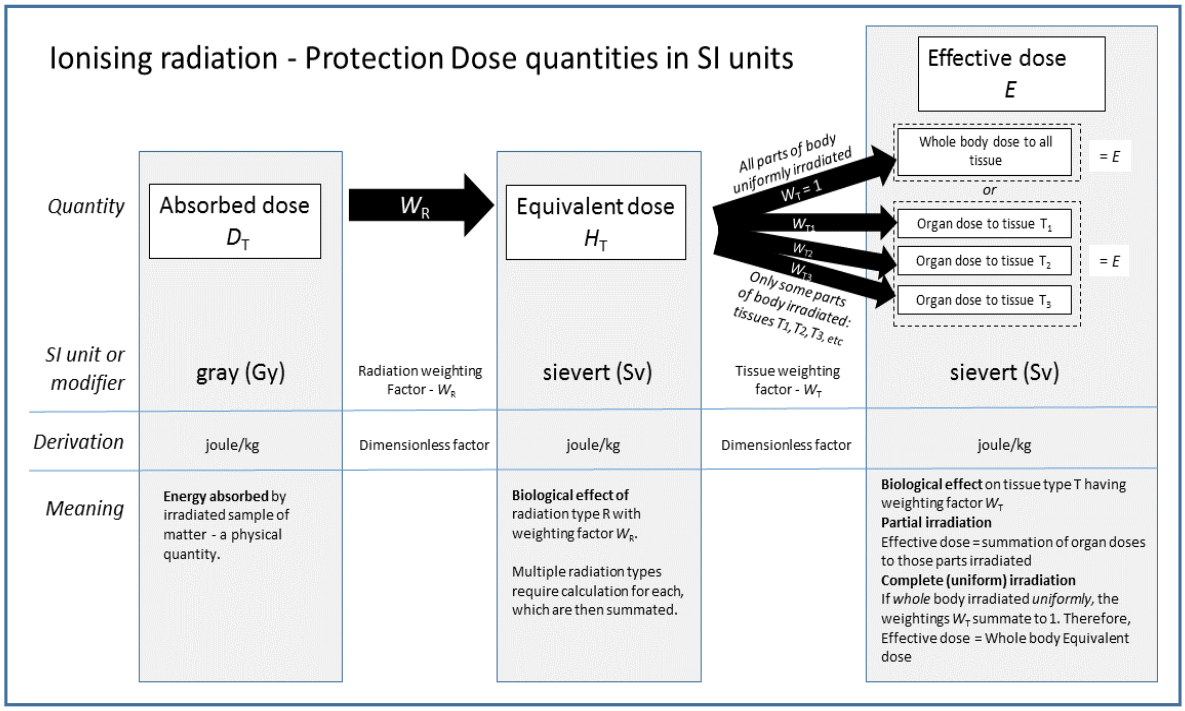

Figure 3. Radiation Protection Units, SI dose units: gray, sievert

Original graphic by Doug Sim, CC-BY-SA-3.0 Original from: http://commons.wikimedia.org/wiki/File:Graphical_relationship_of_SI_radiation_dose_units.svg)

1.1.4 X-ray Generation

X-rays used in diagnostic imaging are generated in a X-ray tube, which consists of a vacuum tube with a cathode and an anode. At the cathode, a current is applied to heat a filament, which releases electrons by thermal excitation. These electrons are accelerated toward the anode by a voltage applied between the cathode and the anode. The electrons hit the anode at high speed and release their energy, partly as heat, partly in the form of X-rays. The process is inefficient, as only 1% of the energy is generated as X-radiation; this is a limiting factor for high output X-ray tubes that have been addressed in the design of modern x-ray tubes (10,14,15).

1.1.4.1 Energy of X-ray Beams

X-ray are generated by energy conversion of the kinetic energy of accelerated electrons colliding with the atoms of the target. This happens in two processes: as **general radiation ('bremsstrahlung')** and as **characteristic radiation**, depending on the interaction of accelerated electrons with anode target atoms, usually tungsten. In the process of general radiation, the negative high speed electron interacts with several positive atomic nuclei slowing down, in stages, and releasing its kinetic energy directly in the form of several photons. If the electron, eventually, collides head-on with a nucleus all the energy of the

electron will be released as a single x-ray photon. In the process of characteristic radiation the high speed electrons eject electrons from the inner orbit (K-shell) of the target atoms. Bremsstrahlung yields a continuous X-ray spectrum, that represents most of the X-ray generation, while characteristic radiation yields characteristic peaks superimposed onto the continuous spectrum, at a few discrete frequencies, sometimes referred to as the spectral lines.

The voltage applied to an X-ray tube is expressed as **peak kilovoltage** (**kVp**). Adjusting this parameter the operator set the maximum voltage across the tube, as the applied voltage pulsates between a lower and a peak value in common x-ray generators. After applying 100 kVp to an X-ray tube, few excited electrons will acquire up to 100Kev of kinetic energy, most of them less. The spectrum of energies of the accelerated electrons that impact the anode, in addition of several stage interactions generate a spectrum of electromagnetic radiation, 1% of X-ray, but most of the energy is wasted as heat (99% is heat, with wavelengths longer than 0.124 Å). As being stated, general radiation is the main process in the X-ray generation process, as below 70 kVp there is no characteristic radiation, at 80 kVp is about 10%, increasing with the kVp, so at 150 kVp if goes up to 28% share (10,14,15).

1.1.4.2 Intensity of X-ray beams

The intensity of an x-ray beam is defined by the number of photons in the beam multiplied by the energy of each photon. This intensity depends on the kilovoltage peak, the x-ray tube current, the anode target material and the filtration.

A high atomic number of the anode material (as Tungsten) determines that most of the x-rays generation will be efficient and mostly as general radiation ('bremsstrahlung'). Reducing the atomic number reduces the yield of the X-ray tube, as happens by reducing the kVp. Using a low atomic number and low kVp (as Molybdenum) makes that characteristic radiation assume greater importance. Summarizing, the target material and the kVp impact the wavelength, energy, spectrum and penetration of an x-ray radiation.

The current intensity applied to the cathode filament of an X-ray tube is expressed as **mA**. The number of excited electrons on the cathode depends on the tube current (mA) used. The greater the mA the more electrons produced: consequently more x-rays will be produced. Taking in consideration the period of time (sec) while the filament current (mA) is applied, we obtain an operational unit 'mA x sec' (expressed as **mAs**) that is proportional to X-ray exposure. This is a common technical parameter used in radiography, that linearly

corresponds to the final radiation exposure. Summarizing, x-ray tube current match the amount of x-ray generated and has a direct relation to final x-ray exposure (10,14,15).

1.1.5 Interaction of X-ray with matter

Although photons with energy less than 13.6 keV are non-ionizing, being only are able to raise atom's shell into a higher energy level, a process called excitation, photons with higher energy, ionizing photons, can interact with matter in different ways (10,14,15) :

The energy of X-ray photons can be absorbed by an atom and immediately released again in the form of a new photon with the same energy but traveling in a different direction. This non-ionizing, elastic, process is called **Rayleigh scattering** or coherent scattering and occurs mainly at low energies (<30 keV). The lower the energy the higher is the scattering angle. In most radiologic examinations it does not play a major role because the voltage used is typically in the range from 50 to 125 kV. However, for mammography, as the voltage is lower (22–34 kV), Rayleigh scatter cannot be neglected. (10,15,15,19,20)

A photon can be absorbed by an atom while its energy excites an electron of an inner atomic shell leaving the atom in an excited state. The electron then escapes from its nucleus **in the same direction as the incoming photon** was traveling. This mechanism is called **photoelectric absorption,** and it is the expected interaction for diagnostic imaging, because it conveys information (energy) in the same direction than the original beam, allowing precise depiction of morphology and density. X-ray spectrum depends on the possible transitions following a photoelectric interaction that involve the K, L, and M shells, resulting in the emission of characteristic x rays and Auger electrons. Some of this photoelectric electrons. (10,14,15,21,22)

A third possibility is that the photon transfers only part of its energy to eject an electron with a certain kinetic energy. The electron then escapes in another direction. In that case, a photon of the remaining lower energy is emitted and its direction deviates (secondary x-ray) from the direction of the incoming photon (primary x-ray). This process is called **Compton scattering**. At the diagnostic radiology energies a large portion of the photons engage in Compton interactions and produce **scatter** (or **scattered radiation)**. Some of this scattered radiation leaves the body in the same general direction as the primary beam and exposes the image receptor. In fact, in most radiographic or fluoroscopic procedures, the major proportion of the x-ray beam leaving the patient's body is scattered radiation, which reduces image contrast. The degree of lost contrast depends on the scatter content of the radiation emerging from the patient's body. For these reasons, this is a common, but

the least desired, interaction in diagnostic imaging. (10,14,15,20,23–25)

A fourth and fifth mechanism of interaction are not related to diagnostic radiography energies. If the energy of a photon is at least 1.02 MeV, the photon can be transformed into an electron and a positron (electron–positron pair), it's a **pair production**. A positron is the antiparticle of an electron, with equal mass but opposite charge. Soon after its formation, however, the positron will meet another electron, and they will annihilate each other while creating two photons of energy 511 keV that fly off in opposite directions. This process finds its application in PET imaging studies (26,27). At still higher energies, photons may cause **nuclear reactions**. (10,14,15).

1.1.6 Scattered radiation and Diagnostic imaging

Scattering radiation is the phenomenon where secondary x-ray photons are generated within the body, or within exposed materials surrounding it, contributes to the total dose. This radiation has low energy and its direction is aleatory. In diagnostic radiology, it is noticeable following the increments with incident energy, over 50 keV, and with density and volume of the specimen, but is present along the whole diagnostic energy spectrum (10,14,28,29). The ratio of the scatter fraction, scatter radiation to total radiation, grows related to x-ray beam energy, but becoming more relevant as when we exceed 70 keV. For current diagnostic imaging energies between 80 and 150 keV scatter-to-primary ratio can be up to 7.9, adding dose and anisotropic noise (image fog) (30,31). The irradiated volume is also a main component in scatter production, so very thin collimation may reduce scatter formation to a not perceptible level but requires non-standard equipment for full field imaging (32).

In order to remove scatter, and improve contrast, radiographic **grids** are used, since its invention by Dr. Gustave Bucky in 1913, in most from large field x-ray exams. Grids consist of a series of lead foil strips separated by x-ray transparent spacers, manufactured as a flat plate. Grids (or '**Bucky**') have the spaces between the lead strips oriented, focused, towards the focus so primary beam x-ray photons, coming straight from photoelectric interactions cross neatly the grid, and multi-directional scattered photons, coming from Compton's interactions, are attenuated by lead strips. The main characteristics of a radiographic grid are 'grid ratio', the ratio between the height of the lead strips and the distance between them, 'grid pattern', but nowadays almost all radiographic grids are focused, meaning that the strips are convergent to the focal distance, and lines per cm, that corresponds to the number of lead strips and interspaces per cm. Most grids have grid ratios between 8:1 to 12:1 to balance scatter attenuation, contrast, and patient dose. (10,14,25,28)

The ideal grid does not exist. Lead strips not only attenuate scatter but a part of the primary radiation. Grids with a high ratio gives better contrast but at the price of increased patient exposure. Grid attenuation of the can be assessed with three parameters; Primary transmission factor, contrast improvement factor, and Bucky factor. Bucky factor is used as a simple operational parameter, that allows to derive from a known exposure without a grid, the required exposure if the exam is performed with a grid, by multiplying the original mAs by the Bucky factor (usually x3 to x5). The dose to the patient follow this multiplied exposure, therefore grids should be avoided whenever it may be feasible as in small children, where the body size and moderate kVp technique does not convey a significant scatter fraction. (10,33–36)

An alternative method to control scatter has been '**air gap techniques**', used in magnification radiography and in chest imaging. With air gaps, scatter radiation decreases not from filtration but from scattered photons missing the detector. The focal-detector distance should be increased to avoid magnification. A usual chest x-ray air-gap configuration would be with 25 cm air and focal distance of 3 m, but still has slightly greater magnification than conventional techniques. Patient exposures are usually much less with air gaps than with grids (reduced by a factor of 3.8 compared with a 12:1 grid), because grids absorb primary photons. (10,14,28,37–41).

The last alternative for scatter reduction is **slot scanning** devices, that have inherently less scatter but also have the potential for motion artifacts, especially with young noncompliant patients. (28,42–46)

In chest imaging, where the irradiated volume is a large field of 43x43cm, and optimum imaging energies are in the range of 120 to 150 keV, is mandatory to filter scatter otherwise a 'scatter fog' will darken and blur the image. It has been achieved with grids, rotating slits, sliding slot collimators, air gaps, or slot detectors. (37,41,43,47–50)

The EOS prototype assessed in the present work addresses the issues of dose, and contrast by using scanning x-ray source and detector, with two very thin x-ray collimators of 0.5 mm: one before the entrance surface of the patient and a second at the detector window, so scatter will be reduced, with the aim of reducing absorbed dose and improving image contrast. Related x-ray scanning approaches, by modulation of a narrow/thin x-ray beams, and film, CCD scanning, or image-intensifier x-ray detectors, or a reverse approach where x-ray source is a scanning electron beam over a large focused target, has been reported in the literature. (4,44,47,51–54)

1.1.7 X-ray Detection and Image Quality

To obtain an image from the attenuated X-ray beam that crossed the patient, the X-rays need to be captured and converted to image information. The oldest detectors where fluorescent screens, superseded by **screen-film** and nowadays by several families of **digital detectors**. The common characteristic is that all these systems provide a transducing media surface where invisible x-ray is converted to chemical latent image, visible spectrum light or an electric signal. Radiographic film was itself an inefficient detector as the interaction volume of the detection media is very thin (a thin gelatin layer with embedded silver halide grains). Phosphorescent 'intensifying' screens where present in almost all radiographic systems as they provide an intensification factor between x15 o x50 allowing a parallel reduction of radiation exposure to obtain the same image. Thicker or more efficient intensifying screens (rare hearth salts), or coarser silver halide grains, allow to have better x-ray sensitivity, reducing required exposure, but at the price of image graininess and image blur. This trade-off between image quality and dose is present, and should be considered, for any imaging technology. The detective quantum efficiency (**DQE**) and the effective DQE (**eDQE**) are relevant metrics of image quality for digital radiography detectors and systems, respectively. In a-Se detectors, photoelectric interaction electrons start to play a significant role in degrading the DQE at two cycles/mm at an incident photon energy of 80 keV. A new metric for radiography, effective dose efficiency (**eDE**), has been proposed, measuring the normalization of the eDQE by the effective dose (**ED**) as a application-specific metric of imaging performance. EDE is reflective of the body habitus, as pediatric or adult, and radiographic technique, with utility for radiography protocol assessment and optimization. (10,14,15,55–57)

1.1.7.1 Quantum Mottle and Image Noise

Quantum mottle, usually detectable as graininess or 'snow', results from the statistical fluctuations in the number of x-ray photons (quanta) absorbed per unit area by the detector. It depends on detector efficiency. Besides quantum mottle, other sources of noise are **electronic noise** in the image acquisition chain. Nevertheless, the presence of noise is considered a desirable feature, under the current awareness on dose exposure, as it translates a relative low exposure for a given x-ray detector (10,14,15,28,58–62)

1.1.7.2 Receptor Sensitivity, System Speed, latitude

Sensitivity is the exposure required in mR to produce an equivalent film (or image) density of 1 unit above the base plus fog level. The **system speed** scale compares the relative exposure requirements of different receptor systems. Most speed numbers are refer-

enced to a standardized film density protocol, so-called **par speed** system that is assigned a speed value of 100, with a required exposure of 1.28 mR. The relationship between sensitivity and speed follows this formula:

Sensitivity (mR) = 128 / speed

The most common speed values in current digital systems are between 400 (0.32 mR) and 800 (0.16 mR), but they can be raised to 1200 (0.1 mR) in order to reduce exposure. Digital detectors can be forced to behave as more sensitive, faster, by increasing the detected quanta gain, with the usual trade-off of increased noise. Speeds below 200 (0.64 mR) are restricted to bone, mammography or special applications.

Associated to sensitivity are latitude and linearity, that are the main advantages of new digital detectors. **Latitude,** or **dynamic range**, is the operational range of energies of an x-ray exposure that can be registered, from the minimum level of detection, the sensitivity threshold, to the maximum, or saturation threshold. **Linearity** is the shape of the response relationship between exposure and detected photons (= image density); it was referred in screen-film systems as "**characteristic curve**", because it follows a curve function with a 'S' shape. The linearity permits to predict the degree of change in image display density, after a change in the radiation exposure. The main advantages of digital detectors over old screen-film systems, besides direct PACS integration, are in latitude (x100) and almost flat linearity at their nominal range. Quantum mottle can be noticeable in high sensitivity low-dose detectors and it is related to high detection efficiency with low fluence. (10,14,61,63,64)

1.1.7.3 Image Quality, Contrast, Blur, Resolution and MTF

The visibility of anatomic and pathologic features in a radiographic image depends on contrast and image quality. **Contrast** refers to the difference in density, between gray levels, in the radiographic image, that depends on subject contrast, radiation quality, detector performance, and fog and scatter. High kVp technique, associated to low-dose radiography, reduce contrast as many photons will have enough energy to cross patient. Digital detectors are able to amplify contrast, using its wider dynamic range and better linearity, allowing current high kVp techniques.

Fog, caused by scattered radiation, is the unwanted exposure reaching the image detector, that adds an undesired density background that reduces general image contrast.

Blur or **image unsharpness** is the lost of precision of a shape caused by the combination of geometric, motion, absorption, and detector unsharpness. No medical imaging method

produces images that are free of blur. The contrast of the larger objects is not affected, as the loss of contrast caused by blur increases with decreasing object size. For objects that produce relatively low contrast, even without blur, the threshold of visibility might occur at object sizes larger than the point at which blur produces zero contrast.

Resolution describes the ability of an imaging system to resolve or separate objects that are placed very close together, and it is determined by the amount of blur. It is expressed as resolving power of n lines per mm. The resolution depends on the detector design, efficiency, and noise. ie. lateral cross-talk of the scintillation light between the individual crystals in solid state detectors. The test object used for this purpose consists of a ruler with several patterns of parallel lead strips separated by a distance equal to the width of the strips. The common practice is to describe resolution as line pairs per millimeter (lp/mm). One line pair consists of one lead strip and one adjacent separation space. Current digital radiography systems have a spatial resolution from 2.5 to 5 lp/mm.

The **modulation transfer function** (**MTF**) is an objective measurement of the combined effects of sharpness/blur and resolution on exposure amplitude (contrast), as the ability of a system to image different spatial frequencies is related to the amount of blur present. Rather than line pairs, a true MTF test object has peaks and valleys, and is derived from a line spread function, where the test object may be a very thin slit (10 μm) on a highly opaque metal (platinum).

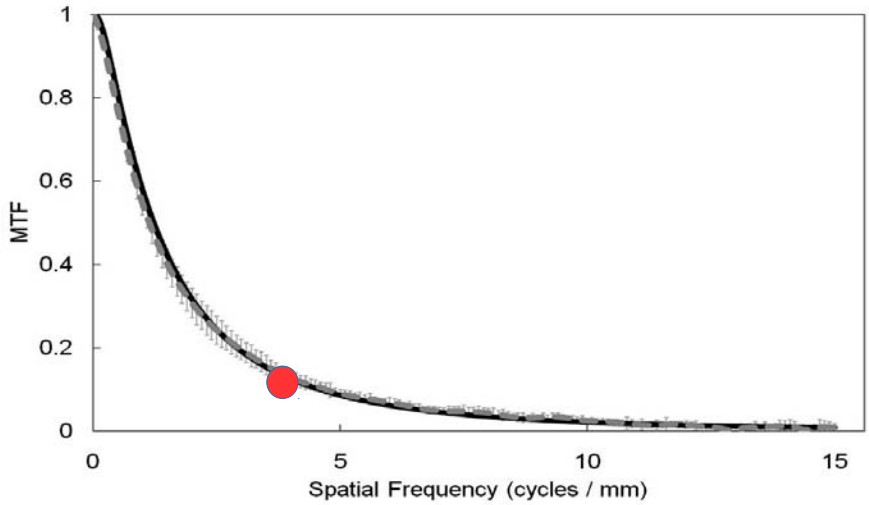

Figure 4. Modulation transfer function (MTF) curve.

The system has a MTF of 0.1 at 4 lp/mm. Meaning that the ratio of output information versus input information is 10% (contrast/resolution). Modified form Kuhls-Gilcrist (2010)

MTF represents the ratio (as %) between information recorded to information available, and therefor never can be greater than 1. MTF can be calculated as MTF = exposure am-

plitude output / exposure amplitude input. In a complex image acquisition chain, the final MTF is the result of multiplying each individual component MTF value, and will depend on the lowest MTF. It is usually presented as a graphical description (**MTF curve**) of the blur, or resolution characteristics, of the complete imaging chain, or of its individual components. (10,14,15,61,65–71)

1.1.7.3.1 Image quality requirements in biology: spatial resolution and contrast

The basic functional unit **BFU** of organs seems like a reasonable goal for the highest spatial resolution of clinic imaging systems. BFUs are the smallest accumulations of diverse cells that function like the organ they are in, e.g., the hepatic lobule in the liver or nephron in the kidney. Generally, they occupy about 0.01 mm3, i.e., about 200 #m in diameter. The volume of a BFU is considered the upper limit of a spherical assembly of cells, immersed in a suitable nutrient medium, which can survive without its own blood supply. However, each BFU has its own capillary blood supply to support the extra energy needed for the physiological function -i.e. secretion or filtration- of the BFU. Similarly, early “solid” cancers could grow to this size in perfused tissues before a blood supply is needed to sustain further growth. (72,73)

BFUs differ little in x-ray contrast from surrounding tissues because they are elementally not very different from the connective tissue in which they are embedded. It is difficult for attenuation-based x-ray as CT imaging. With current attenuation-based x-ray imaging, exploitation of any attenuation-based contrast difference would require either very high radiation exposures to provide the signal-to-noise ratio needed for discriminating these tiny BFUs from their surrounding tissue matrix, or would require administering a contrast-enhancing agent generally involving a high-Z element such as iodine that selectively delineate, as positive or negative contrast, BFUs. The goal for improves contrast resolution is to have the modulation of the transmitted x-ray signal be greater than the noise in that signal for unequivocal detection of the signal. However, contrast depends radiation exposure, sensitivity of f x-ray detection by improved detector efficiency, and by increasing specificity by rejecting scattered x rays which adds noise, without use of anti-scatter grids, and by use of X-ray of narrow spectrum by beam filtration or, ideally, by using a monochromatic radiation source. (72–76)

1.2 The Risks of Diagnostic Radiology

The somatic effects of x-ray where reported very early after the discovery of X-rays.; by the end of 1896, 23 cases of severe X-ray induced dermatitis had been reported; three sci-

entific reviews published between 1911 and 1914 had collectively identified 198 cases of radiation-induced cancers resulting in 54 deaths (77).

The role of diagnostic imaging in current practice of medicine is so well established that is impossible to imagine making diagnosis, planning therapy, or following the course of most diseases without radiologic images. But radiology uses in many of their imaging activities the interaction of ionizing radiations with the matter of obtain images that by different transduced signals and contrasts depict normal or pathologic morphology and function. The problem is that we have realized that ionizing radiations are a proven human carcinogen, down to doses of around 50–100 mSv, but the current risk estimates that inform health protection strategies are based on the assumption that all radiation exposures pose a risk in linear proportion to the dose. Without medical exposure, on average, a citizen receives an annual effective dose from natural sources of 2.2 mSv. Natural sources are radon emissions, cosmic rays, etc. Medical exposure has been growing exponentially, and in some countries has almost surpassed the natural exposure dose. Exposure to radiation in some contexts elicits fear and alarm (nuclear power for example) while in other situations, diagnostic x-rays for example until recently at least, it was accepted with alacrity. (78–90)

The concerns over the radiation dose coming from radiology have been reported for more than 60 years, bearing to procedure and technology improvements that have allowed to reduce the dose per procedure over the last decades. The number of examinations per inhabitant/year in different countries present a wide rank: from 0.48 for the UK to 1.7 for Germany. The annual per capita effective dose also varied from 0.38 mSv for the UK, 0.59 mSv for The Netherlands,1.34 mSv for Switzerland, to 2 mSv for Germany. (91–97)

The largest single source of radiation exposure to the population is from computed tomography. As CT usage over the past quarter of a century has increased about 12 fold in the UK and more than 20 fold in the US. Among OECD countries, between 50 and 90% of the collective population dose from diagnostic x-rays comes from the few high-dose procedures, such as interventional radiology, CT scans, lumbar spine x-rays and barium enemas. (80,94–110) One element of concern in cancer risk is that the number of CT exams per relative population is growing and have a large variation among the OECD countries, between 50 to 490/1000 person·year. These number translates the problem of unrestricted exposure depending on multiple factors installed base, local availability, lack of controls, costs, legal restrictions or economic incentives. (103,111–114)

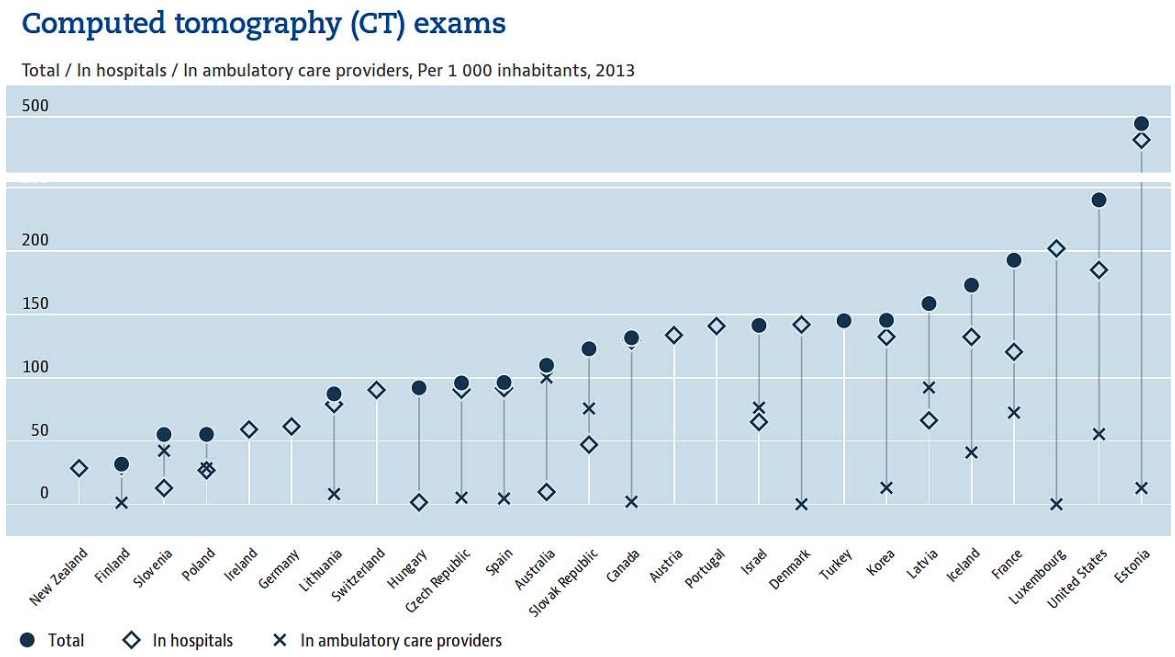

Figure 5. OECD figures for Computed Tomography (CT) exams (2013).

Total, in-hospital, and outpatient data from 26 OECD countries, from private and public health systems. Some countries (i.e. Spain) does not provide data from the private sector, so outpatient number may appear incorrectly low.

1.2.1 Radiation Damage to Biological Tissues

Biological damage following radiation exposures is divided classically in major segments: Deterministic effects, which happens after very high exposures and related to the amount of dose, and stochastic effects, that may happen years later down the life, dependent on nominal risk (sex, age, beside individual susceptibility). (10,115,85,116–119)

1.2.1.1 Deterministic effects:

Deterministic effects are those where the severity of the effect increases with the size of the dose and above a certain threshold dose, the clinical effect is almost certain to appear. These are tissue reactions (injury in populations of cells) which in some cases are modifiable by post-radiation procedures including biological response modifiers. Deterministic effects were of primary concern, and the protection guidelines, primarily aimed at the radiation worker, grew out of the radiologists' endeavors to establish a maximum 'dose' that could be tolerated, more or less continuously by the human body. It should be stated that in the current clinical practice of radiology, deterministic effects are rare, either caused by an accident, poor operational technique, or in isolated high dose interventional radiology procedures, where dose may exceed the threshold for transient erythema (> 2Gy) or threshold for temporary epilation (5-10 Gy). (120–122)

1.2.1.2 Stochastic effects

Effects resulting from damage in a single cell for which the probability of the effect, but not the severity, is proportional to the size of the dose. Genetic effects and cancers are the principal stochastic effects of radiation. For radiation protection purposes, it is assumed that there is no threshold dose for stochastic effects. (123–125)

In the literature, factors can be found that relate the equivalent organ or tissue dose to the risk of stochastic effects. For example, lung cancer occurs on average in 114 cases per 10 000 persons per sievert, yielding a so-called "*nominal risk coefficient"* of lung cancer induction of 1.14%/Sv. (124).

In order to avoid these risks, the annual limit for professional exposure has been reduced progressively to from 50 mSv/year to 20 mSv/year (averaged over defined periods of 5 years), in order to avoid surpassing 1 Sv in a full working life. For general population exposures, excluding medical exposures, ICRP concluded that lowering the annual effective dose limit from the earlier 5 mSv/year to 1 mSv would be appropriate (also a 5-year averaging was allowed in exceptional circumstance) (124,77)

1.2.1.3 Non Linear Threshold (NLT) limit debate

Since 2005, a debate over the current evidence on the effects of low doses of ionizing radiation, on whether there a low-dose limit without biological harm. The National Research Council (USA) concluded that current scientific evidence is consistent with the linear no-threshold dose-response relationship (NRCNA 2005), while the French National Academies of Science and Medicine concluded the opposite: the NLT assumption may greatly overestimate the carcinogenic effects of low doses (<*100 mSv*) and even more that of very low doses (< 10 *mSv*), such as those delivered during X-ray examinations. Nevertheless, advances in human genetics and radiation genetics, as baseline knowledge of frequencies and complex patterns of inheritance of genetic diseases, are forcing a complete re-appraisal of accepted risk. Currently the major component of radiation health risk is considered to be cancer, but there are other potential health effects as germline mutations increasing disease burdens in future generations and possibly heart disease. The most significant change from 1991 has been the six to eight-fold reduction in the risk coefficient for genetic effects. This reduction comes about mainly because the ICRP has chosen to express such risks up to the second generation rather than at a theoretical equilibrium. For cancers, the nominal risk coefficients were based on lifetime *incidence* estimates corrected for effects at low doses using a dose- and dose-rate reduction factor of 2. (90,126–132)

Exposed Population	Cancers		Genetic effects		Total	
Population	2007	1991	2007	1991	2007	1991
Whole	5.5	6	0.2	1.3	5.7	7.3
Adult	4.1	4.8	0.1	0.8	4.4	5.6

Table 1: detriment-adjusted nominal risk coefficients of ICRPs 2007 vs 1991 (in percent per Sv, or $\times 10^{-2}Sv^{-1}$) after exposure to radiation at low dose rate for cancer and genetic effects

New research, as the 2015 study on a large cohort (INWORKS) of 308297 nuclear workers (from France, UK, and USA), with an assessed colon average dose of 20.9 mSv (median 4.1 mSv, 90th percentile 53.4 mGy, maximum 1331.7 mGy). For doses below 200, 150, and 100 mGy showed that the estimated excess relative rate per Gy for all cancers other than leukemia were not driven by the highest dose categories. This study suggested again a linear no threshold increase in deaths by solid tumors after low dose expositions, with an excess relative death rate between 0.46 to 0.51 per Gy. (133)

1.2.1.4 Individual Risks

1.2.1.4.1 Children

Young and growing children have higher radiation sensitivity than adults and have a longer life expectancy. Therefore, imaging techniques that do not use ionizing radiation should always be considered as an alternative. Nevertheless, increasing numbers of radiological examinations are being performed in infants and children, and millions of children undergo high dose procedures such as computed tomography and interventional procedures. Pediatric radiological procedures should be individually planned and, technique and dose should be limited to what is absolutely necessary for a diagnosis. When CT use is justified, the radiation doses from CT scans must be kept as low as possible and appropriate for the size and weight of a young patient. (79,134,124,135–140)

1.2.1.4.2 Pregnancy

Pregnant women are subjects of special protection. The potential biological effects of in-utero radiation exposure of a developing fetus include prenatal death, intrauterine growth restriction, small head size, mental retardation, organ malformation, and childhood cancer. The risk of each effect depends on the gestational age at the time of exposure, fetal cellular repair mechanisms, and the absorbed radiation dose level. A '10-day rule', was established by the International Commission on Radiological Protection (ICRP), stating that "whenever possible, one should confine the radiological examination of the lower ab-

domen and pelvis only during the 10 days following the onset of menstruation, to minimize the potential for performing x-ray exams on pregnant women. The original proposal was for 14 days, but this was reduced to 10 days to account for the variability of the human menstrual cycle. In most situations, there is growing evidence that a strict adherence to the "ten-day rule" may be unnecessarily restrictive. When the number of cells in the conceptus is small and their nature is not yet specialized, the effect of damage to these cells is most likely to take the form of failure to implant, or of an undetectable death of the conceptus; malformations are unlikely or very rare. Since organogenesis starts 3 to 5 weeks post-conception, it was felt that radiation exposure in early pregnancy couldn't result in malformation. The main risk is that of abortion if the radiation exposure results in death of the conceptus. It requires a fetal dose of more than 100 mGy for this to occur. Based on this, it was suggested to do away with the 10-day rule and replace it with a 28-day rule. This means that radiological examination, if so justified, can be carried throughout the cycle until a period is missed. Thus, the focus is shifted to a missed period and the possibility of pregnancy. If there is a missed period, a female should be considered pregnant unless proved otherwise. In such a situation, every care should be taken to explore other methods of getting needed information by using non-radiological examinations. (141–148)

1.2.1.4.3 Congenital syndromes with increased risk

Several congenital syndromes, usually associated to spontaneous primary neoplasms bear an increased risk of DNA damage, with secondary radiation induced neoplasms: Retinoblastoma, Neurofibromatosis type 1 (NF1) and type 2 (NF2), Li-Fraumeni Syndrome, Ataxia-telangiectasia, *BRCA1* and *BRCA2* carriers, xeroderma pigmentosum, Bloom syndrome. In this cases, wise use of diagnostic radiology is required to avoid unnecessary risk for secondary malignancy. (123,125,149,150)

1.2.2 The measurable biological effects

There were four basic radiation principles guiding the radiation protection committees in the mid-1950s, all of which emerged from extensive work with Drosophila on the induction of mutations primarily in mature spermatozoa: (1) Mutations, spontaneous or induced, are usually harmful. (2) Any dose of radiation that reaches the reproductive cells entails some genetic risk. (3) The number of mutations produced is proportional to the dose such that linear extrapolation from high dose data provides a valid estimate of low dose effects. (4) The effect is independent of the rate at which the radiation is delivered and of spacing between the exposures (85,77).

New methods and instruments coming from the fields of genetic research and molecular

biology allow in-vivo appraisal of morphology and function, at the scale of a single cell or complex tissues, at unprecedented detail. Diagnostic levels of radiation, at the doses of a single standard CT (10 mSv), are now associated to DNA double strand breaks, which is followed by in-vivo repair in most cases, that widely depends on individual susceptibility factors (as genetic disorders mentioned). The effects of very low exposure, at the level of professional exposure in the range of 1mSv/year are associated a demonstrable mutations, that subsequently express mutated proteins, that subsequently modify biological parameters as blood cell count. Other research are validating translocation analysis as a valid retrospective biodosimetry for cases of occupational exposure. (151–163)

Meanwhile, it would be prudent to assume that the low dose of radiation received during imaging studies, produces a small additional risk of radiation-induced solid cancers compatible with the predictions of conventional linear dose-response risk models, and clinical practice should be guided by this assumption. (80,85)

1.2.3 The recommended ALARA strategy

ALARA stands for '*As low as reasonably achievable*', meaning that the exposition to ionizing radiation should be kept at the lowest achievable level while it provides sufficient image quality. This is achieved by a set of principles that apply equally to all controlled exposure situations; includes justification, optimization of protection and application of limits on maximum doses in planned situations. Justification refers to the process of determining whether either (a) a planned activity involving radiation is, overall beneficial, i.e., whether the benefits to individuals and to society from introducing or continuing the activity outweigh the harm (including radiation detriment) resulting from the activity; or (b) a proposed remedial action in an emergency or existing situation is likely, overall, to be beneficial, i.e., whether the benefits to individuals and to society (including the reduction of radiation detriment) from introducing or continuing the remedial action outweigh its cost and any harm or damage it causes. Optimization is the process of determining what level of protection and safety makes exposures, and the probability and magnitude of potential exposures as low as reasonably achievable, economic and societal factors being taken into account. The dose limit is the value of the effective dose or the equivalent dose to individuals from planned exposure situations that shall not be exceeded. Dose limits are determined by regulatory authorities and apply to workers and to members of the public in planned exposure situations, but do not apply to medical exposure of patients, or to public exposures in emergency exposure situations, or to public exposures in existing exposure situations. (164–171)

Intercenter technical variability is an important issue, that depends on local obsolete protocols, re-training of radiographers and quality control than the age or model of the radiology technology. The risk for overdose in digital radiography studies has been reported with concern, as digital systems correct the density, both for under- and over-exposed images. In fact, overexposed images may look better, by a frequently unremarked alarm sign: the lack of image noise in overexposed images. This only can be addressed if exposure parameters, dose, DAP, or exposure index, are presented or trigger an alarm related to predefined tables or statistical usage patterns. (172–178)

Several specific initiatives participated by scientific societies, governmental organizations and the imaging manufactures are promoting the ALARA principles, mostly oriented to CT and fluoroscopy studies: Image gently, Image wisely, and Eurosafe imaging with several subgroups EMAN (European ALARA Network) PIDR (Pediatric reference levels). (33,179–181)

1.2.4 Scoliosis Radiation Risk and the EOS motivation

Scoliosis is defined as a lateral deviation of the vertebral spine in the coronal plane with a Cobb angle greater than 10º and rotation of the vertebral bodies (182–184). The total number of radiographs needed for monitoring scoliosis patients varies, but in some cases, imaging follow-up is performed every 4 to 6 months until skeletal maturity is completed. This may involve more than 22 full-spine radiographs, and the number is much higher in patients with severe scoliosis who undergo surgical treatment. (185–191) The exposure to ionizing radiation incurred during these examinations leads to a higher risk of death due to breast cancer in scoliosis patients compared to the general population. Hence, it is imperative to implement measures focused on reducing the radiation dose by optimizing the imaging technique used. (186,192–195) Alternative radiographic procedures as scanning fluoroscopy with digital stitching of collimated digital spots allows reducing the dose more than computed radiography standards but with low spatial resolution. (196–198)

Considering 3D planning the alternative for bony spine structures is helical CT., but with a dose burden of 7.76 mSv with standard techniques, that can be reduced to 0.33 mSv with a helical CT optimized dose (199,200). Upright or recumbent MRI procedures have been reported. (7–9,201–203)

EOS, a slot scan imaging modality with a high efficiency detector was considered a new alternative for scoliosis imaging. The bi-planar standing acquisition allows a 3D weight-bearing spine reconstruction with less dose than computed radiography, and potential frac-

tion of the dose (0.1-0.2 mSv) of the alternative 3D modalities as CT.

1.3 Chest X-ray Imaging, Medical interest and challenges

1.3.1 Medical indications of Chest x-ray

The role of plain chest X-ray, just projecting a flat x-ray image of the thorax has diminished in front of tomographic imaging modalities that can see-through the rib cage, as computed tomography, magnetic resonance imaging, and ultrasound that may display visceral and pathologic body parts, adding information on density, signal intensity, or acoustic characteristics that x-ray cannot provide. Nevertheless, the universal availability of x-ray system able to explore the thorax, and its role as gatekeeper of complex, invasive, expensive, or less available modalities, contribute to maintain chest X-ray as the most common radiographic study, accounting for the 30-35% of all imaging studies. (94–97,204)

Being an easy available, low dose, relative low cost exam, chest x-ray has been used for many years as a low-risk procedure to screen or evaluate for occult o known cardiopulmonary disease. However, in the past two decades, the efficacy of its use has been the issue of multiple studies The utility of routine chest radiographs in patients admitted for various clinical has been reassessed, as many studies does not support the universal use of routine chest x-ray except in selected conditions. Different bodies, as scientific societies, governmental offices have agreed in several recommendations or appropriateness criteria, being more stringent in pediatric patients. (i.e., acutely dyspneic children as asthmatic or bronchiolitis are now not considered tributary for routine x-ray exam), and lateral chest X-ray is rarely indicated and should be consulted with the radiology consultant. (205–211) A few of these recommendations are listed below, as appropriate, not appropriate and still under debate:

Usually appropriate, or may be appropriate chest X-ray exams on admission or preoperative:

- Acute cardiopulmonary or thoracic findings by history or physical examination.
- Chronic cardiopulmonary disease in the elderly (>age 70), previous chest radiography within 6 months not available.
- Chronic cardiopulmonary disease in the elderly (>age 70), previous chest radiography within 6 months available.
- Moderate or severe hypertension: diastolic pressure ≥105 mm Hg.

Usually not appropriate chest X-ray on admission or preoperative

- Routine Admission and Preoperative Chest Radiography in asymptomatic patients; history and physical exam unremarkable.
- Mild hypertension: diastolic pressure <105 mm Hg

- Blunt Chest trauma
- Asthma in children without atypical symptoms, or additional suspected diagnosis or complications, as high fever or chest pain.
- Bronchiolitis in children without atypical evolution, except severe symptoms or complications are present or suspected.
- Lateral chest x-ray in children, without radiology prior assessment.

Debated appropriateness indications, low yield

- Daily routine chest x-ray on ICU's patients with mechanical ventilation vs on-demand, as the latter generates more requests.
- Chest x-ray screening in smokers for lung cancer detection (low yield).

1.3.2 Chest imaging technologies

For many years after the discovery of X-ray; the X-ray examinations were fluoroscopic exams performed in a dark room by observing images glowing on a fluorescent screen in response to X-ray that had passed through the patient's body, with few selected studies recorded and stored as photographic glass plates. In the 1950s, the development of conventional X-ray was a major step forward in fluoroscopy, first with the intensifying fluorescent screens that allowed to reduce dose significantly in radiography, and in fluoroscopy where the electronic image intensifier, based on television technologies, resulted in a significant increase in image brightness and dose reduction in fluoroscopy, for general radiography and contrast studies.

The advances in computer technology leaded to digital subtraction angiography (DSA), allowing to clearly display vascular structures through digital processing and subtraction of non-vascular anatomy.

The invention of computed tomography (CT), with high quality tomographic images and 3D reconstruction was a breakthrough as CT is now the key exam for molt clinical decisions in clinical practice. Recent developments in multidetector helical computed tomographic scanners capable of rapid scanning and acquisition of thin sections has revolutionized the thin-section CT technique. Volumetric thin-section CT with thin detectors (0.5–0.625 mm) has become the routine in many institutions. Computed tomography has progressively taking the main diagnosis role in chest complex or life-threatening pathologies, to become nowadays the essential tool for imaging chest pathology.

Digital radiography technology had been present since the '70 with digitized image intensifier or with CCD based detectors, (212,213) but exploded with the development of computed radiography (**CR**) based in storage phosphor plates in 1983 (Sonoda, 1983) (214–216). This technology allowed using existing of X-ray devices simply by using new CR ra-

diographic cassettes, with a reusable phosphor plate replacing the film, and CR plate readers. The advantages of linearity, wider latitude and digital communication of images were apparent, and the radiologic community quickly started replacing classical screen-films systems by CR since 1990, for general, chest, bone or breast radiographic imaging. (217–222)

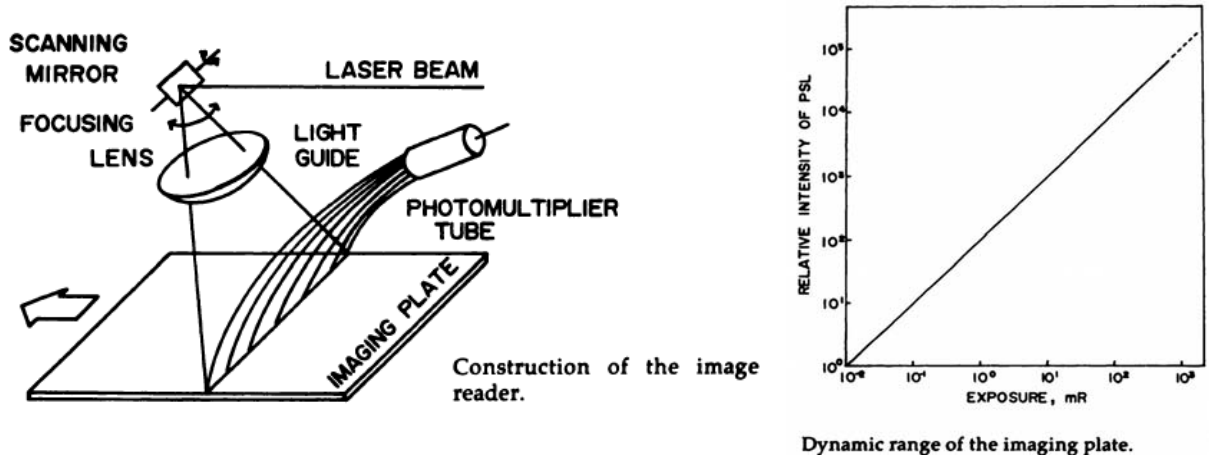

Figure 6. Computed radiography (CR) image reader and CR dynamic range.
Exposed plates to X-ray are read by photostimulation, and finally erased by intense illumination and re-used. This technology was developed by Fuji Film Co (JP). Images taken from the original paper by Sonoda et al. 1983 (214)

Since1990 researchers in X-ray physics recognized that the development of a **flat panel X-ray detector** would be a mayor technological breakthrough in X-ray imaging, and soon began to develop such a detector. It may provide better detection efficiency and improve ergonomics as no physical cassette should be handled or processed for each exposure, allowing to be used for radiography as well as for fluoroscopy. The same technology used to manufacture arrays of **thin film transistors (TFT)** in liquid-crystal display (LCD) can be used to fabricate large arrays of X-ray detection elements on two-dimensional surfaces, which accelerated research in the development of practical devices. These devices can be built with the standard full-field size of 43x43 cm.

There are several alternative physical and technical processes that allow to convert X-ray photons to radiographic images, involving direct or indirect detection or the way of conversion of interactions into electronic signals. Every process has its own advantages and disadvantages in terms of efficiency, image quality of radiation dose to images (223–230,76). The table below shows to comparison between different X-ray detection methods for converting X-rays to images.

The most frequently used installations of dedicated digital equipment for plain radiography exams were **CR** (Computed Radiography) imaging plates system, amorphous **selenium**

systems, and **flat panels** of an amorphous silicon active matrix (a-Si) coupled with a CsI (T1) scintillator layer **(direct radiography (DR)**.

	Detection method		Conversion steps from X-ray to images			
Digital	**Direct**	Flat panel detector (TFT technology)	X-ray			image
	Direct	Flat panel detector (amorphous selenium)	X-ray			image
	Direct	EOS (micro-grid ionization chamber)	X-ray			image
Digital	**Indirect**	Flat panel detector (fluorescent material + photo diode)	X-ray	light		image
	indirect	X-ray image intensifier + TV camera	X-ray	light		image
		Imaging plate (CR)	X-ray	latent image	light	image
Analog	**Indirect**	X-ray image intensifier + cine film	X-ray	latent image	light	image
	Indirect	Intensifying screen + X-ray film	X-ray	latent image	light	image

Table 2. Digital Radiography Detecting Methods. Classification

To avoid scatter digital systems also need antiscatter grids, but static grids may cause image artifacts caused by aliasing between the grid frequencies and the number of pixels per centimeter of the digital image:It is a phenomenon of intermodulation, moiré pattern ('corduroy patterns'), that may appear or disappear while re-scaling a digital image. Artifacts that can be produced by grid interaction are not always obvious and can degrade image quality, so caution and proper selection of the grid is advised. (230).

Even one of the main promotion and development points for digital systems was the potential for dose reduction, amorphous selenium and the first generations of computed radiography failed to provide a clear advantage over their contemporary -along the 1984-1995- rare-hearth intensifying screen-film (S/F) cassette systems. Conventional S/F systems that were able to maintain a better spatial resolution (up to 4 lp/mm at 20 % MTF) while reducing dose at the same pace that new digital modalities (231–233). Taking chest x-ray dose as an example,, the effective doses, in PA projection, measured for the different devices were the following: **amorphous selenium system** 0.32+/-0.06 mGy, **CR system** 0.28+/-0.05 mGy, **slot scan CCD** 0.01+/-0.02 mGy. With current **DR systems**, with amorphous silicon CsI flat-panel detectors, the effective dose has been finally reduced to 30-50% (0.010 mSv). (232–236) In particular applications, as spine and bone measurement, dose can be reduced further up to 1/10th of nominal doses maintaining diagnostic quality. (191,237)

1.3.3 Computed radiography (CR)

For almost 25 years, CR has been the workhorse of radiography; the first CR installation in Spain was at Hospital Materno-infantil Vall d'Hebron (Barcelona) in 1988 applied to pediatric radiology.

CR detectors are based in flat plates embedded with crystals of photostimulable phosphors, also known as **storage phosphors,** typically composed of $BaFBr:Eu^{2+}$, where the atomic energy levels of the europium activator determine the characteristics of light emission. The useful optical signal is not derived from the light that is emitted in prompt response to the incident radiation, but rather from subsequent emission when electrons and holes are released from traps in the material. By stimulating these crystals by irradiation with red light, electrons are released from the traps and raised to the conduction band of the crystal, subsequently triggering the emission of shorter-wavelength (blue) light. This process is called photostimulated luminescence.(71,214,238)

CR installations closely emulate screen-film radiography by using cassette-based detectors. It is a well-established system that is robust, has good reproducibility. It is nowadays inexpensive, as previous hardcopy, film printing, costs can now completely avoided by PACS image distribution and storage. The CR detection system has a wide dynamic range of over 1:10000, allowing wide ranges of radiographic exposures, and its spatial resolution is between 2.5 and 4 lp/mm. It should be taken in account that high resolution CR plates require higher dose. Image quality and image throughput have been continuously improving, while the physical size of the readout units has been reduced from room-sized to integrated systems inside small mobile x-ray devices (214,233).

Many studies have demonstrated that CR can routinely produce images that are perceived as equal or superior to conventional S/F images, in terms of image quality and/or clinical performance, in chest X-ray digital thoracic imaging, even with less radiation dose. (217,231,239–242)

Computed radiography with phosphor plates allowed the development of PACS, as radiography accounted for more than 50% of the imaging activity performed in any large radiology department. Therefore, CR allowed the separation between image acquisition and image display with soft-copy reporting. Digital acquisition systems allow image processing algorithms that adapt, filter, or improve, the image characteristics to the expected clinical requirements. i.e. image processing algorithms can be applied as noise suppression or edge enhancement. (74,239,243,244)

CR was the only digital alternative to S/F for bedside chest radiographs for many years, but now compact portable, even wireless, flat panels can be used with advantages in image quality and dose.(233,245–248)

Since its inception, CR has had many technical innovations in the detector properties and/or the reading procedure as dual side reading (with plates with dual photostimulable sides), structured (needle) screens avoiding cross talk, and new scanner concepts based on line-at-a-time reading, that allowed improvements in image quality that may be comparable to that of current state-of-the art flat-panel systems), while reducing system throughput, physical size, or costs.(217,238,249–253)

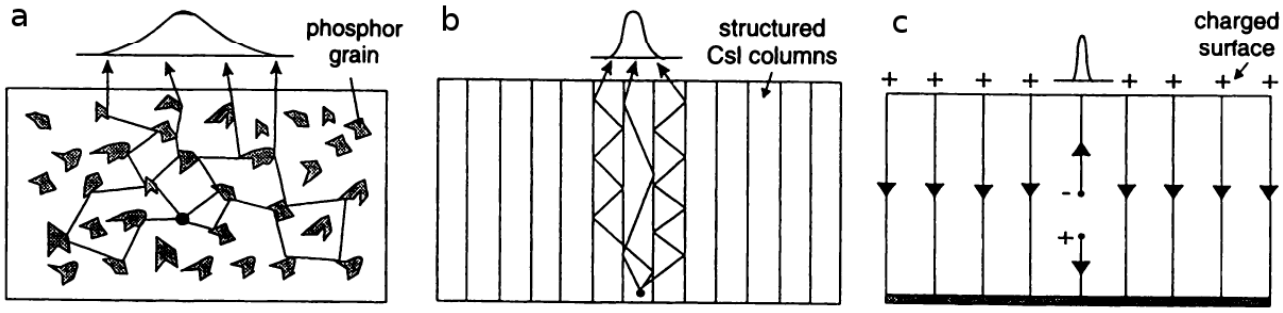

Figure 7. Signal spread and collection at the three common detector structures.
a) Settled phosphor, found in intensifying screens and computed radiography plates.
b) Columnar, crystalline, CsI phosphor used by amorphous silicon DR.
c) Electrostatic collection of charges in a electric field as in direct selenium detectors.
A direct system may give higher resolution by avoiding scattered, spread, signals.
Modified from drawings in Rowlands and Yaffe (71,452)

1.3.3.1 Computed Radiology and the Exposure Creep

Following the generalized introduction of CR, but affects all digital modalities, the potential for decreasing patient dose was one of the main arguments for the justification of the cost of digital imaging. However, for digital detectors, higher doses result in better image quality (i.e. a less “noisy” image) over a certain range of doses. When the dose is increased, the improvement is in the signal-to-noise ratio and graininess disappears. Thus, a tendency to increase doses can occur, especially in those examinations where automatic exposure control (AEC) is not usually available The exposure creep is the gradual increase in x-ray exposures over time that results in increased radiation dose to the patient. (176,254)

Multiple studies are reporting conflicting results reporting both higher than necessary and/or progressive overexposure. The inherent wide latitude of all digital modalities associated to the automatic density and gamma corrections applied to the acquired image hide overexpositions. Large intracenter and intercenter variability is already present, and doses are usually higher than necessary for image quality. Published intercenter dose differences

are up to 250% for chest PA and 200% for lumbar spine, and overexposure rates of 30-40% are being reported. These dose variation can be reduced by standardizing protocol settings, such as the AEC cells used in chest examinations, but a incorrectly calibrated AEC may be an additional source of hidden overexposure. Another source of variation are the differences on pre-configured parameters (APR), for the same diagnostic quality radiograph, among different manufacturer's, with dose differences up to 60%. (176,254–257)

1.3.4 Flat Panel Digital Radiography Systems (DR)

There are two main flat-panel detector technologies. One technology is based on an **indirect conversion** with an intermediate optical process of X-rays while the other one uses a **direct convert X-ray energy** to electronic charge. For radiography and dynamic applications the indirect method provides substantial advantages, while the direct method has some benefits for mammography. In radiography and mammography flat-panel detectors lead to clear improvements with respect to workflow, image quality and dose reduction potentials.(69,71,249,258,259)

Flat-panel detectors (FPD) were a long-searched technology that may allow implementing high throughput digital X-ray rooms with low dose and high quality images. The sensitivity, spatial resolution, frame rate and portability were described as the upcoming technology. Increasing gain and reducing noise will realize higher sensitivity. Layered sensor designed such that **thin film transistors** (**TFT)** layer and sensitive layer are constructed separately will decrease the pixel pitch lower than 100 micron. The requested diagnostic performance of flat-panel detectors should be to comparable to that of asymmetric screen-film system for depiction of all simulated patterns of interstitial lung diseases, nodules, and catheters while offering potential for dose reductions by sensitivity indexes of 400 to 800.

1.3.4.1 Amorphous Selenium detectors

These flat panels are solid state electrostatic systems where the detection media is a photoconductor for X-ray as amorphous selenium. Its amorphous state makes possible the maintenance of uniform imaging characteristics to almost atomic scale (there are no grain boundaries) over large areas. The primary function of the a-Se layer is to attenuate x-rays, generate free electron–hole pairs (in proportion to the intensity of the incident x-rays) and collect them at the electrodes. Before digital imaging, the first medical application of a-Se was xeroradiography, where a latent charge image on the surface of an a-Se plate was read out and printed using liquid toner processing. (260,261)

The first selenium detectors for full-field X-ray applications, as chest radiography, where

drum scanners introduced by 1994 (Thoravision, Philips, Best, NL). In these devices, the selenium layer is deposited on a cylindrical aluminum drum, large enough to cover the full field of view for chest imaging. The electrostatic charge image which is formed on the selenium surface after X-ray exposure is read out by electrometer probes using fast drum rotation. Image quality was considered equal or superior to screen-film systems. (22,262,261,263) The images obtained by selenium detectors had a different aspect of those from screen-film. This was considered a potential bias for image quality assessment studies. (264)

Selenium drums where finally replaced by selenium flat panels (DirectRay, Direct Radiography, Newark, DE, USA) with solid-state detectors of 35 x 43 cm, and pixel size/pitch of 0.139 mm. Image quality studies showed preference of radiologists for selenium images, with 6:11 preferred regions, over computed radiography images, with 2:11 preferred anatomic regions. They provide better performance than that of high-resolution storage phosphor radiography (265–267)

Of particular concern in direct digital flat panels is the uniformity of signal collection across each pixel. If signal collection can be made uniform, then the noise associated with signal collection may be minimized. Therefore, methods are been investigated for active signal focusing. The research in direct digital flat detectors is still open, with groups investigating wide band-gap semiconductor materials, in particular cadmium telluride, CdTe (71,268).

Even selenium detectors proved to provide good image resolution and quality, they were expensive and never gained a widespread use. As their image response at reduced dose levels is inferior to that of amorphous silicon indirect flat panels (aSi-CsI), they have finally replaced by the latter in most clinical radiography settings. (234,235,269–272)

1.3.4.2 Amorphous Silicon Flat panel Detectors

The new category of 'immediate direct digital flat panel detectors' is being considered a direct digitization method, even there is a scintillator crystal involved. In these digital flat panel detectors, based in CsI/a-Si technology, incoming X-rays first strike a cesium iodide layer that converts the X-rays into light. The light then passes through a photodiode matrix of amorphous silicon, where it is converted into electrical signals which are amplified and digitized. The light is directed onto the silicon without lateral diffusion, by the crystalline structure Cs-iodide deposition which ensures image sharpness. The primary benefit of cesium iodide technology is the excellent DQE (detection quantum efficiency). Signal-to-noise ratio is enhanced by using a low-noise semiconductors The use of all theses flat-

panel digital detectors allow a considerable dose reduction during routine chest radiography without loss of image quality (71,273,230,274–278,229).

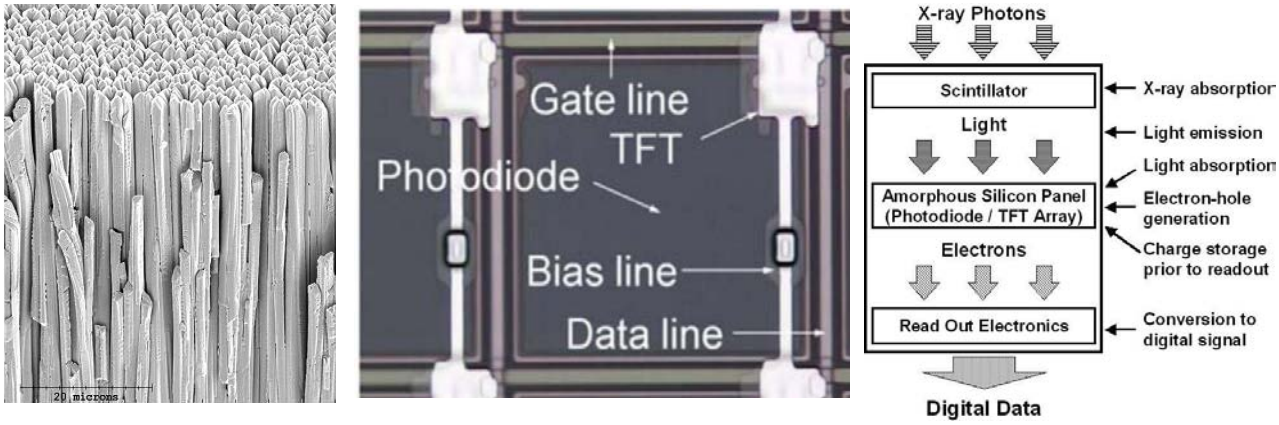

Figure 8. Microphotographs of a-Si:CsI TFT photodiode and its conversion stages

Rigth) The needle structure of overlaying CsI crystals where X-ray to light conversion is done.
Center) A pixel element. The real pixel pitch is 143 µm, and the components of the pixel are annotated. As happens in all current TFT pixels, the photodiode does not cover the 100% of the pixel surface as electric lines and components have their own reserved space, loosing detection efficiency.
Right) Conversion stages at a TFT from X-ray to electrical signal

Operation of a flat-panel x-ray detector can be divided into four stages (figure 8). In the first stage, incident x rays pass through a protective cover and interact with a doped phosphor screen, the scintillator. As the x rays are absorbed in the scintillator, energy is transferred creating a “cloud” of high-energy electrons. Although most of the energy from these electrons is eventually transferred to vibrational modes in the solid, essentially turning into heat, a small fraction will undergo a radiative transition and emit optical photons. In the second stage, this light travels through the nearly transparent scintillator and interacts with the array of photosensitive elements on the flat-panel substrate. A typical array element is a reverse-biased amorphous silicon- based 'p–i–n' photodiode. For each optical photon absorbed in the active i-layer of this device, an electron–hole pair will be generated, and the electric field will transport this charge to the contact regions. The electrons collect and are stored on a metal contact under the n+ layer. In the third stage, a field-effect transistor (FET or TFT) is activated and transfers the charge from the diode bottom contact onto a metal transmission line, called the data line (as columns in Fig. 8). The FET is activated by pulsing a gate line, or scan line (as rows in Fig. 8) which is perpendicular to the data lines, from a negative voltage to a positive voltage. The FET is held at a positive voltage long enough for nearly all the charge to be transferred onto the data line. In the fourth stage, this charge is transferred through a finger contact region at the edge of the panel and into

a charge- integrating amplifier with an A/D converter. Since there is a dedicated amplifier on each data line, the panel can be read- out by sequentially activating all the scan lines. (278)

1.3.4.2.1 Design, performance, and operational metrics

Medical applications for flat-panel x-ray detectors span the range from high-dose single-shot radiography to ultra-low-dose fluoroscopic applications. A number of design and operational issues should be considered over this range of applications in order to optimize the detectors. First, the array size and pixel pitch need to be determined based on the anatomy of the patient and the target of the procedure. Second, the desired read-out speed must be determined in order to set the requirements of the time constants on the panel and the speed of the read-out amplifier. The required dynamic range of the intended medical procedures must be determined in order to optimize the trade-off between the signal-to-noise ratio and available dynamic range. Finally, a calibration strategy must be developed in order to satisfy patient work-flow requirements while assuring artifact-free operation of the detectors.

The required size of a flat-panel medical x-ray detectors is governed primarily by patient anatomy. Although technology has been developed that allows one to focus x-ray beams, this process is extremely inefficient and cannot be used in medical x-ray applications due to concerns about patient dose. Thus, the x-ray detector must be designed to match the desired size of the actual anatomy to be imaged. For cardiac or breast imaging, 20×20 cm or 30x30 cm arrays are sufficient. For mammography, but for chest of limbs radiography, including vascular applications large array (43x43 cm) are required. Although the largest panel could accommodate all applications, there are cost, performance, and ergonomic issues that require each application to use an optimally sized detector (278–280). Although the pixel pitch is primarily determined by the size of the features that needs to be imaged, the optimization of the pixel size is not straightforward. At first thought, smaller pixels would seem to give better image quality, but this is not always the case. Due to concerns about x-ray dose to the patient, low x-ray exposure levels are used Therefore, the signal-to-noise ratio of the resulting image is quite poor, and falls off at high spatial frequencies (small feature sizes). For a given dose level and object contrast, there is a minimum feature size above which all information is hidden in the noise; the picture becomes grainy and loses its sharpness. In addition to the constraints imposed by very low signal levels, there are a number of parameters that get worse as the pixel size is reduced. These include the capacitance of the scan line and data line, the capacitance and fill factor of the

photodiode, the “dark” noise in the pixel per unit area, and the read-out rate of the detector. Finally, small pixels also increase the overall cost of the detector and the cost and speed of the viewing and archiving systems. Given all these constraints, flat-panel manufactures have chosen pixel pitches ranging from 70 to 200 μm, where mammography applications use the lower end of this range and all other applications use the higher end (278,280,281).

Radiographic images acquired by flat-panel detectors requires that the acquisition matches to length of the x-ray pulses, between 3 sec to 0.001 sec. These applications present challenges to the x-ray detector. In order to integrate for this period of time, both the FET and the photodiode must be carefully optimized in order to avoid artifacts and excess noise. In particular, the leakage in each of these devices must typically be in the femtoampere (fA) range.

One of the most important metrics for the detector is the signal-to-noise ratio in the image which must be maximized while delivering the lowest possible x-ray dose to the patient. As mentioned previously, the best objective measure of detector dose efficiency is **DQE**, which measures how much the detector degrades the signal-to-noise ratio of the incoming x rays. There are a number of parameters that determine the DQE. First, one wants to minimize the x-ray absorption in the protective covers of the detector by using the materials with a low density and low atomic number and by minimizing the thickness while maintaining the required mechanical properties. Second, one wants to maximize the x-ray absorption of the scintillator layer while maintaining the required optical properties. Scintillators can achieve excel- lent x-ray absorption properties if dense, high-atomic- number materials are used, and they are deposited in thick films. Since scintillators emit optical photons isotropically after absorbing x-rays, however, thin scintillators are preferred in order to prevent the spread of the signal to neighboring pixels (as measured by the **modulation transfer function (MTF)**. Other optical constraints include the efficiency of generating optical photons, and the spectrum of the optical emission, which needs to be matched to the photodiode. Optimizing the type, thickness, structure, and optical properties of the scintillator in order to give the best DQE is a challenging problem .

Although the DQE is the most critical factor in determining the performance of the detector, it is also important that this be maintained over a wide range of x-ray exposure levels. At low exposure levels, the DQE can be degraded by other noise sources in the detector (electronic noise). At high exposure levels, the photodiode becomes non-linear and artifacts can appear in the image. The **dynamic range** of the detector can be defined as the

range between these extremes. The three most important variables in determining the dynamic range of a flat panel detector are: electronic noise, the conversion factor, and the pixel capacitance (278,282–285).

The **maximum exposure level** is related to the amount of effective charge that can be stored at each pixel. The **minimum exposure depends** on the low-noise floor, that is linked to electronic noise, applied gain, pixel pitch, and MTF (through optimizing optical properties of the scintillator). The **conversion factor** (CF) is a parameter that depends of the particular design and scintillator materials of a detector. There is a negative influence of using small pixels at low x-ray exposure levels. Additionally, it shows that while the CF must be chosen carefully to address both ends of the dynamic range, the electronic noise should be minimized to allow dose reduction. Sources of electronic noise can be found throughout the panel and readout electronics. They include charge-trapping effects, diode leakage, TFT switching noise, amplifier noise, and thermal noise in the resistors.

Calibration is an essential factor in the operation and design of flat-panel x-ray detectors. Three basic types that are performed on every image – offset subtraction, gain correction, and bad pixel replacement. The offset calibration starts by acquiring an offset image (or “dark” image), that is read-out of the detector in the absence of any x-ray exposure. This image includes sources of noise as electronic leakage of photodiode, de-trapping of the TFT and photodiode, associated with a previous exposure to x-ray signal; the residual light output from the scintillator associated with a previous x-ray exposure (or “afterglow”); and signals associated with lack of uniformity. This complex set of time-dependent signals may depend on the frame rate, applied voltages, panel temperature, and previous exposure conditions. For these reasons, an offset image is typically collected immediately before or after the x-ray image to minimize errors due to the time-dependent nature of this calibration. The second calibration that is performed is known as a gain correction. In this process, the offset-corrected x-ray image is divided by a previously collected, offset-corrected x-ray image that was obtained with a flat field exposure (i.e., no object between the x-ray tube and the detector). This process eliminates the pixel-to-pixel gain variations that are caused by many effects including . Gain calibrations are usually taken using several x-ray spectra and averaged over many images to eliminate the inherent x-ray quantum noise. Unlike the offset calibration, the gain correction has a weak or negligible dependence on the temperature, frame rate, applied voltage, and previous x-ray exposure. the gain-calibration image can be re-used over a long period of time (i.e., every few months or one per year along routine service calibrations). The third calibration is known as a bad-

pixel replacement. A series of electrical tests are performed on every pixel to verify that its offset, gain, noise, lag, and linearity are within the specifications. Pixels that fail any of these tests are marked in the bad-pixel correction image and their values are replaced by an average of their nearest neighbor values. An allowable number of bad pixels is set by the manufacturer after careful clinical studies to assure that they does not surpass the threshold of clinical impact (278,286). Besides these basic calibrations performed on every image, there is a wide range of advanced image-processing techniques that can also be applied to images. These include spatial sharpening or noise-reduction filters, linearity corrections, temporal averaging, spatial and temporal artifact corrections, rotation, zoom, and computer- assisted diagnosis.(278,286,287)

1.3.4.2.2 Fluoroscopy and dynamic imaging using Flat-panel detectors

Besides radiographic as single-frame acquisitions, flat-panel detectors are extensively used today for dynamic imaging. Flat-panel detectors are also used for diagnostic procedures that require visualization of motion such as vascular imaging, where one views the progress of an intravascular contrast medium through the blood vessels, or motion of administered barium contrasts such in upper and lower GI exams. These applications add additional requirements for flat-panel detectors. Since the output of the detector is a rapid sequence of images, as many as 30 frames/sec (fps) or more, the temporal properties of the detector become important; i.e., it is important to limit the retention of signal by the detector (or lag) from one frame to the next. Additionally, for fluoroscopic imaging, the dose per frame is greatly reduced compared to that in radiographic images; so the low-dose performance of the detector becomes more important. The x-ray fluence at the detector input surface for the lowest exposure levels in a fluoroscopic image is about one x-ray photon per pixel per frame (228,278,279,288–290).

1.3.4.2.3 Spatial, Spectral and Computed Tomography Imaging with Flat panels

Increasingly, flat-panel detectors have been applied to advanced three-dimensional imaging applications such as **cone-beam CT**. For this application, the detector acquires a series of images while the x-ray source and detector rotate around the patient. The images are subsequently reconstructed to obtain a three-dimensional data set (291–293).

Tomosynthesis is an application in which a rapid sequence of images of a subject is obtained while the x-ray source is moved relative to the detector. These images are then combined to reconstruct slices of the patient and thus reduce clutter from overlying structures that are present in a conventional projection radiography (294–297,55).

Flat panels can be use for **dual energy imaging,** where two acquisition of images are

taken with two different x-ray energy spectra. The two images are then combined to isolate materials of different compositions, for example bone and soft tissue, which have differences in attenuation at each x-ray energy (298–300).

1.3.5 Standards in Chest Imaging

The concerns about the risks of ionizing radiation used in medical procedures to the general population has conducted to develop technical scientific and legal documents, trying to inform, advice and regulate the practice of radiology. In Europe the main document has been the **EURATOM** 97/43 Directive, following **ICRP** recommendations, that developed many of these recommendations as a normative legal framework. (301–303)

The EURATOM directive lays down the general principles of the radiation exposure protection of individuals, of patients as part of their own medical diagnosis or treatment, of individuals as part of occupational health surveillance, of individuals as part of health screening programmes, of healthy individuals or patients voluntarily participating in medical or biomedical, diagnostic or therapeutic, research programmes, of individuals as part of medico-legal procedures, and of occupational exposure of health-related professionals.

Justification is the first step in radiation protection. No diagnostic exposure is justifiable without a valid clinical indication, no matter how good the imaging performance may be. Every examination must result in a net benefit for the patient. This only applies when it can be anticipated that the examination will influence the efficacy of the decision of the physician with respect to diagnosis, clinical management and therapy, and/or final outcome for the patient.

Optimization evinces that all doses due to medical exposure for radiological purposes except radiotherapeutic procedures shall be kept **as low as reasonably achievable** (**ALARA**) consistent with obtaining the required diagnostic information, taking into account economic and social factors.

Other aspects as professional training, equipment surveillance, and consideration to special groups as children, health screening, and special attention to modalities involving high doses as interventional radiology, computed tomography and radiotherapy. (301–303)

ICRP does not recommend the application of dose limits to patient irradiation but draws attention to the use of dose reference levels, as an aid to optimization of protection in medical exposure. ICRP promotes local reference levels, that should assessed and reviewed, associated to dose audits, in order to control and reduce patient exposure in existing and new modalities. IRCP advices precaution in new DR modalities, requiring new procedures

and controls, as disregarded overexposure with them is a known risk. (304–306)

Guidance on referrals has appeared since then, as guides of appropriateness of clinical referral for diagnostic imaging. The first comprehensive guide was issued by the Royal College of Radiologist (RCR, UK), that was latter transposed as a European Union document. This guide has been adapted to several national health systems in Europe. Different solutions as documents or websites have been published in Germany, France, Spain, and almost all countries of the OECD (307–309). In the USA, different professional organizations, mainly the American College of Radiology (ACR), under the support of the Federal Health and Drug administration (FDA) have been addressing the topic of appropriateness of examinations involving ionizing radiations.

1.3.5.1 European recommendations in chest Imaging

The European Commission document “European Guidelines on Quality Criteria for Diagnostic Radiographic Images – EUR 16620” is the reference document directed to technical and clinical staff involved in taking radiographs and reporting them (310). It presents diagnostic requirements presented as image quality criteria deemed necessary to produce an image of standard quality in the most common radiographic studies. It does not address referral acceptability (appropriateness) for any clinical condition. The criteria for radiation dose to the patient are expressed as reference dose values for each type, that are based on the data coming from the third quartile in earlier European dose surveys, that should be take as a ceiling. Lower doses should be pursued in line with the ALARA principle. (310)

1.3.5.2 Requirements Image Criteria

The criteria in most cases specify important anatomical structures that should be visible on a radiograph to aid accurate diagnosis. Some of these criteria depend fundamentally on correct positioning and cooperation of the patient, whereas others reflect technical performance of the imaging system. Awareness of the positional and technical dependence of the criteria can stimulate further work aimed at gaining a more detailed understanding of those factors which can influence image quality, and may lead to improved mechanisms for auditing both existing as well as new and/or modified radiographic techniques and training programmes for radiological staff, as described by Vaño et al in 995 (311).

A qualitative guide to the necessary degree of visibility of these essential structures is provided in the following Description of Terms. These criteria can be used by radiologists as they report on radiographs to make a personal visual assessment of the image quality as well as an audit mechanism for radiographic procedures within a department. presented

for PA and for lateral projections even though many of the ost of them

1.3.5.2.1 PA Chest Projection

- **Image criteria**

1. Performed at full inspiration (as assessed by the position of the ribs above the diaphragm — either 6 anteriorly or 10 posteriorly) and with suspended respiration
2. Symmetrical reproduction of the thorax as shown by central position of the spin- ous process between the medial ends of the clavicles
3. Medial border of the scapulae to be outside the lung fields
4. Reproduction of the whole rib cage above the diaphragm
5. Visually sharp reproduction of the vascular pattern in the whole lung, particularly the peripheral vessels
6. Visually sharp reproduction of:
    1. (a) the trachea and proximal bronchi, (b) the borders of the heart and aorta,
    2. (c) the diaphragm and lateral costo-phrenic angles
7. Visualization of the retrocardiac lung and the mediastinum
8. Visualization of the spine through the heart shadow

- **Important image details**

1. Small round details in the whole lung, including the retrocardiac areas:
    1. High contrast: 0.7 mm diameter
    2. Low contrast: 2 mm diameter
2. Linear and reticular details out to the lung periphery:
    1. High contrast: 0.3 mm in width
    2. low contrast: 2 mm in width

1.3.5.2.2 Lateral Chest Projection

- Image criteria

1. Performed at full inspiration and with suspended respiration
2. Arms should be raised clear of the thorax
3. Superimposition of the posterior lung borders
4. Reproduction of the trachea
5. Reproduction of the costo-phrenic angles
6. Visually sharp reproduction of the posterior border of the heart, the aorta, mediastinum, diaphragm, sternum and thoracic spine

- Important image details

1. Small round details in the whole lung:
    1. high contrast: 0.7 mm diameter
    2. low contrast: 2 mm diameter
2. Linear and reticular details out to the lung periphery:
    1. high contrast: 0.3 mm in width
    2. Low contrast: 2 mm in width

1.3.5.3 Example of Good Chest Radiographic technique

The example provided below is a set of radiographic technique parameters, for postero anterior and lateral projections, that has been found to result in good imaging performance

that is capable of meet all the above 'Quality Criteria'.

Projections	Postero-anterior X-ray	Lateral X-ray
Radiographic device:	Vertical stand with stationary or moving grid	Vertical stand with stationary or moving grid
Nominal focal spot value:	≤ 1.3	≤ 1.3
Total filtration:	≥ 3.0 mm Al equivalent	≥ 3.0 mm Al equivalent
Anti-scatter grid:	r = 10; 40/cm	r = 10; 40/cm
Screen film system:	nominal speed class 400	nominal speed class 400
Film-focus distance (FFD):	180 (140-200) cm	180 (140-200) cm
Radiographic voltage:	125 kV	125 kV
Automatic exposure control:	chamber selected - right lateral	chamber selected - central
Exposure time:	< 20 ms	< 40 ms
Protective shielding	standard protection	standard protection

Table 3: Example of Good Chest Radiographic technique (EUR 16260)

1.3.5.4 Chest reference doses

Entrance surface dose for a standard-sized patient is considered the reference dose.

The entrance surface dose for standard-sized patient is expressed as the absorbed dose to air (mGy) at the point of intersection of the X-ray beam axis with the surface of a standard-sized adult patient (70 kg body-weight), backscatter radiation included.

Chest X-ray Reference Dose [EUR 16260]		
Front view (PA-AP)	**125 kV**	**0.3 mGy**
Lateral view	**125 kV**	**1.5 mGy**

Table 4. Chest Reference Doses for a standard-sized patient, as EUR 16260 (mGy)

1.4 The EOS imaging Device

1.4.1 The invention of Multiwire / Microgrid Ionization chambers

The EOS prototype device is a radiographic imaging system intended for the simultaneous acquisition of posterior-anterior and lateral planar views of a human being in standing position and using a low-dose X-ray detection technology. The low-dose is achieved thanks to micro-grid ionization gas chamber detectors, that where developed by **Georges Charpak** (1924-2010) and extensively used in high-energy physics experiments. The micro-grid detector is a sophisticated evolution of the ionization chambers, as are the Geiger Muller tubes, that can tell when a particle passes through but can say little about its position and

direction. Charpak conceived what he called multiwire proportional chambers, in which a series of thin wires in parallel roles were suspended between two flat cathodes. Layering many of these chambers and attaching the output of each wire electrode directly to a computer made it possible to determine the track of each particle precisely in real time. Moreover, the device could track hundreds of thousands of particles every second. Micro-grid detectors allow to accurately register ionizing radiation events by their energy, time and position at high sampling rates. Georges Charpak was awarded with Nobel Prize in Physics in 1992 for “his invention and development of particle detectors, in particular the multiwire proportional chamber”. The EOS prototype assessed in this work was developed ad built by Biospace Instruments (now EOS imaging, Paris, FR), a company, founded by Georges Charpak, that developed along its history implantable particle detectors for in-vivo studies, small high-resolution gamma-cameras, and the EOS device. (2–6,312–314).

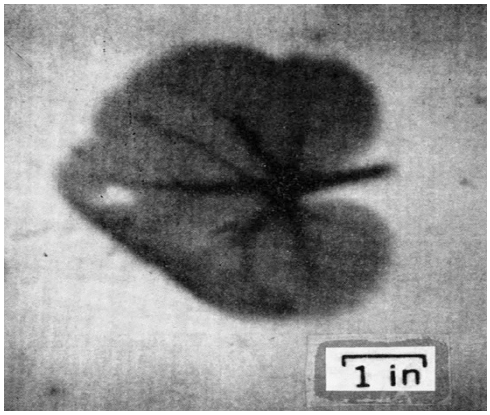

Figure 9. Radiography of a leaf obtained with a proportional chamber.
Image taken with a 6 keV x-ray source, as a photo of the oscilloscope screen. Taken from Charpak 1973.

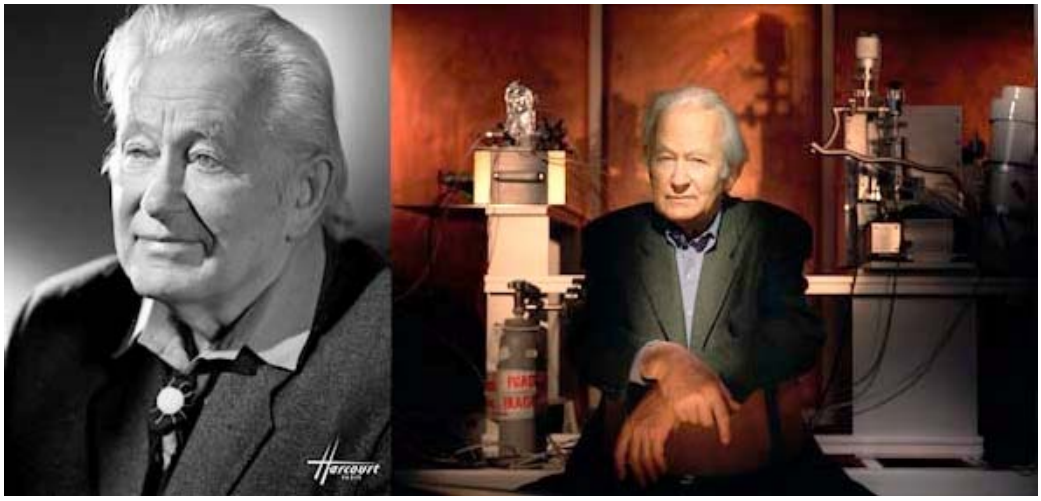

Figure 10. Georges Charpak (1924-2010). Portrait with the EOS prototype
Left) He was the inventor of the Micromegas detectors (Nobel prize 1992). Right) Behind him, a complete EOS prototype in the test bench, with the EOS microgrid detector (left side) and the tilted x-ray tube (right side)

Several groups have been doing research in multiwire imaging devices and have built several prototypes based on the initial works of Georges Charpak. All these devices experienced successive improvements, detector size and technical additions as the drift mesh, that improved the efficiency and spatial resolution, being finally known as the “Micromegas” family of detectors. In medical imaging devices, where the detector is not stationary, the multiwire system was converted into a micro-grid of multiple copper lines printed by lithography on an electronic circuit board. (4,54,315–329)

1.4.2 The EOS imaging prototype

The EOS prototype was built by Biospace Instruments in Paris, tested clinically in Paris (FR), Brussels (BE) and finally dispatched to Montreal (CA). The description of the prototype comes from the original works of the EOS Project Consortium and from peer-reviewed publications (1,330,331)

In the EOS imaging prototype two micro-grid detectors were set at 90 degrees, each aligned with its corresponding X-ray tube with thin slit collimators, and all attached to a twin large and rigid 'C' shaped arms obtaining two coplanar X-ray fan beams. This double X-ray detection system is enabled to slide along a vertical stand, allowing the scanning the whole body of a patient, in standing weight-bearing position, in postero-anterior and lateral views simultaneously. Planar (2D) images can be reconstructed by summation of multiple thin images obtained along the two coordinated scans. Using the coplanar reference points obtained after the simultaneous x-ray acquisition a 3D model of the skeletal structures can be calculated, allowing the representation of the spine, pelvis, and lower extremities of the patient in physiologic weight-bearing standing position. The EOS detector sets mounted on the C art are a combination of four elements, the first two elements in to source (and 2) and the last two elements in the detector subsystem (3 and 4):

1. A conventional radiography high-output X-ray tube (20 Kw).
2. An output collimator that generates thin fan-shaped beam, with a fixed vertical beam shutter collimator (500 μm), a fixed horizontal beam aperture collimator, and the beam calibration system.
3. A micro-grid detector with 1764 strips (4 per mm., with a pitch of 250 μm), with a secondary slit collimation at the X-ray entrance window, the sealed micro-grid gas chamber with xenon (at 6 bars) and a small concentration of organic gases, the gas circuit and gas purifier system with compensation of micro-leaks. Part of the gas circuit is common for both detectors

4. The detector electronics allowing 1764 channels (one per each vertical strip) detection.

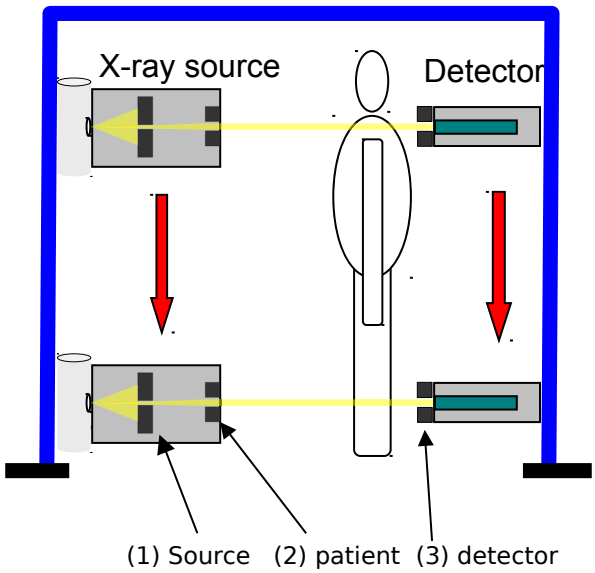

Figure 11. EOS scanning schema: Sliding X-ray tube, collimators and detector.
Three sets of collimators shape a very thin X-ray beam between the source and the detector. Collimators (arrows) (1) Source, (2) Patient and (3) Detector collimator) minimizing scatter radiation.

Scanning geometry: three sets of collimators imaging

As in many conventional radiography systems, the patient stays between the X–ray tube and the detector. EOS has two linear detectors and the 2D radiologic images are obtained by a scanning fan beam, which is produced simultaneously from two X–ray tubes, on both sides of the patient, who will be examined in a standing position and each 2 dimensional image is made line by line.

For each x-ray tube, the alignment of three collimators ensures the horizontal fan beam geometry. The first collimator is at the exit of the x-ray tube, the second is at the entrance of the patient, and the third one is in front of the detector. The alignment of these three 0.5 mm. Parallel collimators required careful and arduous re-calibration of the prototype when it was moved between different test sites (H. Saint Vincent de Paul (Paris, FR) to Hôpital Erasme (Brussels, BE).

The collimator at the exit of the x-ray tube allows a beam limitation aiming at reducing the scattering while proving shielding. The second collimator selects out of the preliminary fan beam passing through the first collimation a fraction of radiation, which is going to be used to expose the patient. Finally the third collimator (in front of the detector) ensures the verti-

cal spatial resolution and eliminates as much as possible the scattered radiation coming out from the patient. If we add the post-patient barrier of the detector and electronics, no primary or secondary x-ray reaches outside of the examination area, By suppressing almost all scattered radiation to patient and personnel., the EOS system is a self shielded x-ray device (330,331).

1.4.3 The EOS detector

The EOS detector is a “Micromegas” family detector, an evolution of a multiwire ionization chamber as a micro-grid ionization chamber detector. It consists in essence of a parallel plates gas chamber with photolithographic printed micro-strips as readout elements on a fiberglass printed circuit board, and a fine mesh placed above the strips acting as a delimiter between two functional zones(322,330).

The Micromegas detectors consisted of a two-stage parallel-plate avalanche chamber of small amplification gap (100 μm) combined with a conversion-drift space. It followed a fast removal of positive ions produced during the avalanche development, with fast signals (≤1 ns) during the collection of the electron avalanche on the anode microstrip plane, allowing positive ion signal of 100 ns., providing high granularity, high rate, and gas gains of up to $x10^5$. This family of detectors may detect a large spectrum of electromagnetic radiations. (322,332,333)

In the EOS prototype the layout as a Micromegas device is shown in the following figure. The detection space has a height of 1.1 mm., and a depth of 10 mm. The width of the detector is related to standard radiographic image width of 448 mm. :

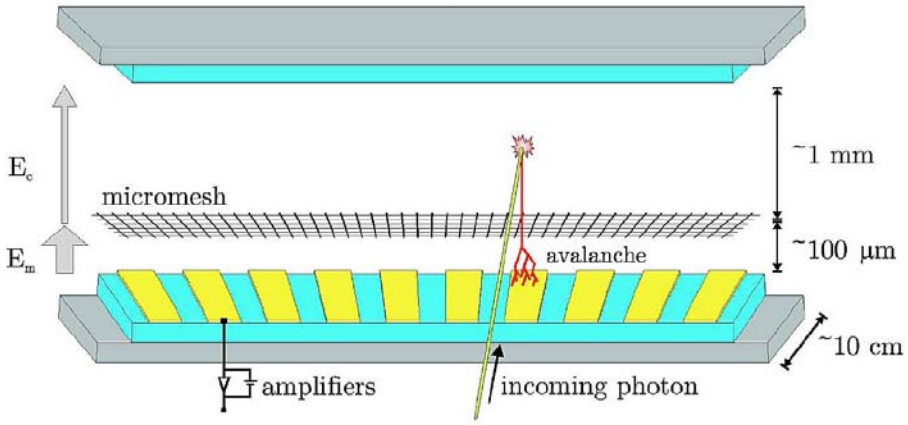

Figure 12.Microgrid components and detection geometry of the EOS detector.
Cooper strips are not parallel but focused to the x-ray focal spot.

The fan-shaped collimated x-ray beam, obtained by collimation at the exit of the x-ray tube, reaches the detector by a 0.5 mm entrance slit, and penetrates in the gas vessel through a 0.5 mm thick Al window. The photons then may interact in the 10 cm long conversion zone.

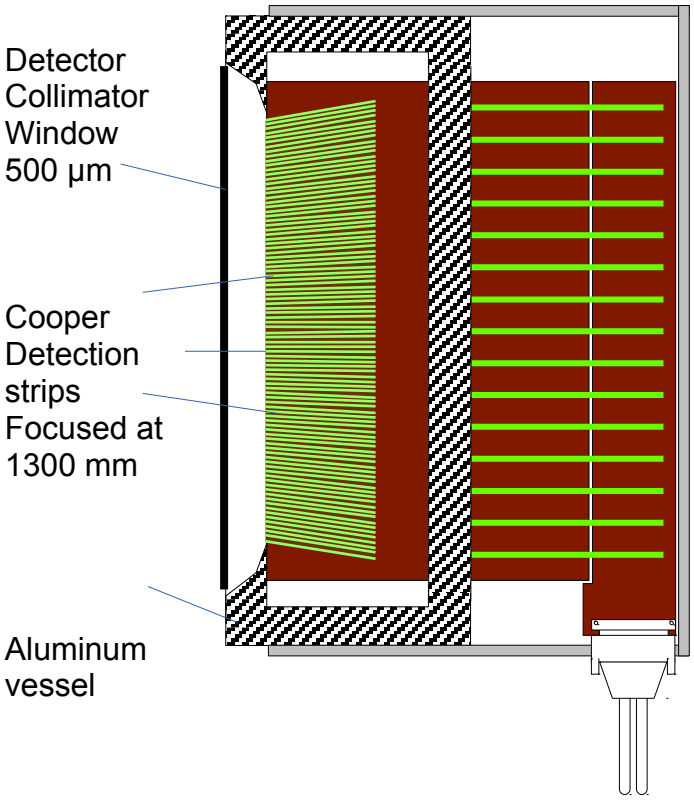

Figure 13: Drawing of the top view of the internal geometry of the EOS Detector.
Photons enter through a 0.5 mm collimation slit, through a 0.5 mm thick Al window into the interaction gas-filled space. Cooper detection strips are focused to the x-ray source

A pressurized gas mixture, composed of Xe with 5% ethane, at 6 atm., is used as a quencher, providing a high interaction cross section within the radiological energy range. By choosing a high atomic number conversion medium, the photoelectric effect is favored over the scattering processes. The predominance of the photoelectric process also contributes to the preservation of geometric information, as it avoids scattered photons, that could interact at random locations in the detector. According to experimental results, 10 cm of Xe at 6 atm is better than 500 µm of CsI (as in the flat panel detectors), or 1 mm of Se, in terms of quantum detection efficiency, especially for high quality beams. The use of Ar or Kr would lower operational costs but would necessitate higher pressures to achieve the same conversion efficiency of Xe at 6 atm Therefore, the energy of the incoming photon is

more likely to be deposited at a single location thus providing more primary charges. As can be seen in the attenuation data from XCOM presented on the next, the interaction efficiency for a Xenon gas absorber is higher than CsI at the current energy levels of diagnostic radiology. (330,334)

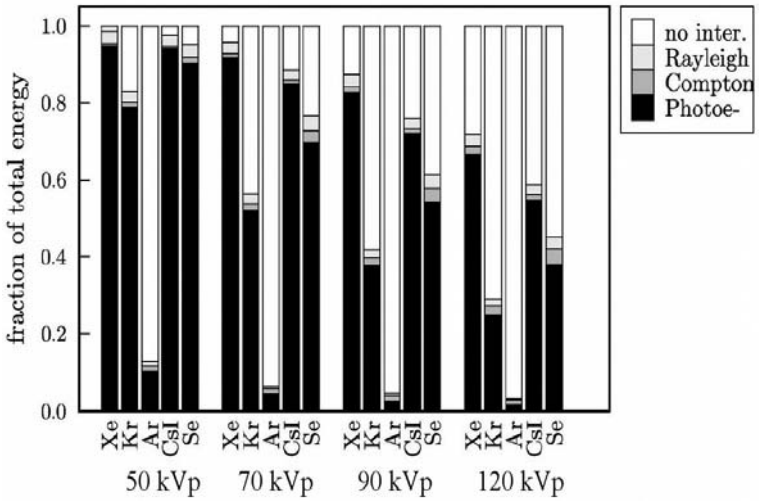

Figure 14. Fractions of the total energy converted by each electromagnetic process for different absorbing media for different energy spectra 50, 70, 90 and 120 kVp. Measurements for Xe, Kr, and Ar gases were of 10 cm thick at 6 atm., CsI and Se are 0.5 and 1 mm thick, respectively. The attenuation data from XCOM 2000. (Modified from Després 2005)

The detectors require controlled pressure (6 bar.) and should be calibrated prior to image acquisition, whenever an acquisition parameter is changed, because of the small gain and offset variations between each signal channel. The calibration procedure consists of an offset signal acquisition followed by a full illumination of the detector that generates the reference signal upon which further measurements will be compared. In the setup, the tubes are oriented vertically to avoid the heel effect. However, slight misalignment of the collimators may lead to a nonuniform illumination of the detector entrance slit. This is corrected by calibration, which ensures a uniform background in flat-field images. The optimal amplification potential is also determined during the calibration procedure. Also, the voltage on the micro-mesh is set in function of the exposure level in order to achieve optimal SNR. The whole calibration sequence is automatic and takes less than 30 s., and always performed without the patient in the examination gantry.

Figure 15: External views of the EOS micro grid X-ray detector.

The EOS Micro-grid Detector with gas purifier system. Left) Front view. The detector with gas purifier system on top. The detection window line can be seen between the collimator plates as a thin slit (0,5 mm. height) in this frontal side. Right) Side view. The complete detector with electronic box, and data acquisition boards and harness.

The EOS prototype device allows the acquisition of one view or two simultaneous orthogonal views of the human body. Therefore, the EOS device is composed by two X-ray generators, the acquisition device itself as a vertical gantry with the sliding x-ray tubs and detectors, a computer controller, and the operator control console, allowing to set acquisition and image parameters for each exam, and the main X-ray start switch.

Figure 16. The EOS imaging prototype at SVPH (Paris).

Left) Without the covers, paired X-ray tubes -collimators and detectors at 90 degrees are seen.

Right) with its plastic translucent covers in place . A staff is standing as a patient positioned at the gantry.

The images on the EOS system are acquired line by line by sweeping the fan beam across the subject. Square pixels are obtained by adjusting the integration time per line and the scanning speed to the pitch of the microstrips. The vertical acquisition scanning speed is variable between 4 and 30 cm/sec.

Images are intrinsically orthographic in the vertical scan direction, without magnification while magnified in the transverse direction. Clinical images are stretched vertically to simulate a cone-beam projection when they are exported for clinical review .

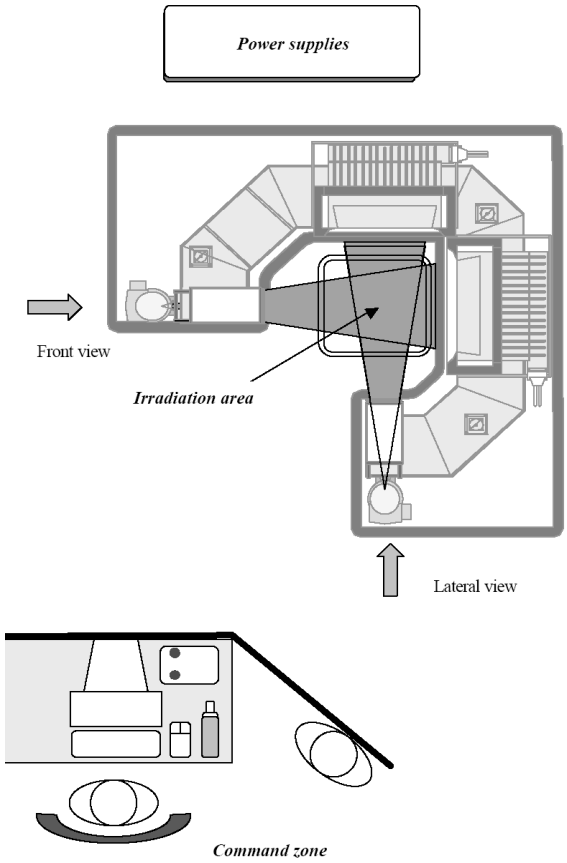

Figure 17. EOS acquisition device prototype room layout.

A control console and workstation controls the overall operation of the device, timings, translation motions, X-ray settings and generators, detector operation (gas regulation, detector and electronics voltages) and other active and safety elements. The same workstation takes care of image acquisition, display, 3D reconstruction and DICOM communications. A separate closet contains the high-voltage X-ray generators

1.5 Dosimetry and the EOS specific features

1.5.1 General concepts

1.5.1.1 The concept of dose

To assess the exposure to the patient from a radiological examination different physical measurements are used: Air kerma in air, entrance skin dose, organ, or tissue equivalent dose and effective. These detection areas are shown on the figure

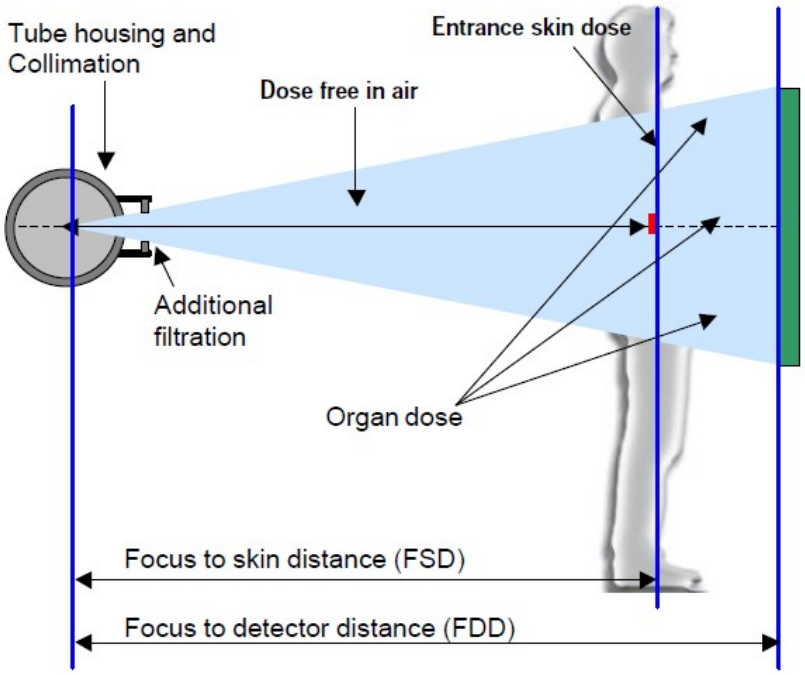

Figure 18: Different concepts of dosimetry quantities (conventional system)
1. Dose free in air, 2. Entrance skin dose, 3. Organ dose

1.5.1.2 Air Kerma

The air kerma D_{air} is associated to the kinetic energy released in a medium by ionizing radiation (here X-rays). This quantity is measured either directly by means of a dosimeter, or indirectly from a calculation based on source characteristics (*Equation .1).* The international unit for air kerma is the Gray (Gy). Expressed as

$$\mathbf{D_{air} = A.D_r(kV, X_F @100\ cm).(100/FSD)^2.mA.T}$$

A: The beam factor. It takes into account the beam geometry. In the case of a collimated fan beam (scanning system), where the detector lies in the beam plane, this factor is a function of the dose profile across the beam plane. With a conventional system the beam profile being nearly perfect,

i.e. stepwise shaped, then the factor value is close to 1.

Dr: Dose rate 100 cm from source. It is a function of tube potential (kVp) and total filtration (XF), and is expressed in milligray or mAs^{-1}(mGy / mAs).

FSD: Focus to skin distance

mA: Tube intensity

T: Exposure duration

1.5.1.3 Organ dose and effective dose

1.5.1.3.1 Absorbed Dose

The absorbed dose D_T is related to the mean energy dE imparted by ionizing radiation (here X-rays) to a volume element dV of mass dm in a particular tissue or organ. In the vicinity of a point P, the absorbed dose is expressed as:

$$D_T = dE/dm$$

1.5.1.3.2 *Equivalent Dose – Organ Dose*

The equivalent dose is the absorbed dose defined for a volume element of an organ or a tissue. The organ dose H_T is the average of absorbed dose over the organ volume. H_T is expressed as the product of the absorbed dose by the radiological weighting factor W_R (1 for photons). Its unit is the Sievert (Sv) and expressed as :

$$H_T = D_T \cdot W_R$$

1.5.1.3.3 Effective Dose

The effective dose E takes into account the total detriment to all organs directly or indirectly affected by radiation exposure. It is the weighted sum of organ equivalent doses in all tissues or organs with weights W_T , and expressed as:

$$E = ?_T [H_T \cdot W_T]$$

Effective dose cannot directly be measured while a radiological examination is performed, as it would require the presence of detectors inside patient's body. The assessment of in depth dose for the different organs is obtained through a Monte Carlo computer model simulating photon transport and energy deposition processes, based on the following parameters: X-ray beam spectrum, patient characteristics (morphology), X-ray field and projection type for the examination.

1.5.1.3.4 Parameters for the assessment of doses

Once a dose quantity is chosen, it is interesting to look at the influence on the dose associ-

ated to a radiological examination, due to the parameters involved in the examination.

Those parameters are shown in the following table together with their influence on the exposure.

Effects of Exposure Factors on Radiation Exposure	
X-ray Factors	**Effect on dose**
X-ray tube potential (kVp)	Dose roughly increases with the square of potential
Tube current and exposure time (mAs)	Dose varies linearly with intensity
Field size	Scattered radiation increases with the field area
Focus to skin distance	Dose decreases as the inverse square distance law ($1/d^2$)
Patient's thickness	Scattered radiation increases with the thickness of the irradiated volume

Table 5. Effects of exposure factors on radiation dose

Tube potential (kVp)

The X-ray spectrum depends on the tube voltage and accordingly affects both the attenuation of the in depth dose, and the backscatter to primary ratio, of incident X-ray photons. The high photon detection efficiency of multi-grid x-ray detectors allows to use lower tube potentials by reducing scatter radiation.

Tube current (mAs)

The dose follows a direct relationship to filament current for all X-ray modalities. It should as low as feasible to allow the necessary photons reaching the detector. The photon counting detectors may allows to use the lowest intensities but quantum mottle noise may be visible easily visible, as it depends of the statistical variation.

Field size

The irradiation field should adjust to the region of interest required for the diagnosis. At the same time, for a given source-to-skin distance, the dose increases with the field size due to the growing importance of backscatter from the patient. The thin geometry of the collimated EOS x-ray beam may be considered the most significant advantage of the EOS in front of planar modalities

Focus to skin distance

Considering the absence of X-ray photon interaction within the air volume between source and patient, the dose follows simply the inverse square law.

Scatter fraction

The primary to scatter ratio is reduced proportionally to the kVp and field size. For a large

field, as in chest imaging scatter contribution to exposure increases, both with field size and for kV intensity. With a fixed field size of 30x30 cm the primary to scatter fraction decreases from 0,85 to 0,68 when kVp is increased from 70 to 100 kVp.

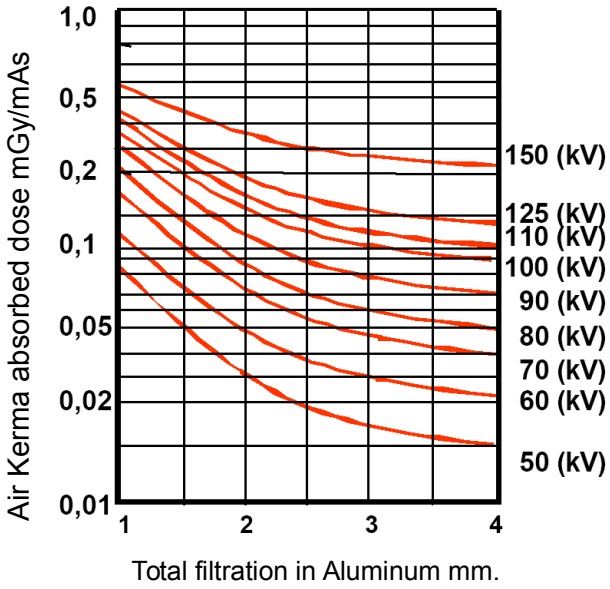

Figure 19. Dose variation as a function of kVp and medium thickness

1.5.2 Dosimetry with the EOS planar scanning system

The shape of the X-ray fan beam, collimation and translation of the scanning X-ray source confer to the EOS device several differences in front of common radiographic planar systems, that translates into different demands for the assessment of static dose and the scan dose, mostly dependent of the thin collimator geometry.

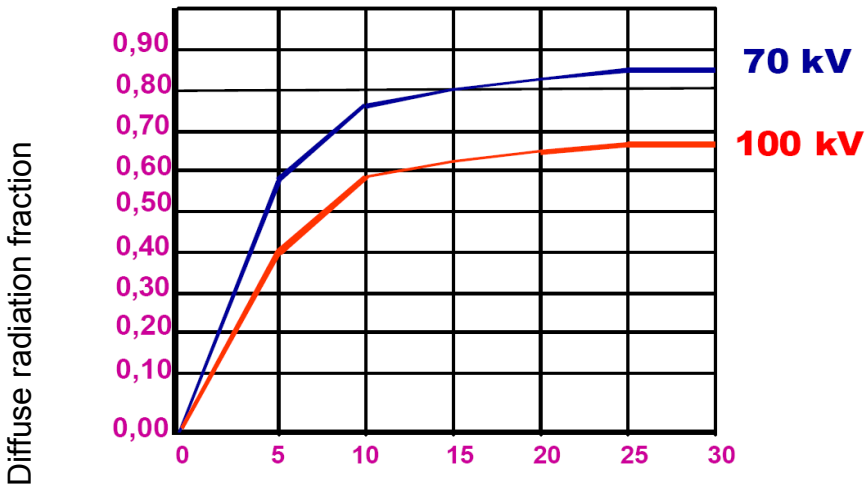

Figure 20. Fraction of scattered radiation as a function of field size

1.5.2.1 Geometry of the EOS beam: Collimation and beam slice profile

In the usual radiography systems the X-ray beam is a cone and the dose follows the law of being reduce by the square root of the focus to detector distance.

In the EOS scanning system, the detector array lies in a plane determined by means of two collimator slots, namely the detector and the object collimator slots. The resulting beam profile is a fan shaped (flat) beam, with its “thinness” across the collimator plane (along the vertical axis, parallel to the floor).

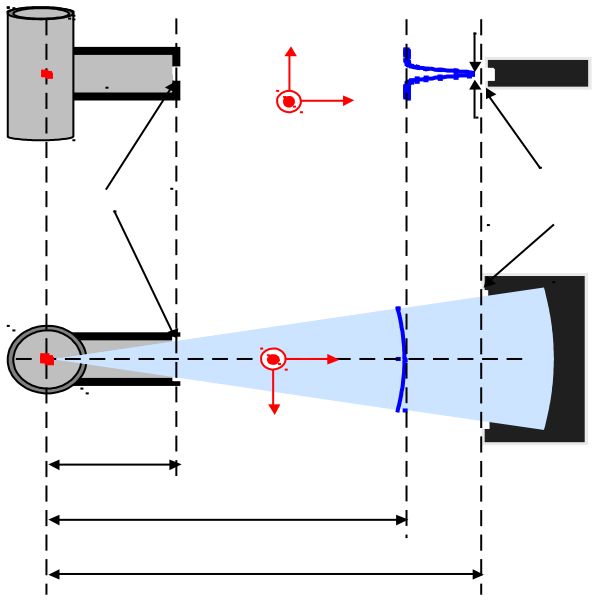

Figure 21. EOS Collimation geometry in two views, side view, and top view.
The collimators (arrows) shape the X-ray as a very thin fan.

The beam profile across the beam plane depends on the collimation geometry, which is itself a function of the focal spot size (h), the source to collimator distance (d1) and the object collimator opening Co. Besides it varies with the distance to the (Y) plane where it is examined.

$$PY(z) = G[h, Co, d1](z) \times f(Y).$$

The entrance plane corresponding to the patient irradiated surface will be called the object plane. This will be the reference plane where the beam profile and air doses will be assessed.

1.6 EOS Skeletal application

1.6.1 Skeletal Features

EOS device and micro-strip detector was intended, since its design, for spine and skeletal applications as gas detectors, with the dimensions feasible for full-field radiography, have a relative low spatial resolution, comparable to computed radiography systems (2.0 lp/mm) but below to digital flat panels or screen-film systems. The EOS gantry was intended for standing (or seated), weight-bearing, examinations of the spine, and this was prototype was tested and validated for full spine radiography (scoliograms) with subsequent 3D spine reconstructions. The prototype received many improvements as advanced 3D software by the Laboratory of Biomechanics of the French 'École Nationale des Arts et Métiers' (ENSAM, Paris) together with the Canadian Laboratory of Research in Imaging and Orthopedics (LIO, Montreal).Since 2007 EOS became a commercial product, approved in 48 countries for spine imaging. Since then, the EOS imaging device imaging has been assessed and reported in its technical, dosimetric, functional and economical aspects in the literature. (4,330,331,335–349)

As the EOS device was a low-dose skeletal imaging system, it was promptly adapted to image the pelvis, hip joint, and lower limbs, including full skeleton, all as weight bearing studies. All these skeletal examinations may be biplanar acquisitions that allow the projection of a 3D models following the automatic extraction of reference points and software reconstruction. One known and intrinsic aspect of scoliosis is vertebral body rotation, but EOS has been able to depict not only rotation, but translation of the over the vertical axis. Many papers have covered these new imaging applications, that are providing new insights in spine and lower limbs biomechanics. Results ex-ante or ex-post of orthesis, surgery, or podiatrist treatments can be documented. EOS can assess the spinal penetration index (SPI), a concept introduced in neuromuscular lordoscoliotic patients with airway compression, and its 3D reconstructions have proved to be efficient to determine levels, amount and technique of corrective osteotomies to correct complex spinal deformities. (339,350–368)

These

This simultaneous biplanar controlled acquisition allows better results than software projection without calibration objects method, a promising approach reported by Moura et al (369,370).

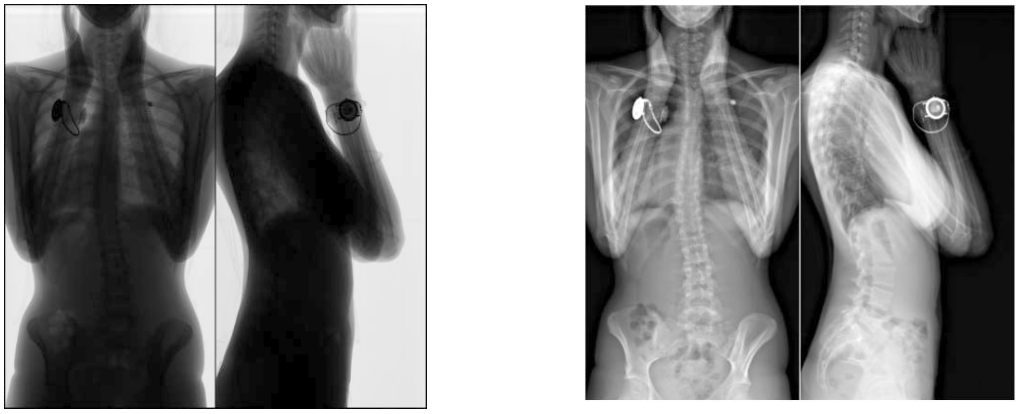

Figure 22: Spine imaging by the EOS prototype: system image display image.

(Left) System image is a positive image where pixels with higher pixel values are those with higher detected radiation (bone is black): light areas are those with less density (air/fat). (Right) Display image is a negative as in conventional film-screen radiography with gray-scale inversion and window level adjustment (The bone is white): dark areas are those with less density.

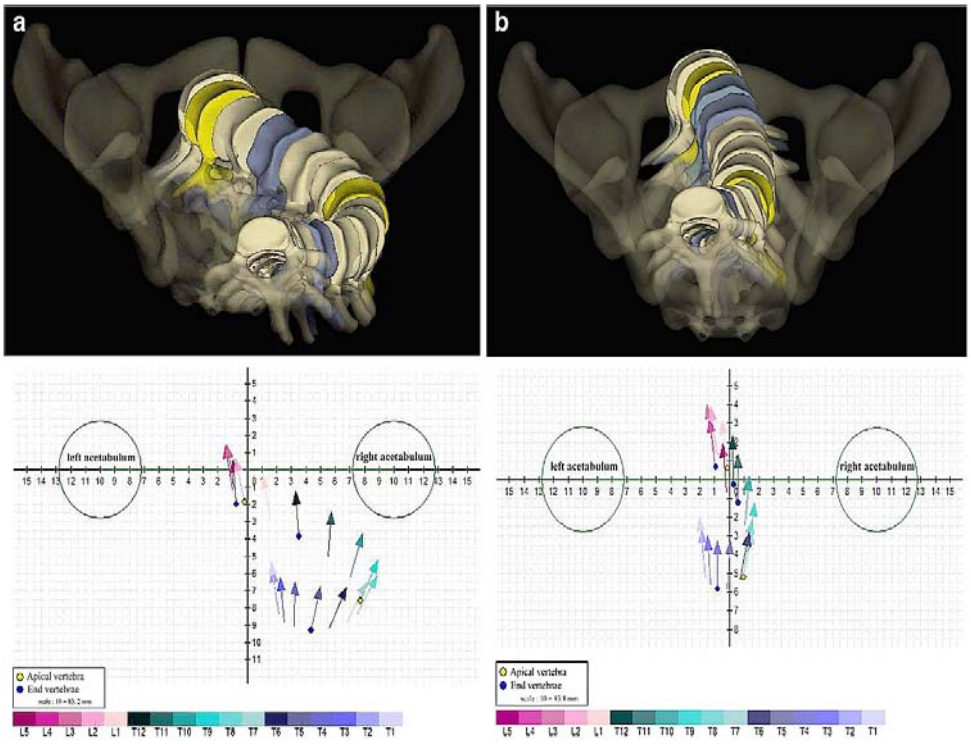

Figure 23.Axial vertebral rotation assessed by the EOS method

Imaging by EOS before and after surgery. Corresponding top view 3D reconstructions and vertebral vectors, before (a) and after (b) surgery in the same patient as in Fig. (Taken from Amzallag-Bellenger, 2014) (453)

Since 2007, EOS has presence in the market as an approved medical device for skeletal morphologic examinations (EOS Imaging, Paris, FR), and has (2015) an installed base of more than 100 units. One-hundred-fifteen scientific papers have been published in peer-reviewed journals around the features, technical assessment and/or clinical applications of

EOS in spine, pelvis and lower limbs imaging. The average price was at €393,000 per system (2014, with 44 systems sold).

Figure 24: EOS full body skeletal 2D images and 3D reconstruction
Left: 2D biplanar images and 3D reconstruction. Right: The EOS system gantry (images taken from http://www.eos-imaging.com)

1.7 EOS Application in Thorax Imaging

The research presented in this work is the first exploratory analysis of the potential of the EOS x-ray device for chest imaging. Image quality and dose should be assessed allowing to use this s-ray device for chest applications. This will allow a complementary use of this modality in the same clinical settings where it is primarily used for skeletal imaging.

To our knowledge, no other clinical assessment of chest imaging with the EOS device has been undertaken till the writing of this manuscript (Q3 2015).

The application of EOS in chest imaging is an off-label use of the modality, and was underwent under the research restrictions of the EOS Project, funded by the EU ave been funded by the Competitive and Sustainable Growth (GROWTH) Programme of the European Union (EU): **GROWTH Project GRD1-2001 – 40084 EOS** (1998-2002)**.** EOS. Low dose X-ray diagnostic imaging: a new modality for planar and three dimensional applications in rheumatology, orthopaedics and chest radiography (2002-2006) (1)

2 Objectives

2.1 Main objectives

1. To assess if EOS imaging device may be used in a clinical setting for chest examinations in adults
2. To assess dose delivered to patients for diagnostic or follow up purposes, comparing them with digital modalities, computed radiography and/or digital radiography.
3. To assess the detector performance in terms of its physical parameters
4. To assess chest image quality by a comparative study by repeated examination between EOS and a state-of-the-art chest digital modality (an amorphous Si CsI detector flat panel x-ray system).

2.2 Secondary Objectives

5. To assess if EOS may be able to display pathologic features in the chest that may be present in the group of patients recruited for the image quality study

3 Material and Methods

3.1 The EOS Clinical Chest experiment

The aim of the EOS clinical chest experiment was to compare the EOS imaging device performance for planar chest imaging to those of the current gold standard as a flat-panel digital radiology system. The experiment was held at the Erasme Hospital, associated to the Free University of Brussels (ULBE, Belgium) where the EOS device was installed for a period of research and development along 2005, after the first set of development and clinical experiments in the 'Hospital des Enfants Malades' in Paris (France). The device was initially planned moved to Barcelona (Spain) but the problems arising after the first transportation of bulky medical device (>2000 Kg) between the Paris and Brussels, and the additional delays associated to recalibration after transportation, additional development and improvements (as automatic image handling, better operator interface) leaded to several delay and finally cancel this second transportation and installation to Barcelona. Therefore, the experimental slot available for chest exams on the EOS prototype in Brussels was limited between 04.April.2005 and 01.June.2005. The chest experimental research was coordinated by the original team in Barcelona (JP, PSC).

3.2 Patient selection

A group of 40 consecutive adult patients referred to the Department of Radiology of the Hôpital Erasme (ULBE, Brussels, B) for clinically indicated x-ray examinations of the chest where the candidates to be enrolled as volunteers for comparative studies by standard and EOS low-dose radiography devices.

3.2.1 Inclusion criteria

They are already scheduled for a chest x-ray examination, should be able to be standing up during the x-ray acquisitions, should be 18-year-old or older, and they should consent to participate in the study.

3.2.2 Ethical Committee approval

The proposal of the clinical chest experiment was granted and approved by the Ethical Committee of the Erasme University Hospital Brussels (ULBE).

1. The EOS device is already fulfilling technical, electrical, medial, radiation protection and other safety standards.

2. The device prototype is already able to provide diagnostic images of the body.
3. The radiation dose for the EOS device examinations will be adjusted to be the 50% of the DR system for the same patient. The resulting additional dose would be less than the standard DR system.
4. An informed consent will be granted for participant patients examined by EOS radiography.
5. Patients will be adults already scheduled for chest radiographic examinations required for the follow-up of their existing medical conditions. They will only receive one additional examination or views with both modalities, except for technical problems in any modality.

3.2.3 Clinical Examination procedure

If they accept the informed consent, they underwent two consecutive chest x-ray examinations, both with anteroposterior and lateral projections) first on a state of the art flat-panel digital radiography system (Siemens Thorax FD, DX) and after quality control, a second examination on the EOS-1 prototype. Standard DR images were automatically sent and archived on the Hospital Picture and Communication System (PACS) in DICOM format, prior to routine soft-copy reading and reporting. EOS images were stored locally as DICOM and 16 bit TIFF images at the EOS modality workstation for later review. The two sets of images would be finally collected and anonymized for image quality assessment along the EOS project.

The EOS chest experiment in ULBE lasted just 2 months, between March-June 2005, along an experimental period where spine examinations, the main imaging purpose and experimental assessment of the EOS device were also performed. After this period, the EOS prototype device was disassembled and dispatched to Montreal (Ca) where is was re-assembled for further clinical assessment. Time-constrains and the nature of the prototype constrained to finish the study with fewer patients than initially planned. Nevertheless, the sample was adequate for the study purposes.

3.2.4 Clinical Examination Data Collection

After enrolling a patient to the study, individual patient information will be collected in a ad-hoc database. Basic patient protocol Information will be collected manually in paper forms while the patient is at the examination rooms. DICOM images will be sent routinely to ULBE PACS. A duplicate EOS image folder will be automatically created in the local EOS workstation, for EOS image analysis in its workstation, without interfering with the clinical

requirements of the medical treatment. Technical parameters will be recovered from the DICOM file headers and TIFF-EXIF file headers enclosed in every acquired image with the software extraction tool Exiftool (371). Image quantitative data, as histograms and pixels values, will be recovered by the Image analysis software ImageJ (372–374). Both software's are in the public domain.

Patient data will be anonymized (ID number and, name removed) and a project identification code will be used in all consequent data storage and analysis. Collected master data was restricted to:

Patient identification and demographics, that was stored as

Patient identification number

X-ray session number

X-ray session date : time

Age, Sex, Height, Weight, calculated BMI (body mass index)

Medical referral

3.3 EOS equipment description and protocol

3.3.1 The EOS detector specifications

These specifications correspond to the EOS prototype, EOS1, (Biospace Instruments, Paris, France). The system has 4 pixels per linear mm, 16 pixels per square mm.

3.3.1.1 Bi-planar digital radiological image specifications

Pixel size at detector entrance (µm)	250×250 µm
Image detector slit resolution	1764 columns
Image matrix (width x n lines)	1764 x n lines
Image size typical. (mm)	440×900 mm
Image matrix typical (column x row)	1764×3600 pixels
Electronic encoding (bits/pixel)	16 bits (64000 gray-levels)
Maximum scanning range	1800 mm
Scanning speed	up to 254 mm /sec maximum

3.3.1.2 X – ray source (water-cooled conventional medical radiology type)

Generator power	60 kW
Tube voltage range	40 – 150 kVp
Tube current	up to 800 mA
Time exposure	up to 31.5 seconds; (up to 20 kW during 10 seconds)
Anode capacity	740kJ, 1000kHU
Power 2.5 – 5 -10 sec	40 – 31 -20 kW
Anode speed	10000 rpm
Focal spot size	1 mm
Intrinsic filtration	2.5 mm aluminum (fixed)

3.3.1.3 High Voltage Generator

Maximum nominal power	63 kW
Voltage range, increment	40-150 kVp, +/- 1kVp step
Current range, increment	10 mA – 800mA, 20 steps
Anode starter speed	10000 rpm
Nominal power	35 kVA

3.3.1.4 Collimators (3 steps)

Source Collimator

Material	Brass
Slit aperture, height x width	4 x 50 mm
Thickness	15 mm
Distance from focal spot	150 mm

Patient Collimator

Material	Tungsten
Slit aperture, height x width	0.5 x 180 mm
Thickness	3,5 mm
Distance from focal spot	450 mm

Detector Collimator

Material	Brass
Slit aperture, height x width	0.5 x 500 mm
Thickness	5 mm
Distance from focal spot	1250 mm

3.3.1.5 Equipment physical specification

EOS is a radiation self-shielded system.	
Cabinet entrance aperture	492 mm.
Overall Imaging Cabinet size (excepted HV generator and console)	2100 x 2100 x 2700 mm (H)
Generator size	550 x 550 x 1900 mm (H)
Total weight	2 400 kg static, 3 000 kg dynamic
Load in motion	600 kg at scanning speed of 254 mm / s
Acceleration /deceleration range	50 mm / sec

3.3.2 Design Considerations

The following tables give the typical working parameters for several sizes in the high and low acquisition speed modes.

Chest image 44 cm x 45 cm (1 800 lines) takes between 1.5 and 3 seconds

Full size image (spine) 44 cm x 90 cm (3 600 lines) takes between 6 and 12 seconds

The corresponding estimated patient skin dose range between 50 and 500 µGy.

This dose takes into account the collimation geometry.

The table below shows the patient skin dose according to the European recommendations for adults.

	High speed (30 cm/s, 1.5 sec)		Low speed mode (4.3 cm/s, 10 sec)	
Voltage	Tube current	Radiation per line	Tube current	Radiation per line
70 kV	500 mA	0.42 mAs	320 mA	1.8 mAs
100 kV	400 mA	0.33 mAs	200 mA	1.11 mAs

Table 6. EOS Scan Speed, current, and radiation per scan line

3.3.3 EOS Acquisition Parameters

The EOS device is a slot scan X-ray system that has the following imaging parameters associated, and configurable, for each image and acquisition that will be used elsewhere in this manuscript:

X-ray Tube Tension	**kVp**	kV
Intensity	**mA**	mA
Exposure-scan time	**T**	second
Image length (lines)	**n**	lines
Focus-skin Distance	**FSD**	mm
Filtration	-	material and thickness
Scan speed	**mm/s**	mm/s
X-ray exposure	**mAs**	mA · T
Exposure time per line	**Dt**	T / n
Radiation per line	**mAs/L**	mA · T /n
Patient skin dose	**mGy**	mGy

The patient is scanned at a uniform linear speed and the final image is the concatenation of multiple (**n**) lines of thickness L sampled in the direction of the scanning, that last **T** seconds. The EOS device may be adjusted to several linear speeds: 43, 60, 100, or 300 mm/sec. The dose is proportional to the exposure time Δt

$$\Delta t = T / n$$

The total exposure and scan time may take several seconds depending on the vertical size of the subject and imaging area and the intrinsic scanning speed. Low linear speeds increase the exposure in inverse proportion. The X-ray tube output depends on the X-ray source intensity (mA). The EOS operator will set the upper and lower limits of imaging area, the tube voltage and the exposure time. The EOS system will calculate the appropriate scanning speed and exposure time per line, and therefore the suggested tube current and radiation per line depending on tube power.

So exposure for a given acquisition line can be expressed as: mAs/line

$$\textbf{mAs / line = mAs. Dt = mA} \cdot \textbf{T/n}$$

The calculated skin dose (**D**) can be expressed as:

$$\textbf{D} = \textbf{A} \cdot \textbf{D}_r \textbf{(kVp, mm Al, @ 1000 mm) x (100/DFP)}^2 \cdot \textbf{mA} \cdot \textbf{Dt}$$

Where:
$\mathbf{D_r}$ is the dose measured per mAs, at 1 m of the X-ray source, for a given tube tension and X-ray filtration.
A is the beam coefficient related to beam profile and image linear sampling along the scan path. This profile is defined by collimation geometry and X-ray focus spot, that depends from device design and manufacture, and it is calibrated for each collimation geometry.

3.3.4 Typical EOS working parameters

The following tables give the suggested working parameters for several sizes in the high and low speed EOS acquisition modes. The EOS device has several parameters in common with planar X-ray systems but its linear scan acquisition and fixed collimation is affected by scan speed and this offer a few additional parameters, calculations, that convey the final image quality and x-ray dose:

Example of examination parameters and dose		
Tube voltage	kVp	100 kV
Tube current	mA	500 mA
Total exposure time	T	1000 ms
Number of lines per image	n	1000 lines
Focus-skin Distance	FSD	1300 mm
Dose rate (100 cm) @ 100 kV, 2.5 mm Al	Dr	100 µGy / mAs
Radiation per line (mAs/L)	(500 x 1) / 1000	0.5 mAs
Radiation (mAs)	3.5 x 0.5	1.75 mAs
Patient skin dose	100 x 1.75 µGy	0.175 mGy

Table 7. Example of examination parameters and dose

3.3.5 EOS image acquisition process

A series of linear samples are acquired along the vertical scan of the patient. This set is integrated a planar bi-dimensional image data array. A first set of system corrections is applied in the data image such as offset, gain, and time modulation corrections. This results in “System Image” which is not displayed but saved in a temporary file structure as TIFF file format (.tif), and associated to patient and technical acquisition data.

A subsequent additional automatic processing is done on this “System Image” to obtain the “Display Image”, saved in DICOM format (.dcm), that will be stored locally, displayed for diagnosis, and transmitted to the main PACS system

3.4 EOS clinical chest experimental protocol

3.4.1 Patient protocols

Patients were examined with a homogeneous protocol, with the voltage fixed at 125 kVp, but the mAs were fixed manually according to the patient corpulence. As the EOS prototype was intended for skeletal imaging, it is to a set of three morphotypes estimations for exposure chest imaging. They were derived from the original proposed protocol requirement: dose 50% of Chest CR examination. This 50% CR dose protocol was initially tested with small variations of the technique in a small set of patients.

3.4.1.1 Chest image 44 cm x 45 cm (1800 lines)

The standard EOS chest image is a square acquisition of 44 cm x 45 cm, 1800 x 1760 pixels, and may take between 1.5 and 3 seconds depending on scan speed mode.

	High speed (30 cm/s, 1.5 seconds)		**Low speed mode (4.3 cm/s, 10 seconds)**	
	Tube current	Radiation per line	Tube current	Radiation per line
70 kV	500 mA	0.42 mAs	320 mA	1.8 mAs
100 kV	400 mA	0.33 mAs	200 mA	1.11 mAs

Table 8: Chest image 44 cm x 45 cm (1800 lines) scanning parameters

3.4.1.1.1 Comparative to techniques Reference dose for Spine images

EOS prototype was intended and optimized for spine imaging. In spine the image is a rectangular portrait acquisition of 44 cm. width and adjustable length of up to 90 cm. p.e.: for 62,5 cm long: 2500 lines x 1760 pixels; for 90 cm. long: 3600 lines x 1760 pixels. These acquisitions may take between 2.1 and 3 seconds depending on adjustable scan speed mode. Dose was adjustable and may be reduced just to gain a balance between image quality and dose. The ALARA principle for EOS spine imaging is that it should allow assessing morphology, making measurements and extracting reference points to generate a 3D model.

Spine image 44 cm x 62.5 cm (2500 lines)				
	High speed (30 cm/s, 2.1 seconds)		Low speed mode (6.0 cm/s, 10 seconds)	
	Tube current	Radiation per line	Tube current	Radiation per line
70 kV	500 mA	0.42 mAs	320 mA	1.28 mAs
100 kV	400 mA	0.33 mAs	200 mA	0.8 mAs

Table 9: Spine image 44 cm x 62.5 cm (2500 lines) scanning parameters

Full size image 44 cm x 90 cm (3600 lines)				
	High speed (30 cm/s, 3 seconds)		Low speed mode (10.0 cm/s, 10 seconds)	
	Tube current	Radiation per line	Tube current	Radiation per line
70 kV	400 mA	0.33 mAs	320 mA	0.89 mAs
100 kV	250 mA	0.21 mAs	200 mA	0.56 mAs

Table 10. EOS Reference Techniques Spine for 60 and 90 cm

* In the above table, the low speed mode corresponds to 10 seconds total time exposure.

The corresponding estimated patient skin doses range between 50 and 500 µGy. Note that this dose takes into account the beam geometry, and results from the available tube power during 10 seconds, (in the EOS prototype 20 kW for 10 seconds).

The radiation per line and patient skin dose can be increased by increasing the exposure time (up to 31.5 s), and, eventually, with a more powerful X-ray source.

3.5 Flat Panel equipment description and protocol

The chest imaging device used at ULBE was a digital flat panel radiography, a 'Siemens Thorax FD-X' (Serial number 1010, Siemens Medical System, Erlangen, Germany) (DX), with a detector size of 43x43 cm, and 2881x2880 pixels. The flat panel is indirect TFT x-ray detector based on amorphous silicon and Cs-iodide “Trixell Pixium 4600” (Trixell, Moirans (France), is a joint venture of Philips Medical Systems, General Electric, and Siemens, so this detector is used in many products manufactured by these companies). This detector is built with four 21.5 x21.5 smaller elements tiled together and mounted on a common glass substrate. The X-ray to light conversion is done by a layer of 500 µm of Thallium-doped Cesium Iodide (CsI:Tl). This detector has a spatial resolution of 143 x 143 µm² (3.5 LP/mm., 6.99 pixels per linear mm, and 48.9 pixels per square mm.), providing 12 or 14 bit images (up to 4096 or 16384 grays) with a modulation transfer function (MTF) of 18% (30% at 2.5 lp/mm) (232). The light channeling property of the pillar-like crystalline structure of the CsI and the pixel size provide the spatial resolution. A fixed 13:1 anti-scatter grid (Mitaya Manufacturing, Tokyo, Japan) with 78 lines per centimeter, 180-cm focal distance, 20 µm lead strips, and aluminum interspace is placed before the detector..

Amorphous silicon flat panels detectors have been considered the 'Gold Standard' in this study, as since 2002 they have attained and maintained this level of appraisal in all comparative studies, in terms of image-quality, and by the potential for dose reduction, in digital chest x-ray imaging (69,234,375–380).

The standard 'Chest program" (APR) with automatic exposure control was used: with X-ray tube voltage fixed at 125 kVp, current (mAs) automatically limited by the automatic exposure control (AEC), and radiographic sensitivity of the detector set to 400.

DX Digital Radiology Flat panel characteristics (DR)	
Model	Siemens Thorax FD-X
Detector manufacturer - model	Trixell Pixium 4600
Detector Characteristics	Flat panel, CsI scintillator, amorphous silicon
X-Ray Generator	Siemens Polydoros Lx 50 Lite (50 kW at 100 kW IEC)
X-Ray Tube	Siemens Optilix 150/30/50 HC-100 for 150 kV, Focus 0.6 and 1.0 mm. (30/50 kW)
Additional filtration	Cu 0.3mm
Auto Exposure Control	Yes
Sensitivity (SI)	400 (default, not modified)
Fd Distance (Vertical stand)	180 cm
Grid	Fixed focused grid
Image Size Limit	43 x 43 cm 2881x2880 pixels (8297280 pixels)
Pixel Size	0.143 x 0.143 mm
Image gray-level depth	12 bit, high bit 11
Tube Mount	Ceiling suspended
Vertical stand range	35-172 cm
Room Size requirement	305 x 300 x 245 cm.
Weight (stand)	184 Kg detector and stand,
Patient Identification	Dicom Work-List, Manual Entry
Other characteristics	Digital Dicom-Compatible image management
Cycle Duration,1 image	5 sec
Throughput	>150 Images/hour Typical

Table 11: DX Digital Radiology Flat panel characteristics (DR)

Figure 25: Siemens Thorax FD-X Vertical Stand Detector

Table Comparative image detector parameters (DX and EOS)		
Parameters	**DX**	**EOS**
Detector type	Flat panel	Microgrid ionization chamber
Detector size (Width x Height)	43 cm x 43 cm	44.8 cm x 90 cm
Image matrix	3001 x 3001	1760 (x 3500)
Pixel size / pitch	143 µm	254 µm
Spatial Resolution	3.5 pl/mm	2 pl/mm
Dynamic Range	12 bit	16 bits
Sensitivity (SI)	400	-
X-ray generator voltage	40 to 150 kVp	40 to 125kVp
X-ray generator current	1 to 650 mA	10 to 400mA (discrete values)
Acquisition time	1 ms à 6/16 s	0,83 to 100ms per line.

Table 12: Comparative image detector parameters (DX and EOS)

3.6 Dosimetry EOS and DX

3.6.1 Dosimetry with the EOS planar scanning system

The shape of the X-ray fan beam, collimation and translation of the scanning X-ray source confer to the EOS device several differences in front of common radiographic planar systems. These bear different demands for the assessment of static dose and the scan dose caused mostly by the thin collimator geometry.

The particular geometry of the EOS x-day device make it apart than conventional chest radiography units. Planar systems performance, being conventional screen-film, computed radiography, or digital flat-panel technologies, requires well-known procedures with TLD or solid state detectors. EOS requires additional techniques, some close to those used in CT dosimetry, some close to x-ray bi-plane dosimetry assessment.

3.6.1.1 Geometry of the EOS beam: Collimation and beam slice profile

In the usual radiographic systems the X-ray beam is a cone and the dose follows the law of the inverse of the square root; being the dose per area reduced by the inverse square root of the focus to detector or patient distance.

In the EOS scanning system, the detector array lies in a horizontal plane determined by means of two thin collimator slots, namely the detector(Cd) and the object collimator (Co) slots. The resulting beam profile is a fan shaped (flat) beam, with its “thinness” across the

collimator plane (along the vertical axis, parallel to the floor).

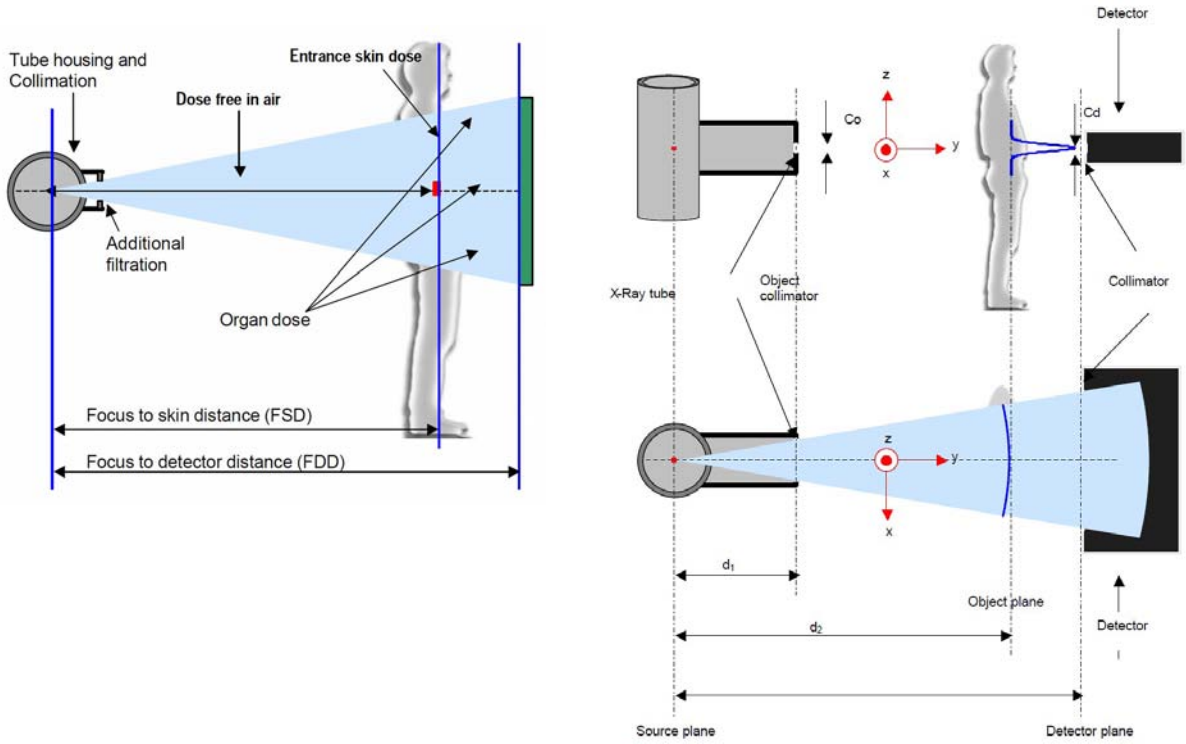

Figure 26: Beam profile and standard TLD placement for entrance dose assessment
Left) Conventional radiography: exposure is like the detector a planar full-field area
Right) EOS: exposure is a thin laminar fan of 500 µm

Dosimetry was carried to assess EOS characteristics:

- The effect of collimator geometry on the dose delivered during the scan and static mode.
- Characterization of EOS equipment radiation parameters as scan dose, detected dose, dose utilization factor, skin dose, and organ dose.

3.6.2 Dose Measurements

a) The integrated dose was measured directly with a standard pencil dosimeter, as used in CT dose measurements, with a cylindrical ionization chambers with an active zone of 10 cm long. These dosimeters are qualified for measuring the integrated dose associated to a given beam profile when its broadness is less than 10 cm. The pencil is positioned perpendicular to the horizontal beam plane and provides the integrated dose expressed in mGy. Such a dosimeter can also be used for the scan mode under narrower beam width conditions, scanning lengths less than 10 cm.

b) Measurement of the dose from a scan. Dose rate measurements are done with the pencil dosimeter and with a solid-state dosimeter: The dosimeter is a diode with a 1 cm²

square cross section. It should be entirely placed within the x-ray beam. Doses are expressed in Gy.

c) For digital flat panel modalities a solid-state dosimeter (RTI Electronics Solidose 300-R100) was used whilst a dose-area product-reading device (Diamentor PTW) was installed at the X-ray tube housing to monitor the total value (mGy cm^2).

3.6.3 Image detector efficiency, Modulation Transfer Function (MTF) And Detection Quantum Efficiency (DQE) assessment

The modulation transfer functions (MTF) and the detection quantum efficiency have been measured both along the horizontal and the vertical directions. Along the horizontal direction both results are related to the performance of the detector, while the other direction, the results are related to the alignment of the collimation slits including the tube focal spot of the scanning system.

The measurements have been done with a 70 kV X-ray spectrum, and 2.5 mm aluminum filtration, using a narrow slit (10µm) at angle (2°) with the plane orthogonal to the axis under study. The incident flux, inferior to 100 kHz by channel, is set so that measurements are not biased by the space charge phenomenon. The detector gain effect has

3.6.4 Experimental working parameters

The following tables give the typical working parameters for several sizes in the high and low acquisition speed modes.

In the EOS device a chest image of 44 cm x 45 cm (1760 x 1800 lines) will take an acquisition time between 1.5 and 3 seconds. As a reference a full size image (full spine) 44 cm x 90 cm (1760 x 3600 lines) takes between 6 and 12 seconds.

The corresponding estimated patient skin doses will range between 50 and 500 µGy. This dose takes into account the collimation geometry.

The table below shows the patient skin dose that will be in accordance to the European reference doses recommendations for adults (EUR 16260) (310).

	High speed (30 cm/s, scan time 1.5 sec)		**Low speed mode (4.3 cm/s, scan time 10 sec)**	
	Tube current	Radiation per line	Tube current	Radiation per line
70 kV	500 mA	0.42 mAs	320 mA	1.8 mAs
100 kV	400 mA	0.33 mAs	200 mA	1.11 mAs

Table 13. EOS working mAs per line at different mA and scanning speeds

A comprehensive culture of radiation protection and safety in medicine has been adopted by international regulation bodies and the European Union with regard to the medical use of ionizing radiation and has been integrated into the various branches of diagnosis and treatment. The European Commission has contributed to this evolution with the establishment of legal requirements to be implemented by Member States for the radiation protection of persons undergoing medical examinations or treatment.

The approach taken is based on the European study were published in the EUR-1620-EN report “European guidelines on quality criteria for diagnostic radiographic images”, 1996.

The table below shows the patient skin reference dose according to the European Recommendations (EUR 16260):

Chest X-Ray Recommendations (as doc EUR 16260)		
Front view	125Kv	0.3 mGy
Side view	125Kv	1.5 mGy

Table 14. European Chest Dose reference level and suggested kVp Eur 16260 (310)

3.6.4.1 EOS settings and collimation requirements

EOS dosimetry characteristics depend on collimation geometry, the latter being settled when manufacturing the prototype. Moreover, while examination images are being taken, the patient is centered at the intersection of both X-ray beams; therefore focus-to-skin distances in both directions keep rather unchanged during the linear scan except for body thickness variations. The air dose delivered at the meeting point of both beams is consequently a good dosimetric indicator. Complete characteristics of collimation geometry are the following:

Table: Complete characteristics of collimation geometry		
Focus spot size at 0° (apparent)	h_o	1.2 mm
Anode angle	φ	10°
Tube angle	α	5°
Source to object collimator distance	d1	450 mm
Object collimator opening	Co	500 µm
Source to beam intersection distance (front)	d2F	986 mm
Source to beam intersection distance (lateral)	d2L	916 mm
Source to detector collimator distance	d3	1260 mm
Detector collimator opening	Cd	500 µm

Table 15. Complete characteristics of collimation geometry

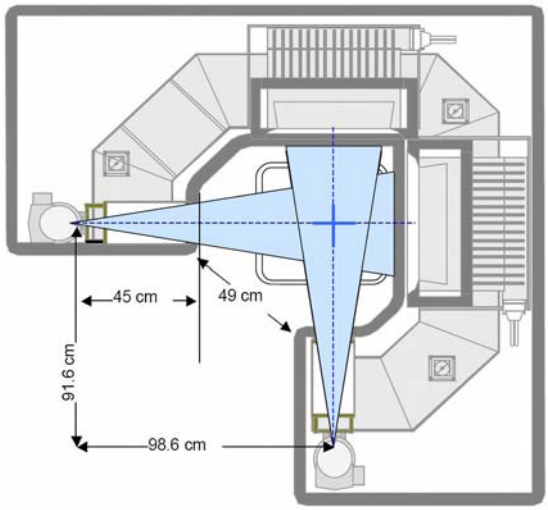

Figure 27: EOS device layout with X-ray beam intersection.
The pencil dosimeter is placed at the intersection hold in a stand

3.6.5 Measurement of the dose from a scan

3.6.5.1 Dose rate measurements

Were done at the intersection of both X-ray beams with both projections (A-P or P-A and lateral). Doses D_{BAL} (kV) were obtained from direct measurements using a solid-state dosimeter at 98.6 and 91.6 cm distances respectively for face and profile projections.

Sampling interval: 0.25 mm Power rate: 1.67 mAs / line

These measurements wiil be compared with those obtained a the solid-state detector. The scan dose rate value, expressed for a unit mAs, is based on the integrated dose as follows:

Scan dose / mAs/L = δINT (kV) / (p · mAsTOT/n)

= δINT (kV) / (p x 333.2/n)
= DINT (kV) / (p x 333.2)

3.6.5.2 Entrance Dose Dosimetry: TLD measurements

Thermo-Luminescent detectors (TLD-100, OptoScience, Tokyo, Japan) (TLD) were used to measure entrance radiation dose including the backscattering. Two protocols have been designed in order to compare entrance radiation dose between EOS (2 simultaneous TLD detectors) and conventional DX acquisitions (1 TLD per x-ray exposition). EOS bears a simultaneous exposition of the 2 TLD from two simultaneous beams, while DX only exposes one of them each time, conveying a penalty for the EOS detected dose. This bias discour-

ages a direct comparison of measurements with both modalities, however, it still enables correlated measurements from the both modalities.

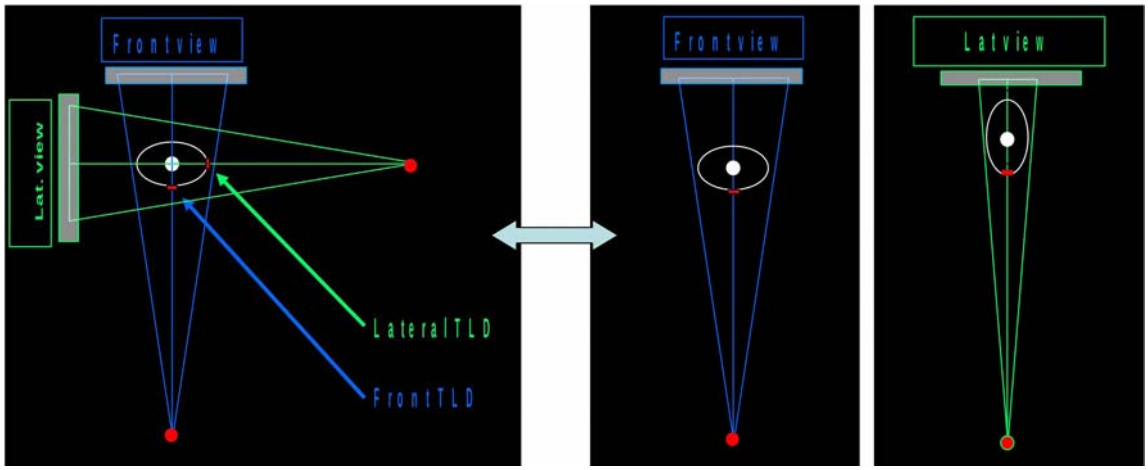

Figure 28. TLD position for dose measurement in a biplane exposure
Left) Measurement under EOS biplane exposure . Two simultaneous beams and TLDs.
Right) Standard dose measurement. One TLD per exposure.

On the 40 image quality patients, TLD measures were done 18 of them during DR and EOS exam for the frontal and lateral views. However, the acquisition parameters were very low concerning the DR device, with TLD measurements below the minimal evaluable measurement threshold. Only 2 DR TLD were found to have evaluable dose for the frontal view, and 12 for the lateral views.

Thus, we had too few TLD values of the frontal views to provide significant results. However, lateral TLD measurements are shown in the results table below to give an idea of the dose ratio between the two modalities.

3.6.5.3 Effective dose calculation in mSv

From the kerma free in air, the morphologic data of a given patient (weight, height, lateral width…), his/her age and the acquisition area, it is possible to calculate and compare the effective dose absorbed during the conventional exam and the one absorbed during EOS exam.

The patient and data used for this assessment correspond to second group of patients focused on spine dose, that allow to have a wide range of morphologic data.:

The data of a cohort of 65 patients exposed to EOS prototype and CR imaging was analyzed, with data linked to the corpulence of some patients (weight, lateral and postero-anterior width) and to the acquisition parameters (kVp, mAs, Film-Source Distance) during EOS or conventional exams.

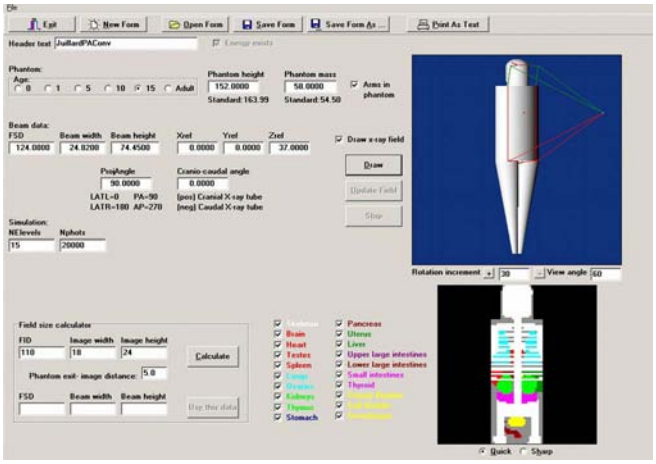

Figure 29. Monte-Carlo simulation software (PCXMC) MAIN SCREEN, used to calculate effective dose for planar radiographs (EOS or conventional)

The PCXMC software, shown above, was used to simulate the effective dose absorbed by each organ as well as the total effective dose. Thus, for a patient, it was possible to compare the effective dose absorbed during the conventional exam and the one absorbed during the EOS exam.

3.6.6 EOS operational dose levels

Corrected Dose by the distance allowing assessing, for any projection, the dose delivered at the reference point (intersecting optical beam axes) and expressed in kerma free in air.

The patient entrance dose will correspond to the displayed value, corrected to make allowance for the source to skin distance (with a resulting increase of 10 % or 20 % respectively for face or profile projections).

The linear scan dose rate is expressed for a mAs/L @ 100 cm unit, as it follows

$$\delta BAL0\ (kV, G) = 8.00.10\text{-}3 \times kV\ 2 + 3.12 \times kV + 102.4$$

The EOS dose is then obtained as a function of kV and mAs/L as it follows:

$$DBAL\ (face) = \delta BAL0\ (kV, G) \times 100/98.6 \times mAs/L$$

$$DBAL\ (profile) = \delta BAL0\ (kV, G) \times 100/91.6 \times mAs/L$$

3.6.6.1 Scan Dose Associated To EOS operating parameters

EOS operating parameters

Due to its peculiar reconstruction mode of the radiological images EOS has some differences comparatively to the conventional radiological systems currently in use (see Table 16 below).

Table. Image parameters associated to a scanning mode	
EOS parameters	Symbol and expression
Image size (number of lines)	n
Tube voltage (kV)	kV
Tube current (mA)	mA
Scanning speed (cm/s)	V
Focal Skin Distance (cm)	FSD
Total exposure time (millisecond)	T
Time exposure per line (millisecond)	$\Delta t = T / n$
Radiation per line (mAs)	mAs/L = mA x T / n
Patient skin dose	D (kV) = δ_{BAL0} (KV) x mAs/L x (100/FSD)

Table 16. Image parameters associated to a scanning mode

Patient skin dose will be measured and organ-dose will be calculated.

X-ray tubes limitations, in terms of tube power and anode heat capacity may limit the length and x-ray intensity available for a long scan. These parameters depend on the original engineering design and cannot be modified. Most x-ray and energy is wasted as heat in all x-ray tubes. As the operative x-ray beam in EOS is extremely restricted, with most photons stopped by the tube and patient collimators, the EOS' x-ray tub should support the loads for expositions of several seconds as in clinical examinations.

3.6.6.2 Maximum available EOS dose values

In order to o measure the maximum available radiation (mAs/L) as a function of kVp, for two types of image and for different scanning speeds

The curves where derived from manufacturer data-sheet and testing and can be found in results as figure 53 data represent the maximum dose obtainable as a function of kVp, for two image length, and for scanning speeds 3.75, 7.5 and 30 cm/s.

3.6.6.3 Dose in Scan mode and presence of a Scattering Medium

3.6.6.3.1 Measurement of the entrance surface dose with a phantom

In order to estimate the entrance surface dose in the presence of a scattering medium, several blocs of Plexiglas of different thickness were used to simulate the patient attenuation. TLDs were placed at the entrance of the Plexiglas phantom according to the scheme detailed in the figures here below. Such dosimeters allow the contribution of backscatter radiation to be measured and are currently used in the field of medical diagnostic radiology. The TLDs were aligned along the scanning axis of the beam in order to appreciate the possible dose variation from the center of the beam to the periphery. Both front and lateral projections were considered and two different patient thicknesses were taken into consideration, 10 cm and 20 cm of Plexiglas respectively.

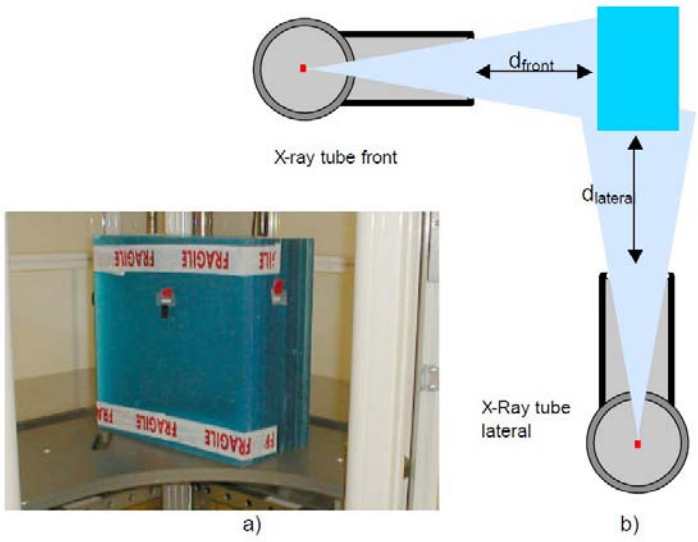

Figure 30: Experimental conditions and both TLDs positions in EOS

In order to get reliable values, TLDs were exposed three times while keeping the irradiation settings constant. Due to the phantom dimensions, the irradiation geometry led to the experimental conditions, which are summarized in the following paragraphs

As it can be seen from the figure 30, with the 10 cm phantom thickness, the entrance surface of the phantom was at 54 cm far away from the front X-ray tube and at 27 cm from the lateral X-ray tube respectively while, with the 20 cm phantom thickness, the front distance from the X-ray tube was shortened to 44 cm. The following table, details the dosimetry results obtained for the experimental settings corresponding to the irradiation conditions

3.6.7 Digital Flat Panel Detector Dosimetry

Dosimetry methods for digital flat panels are the same than for conventional screen-film ra-

diography. Direct measurements with TLD, were performed concurrently with the EOS device, as comparative studies. As described previously, the TLD were independently exposed for each incidence, the norm in standard radiography dosimetric studies. This study will present data from the dose and image study group (40 patients). Individual dose data may be gathered from DICOM image headers. Siemens Thorax FD-X provides two dose related parameters: EXI (DICOM tag '0018,1405') and DAP (DICOM tag '0018,115E'). EXI, Siemens exposure index, has a direct correspondence to air KERMA EXI, corresponding to '*µGy air Kerma *100*' (as calibrated by SIEMENS under the following standard conditions: RQA5, 70 kV +0.6 mm Cu, HVL=6.8 mm Al). Any EXI value can be converted to µGy air Kerma by dividing its value by 100, using the formula (µGy=EXI/100). DAP, Dose Area Product, gives the directly estimated dose as $dGy \cdot cm^2$ (381,382).

3.7 Chest Images Assessment

3.7.1 Chest Radiography Image quality criteria

The objective was to compare image quality of the EOS device in chest imaging compared to a state-of-the-art digital radiography device. Image quality assessment was planed on the sample of 40 patients where two successive Chest x-ray examinations where acquired by the EOS device and by the DX flat panel device. Two subsets, two pairs of images, were analyzed as Posterior-anterior images and Lateral projection images. Image quality assessment followed the approach taken is based on two European trials of the “Quality Criteria” that had been first identified by a panel of experts in the field of diagnostic radiology. The final results of these studies were published in the EUR-16260-EN and EUR-16261-EN reports ”*European guidelines on quality criteria for diagnostic radiographic images*”, in 1995 for adults (310) and in 1996 for pediatric patients (383). These criteria involved position, coverage, and anatomical details, which have been considered as essential to reflect a proper coverage of the whole chest field, centering of x-ray beam or the patient positioning into the region interest, spatial and density resolution.

The table below lists the corresponding image quality criteria according to the European recommendations (EUR 16261) for posterior-anterior or anterior-posterior (PA/AP) and for lateral (LAT) projections.

Table : "European quality criteria" for chest AP/PA and LAT projections.	
AP/PA Projection	**LAT Projection**
Performed at peak of inspiration, except for suspected foreign body aspiration	Performed at the peak of inspiration
Reproduction of the thorax without rotation and tilting	True lateral projection
Reproduction of the chest must extend from just above the apices of the lungs to T12/L1.	Reproduction of the chest must extend from just above the apices of the lungs to T12/L1.
Reproduction of the vascular pattern in central 2/3 of the lungs	Reproduction of the hilar vessels
Reproduction of the trachea and the proximal bronchi	Visualization of the trachea from the apices of the lungs down to and including the main bronchi.
Visually sharp reproduction of the diaphragm and costo-phrenic angles	Visually sharp reproduction of the whole of both domes of the diaphragm
Reproduction of the spine and paraspinal structures and visualization of the retrocardiac lung and the mediastinum.	Reproduction of the sternum and the thoracic spine

Table 17. European quality criteria" for chest AP/PA and LAT projections.

Several image quality scored items are the same for both projections, but few of them differ as they are related to the symmetry, anatomy, shape and densities of the thorax in each projection (310,383,384). Being EOS a linear scan acquisition radiography device, its radiation dose and geometry, but also its acquisition geometry and detector, are different from a conventional planar x-ray modality, and may show completely different image quality assessment profiles. A modified table of criteria was applied for the assessment image quality trying to catch potential weak points of the EOS modality. Fissures visualization as it can be affected by slow vertical scan acquisition, image-line stitching and spatial resolution, as may be Interstitial/thin vessels structures on the outer third of the lung field.

Combining theses proposition, the study Image quality analysis involves both the assessment of anatomical details, which have been considered as essential to reflect a proper centering of x-ray beam or the patient positioning into the region interest, and assessment of anatomic structures that may challenge the EOS device, mainly small size objects and lines.

The Europeans Guidelines were modified in three items :

- item 5 - **reproduction of peripheral structures**. In the periphery of the lung this fine, low contrast, structures are usually perpendicular to the chest wall. The spatial resolution of the thin EOS detector, combined with its vertical motion and sequential reconstruction, may be a challenge in the visualization of these structures.
- item 6 – **reproduction of fissures**. Fissures are anatomical thin structures, high

contrast, than can be identified in many patients. The major fissures have a vertically-oblique plane (in the lateral projection) and can be seen in most patients, but a slower scanning modality may allow blurring by patient or breathing movements. The minor fissures can be seen in both projections but it is thin, parallel to the floor plane, and sometimes does not generate a visible density in neither projection; making it an additional challenge for the EOS prototype.

- Item 10 – **reproduction of soft tissues and fat pads** of the chest and thorax wall. EOS device is expected to outperform digital radiography systems as its theoretical acquisition dynamic range is nine-folds superior.

Each item was scored following a homogeneous ordinal scale, from 1 to 5:

1: Not seen: The image does not depict this structure or criteria.

2: Poor: the image allows to barely assess the evaluated structure or criteria.

3: Good: the image allows an adequate assessment the evaluated structure or criteria

4: Very Good: the image allows an excellent assessment of the evaluated structure or criteria.

5: Outstanding: the image quality allows to depict with outstanding resolution or contrast the evaluated structure or criteria.

3.7.1.1 EOS AP-PA projection criteria

1. Performed at the peak of inspiration. Except for suspect of foreign body aspiration.
2. Reproduction of the thorax without rotation and tilting
3. Reproduction of the chest must extend from just above the apices to the lungs to T12/l1
4. Reproduction of the vascular pattern in central 2/3 of the lungs
5. Reproduction of fine interstitial structures in the 1/3 periphery of the lungs.
6. Reproduction of fissure major and fissure minor
7. Reproduction of the trachea and the proximal bronchi
8. Reproduction of the spine and paraspinal structures and visualization of the retrocardiac lung and the mediastinum
9. Reproduction of the spine and paraspinal structures and visualization of the retrocardiac lung and the mediastinum.
10. Reproduction of the soft tissues and fat pads

3.7.1.2 EOS Lateral projection criteria

1. Performed at the peak of inspiration, except for suspect of foreign body aspiration.
2. True lateral projection
3. Reproduction of the chest must extend from just above the apices of the lungs to

T12/l1

4. Reproduction of the hilar vessels.
5. Reproduction of fine interstitial structures in the 1/3 periphery of the lungs, as retrosternal space.
6. Reproduction of fissure major and fissure minor.
7. Reproduction of the trachea from the apices down to and including the main bronchi.
8. Visually sharp reproduction of the whole of both domes of the diaphragm.
9. Reproduction of the sternum and thoracic spine.
10. Reproduction of the soft tissues and fat pads.

Table . Side by side EOS assessment P-A and Lateral criteria

	P-A Projection	Lateral Projection
1	Performed at peak of inspiration, except for suspect of foreign body aspiration	Performed at the peak of inspiration, except for suspect of foreign body aspiration
2	Reproduction of the thorax without rotation and tilting	True lateral projection
3	Reproduction of the chest must extend from just above the apices of the lungs to T12/L1.	Reproduction of the chest must extend from just above the apices of the lungs to T12/L1.
4	Reproduction of the vascular pattern in central 2/3 of the lungs	Reproduction of the hilar vessels
5	Reproduction of fine interstitial structures in the 1/3 periphery of the lungs	Reproduction of fine interstitial structures in the 1/3 periphery of the lungs (Retrosternal space)
6	Reproduction of fissures major and fissure minor	Reproduction of fissures major and fissure minor
7	Reproduction of the trachea and the proximal bronchi	Visualization of the trachea from the apices of the lungs down to and including the main bronchi.
8	Visually sharp reproduction of the diaphragm and costophrenic angles	Visually sharp reproduction of the whole of both domes of the diaphragm.
9	Reproduction of the spine and paraspinal structures and visualization of the retrocardiac lung and the mediastinum.	Reproduction of the sternum and the thoracic spine
10	Reproduction of the soft tissues and fat pads.	Reproduction of the soft tissues and fat pads.

Table 18: Side by side comparison of EOS assessment criteria, PA and Lateral views

3.7.2 Reading sessions

The assessment involved independent blinded reading of the image datasets by several radiologists. Thus, prior to starting the sessions, all images were fully anonymized and pa-

tients where re-numbered, allowing presenting them in a randomized controlled sequence.

Four senior radiologists, acting as readers, where involved in this study (GK, PS, JP, PSC), with a combined radiology reporting experience between 5 and .30 years, including previous exposure to digital and conventional chest images, radiology workstation and image display manipulation tools. All four readers had previous experience in image quality assessment studies, in x-ray images and/or CT images. The radiologists belong to the staff of three different hospitals in Paris, Brussels, and Barcelona, working with their local radiology workstations. EOS and DX exam where analyzed on a CRT screen (19 inch, 1280x1024) with a classical DICOM viewer, Osiris viewer v.3.6 (Univ Geneva CH), that allowed the display and adjustment of window width and level for 16 bit gray-scale images. No consensus meeting was done prior to the reading sessions. A time up to 3 minutes was allocated per case (2 images) with a scheduled reading time of up to 222 minutes (37 x 2 x 3'). Reading sessions where scheduled to last up to 60 minutes, in order to avoid reading fatigue biases, and held with optimal reporting room light conditions. Sessions were completed with the help of a second person who assists in recalling the image sequence, reminding criteria items to be score, and doing the data collection tasks, controlling the time elapsed, but avoiding being involved in the quality score.

Images were presented at the monitor screen in a random sequences, mixing DX and EOS exams. Even the modality/device was blinded, the EOS modality nature may be suspected by its broad window-width available, maybe allowing to somewhat 'tag' the reading as being the EOS modality in many cases. The scores where collected in the following numbered scorecards where used allowing to collect an ordinal score for each criterion.

SYSTEM	EOS					DR CONVENTIONAL				
AP/PA projection	Image quality score					Image quality score				
Criteria	1	2	3	4	5	1	2	3	4	5
1. -Performed at peak of inspiration, except for suspected foreign body aspiration										
2.- Reproduction of the thorax without rotation and tilting										
3.- Reproduction of the chest must extend from just above the apices of the lungs to T12/L1.										
4.- Reproduction of the vascular pattern in central 2/3 of the lungs										
5.- Reproduction of fine interstitial structures in the 1/3 periphery of the lungs										
6.- Reproduction of fissures major and fissure minor										
7.- Reproduction of the trachea and the proximal bronchi										
8.- Visually sharp reproduction of the diaphragm and costophrenic angles										
9.- Reproduction of the spine and Paraspinal structures and visualization of the retrocardiac lung and the mediastinum.										
10.- Reproduction of the soft tissues and fat pads.										
Total										

Image quality Score:
1: Not seen, 2: Poor but usable, 3: Good, 4: Very Good, 5: Outstanding

SYSTEM	EOS					DR CONVENTIONAL				
Lateral projection	Image quality					Image quality				
Criteria	1	2	3	4	5	1	2	3	4	5
1.- Performed at the peak of inspiration										
2.- True lateral projection										
3.- Reproduction of the chest must extend from just above the apices of the lungs to T12/L1.										
4.- Reproduction of the hiliar vessels										
5.- Reproduction of fine interstitial structures in the 1/3 periphery of the lungs										
6.- Reproduction of fissures major and fissure minor										
7.- Visualization of the trachea from the apices of the lungs down to and including the main bronchi.										
8.- Visually sharp reproduction of the whole of both domes of the diaphragm										
9.- Reproduction of the sternum and the thoracic spine										
10.- Reproduction of the soft tissues and fat pads.										
Total										

Image quality Score:
1: Not seen, 2: Poor but usable, 3: Good, 4: Very Good, 5: Outstanding

Figure 31: Image quality score-cards for Postero-Anterior and Lateral Chest images

3.7.3 Statistical Analysis

Descriptive and analytical statistics have been applied collected data, experimental radiation results, functional parameters, and image quality assessment scores of both compared systems, EOS and DX. Many of the analyzed parameters in this study are non-parametric, so they require non-parametric, distribution free, methods. The description and description of default statistics values and applied methods are enclosed in the following subheaders:

3.7.3.1 Significance levels

The P value, or calculated probability for significance test (hypothesis tests), is the probability of finding the observed, or more extreme, results when the **null hypothesis (H0) is true.** The **null hypothesis** is applied to a hypothesis of “no difference”: along this work, usually, as no difference of observed values between EOS and Digital radiography. In correlation tests, the null hypothesis is for independence between. For all statistical analyses, It will be set as **statistically significant** as **P < 0.05**, and **statistically highly significant** as **P < 0.001. Between both values** (385) (386)

3.7.3.2 Errors I, II, and Sample size

Type I error (alpha) is the false rejection of the null hypothesis and **type II error (beta)** is the false acceptance of the null hypothesis. The significance level (alpha) is the probability of type I error. **Alpha** has been set to **5%** in all presented analysis. The power of a test is one minus the probability of type II error (beta). Beta depends upon sample size and alpha; it gets smaller in reverse to the sample size, and affects the **power** of a study to detect true effect (385). This aspect has been addressed in this work for determining sample sizes in order to avoid wide confidence intervals.

3.7.3.3 Analysis and Agreement between Categorical Measurements

For cases in which the two experimental conditions where parametric, the differences between the two imaging systems and those between the full-field system with and without the grid were examined by using a two-tailed t test, assuming unequal variances. For data that included an equal number of comparative measures, a paired t test was performed; otherwise, an unpaired t test was performed.

3.7.3.3.1 Wilcoxon's Signed Ranks Test (Wilcoxon's matched pairs test)

The Wilcoxon's signed ranks test is a method for the comparison of a pair of samples with ordinal results. Its T+ is the sum of the ranks of the positive, non-zero differences (Di) between a pair of samples. A two sided test is based upon the null hypothesis that the com-

mon median of the differences is zero. The approximate alternative hypothesis in this case is that the differences tend not to be zero. For a lower side test the approximate alternative hypothesis is that differences tend to be less than zero. For an upper side test the approximate alternative hypothesis is that differences tend to be greater than zero. A confidence interval is constructed for the difference between the population medians. In sample terms this is called the confidence interval for the median or mean difference. It is also known as the Hodges-Lehmann estimate of shift.

3.7.3.3.2 Kendall's Tau (τ) Rank Correlation

As image quality data categories are both categorical and ordered, in order to gain more power in tests of independence, we may use an ordinal method as Kendall (tau-b, τ) rank correlation. Kendall's rank correlation (r_τ) provides a distribution free test of independence, and a measure of the strength of dependence between two variables, as observations pairs. Spearman's rank correlation may be satisfactory for testing a null hypothesis of independence between two variables, but it may difficult to interpret when the null hypothesis is rejected. By a two sided test, we may consider the possibility of concordance or discordance, with positive or negative correlation between ordinal variables. A calculated Kendall's rank two sided correlation test improves upon Spearman's by reflecting the strength of the dependence between the variables being compared. The null hypothesis is of mutual independence. The Tau-b statistic makes adjustments for ties. The Tau-b (r_τ) correlation value may be between -1 to +1; values of range from −1 (100% negative association, or perfect inversion) to +1 (100% positive association, or perfect agreement). A value of zero indicates the absence of association

3.7.3.3.3 Estimate of Agreement for between observers, Universal R

Berry-Mielke Universal R coefficient is a generalization of Cohen's kappa coefficient, a function that calculates Berry-Mielke Universal R coefficient of agreement and/or effect size. The generalized statistic accounts agreement for multivariate interval or original observations among several observers. One of the observers, if exists, can be set as the gold standard or reference. This function may also handle multiple aspects or dimensions of observation per observer. With categorical data, R is equivalent to a linearly weighted kappa statistic. The magnitudes of agreement, are the same as for Kappa, interpreted as: values < 0 indicate no agreement, 0–0.20 as poor, 0.21–0.40 as fair, 0.41–0.60 as moderate, 0.61–0.80 as good, and 0.81–1 very good agreement. (387,388)

3.7.3.4 Statistical Tools

All statistical analysis and graphics have been performed with StatsDirect statistical software v.3.0.157, StatsDirect Ltd., (UK). Its mathematical methods are well referenced and provides solid math calculation precision. (389).

4 Results

4.1 EOS Clinical Experiment

4.1.1 Patient selection; Enclosed patients. Excluded patients

The group of 40 adult patients successive scheduled for routine x-ray chest examinations, enrolled after granting their informed consent, underwent, in the same day and facility (ULBE, Brussels, B), two successive chest x-ray exams, each of them with two standard projections (posterior-anterior and lateral views) per exam as planed. The first exam was the clinically indicated with the standard digital radiography unit (Siemens DX Flat-Panel) and the second with the EOS prototype. Three patients were excluded from further study and analysis because their DX image sets become unavailable for review. No other cases were excluded from the initial protocol. The studied group was set to 37 patients, with 37 paired examinations, encompassing 74 images.

4.1.2 Population Demographics, Sex, Age, Height

Table Patient Demographics Age - Sex

	n	%	Age, Mean	Standard deviation	95% CL mean Lower to Upper	Median	Geometric m	Standard error of mean	Range	Maximum	Upper quartile	Lower quartile	Minimum
Total	**37**	100%	56.32	13.69	51.75 to 60.89	58	54.37	2.25	62	81	67	48	19
Female	20	54%	57.35	12.60	51.45 to 63.24	54.5	55.93	2.81	46	76	68	50	19
Male	17	46%	55.11	15.18	47.30 to 62.92	58	52.59	3.68	62	81	65	45	31

Table 19. Patient Demographics, Sex and Age

Table . Patient Demographics Sex and Height

	n	%	Height, Mean	Standard deviation	95% CL of mean Lower to Upper	Median	Geometric mean	Standard error of mean	Range	Maximum	Upper quartile	Lower quartile	Minimum
Total	37	100%	166.41	8.75	163.49 to 169.32	168	166.18	1.44	37	185	171	160	148
Female	20	54%	161.75	7.59	158.2 to 165.3	161.5	161.5	1.7	27	175	168.5	156.5	148
Male	17	46%	171.88	6.7	168.44 to 175.33	170	171.76	1.62	25	185	176	168	160

Table 20. Patient Demographics, Sex and Height

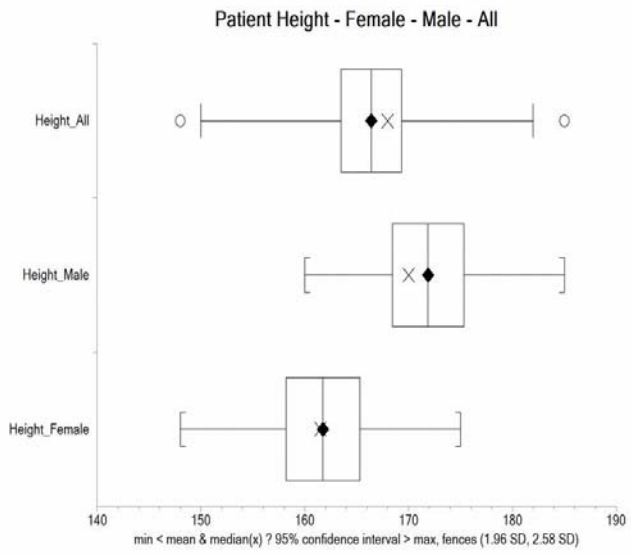

Figure 32: Patient Height. All patients, and female and male patients
(Box and whisker plot)

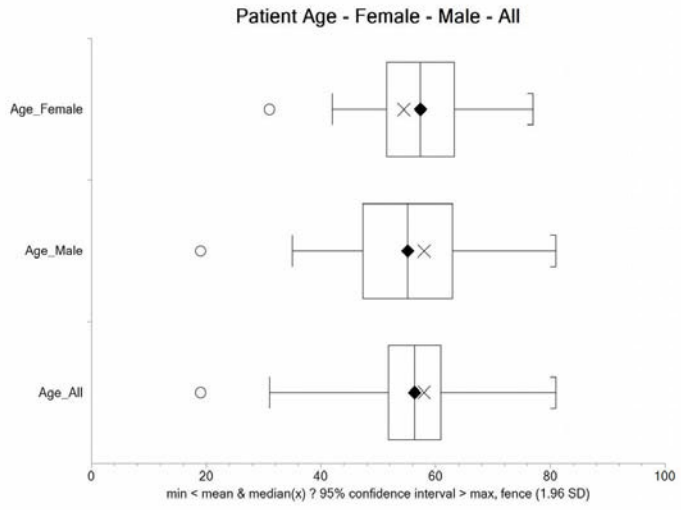

Figure 33: Patient Age. All patients, and female and male patients
(Box and whisker plot)

4.1.3 EOS Examination Request Origin

The study group of 37 patients was referred by 18 departments, 10 from inpatient departments, and 7 outpatient departments. They represent a wide sample of mixed origins including medical and surgical chest disease, oncology, gastroenterology, cardiology, urology, gynecology or outpatient surgery. Examinations were requested by 27 different staff physicians of those departments. In one case both department and physician was unknown. The origins are shown in the next two tables, by department and by physician.

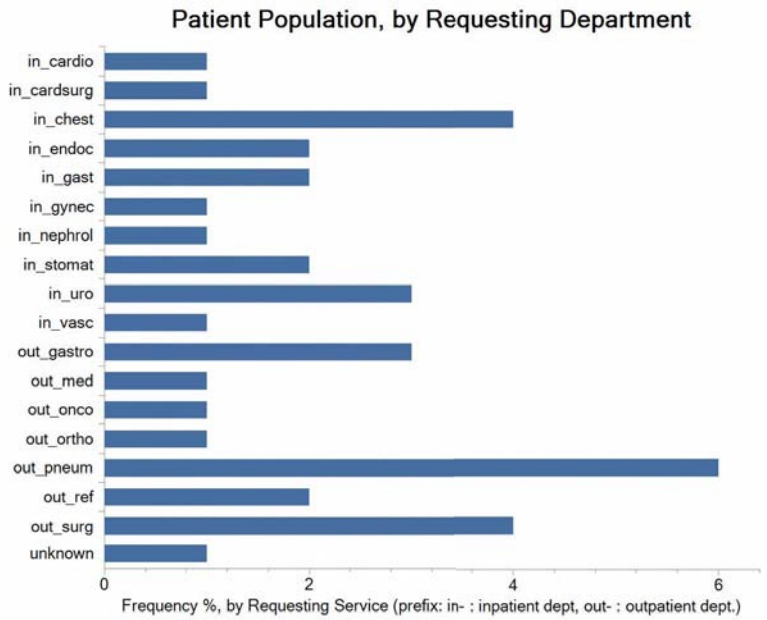

Figure 34. Patients' origin by Ordering Clinical Department

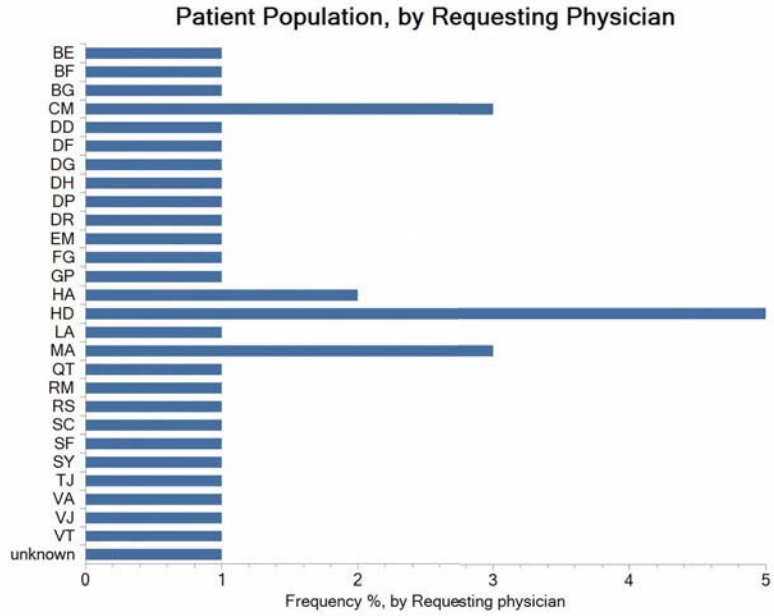

Figure 35. Patients' origin by ordering Clinical Physician

4.1.3.1 Imaging findings in the Image Quality Assessment group

The EOS Chest image quality assessment was a preliminary study not targeted to find chest pathology or clinical performance, but as its sample population comes from patients already referred for chest x-ray examinations at a university hospital, in encloses pathologic findings. Many patients were routine outpatient clinic controls, several come from

pneumology and oncology with chronic diseases at different stages of evolution or under remission. List of origins can be found in figures 34 and 35. Pathologic findings were present in 15 of 37 patients that are summarized in table 21, compiled the list of findings DX and EOS findings, taking DX as the gold standard.

Found Pathologies in Image quality series (in 15 of 37 patients)			
Name	**Findings**	**Identified by EOS?**	
Lung metastasis	2	yes, better	
Atelectasis	1	yes	
Interstitial disease	1	yes	
Lung mass	2	yes	
Pleural fluid	2	yes	
Pneumothorax	1	yes	
Venous catheters	2	yes	
Prosthetic valve	1	yes	
Rib fractures	3	yes	

Table 21: Findings and/or Pathologies in the patients of the image quality series
DX findings were considered as the gold standard

4.1.3.2 Acquisition Procedure Results Data Process, Time and problems

Two experienced chest radiographers were trained in using the EOS prototype. One of them was the responsible for the first exam (patient 1), while the rest of the protocol was completed by the second radiographer (36 of 37 exams).

In three patient the EOS acquisition was repeated by acquisition problems. In two of them, because of an incorrect manual adjustment of the upper limit scan, causing the lost of the apices. Centering was hampered in five patients, two in AP view, and three in the lateral view. In this 5 images, the limits of the chest was cropped in one side as the patient was not correctly centered, partially out of the imaging field, or unable to stay standing in the center plane. The two AP views repeated, but the three lateral where considered acceptable as only the rib margin was affected. No other problems where reported along the experimental period.

Table Elapsed Examination Time EOS and DX (sec)											
n = 35	Seconds, Mean	Standard deviation	95% CL of mean Lower to Upper	Median	Geometric mean	Standard error of mean	Range	Maximum	Upper quartile	Lower quartile	Minimum
DX	258	148	207 to 309	258	214	25.1	581	646	342	122	65
EOS	481	522	302 to 660	327	343	88.2	2382	2419	512	228	37

Table 22: Elapse Examination Time in seconds (Procedure – acquisition)

Elapsed time, in seconds, between admission at the modality console and completion of last image. DX has found to have a faster cycle. Differences are statistically significant.

Elapsed examination time was taken from the elapsed time of examination between the start of the procedure the workstation as DICOM header and the image acquisition time of the last image. It was longer for EOS than for DX, (Mean of differences = -238.56 sec, Two sided P = 0.0139, CI: -52 to 425 sec), with a weak correlation coefficient (r) = 0.08. EOS has had two prolonged acquisition outliers, long acquisition lapses that cannot be traced back to a know cause. In a few patients, examination time has been shorter in EOS as can be seen in the ladder plot.

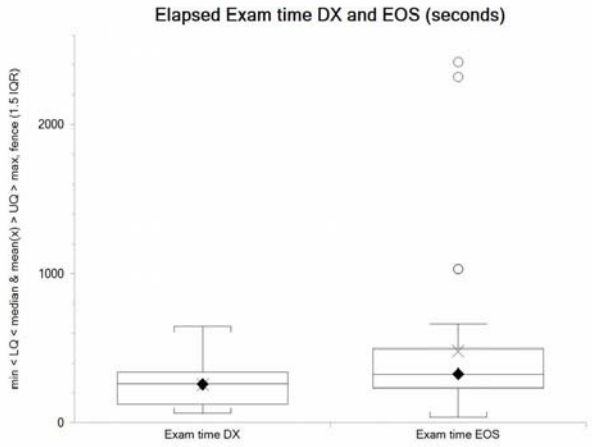

Figure 36. Examination Elapsed Exam time by DX and EOS (sec)

(Whisker plot, time in seconds)

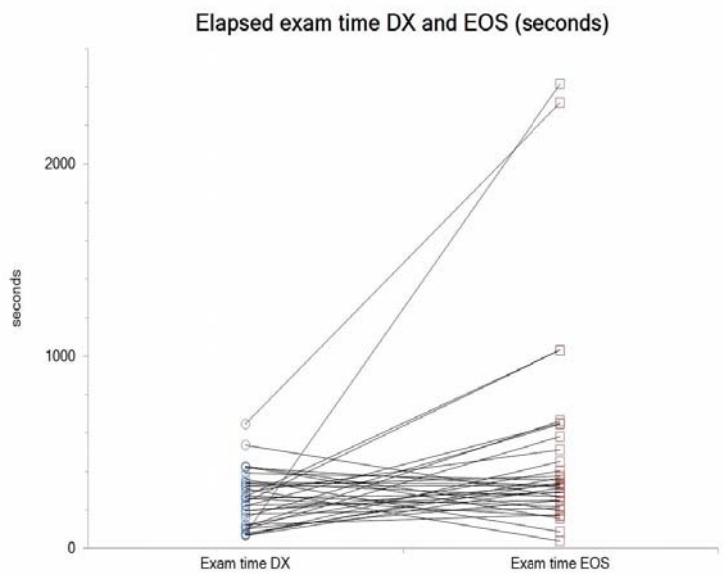

Figure 37. Paired Elapsed Examination Time DX vs EOS (sec)
DX showed less elapse time.Nevertheless, EOS was faster in several patients. (ladder plot, time in seconds)

4.1.3.3 Radiographic Exposure Parameters, for EOS and DX

These parameters were set automatically by a user selection of a pre-programed configuration (APR) at the console of both modalities. The only parameter that was the same and fixed for both modalities was the X-ray tube kilovoltage (kVp), that was set at 125 kVp, for both modalities and for frontal and lateral projections. All other parameters where different. In the DX modality, most of the X-ray tube parameters were automatically set as per patient by the automatic photo-timed exposure. In the EOS modality, all were fixed by three preprogramed exposure settings (Slim, normal, or fat phenotype).

X-ray exposure and acquisition time are longer in a scanning modality (3.3 seconds) than in a planar full-size detector (few milliseconds), with a large ratio, between 1:150 to 1:500 times more for EOS. Two new derived parameters, exposure time per line and mA per line, are calculated by dividing acquisition time by line and intensity by line time.

Tests of significance are presented when their results similar comparison of related parameters may be relevant that show small discrepancies

4.1.3.3.1 X-ray Tube Intensity

Intensity has few steps in both modalities. For DX it was fixed at 200 mA in most patients, as mAs is finally set by phototimed. EOS has used steps depending of the body habitus.

X-ray Tube Intensity (mA) – EOS and DX												
Projection View	**Device DX /EOS**	**Mean**	**Standard deviation**	**95% CL mean Lower to Upper**	**Median**	**Geometric m**	**Standard error of mean**	**Range**	**Maximum**	**Upper quartile**	**Lower quartile**	**Minimum**
AP - PA	DX	211.97	7.46	209.48 to 214.46	212	211.84	1.23	32	229	216	208	197
	EOS	161.76	39.74	148.51 to 175.01	125	157.11	6.53	125	250	200	125	125
Lat	DX	322.47	4.35	321 to 323.94	323	322.44	0.72	19	332	325	319	313
	EOS	160.68	39.21	147.6 to 173.75	125	156.17	6.45	125	250	200	125	125

X-ray Tube Intensity (mA) EOS and DX (paired t test, n = 37)							
Parameter	**Diff. mean**	**Std. dev.**	**Std. error**	**95% CI**	**T value**	**One sided P**	**Two sided P**
mA PA	**50.216**	42.551	6.995	36.028 to 64.403	7.178	**< 0.0001**	**< 0.0001**
mA Lat	**162.889**	40.315	6.719	149.248 to 176.529	24.242	**< 0.0001**	**< 0.0001**

Table 23. X-ray Tube Intensity (mA) - DX and EOS

Differences are statistically significant.

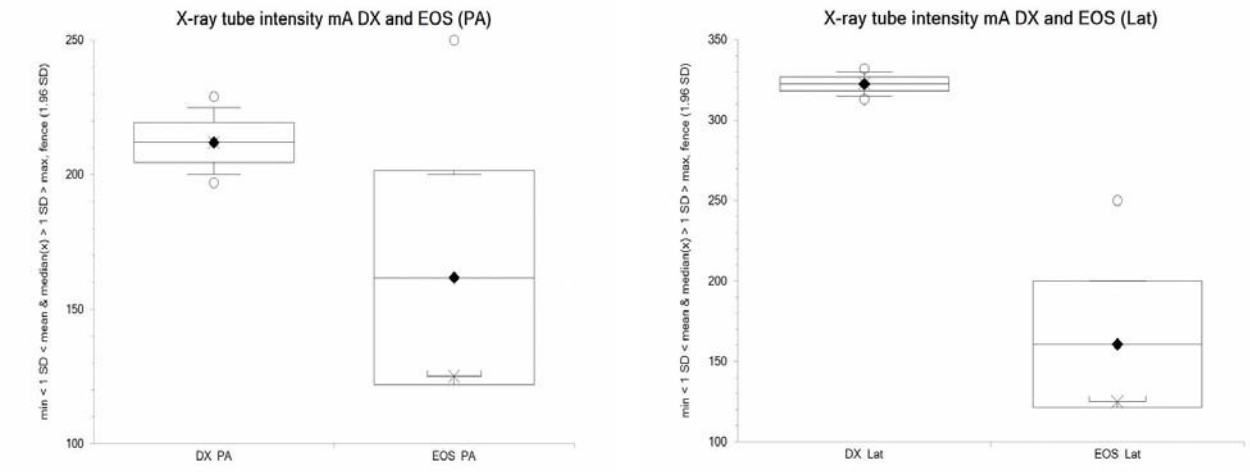

Figure 38. X-ray tube intensity (mA). EOS and DX, in PA-AP and lateral projection

Left) Posterior-anterior projection. Right) Lateral projection. (Whisker plot, mA). Values for DX and EOS fall apart without no overlap.

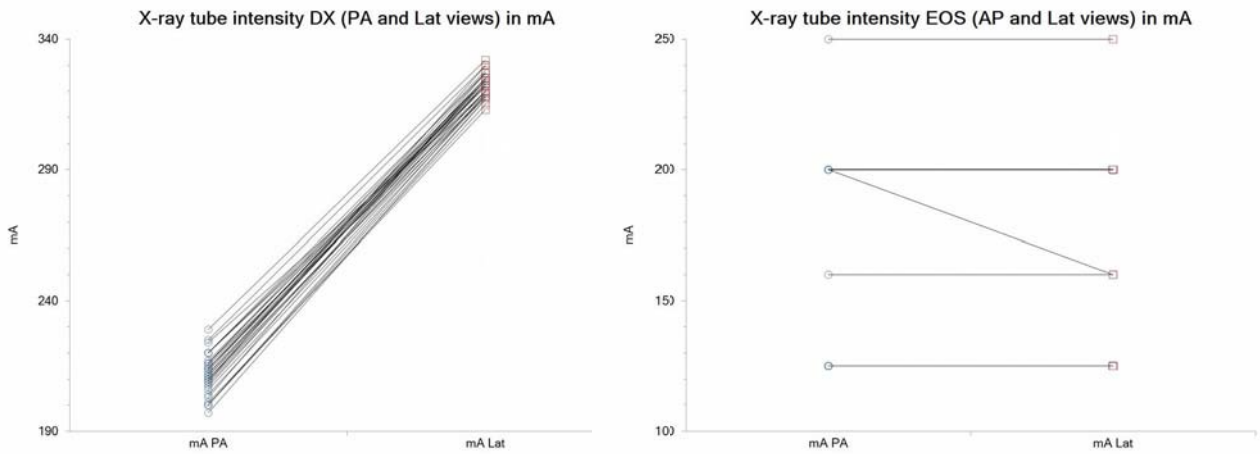

Figure 39. X-ray Tube Intensity from PA to Lateral projection (DX & EOS)
Left) DX Ladder plot. An consistent increase in mA (PA intensity x2) can be observed. Right) EOS Ladder plot. Most patients have the same fixed mA in both views. One case received less mA in the lateral projection.

4.1.3.3.2 Exposure Time

Exposure time is pre-programmed in EOS to allow scanning coverage of the chest at the speed required for correct x-ray fluence. It has been recorded as 3300 msec for all patients. In DX the time in msec, is automatically phototimed by the modality. More time is required for the increased diameter and density in the lateral.

Table Exposure Time (msec) - DX and EOS

Projection View	Device DX /EOS	Mean	Standard deviation	95% CL mean Lower to Upper	Median	Geometric m	Standard error of mean	Range	Maximum	Upper quartile	Lower quartile	Minimum
AP - PA	DX	7.35	3.28	6.26 to 8.44	7	6.83	0.54	16	20	8	5	4
	EOS	3300	0	3300 to 3300	3300	3300	0	0	3300	3300	3300	3300
Lat	DX	17.86	13.73	13.22 to 22.51	13	14.90	2.29	62	68	17.50	10.50	6
	EOS	3300	0	3300 to 3300	3300	3300	0	0	3300	3300	3300	3300

Exposure Time (msec) between EOS and DX (paired t test, n = 37)							
Parameter	**Diff. mean**	**Std. dev.**	**Std. error**	**95% CI**	**T value**	**One sided P**	**Two sided P**
mA PA	**50.216**	42.551	6.995	36.028 to 64.403	7.178	**< 0.0001**	**< 0.0001**
mA Lat	**162.888**	40.315	6.719	149.248 to 176.529	24.242	**< 0.0001**	**< 0.0001**

Table 24. Exposure Time (msec) - DX and EOS

Differences are statistically significant.

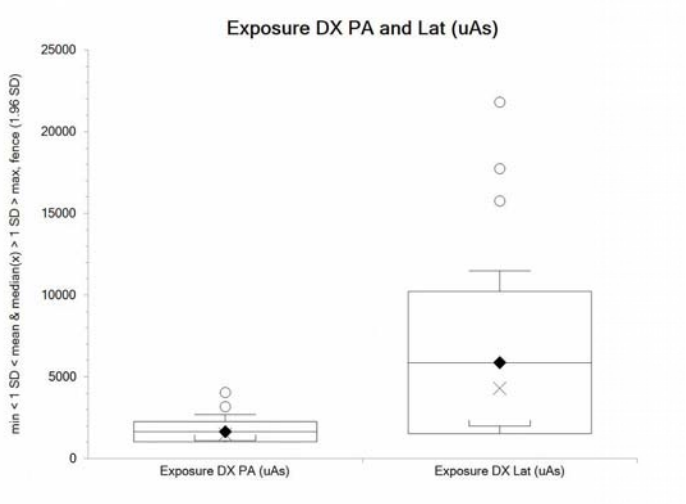

Figure 40. DX exposure time in PA and Lateral projections (msec).
(Box & whisker plots)

4.1.3.3.3 Total Exposure (mAs, µAs), exposure per line and cm, time per line.

Reflecting the different acquisition method and geometry, the found values are completely different total x-ray current values. For DX and EOS are reported as microsecond (µAs), but EOS values are x100 times more. These values in EOS are representative of total tube load and less to delivered dose, as X-ray exposed area in EOS is limited by the thin collimation, and should be evaluated as it would in scanning modalities as computed tomography. Several derived values are also presented: exposure per line (µAs), exposure per cm (µAs) time per line (msec). These values are presented in the following table:

Table Total Exposure (µAs) - DX and EOS												
Device - Param	PA - Lateral	Mean	Standard deviation	95% CL mean Lower to Upper	Median	Geometric m	Std error mean	Range	Maximum	Upper quartile	Lower quartile	Minimum
DX µAs	PA	1639	615	1434 to 1844	1500	1557	101	2960	4040	1750	1190	1080
	Lat	5870	4355	4396 to 7343	4310	4956	726	19810	21810	5795	3630	2000
EOS µAs total	PA	539168	132470	495000 to 583335	416650	523688	21778	416650	833300	666640	416650	416650
	Lat	535564	130708	491984 to 579144	416650	520540	21488	416650	833300	666640	416650	416650
EOS µAs . line	PA	270	62	249 to 290	247	263	10	261	455	325	215	193
	Lat	272	64	251 to 294	258	266	10	261	455	325	215	193
EOS µAs . cm	PA	10623	2439	9810 to 11437	9739	10368	401	10290	17898	12809	8451	7608
	Lat	10724	2509	9888 to 11561	10176	10454	412	10290	17898	12809	8451	7608
EOS msec Line	PA	1683	152	1.63 to 1.73	1717	1676	25	851	2139	1767	1546	1288
	Lat	1705	130	1.66 to 1.75	1672	1700	21	630	2068	1767	1627	1438

Table 25. Total Exposure (µAs), exposure per line and cm, and time (msec) per line.

A large difference in the scale of DX as EOS is present as a consequence of the different technology involved.

4.1.3.3.4 Exposure field limitation (area / collimation measurements)

Several measurements are direct or indirect measures of the exposed x-ray field size, limitation or of the collimation. These values are presented in the following table:

Exposure field size (mm) – EOS and DX (n = 37)												
Parameter	**Device DX /EOS**	**Mean**	**Standard deviation**	**95% CL mean Lower to Upper**	**Median**	**Geometric m**	**Standard error**	**Range**	**Maximum**	**Upper quartile**	**Lower quartile**	**Minimum**
Height PA	DX	391.51	5.22	390 to 394	391.1	391.5	0.9	42	415	391	391	373
	EOS	369.95	34.15	358 to 381	369	368.4	5.6	195	479	399	349	284
Height Lat	DX	391.85	5.31	390 to 393	391.1	391.8	0.9	39	420	391	391	381
	EOS	370.20	33.72	359 to 381	369	369	5.5	195	479	399	349	284
Width PA	DX	401.50	2.50	401 to 402	400.9	401.5	0.4	15	414	401	401	399
	EOS	448	0	448 to 448	448	448	0	0	448	448	448	448
Width Lat	DX	401.67	2.49	401 to 402	401	401.5	0.4	15	414	401	401	399
	EOS	448	0	448 to 448	448	448	0	0	448	448	448	448

Exposure field size (mm) – EOS and DX (paired t test, n = 37)							
Parameter	**Diff. mean**	**Std. dev.**	**Std. error**	**95% CI**	**T value**	**One sided P**	**Two sided P**
Height PA	**21.56**	34.60	5.67	10.02 to 33.10	3.789	**0.0003**	**0.0006**
Height Lat	**22.44**	34.51	5.67	10.94 to 33.95	3.956	**0.0002**	**0.0003**
Width PA	**-46.50**	2.49	0.41	-47.33 to -45.67	-113.2	**< 0.0001**	**< 0.0001**
Width Lat	**-46.33**	2.88	0.47	-47.29 to -45.37	-97.76	**< 0.0001**	**< 0.0001**

Table 26. EOS and DX exposure field size, width and height (mm); PA and Lat. views

All differences are statistically significant.

The shape of the exposure field is different in EOS. It is significantly wider (+46 mm) and shorter (-22 mm) than DX.

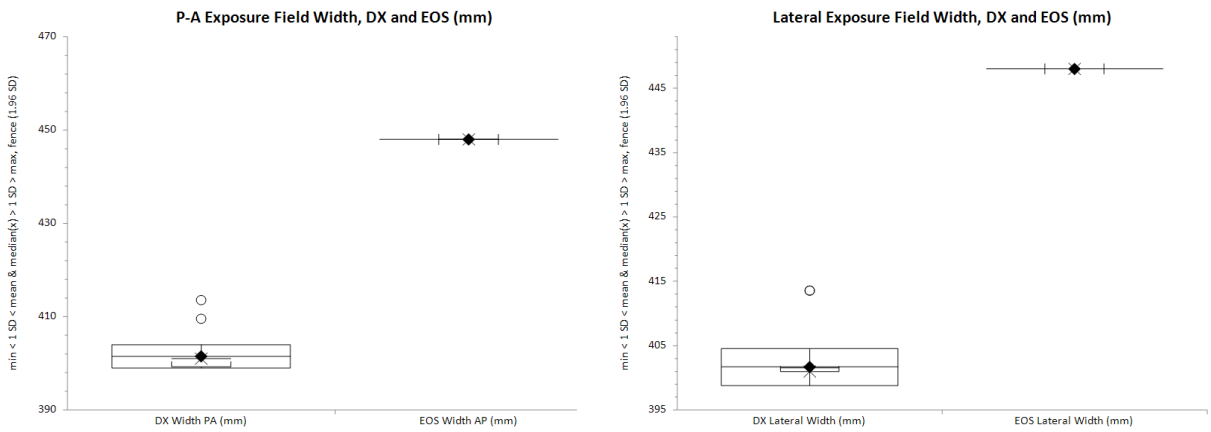

Figure 41. Postero-anterior and lateral exposure field width, DX and EOS (mm)

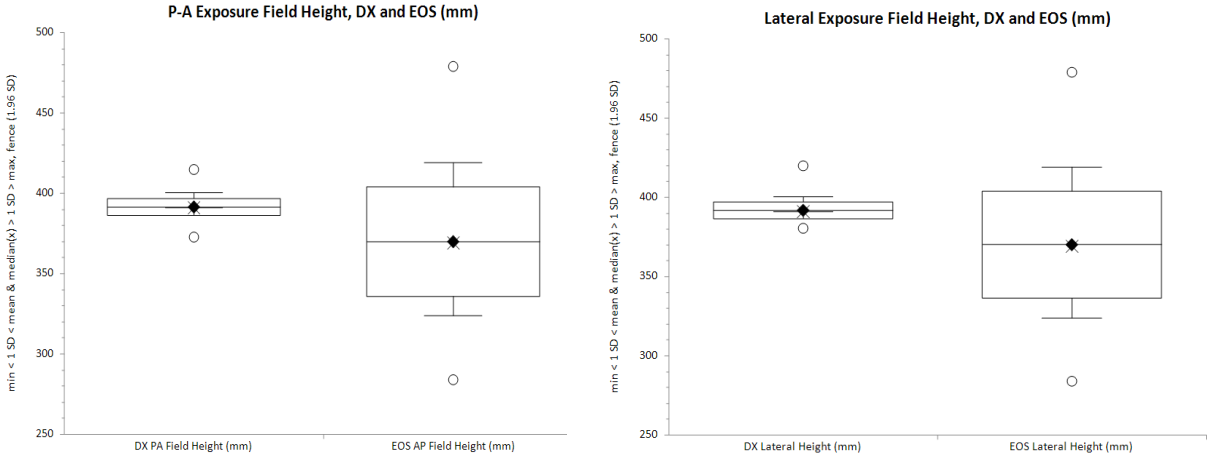

Figure 42. Postero-anterior and lateral exposure field height, DX and EOS (mm)

Exposure field area (sqm) – EOS and DX n= 37												
Projection	Device	Mean	Standard deviation	95% CL of the mean	Median	Geometric m	Std. error of mean	Range	Maximum	Upper quartile	Lower quartile	Minimum
AP-PA	DX	0.1572	0.0023	0.156 to 0.157	0.157	0.157	0.0004	0.016	0.17	0.16	0.16	0.15
	EOS	0.1700	0.0200	0.160 to 0.170	0.170	0.170	0.000	0.09	0.21	0.18	0.16	0.13
Lat	DX	0.1574	0.0028	0.156 to 0.158	0.157	0.157	0.0005	0.017	0.17	0.16	0.16	0.16
	EOS	0.1622	0.0123	0.158 to 0.166	0.162	0.162	0.002	0.056	0.19	0.17	0.15	0.13

Table 27. Exposure field area – EOS and DX (sqm)

Exposure field area (sqm) - EOS and DX (paired t test, n = 36)							
Parameter	**Diff. mean**	**Std. dev.**	**Std. error**	**95% CI**	**T value**	**One sided P**	**Two sided P**
PA	**-0.0085**	0.0156	0.0026	-0.01374 to -0.00336	-3.339	**0.001**	**0.002**
Lat	**-0.0040**	0.0128	0.0021	-0.00836 to 0.00016	-1.95	**0.029**	**0.059**

Table 27 (cont) Exposure field area – EOS and DX (sqm)

Exposed area in square-meter is a bit larger with EOS in PA projection (< 10%) consequence of the absence of lateral collimation in EOS ($p < 0.002$). Results for the lateral view are less significant.

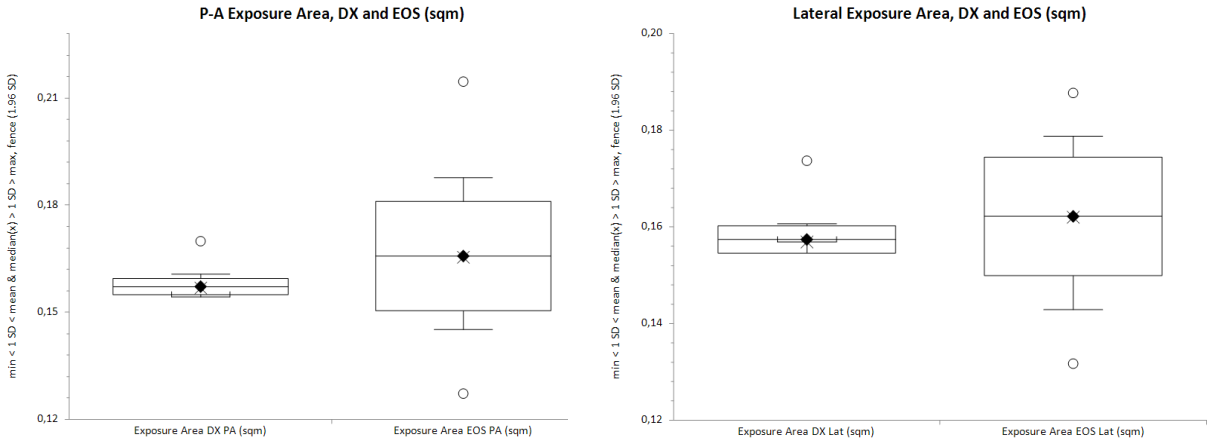

Figure 43. Exposure Field Area for EOS and DX, P-A and lateral (sqm)

4.1.3.3.5 Digital Image characteristics

The following parameters are modality dependent and correlate to exposure image field o detector size. Some on them are constants and modality related. All images from EOS are full range 16 bit-depth images with 65535 gray levels. DX Images are 12 bit-depth with up to 4096 gray levels, but the registered extreme in all patient series have been 521 and 3663, with a range of 3142.

Pixels size and pitch, and pixel aspect ratio are stored bits per pixel, and the high bit are constants. In both modalities pixels are squared.

Maximum, minimum, and pixel value range are modality, software and exposure dependent.

Digital Image characteristics - Pixel Range– EOS and DX (n = 37)													
	Parameter	**Device DX /EOS**	**Mean**	**Std. dev.**	**95% CL**	**Median**	**Geometric m**	**Standard error**	**Range**	**Maximum**	**Upper quartile**	**Lower quartile**	**Minimum**
Maximum density	**PA**	**DX**	3418	111	3380 to 3454	3445	3416	18	499	3663	3489	3353	3164
		EOS	65535	0	65535 to 65535	65535	65535	0	0	65535	65535	65535	65535
	Lat	**DX**	3291	69	3267 to 3314	3284	3290	12	270	3397	3344	3250	3127
		EOS	65535	0	65535 to 65535	65535	65535	0	0	65535	65535	65535	65535
Mínimum Density Value	**PA**	**DX**	790	111	753 to 827	778	782	18	479	1000	852	734	521
		EOS	0	0	0 to 0	0	*	0	0	0	0	0	0
	Lat	**DX**	526	82	498 to 553	527	520	14	392	767	562	476	375
		EOS	0	0	0 to 0	0	*	0	0	0	0	0	0
Display Range	**PA**	**DX**	2628	108	2592 to 2664	2616	2626	18	562	2968	2670	2562	2406
	Lat	**EOS**	65535	0	65535 to 65535	65535	65535	0	0	65535	65535	65535	65535
	PA	**DX**	2765	103	2730 to 2800	2791	2763	17	452	2942	2835	2719	2490
	Lat	**EOS**	65535	0	65535 to 65535	65535	65535	0	0	65535	65535	65535	65535

Table 28. Digital Image characteristics - Pixel Range – EOS and DX

Digital Image System Applied Windowing – DX only (n = 37)												
Paramter	Device DX	Mean	Std. Deviation	95% CL mean Lower to Upper	Median	Geometric m	Standard error	Range	Maximum	Upper quartile	Lower quartile	Minimum
Window Center	**PA** DX	2102	96	2070 to 2134	2113	2100	16	364	2295	2151	2029	1931
	Lat DX	1908	55	1889 to 1926	1906	1908	9	245	2060	1935	1871	1815
Window Width	**PA**	2631	105	2595 to 2666	2616	2629	17	562	2968	2670	2568	2406
	Lat	2765	103	2729 to 2799	2791	2763	17	452	2942	2835	2719	2490

Table 29. Digital Image - System Applied Windowing - DX only

Digital Image characteristics Pixel Data (kBytes) – EOS and DX (n = 37)													
	Parameter	Device DX /EOS	Mean	Standard deviation	95% CL mean Lower to Upper	Median	Geometric m	Standard error	Range	Maximum	Upper quartile	Lower quartile	Minimum
Pixel Data (Kbytes)	PA AP	**DX**	1537	22	1529 to 1544	1534	1537	3.6	154	1662	1534	1534	1508
		EOS	7054	649	6838 to 7271	7035	7026	108	3704	9127	7606	6654	5423
	La t	**DX**	1540	28	1530 to 1549	1534	1539	4.7	165	1699	1534	1534	1534
		EOS	6926	509	6756 to 7096	6943	6907	84	2377	7987	7229	6654	5610

Table 30. Digital Image characteristics - Pixel Data (kBytes) – EOS and DX

Table. EOS linear Scan Exposure parameters (n = 37)

Parameter	Projection View	Mean	Standard deviation	95% CL mean Lower to Upper	Median	Geometric m	Standard error of mean	Range	Maximum	Upper quartile	Lower quartile	Minimum
Total mAs·	AP	539.17	132.47	495 to 583	416.65	523.69	21.78	417	833	666.6	416.6	416.65
	Lat	535.56	130.71	492 to 579	416.65	520.54	21.49	417	833	666.6	416.6	416.65
mAs x line	AP	0.27	0.06	0.25 to 0.29	0.25	0.26	0.01	0.26	0.45	0.33	0.21	0.19
	Lat	0.27	0.06	0.25 to 0.29	0.26	0.27	0.01	0.26	0.45	0.33	0.21	0.19
mAs Exposure	AP	10.62	2.44	9.81 to 11.44	9.74	10.37	0.40	10.3	17.90	12.81	8.45	7.61
	Lat	10.72	2.51	9.89 to 11.56	10.18	10.45	0.41	10.3	17.90	12.81	8.45	7.61
msec · line·cm	AP	1.68	0.15	1.63 to 1.73	1.72	1.68	0.02	0.85	2.14	1.77	1.55	1.29
	Lat	1.70	0.13	1.66 to 1.75	1.67	1.70	0.02	0.63	2.07	1.77	1.63	1.44

Differences between EOS Linear Scan AP and Lat Parameters (paired t test, n = 37)

Parameter	Diff. mean	Std. dev.	Std. error	95% CI	T value	One sided P	Two sided P
Total mAs	3,60	21,91	3,60	-3,70 to 10,91	1	0,162	0,324
mAs · line	-0,002568	0,018026	0,002963	-0,008578 to 0,003442	-0,866609	0,1959	0,3919
mAs ·cm	-0,101107	0,709674	0,11667	-0,337724 to 0,13551	-0,866609	0,1959	0,3919
msec ·Line	-0,00002	0,00007	0,000012	-0,000046 to 0,000001	-1,91862	0,0315	0,063

Table 31. EOS linear Scan Exposure parameters

Table. EOS linear Scan Detector parameters (n = 15)												
Parameter	Projection View	Mean	Std. dev.	95% CL	Median	Geometric m	Standard error of mean	Range	Maximum	Upper quartile	Lower quartile	Minimum
Detector HT voltages	AP	2498	39.81	2475 to 2520	2523	2497	10.28	91	2538	2534	2458	2447
	Lat	2423	26.55	2409 to 2438	2424	2423	6.85	126	2502	2425	2420	2376
Gas (bar) Pressure	AP	6.00	0.01	5.99 to 6	6.00	6.00	0.00	0.03	6.01	6.01	5.99	5.98
	Lat	6.00	0.01	5.99 to 6	6.00	6.00	0.00	0.03	6.01	6.01	5.99	5.98
Mean Gain	AP	37508	1006	36951 to 38066	37049	37496	259.79	2951	39843	37441	36891	36891
	Lat	45758	958	45227 to 46289	45442	45749	247.46	3538	48645	45676	45107	45107
TI Acquisition	AP	0.83	0.00	0.83 to 0.83	0.83	0.83	0.00	0.00	0.83	0.83	0.83	0.83
	Lat	0.83	0.00	0.83 to 0.83	0.83	0.83	0.00	0.00	0.83	0.83	0.83	0.83
0 Value	AP	0.0085	0.01	0 to 0.01	0.009	*	0.0016	0.0186	0.0186	0.0127	0.003	0.0000
	Lat	0.0005	0.00	0 to 0	0.0003	*	0.0002	0.0016	0.0016	0.0009	0.000	0.0000
65536 Value	AP	1.4488	0.07	1.41 to 1.49	1.447	1.447	0.0169	0.2333	1.5436	1.4975	1.411	1.3103
	Lat	1.2694	0.04	1.25 to 1.29	1.278	1.269	0.0092	0.1231	1.3288	1.2943	1.243	1.2057

Table 32. EOS linear Scan Detector parameters

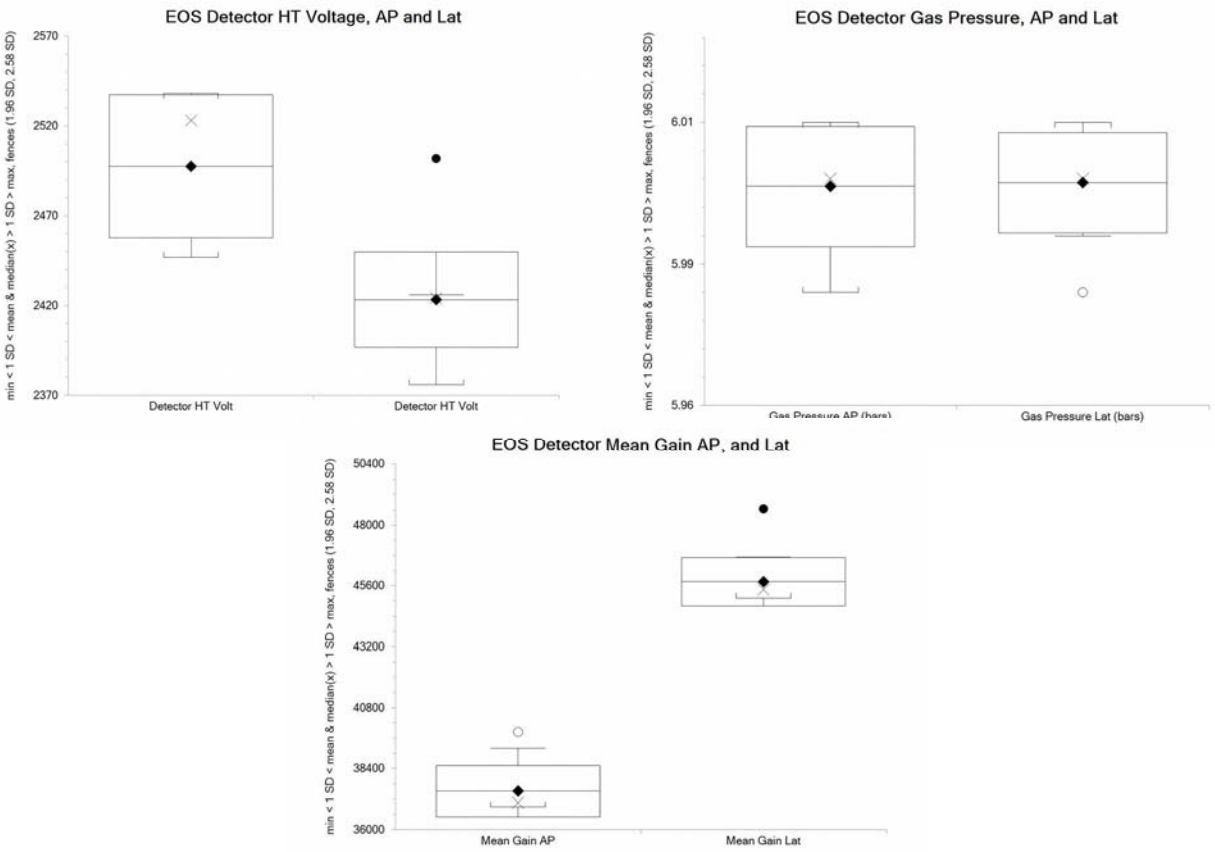

Comparative PA and Lateral results
All differences between AP and Lat are highly significant, two sided p< 0.0001

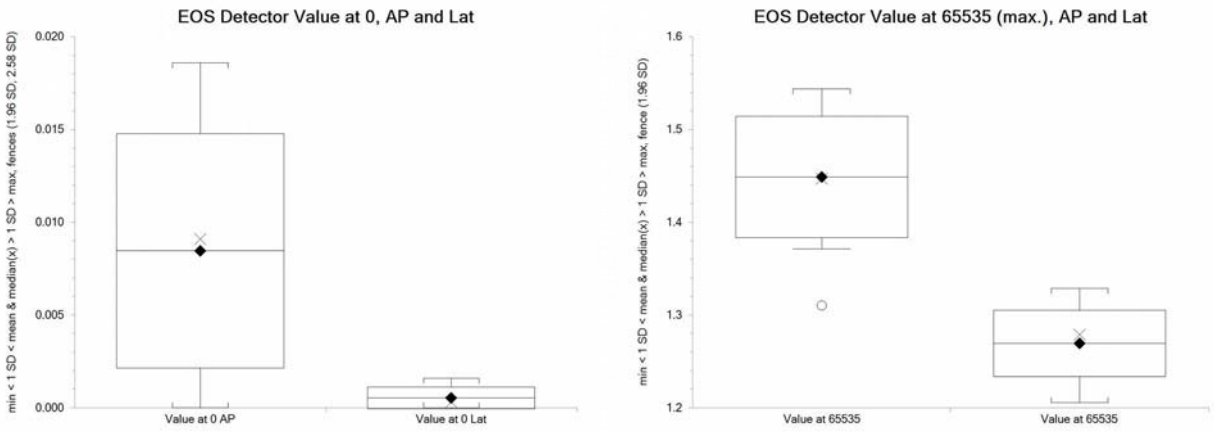

Figure 45. EOS Voltage values at 0 and 65535 values for PA and Lat (n =15).
All differences between AP and Lat are highly significant, two sided p< 0.0001

4.2 Dosimetry

4.2.1 DX Siemens Dosimetry

The Siemens Thorax-FD DX provided dosimetry information in its as EXI (Siemens exposure index) and DAP (Dose Are Product) in their image DICOM headers. EXI, Siemens exposure index, corresponds to µGy air Kerma *100 (calibrated to the detector model by the manufacturer under the following conditions: RQA5, 70 kV +0.6 mm Cu, HVL=6.8 mm Al). The EXI figure can be converted to back to µGy air Kerma with a simple formula, X(µGy)=EI/100, so a Siemens EXI 500 corresponds to 5 µGy air Kerma. The DAP (Dose Are Product) figure corresponds to dGy·cm^2 .

Table DX Dose Parameters (n = 37)

Parameter	Projection View	Mean	Standard deviation	95% CL mean Lower to Upper	Median	Geometric m	Standard error of mean	Range	Maximum	Upper quartile	Lower quartile	Minimum
Exposure mAs	PA	1.65	0.72	1.41 to 1.89	2.00	1.51	0.12	3.00	4.00	2.00	1.00	1.00
	Lat	5.86	4.47	4.35 to 7.37	4.00	4.87	0.75	20	22.00	6.00	4.00	2.00
DAP	PA	0.28	0.12	0.24 to 0.32	0.25	0.26	0.02	0.60	0.76	0.31	0.19	0.16
	Lat	1.12	0.88	0.82 to 1.42	0.80	0.93	0.15	4.00	4.34	1.12	0.68	0.34
Siemens EXI	PA	193.70	32.55	182.85 to 204.56	197.00	190.77	5.35	132	249	212	182	117
	Lat	342.86	48.87	326.32 to 359.4	338.00	339.75	8.15	240	511	362	306	271

Correlations between DX Parameters (Simple linear regression, n = 37)				
Parameter	**Correlation (r)**	**95% CI**	**Two sided P**	
EXI to DAP (PA)	0.008015	0.316827 to 0.331174	0.9624	Not sign.
Exposure to EXI	-0,001692	-0,325533 to 0,322504	0,9921	Not sign.

Table 33. DX Dose Parameters: Exposure, DAP and EXI

The next graphics, box and whisker and ladder plots, illustrate DAP, EXI for Postero-anterior and lateral x-ray projections

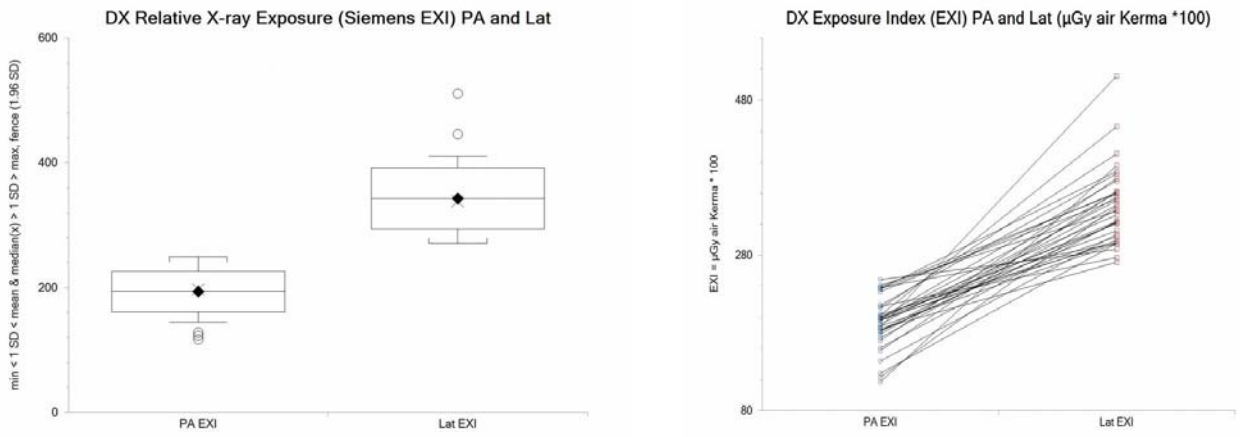

Figure 46. Siemens EXI Exposure index of DX studies in PA and Lateral views

EXI corresponds to µGy in air Kerma
Left) Box and whisker plot in P-A and lateral
Right) Ladder plot between PA and lateral. All patients had higher dose in lateral exposure

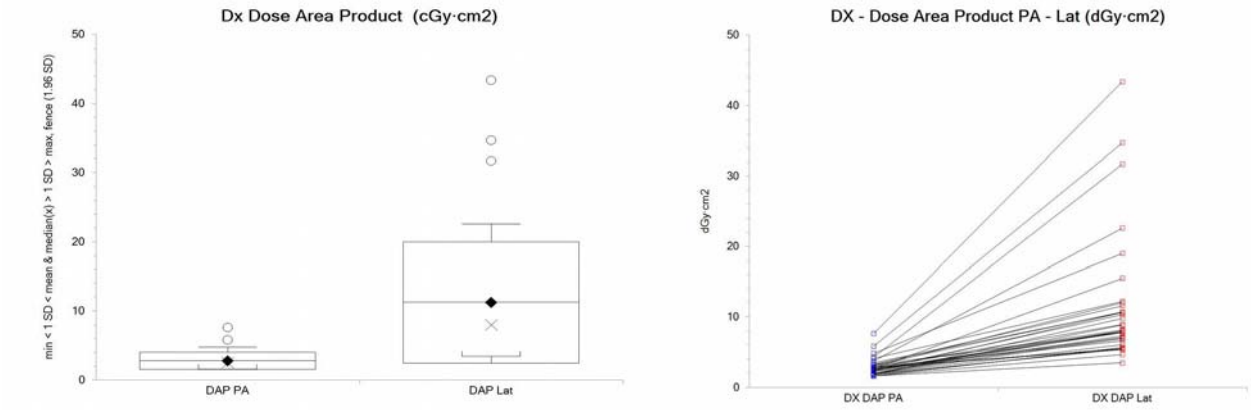

Figure 47. DX Dose Area Product for DX in PA and Lateral. (dGy·cm^2).

Left) Box and whisker plot in P-A and lateral
Right) Ladder plot between PA and lateral. All patients had higher dose in lateral exposure

4.2.2 EOS dosimetry data gathering

4.2.3 Measurement of the dose from a scan

Dose was measured at the center of the intersection of both x-ray beams using a pencil ionization chamber with the following conditions: Sampling interval: 0.25 mm. Radiation: 1.67 mAs / line. Scan length: 50 mm., equivalent to Integrated dose of 200 lines

4.2.3.1 Dose rate measurements

The figure 48 presents a plot of doses delivered at the intersection of both X-ray beams with both projections (A-P or P-A and lateral). Doses D_{BAL} (kV) were obtained from direct measurements using a solid-state dosimeter at 98.6 and 91.6 cm distances respectively for face and profile projections.

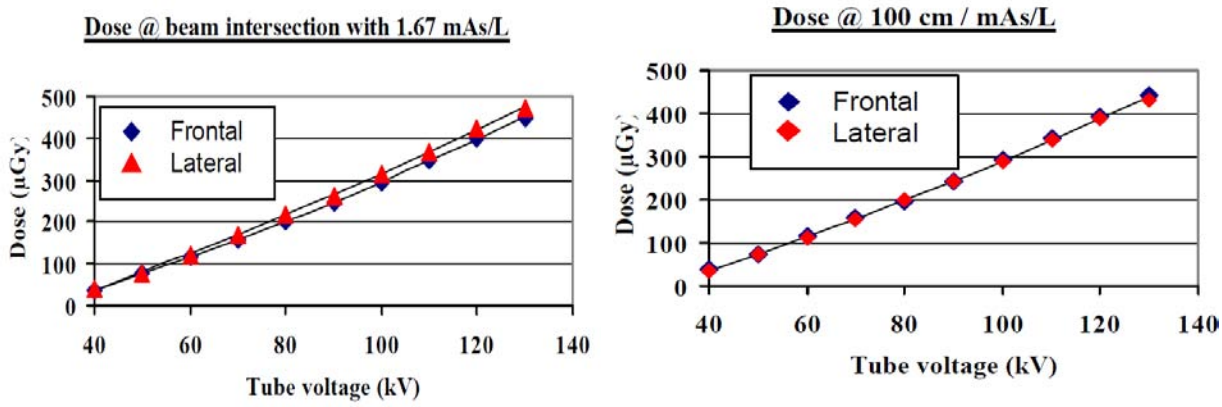

Figure 48: Measurement of dose at the beam intersection point at 1.67 mAs/L a) beam intersection dose. b) standardized dose at 1 meter

A small dose gap is visible between A/P and lateral measurements, due to the small difference between distances to focus. With allowance for this difference (using the inverse distance law), the agreement is found excellent (Figure 48-b):

Sampling interval: 0.25 mm Radiation: 1.67 mAs / line
Scan length: 50 mm i.e. dose · 200 lines **Total irradiation: 333.2 mAs**

Those measurements are compared with measurements made with the solid-state detector. The scan dose rate value, expressed for a unit mAs, is based on the integrated dose as follows:

$$\text{Scan dose / mAs/L} = \delta\text{INT (kV)} / (p \cdot \text{mAsTOT/n})$$

$$= \delta\text{INT (kV)} / (p \times 333.2/n)$$
$$= \text{DINT (kV)} / (p \times 333.2)$$

Dose rates D0conv and D0EOS corresponding respectively to the conventional and EOS devices have been measured for full-emitted dose characterization and comparison. For each device measurements have been performed using a solid-state detector of 10 mm x 10 mm sensitive area. The dosimeter was centered on the beam axis in the conventional system, and was scanned in EOS system, separately on each view.

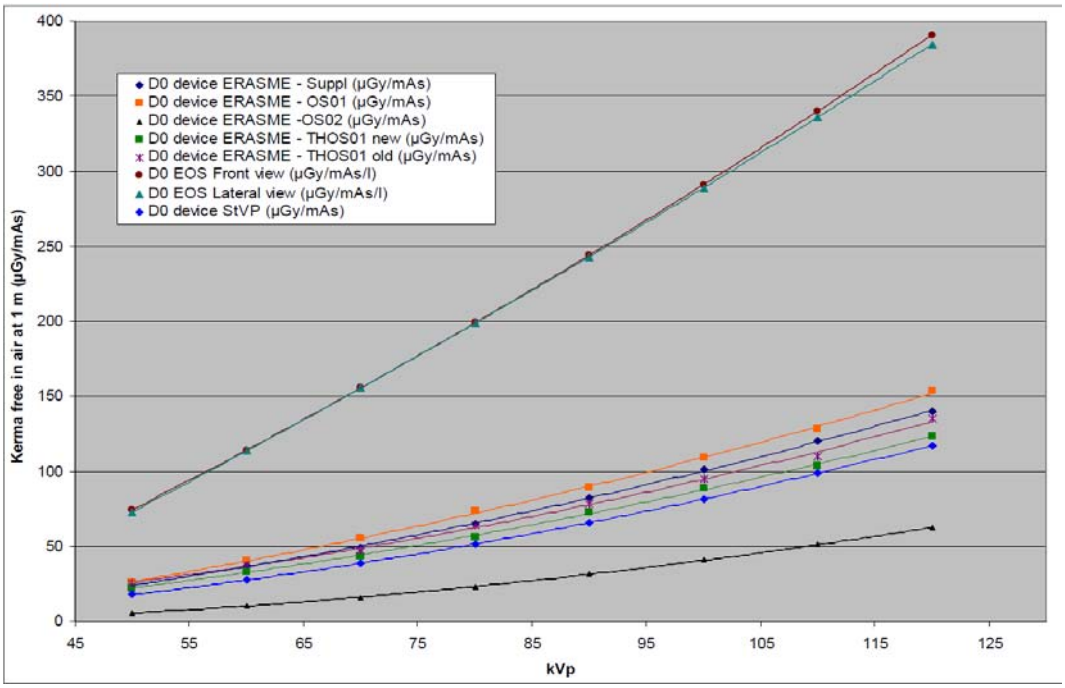

Figure 49: Dose rate measurements for EOS prototype and conventional geometry x-ray equipment, assessed along the EOS clinical trials .

The figure 49 shows the dose rates at 1 m (in µGy/mAs), of the EOS prototype (front and lateral views) and the different conventional devices used at ULBE (ULB-ERASME), and St. Vincent de Paul (Paris, F) hospitals. From these measurements a quadratic regression functions was applied in order to obtain dose rate for each voltage, with better than 1% accuracy. The curves describe the dose rate or kerma free in air at 1m (in µGy/mAs) in function of the voltage, for both EOS views and the conventional system.

Once these dose rate curves were obtained, it was possible to calculate the kerma free in air at the entrance of the patient. The equations below define how to calculate this value for a conventional 2D X-ray device with a conical beam and a linear scanning device with a fan beam.

4.2.3.2 EOS emitted dose

Table 34 shows the resulted emitted dose from one EOS projection for 1 mAs, at respectively 100 and 125 cm from the tube focal spot. Figure 50a and 50b show for both distances the dose profiles without collimation, for individual profile, and in scanning mode.

Table: EOS emitted dose summary @ 100 cm and 125 cm for 1 mAs			
Parameter	**Intensity**	**Dose @ 100 cm**	**Dose @ 125 cm**
Emitted dose without collimation (µGy)	1 mAs	79.9	47.9
Dose profile maximum (µGy)	1 mAs	34.8	22.2
Integrated dose (individual profile) (µGy.mm)	1 mAs	49.7	39.7
Scan dose along z axis (µGy)	1 mAs/line	198.0	159.0

Table 34: EOS emitted dose summary @ 100 cm and 125 cm for 1 mAs

1. As expected, the emitted dose without collimation and the dose profile maximum varies with the inverse of the squared distance ratio, while the individual integrated dose, and the scan dose depend on the inverse of the distance ratio.

2. The dose profile maximum, the individual integrated dose, and therefore the scan dose are totally determined by the collimation geometry.

3. The doses involved in a scanning mode and in the 2 dimensional acquisition mode per mAs are not the same and their ratios depend on the collimation geometry as well. In this specific case 1 mAs/L in scanning mode corresponds respectively to 2.65 mAs and 3.32 mAs in a 2 dimensional acquisition mode at 100 cm.

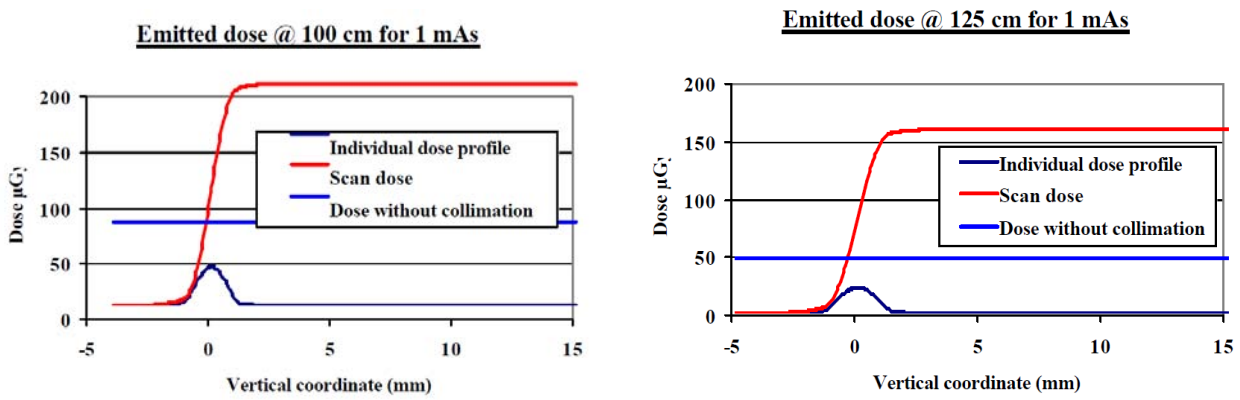

Figure 50: Dose profiles @ 100 cm and 125 cm, both for 1 mAs

4.2.3.2.1 Displaying the dose level

On the basis of the above measurements the linear scan dose rate may be expressed in mAs/L @ 100 cm, noted δBAL0 (kV, G). This quantity δBAL0 (kV, G) is then calibrated, allowing assessing, for any projection, the dose delivered at the reference point (intersecting optical beam axes) and expressed in kerma free in air.

The patient entrance dose will correspond to the displayed value, corrected to make allowance for the source to skin distance (with a resulting increase of 10 % or 20 % respectively for face or profile projections).

The linear scan dose rate is expressed for a mAs/L @ 100 cm unit, as it follows

$$\delta BAL0\ (kV, G) = 8.00.10\text{-}3 \times kV\ 2 + 3.12 \times kV + 102.4$$

The EOS dose is then obtained as a function of kV and mAs/L as it follows:

$$DBAL\ (front) = \delta BAL0\ (kV, G) \times 100/98.6 \times mAs/L$$

$$DBAL\ (lateral) = \delta BAL0\ (kV, G) \times 100/91.6 \times mAs/L$$

4.2.3.3 Scan Dose Associated To EOS Operating parameters

Due to its peculiar reconstruction mode of the radiological images EOS has some differences comparatively to the conventional radiological systems currently in use (see table 35).

Table . Image parameters associated to a scanning mode	
EOS parameters	**Symbol and expression**
Image size (number of lines)	n
Tube voltage (kV)	kV
Tube current (mA)	mA
Scanning speed (cm/s)	V
Focal Skin Distance (cm)	FSD
Total exposure time (millisecond)	T
Time exposure per line (millisecond)	$\Delta t = T / n$
Radiation per line (mAs)	$mAs/L = mA \times T / n$
Patient skin dose	$D\ (kV) = \delta_{BAL0}\ (KV) \times mAs/L \times (100/FSD)$

Table 35: Image parameters associated to a scanning mode

The quantity δ_{BAL0} is the X – ray tube dose rate, per mAs/L @ 100 cm and for the given kVp (and filtration).

As for example, table 36 below shows the associated parameters and the resulting dose for an Image « spine » 90 cm and an Image « thorax » 45 cm:

Image parameters and the resulting doses		
EOS parameters	**Thorax @ 45 cm**	**Spine @ 90 cm «**
Image size	1 800 lines	3 600 lines
Tube voltage	80 kV	80 kV
Tube current	80 mA	200 mA
Scanning speed	7.5 cm/s	7.5 cm/s
Focal Skin Distance (cm)	90 cm	90 cm
Total exposure time	6 sec	12 sec
Time exposure per line	3.33 ms	3.33 ms
Radiation per line	0.27 mAs/L	0.67 mAs/L
Correspondence in mAs with a 2D acquisition mode	0.64 mAs	1.59 mAs
Patient skin dose	59 µGy	147 µGy

Table 36: Image parameters and the resulting doses

4.2.3.3.1 X-ray Tube limitations

The manufacturer charts, giving available power or energy workload as a function of exposure time are shown on the figure 51

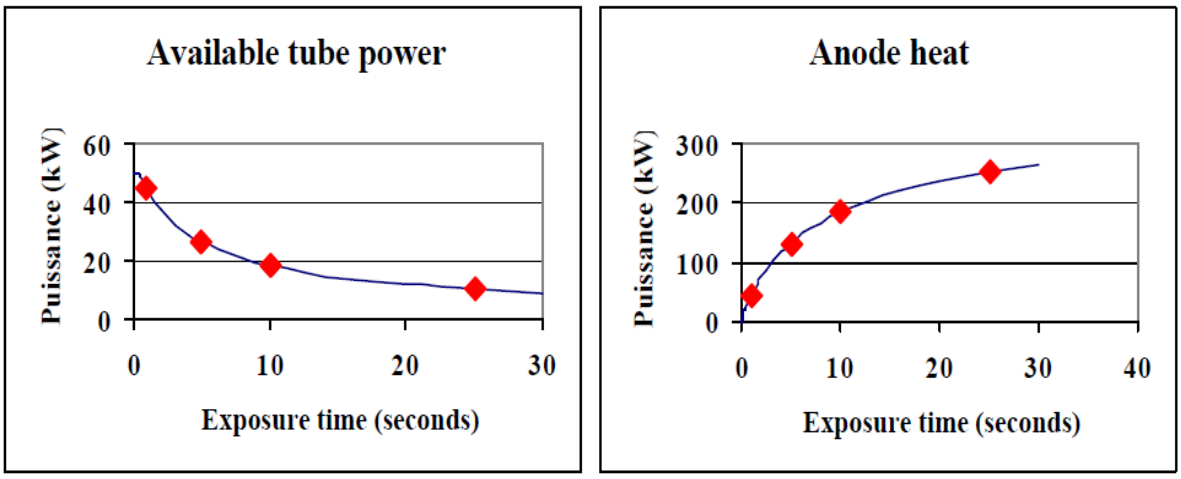

Figure 51: Available X-ray tube power and anode heat capacity

The table 37 gives the main characteristics corresponding to two different image formats.

Available time and power tube characteristics						
	Image « spine » 90 cm			Image « thorax » 45 cm		
	T (s)	P (kW)	kJ	T (s)	P (kW)	kJ
V min = 3.75 cm/s	6	145	24	3	98	33
V nom = 7.5 cm/s	12	199	17	6	145	24
V max = 30 cm/s	24	250	10	12	199	17

Table 37: Available time and power tube characteristics

4.2.3.3.2 Maximum available dose values

The curves on Figure 52 represent maximum available radiation (mAs/L) as a function of kVp, for two types of image and for scanning speeds 3.75, 7.5 and 30 cm/s.

4.2.4 EOS operational dose levels

4.2.4.1 Scan mode

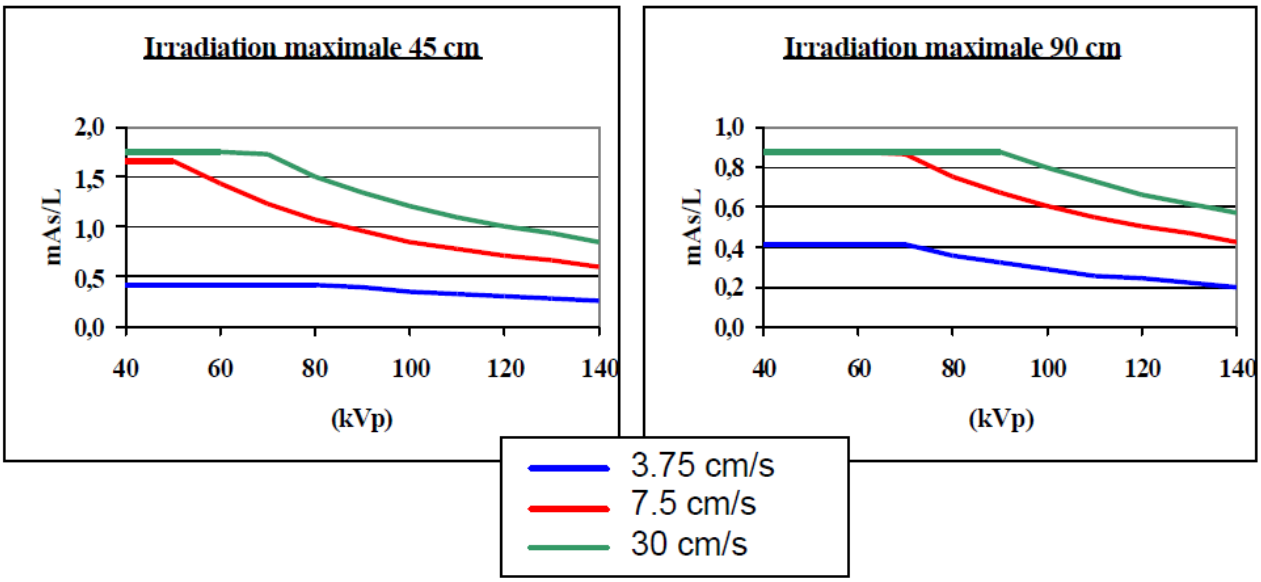

Figure 52: Irradiation under different tube voltage, and mAs/L at 45 and 90 cm

The curves on Figure 53 represent the maximum dose obtainable as a function of kV, for two types of image and for scanning speeds 3.75, 7.5 and 30 cm/s.

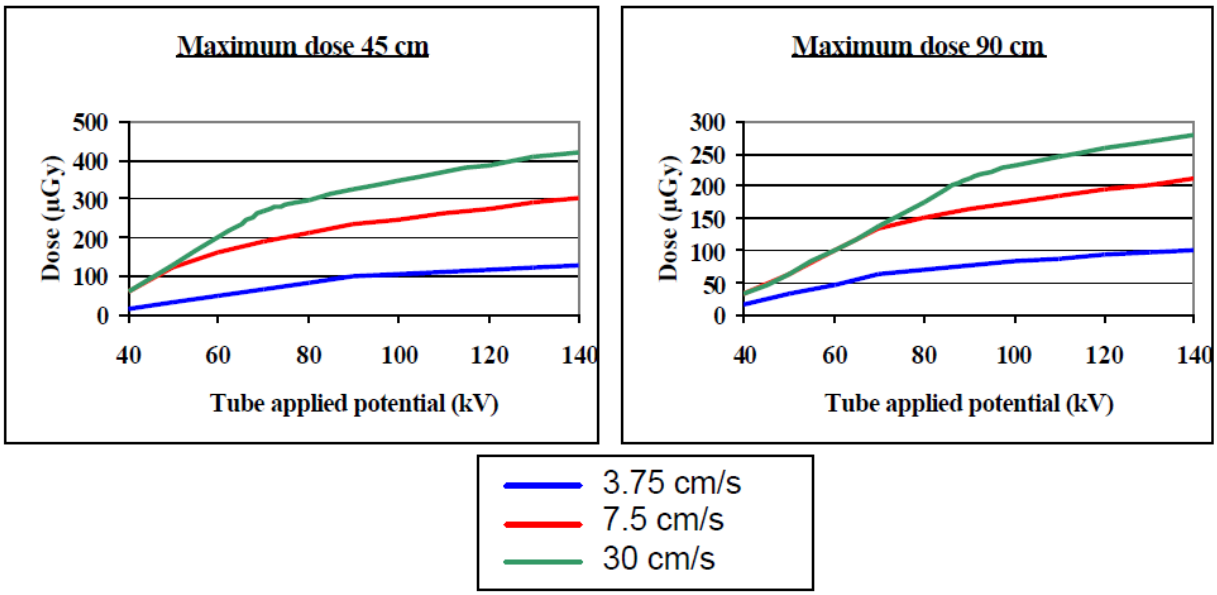

Figure 53: Tube voltage, scan speed, maximum available dose at 45 and 90 cm

4.2.4.2 Dose in Presence of a Scattering Medium

4.2.4.2.1 Measurement of the entrance surface dose with a phantom

In order to estimate the entrance surface dose in the presence of a scattering medium, several blocs of Plexiglas of different thickness were used to simulate the patient attenuation. TLDs were placed at the entrance of the Plexiglas phantom according to the scheme detailed in the figures here below. Such dosimeters allow the contribution of backscatter radiation to be measured and are currently used in the field of medical diagnostic radiology. The TLDs were aligned along the scanning axis of the beam in order to appreciate the possible dose variation from the center of the beam to the periphery. Both front and lateral projections were considered and two different patient thicknesses were taken into consideration, 10 cm and 20 cm of Plexiglas respectively.

In order to get reliable values, TLDs were exposed three times while keeping the irradiation settings constant. Due to the phantom dimensions, the irradiation geometry led to the experimental conditions, which are summarized in the following paragraphs

As it can be seen from the next figure with the 10 cm phantom thickness, the entrance surface of the phantom was at 54 cm far away from the front X-ray tube and at 27 cm from the lateral X-ray tube respectively while, with the 20 cm phantom thickness, the front distance from the X-ray tube was shortened to 44 cm. The following table, details the dosimetry results obtained for the experimental settings corresponding to the irradiation conditions

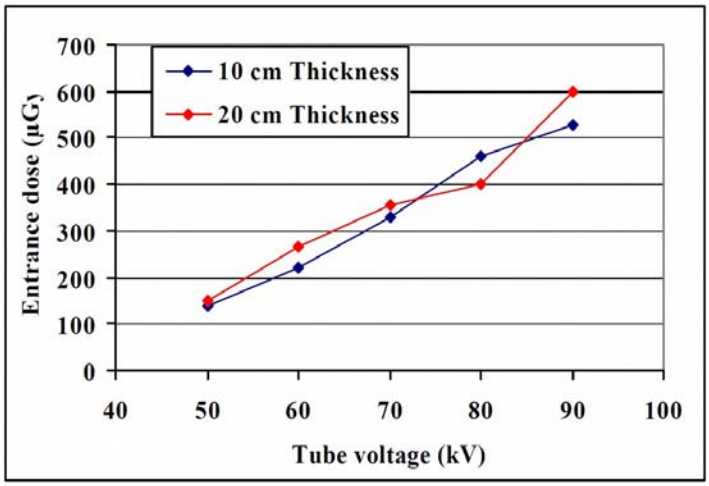

Figure 54. Entrance surface dose (ESD) related to kVp and thickness

The general dosimetry results are given in the following table for both projections and two phantom thicknesses. Doses were measured at constant incident energy of 80kVp and 1.33mAs/line. Two main points need to be discussed. The first one relates to the effect of the beam geometry (tube to phantom surface distance), which, as previously discussed, has simply a linear relationship with the dose. Changing from 10 to 20 cm thickness of phantom, i.e. from 54 cm to 44 cm from the tube, does increase the dose but not significantly as it would in the case of a general radiographic equipment (inverse square law).

Table. Entrance surface dose by x-ray projection and phantom thicknesses

Phantom thickness	Projection	Entrance surface dose Front (µGy)	Entrance Surface dose Lateral (µGy)
10 cm	Front	400	
10 cm	Front and Lateral	Min - Max 366 - 480	446
20 cm	Front	413	
20 cm	Front and Lateral	483	396

Table 38. Entrance surface dose by x-ray projection and phantom thicknesses

The second comment deals with the effect of scattered radiation coming from the lateral projection, which is simultaneously taken with the front projection. Its contribution to the front dose varies from 10 to 20% depending on the phantom thickness considered. Such results suggest that direct dose measurement on the surface of the patient are to be considered with caution since they are affected by a fraction of the scattered radiation inherent to the functioning modalities of the EOS system (two simultaneous exposures). A straight-

forward comparison between this dosimetry quantity and that commonly used in diagnostic radiology for routine examination (entrance surface dose) has therefore to be made carefully because of such a spurious source of information. At the same time, when taking into account the precise radiographic settings used during the examinations, the entrance surface dose value measured with EOS equipment clearly illustrates the overall amount of radiation received by the patient.

The previous figure illustrates the relationship between the incident energy and the entrance surface dose for both phantom thickness considered. As one might expect, independently on the phantom thickness, the entrance surface dose rapidly increases with the incident energy value according to an almost quadratic law.

4.2.4.3 Entrance Dose Measurement by TLD

18 TLD were recovered from DR and EOS exam for the frontal and lateral views. However, the acquisition parameters were very low concerning the DR device which implicated TLD measurements below the minimal threshold for a valuable measure. Only 2 DR TLD valuable measurements were available for the frontal views and 12 for the lateral views.

Thus, we had too few TLD values of the frontal views to provide significant results. However, lateral TLD measurements are shown in the table below to give an idea of the dose ratio between the two modalities.

TLD Dosimetry Lateral view:			
n = 12	EOS	DR	Ratio DR /EOS
Mean Entrance dose (mGy)	0.41	0.24	0.64
Min. (mGy)	0.10	0.06	0.16
Max. (mGy)	0.52	0.72	1.7

Table 39. TLD Dosimetry in Lateral view

Calculated entrance dose without back-scattering

Data linked to the corpulence of some patients (weight, lateral and postero-anterior width) or to the acquisition parameters (kVp, mAs, Detector-Source Distance) during EOS or DR exam were lost for 3 frontal exams and 4 lateral exams. So it remains only 35 and 34 patients for the front and lateral views dosimetric analysis respectively.

Calculated Entrance Dose without back-scattering, Frontal view:			
n = 35	EOS	DR	Ratio DR /EOS
Mean (mSv)	0.22	0.05	0.22
SD (mSv)	0.06	0.02	0.12
Min. (mSv)	0.16	0.02	0.09
Max. (mSv)	0.35	0.14	0.81

Table 40. Calculated Entrance Dose without back-scattering, A-P view

Calculated Entrance Dose without back-scattering, Lateral view:			
n = 34	EOS	DR	Ratio DR /EOS
Mean (mSv)	0.31	0.17	0.54
SD (mSv)	0.05	0.14	0.40
Min. (mSv)	0.18	0.05	0.14
Max. (mSv)	0.41	0.77	2.3

Table 41. Calculated Entrance Dose without backscattering, Lateral view:

4.2.5 Entrance Dose measurements by TLD

On the initial 65 patients, TLD were placed for 46 of them on both conventional and EOS concerning frontal views and for 36 of them concerning lateral views. Results of the TLD measurements are compiled in next two tables:

Frontal view: n =46	EOS	Screen-Film	Ratio SF/EOS
Mean Entrance dose	0.23	1.12	6.08
SD (mGy)	0.10	0.34	5.09
Min. (mGy)	0.03	0.26	2.17
Max. (mGy)	0.59	2.33	33.6

Table 42. Entrance Surface Dose (ESD) measurements by TLD A-P view (mGy)

Lateral view: n =36	EOS	Screen-Film	Ratio SF/EOS
Mean Entrance dose	0.37	2.4	6.94
SD (mGy)	0.14	1.11	3.22
Min. (mGy)	0.14	0.6	2.32
Max. (mGy)	0.81	6.0	17.24

Table 43. Entrance Surface Dose (ESD) measurements by TLD Lateral view (mGy)

4.2.6 Kerma Free in air (Entrance Dose free Kerma in air calculation)

At the end of the EOS dose study the initial cohort of 65 cohort finished with 49 frontal valid records available, and 50 lateral view valid records. 15 cases were rejected as some of their data for required simulation parameters (weight, lateral and postero-anterior width, kVp, mAs, Film-Source Distance) during EOS or conventional exam were incomplete or lost.. Data was available for:

- 49 patients (mean age = 14.9 ± 4.8 y – BMI = 20.2± 4.7 kg/m²) for the frontal view.
- 50 patients (mean age = 15.0 ± 4.1 y – BMI = 20.1± 4.7 kg/m²) for the lateral view.

Frontal view: n =49	EOS	Screen-Film	Ratio SF/EOS
Mean Kerma free in air	0.13	1.27	9.83
SD (mGy)	0.03	0.64	4.05
Min. (mGy)	0.07	0.40	4.16
Max. (mGy)	0.18	4.12	26.71

Table 44. Kerma Free in air EOS and conventional AP view (mGy)

Lateral view: n =50	EOS	Screen-Film	Ratio SF/EOS
Mean Kerma free in air	0.19	1.67	9.11
SD (mGy)	0.04	0.67	3.94
Min. (mGy)	0.07	0.72	3.36
Max. (mGy)	0.27	3.60	22.79

Table 45. Kerma Free in air EOS and conventional Lateral view (mGy)

As we could have expected the Kerma free in air ratios between EOS and conventional devices are higher than the TLD ratios for the front and the lateral views. This difference is caused by the TLD measurement bias previously discussed.

4.2.7 Effective Dose calculations

The Monte Carlo simulation software gives the effective dose from the Kerma free in air for the same previous exam pairs

Effective Dose for EOS and Conventional X-ray Postero-anterior			
Frontal view: n =49	EOS	Conventional	Ratio Conventional /EOS
Mean Effective dose (mSv)	0.02	0.26	11.47
SD (mSv)	0.01	0.10	4.72
Min. (mSv)	0.01	0.13	5.71
Max. (mSv)	0.03	0.49	36.50

Table 46: Effective Dose for EOS and Conventional X-ray Postero-anterior

Effective Dose for EOS and Conventional X-ray Lateral			
Lateral view: n =50	**EOS**	**Conventional**	**Ratio Conventional /EOS**
Mean Entrance dose (mSv)	0.03	0.35	13.52
SD (mSv)	0.01	0.10	5.38
Min. (mSv)	0.01	0.17	4.71
Max. (mSv)	0.05	0.73	30.40

Table 47: Effective Dose for EOS and Conventional X-ray Lateral

The discrepancies between Kerma free in air calculation and effective dose ratios are probably due to the combined efects of collimation and acquisition area of the two devices. On the EOS device there is an outstanding reduction of the divergence due to the highly collimated fan beam (500 µm height), induce a supplement of irradiated volume very weak compared to a conic beam device. That is possibly the reason of this slight difference between the kerma free in air and the effective dose results, because the kerma free in air does not take into account the total irradiated volume whereas the effective dose does. In conventional 2D planar acquisition (conic beam), there is a geometrical divergence between the entrance of the beam and its exit in both planes (cf. figure 47).

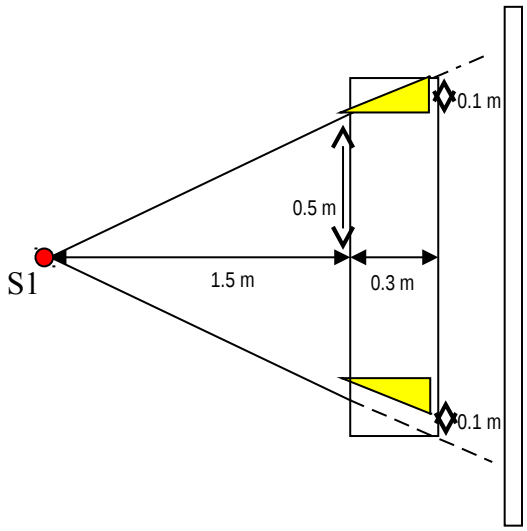

Figure 55. The effect of the conic geometry for conventional radiography

On conventional radiography the conic magnification affects both the vertical and horizontal planes.

In EOS the aperture is limited to the transverse plane of the fan-shaped beam. Clinical images are usually transformed allowing correct measurements.

4.3 Image Detector Performance

EOS provides digital planar radiographic images where the value of each pixel represents the punctual transmission of an X-ray beam. This transmission value may be between 0 (for total opacity) and 1 (for total transparency). This values data results from an X-ray acquisition with the patient in the gantry, but a prior calibration scan should be performed without the patient being exposed. This calibration procedure is required every type the kVp is changed, and defines the internal gain of the detector, which is controlled with the applied high voltage. This calibration allows a first automatic processing of the integrated image signal, which is inherent to the detection process, and results in the first transmission image, called “system image”. A second specific processing stage takes place, according to the patient characteristics and the examination anatomical region, giving a final radiological picture ready for review and diagnosis.

The image performance of EOS relies on the scatter suppression that avoids blur and on the detector conversion efficiency, in its amplifying and resolution characteristics. The detector is composed of a array of electrodes on which high voltage is applied, and immersed in a gas mixture mainly composed of xenon at 6 bars. Conversion efficiency, amplifying and resolution characteristics of the detector highly depend on the gas mixture composition and pressure. Amplifying factor depends on the electrode configuration, which is mechanically fixed and the applied high voltage as well.

X-rays enter the detector through a thin and narrow entrance windows and are converted into photoelectrons interacting in the gas mixture. The emitted photoelectrons loose their kinetic energy by collision producing primary electrons, which are accelerated and multiplied under the electric field effect. The resulted charge is collected on copper strips corresponding to the detector pixels and transferred onto the electronic channels.

The detector specifications are summarized on the table 48.

The electronic system is composed of 1764 channels corresponding to the copper strips. The collected charge on each channel is accumulated in a capacitance of 220 pC full scale, during the integration time. This charge is coded on 16 bits and converted to 65535 gray levels. The electronic specifications are summarized on the table 49.

EOS Detector, Physical specifications	
Copper strips number	1764
Copper strips pitch	254 µm
Sensitive area width	448 mm
Interaction thickness	100 mm
Conversion gap	1.6 mm
Entrance window	500 µm Aluminum
Gas operating pressure	6 bars
Gas flow	300 cc / minute

Table 48: EOS Detector physical specifications

EOS Detector, Electronic Specifications	
Full scale output signal	220 pC
Offset:	33 – 50 pC
Noise (RMS)	5.4 fC
Available signal	170 – 186 pC
Electronic dynamical range	30 000

Table 49: EOS Detector, Electronic Specifications

The detection system performance has been investigated through simulation coupled with direct measurements.

4.3.1 Conversion Efficiency

The conversion efficiency is the fraction of the incoming X-ray in the detector that is converted in the gas and induces the detection process. The Figure III-2 shows the conversion efficiency, function of the tube voltage. This result comes from simulation. For low voltage spectrum, the conversion efficiency limited by the entrance window (500 µm aluminum), for high voltage spectrum the conversion is limited by the gas thickness. The optimum is between 65 and 80 kV X-ray spectra.

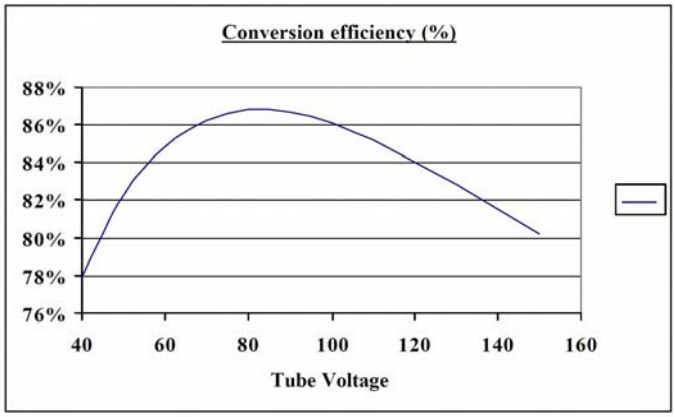

Figure 56: Conversion efficiency plot

4.3.2 X-Ray Beam Attenuation Measurements

X-ray beam attenuation measurements have been done using Plexiglas blocks as it is represented on the figure 57.

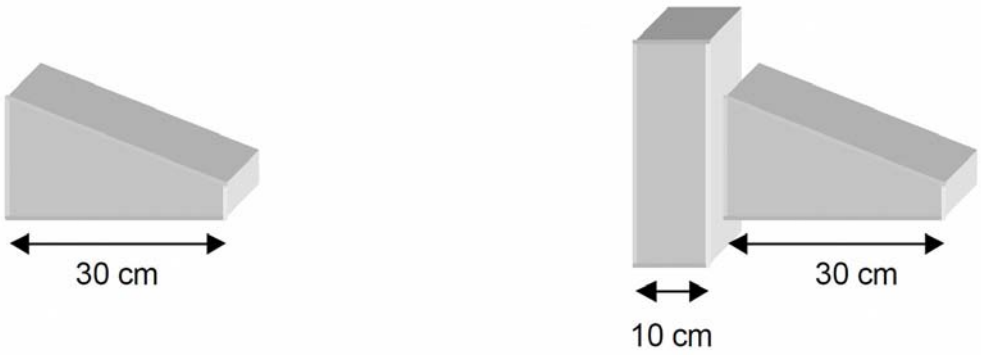

Figure 57: Plexiglas blocks used for attenuation test

The attenuation is measured along the vertical direction. The results are compared to the simulation model and are presented on the figure 58 .

There is a rather good agreement with the model on the total thickness, 40 cm of material. This firstly shows a rather good reliability of this latter, and secondly confirms that the detection system significantly reduces the scattered radiation.

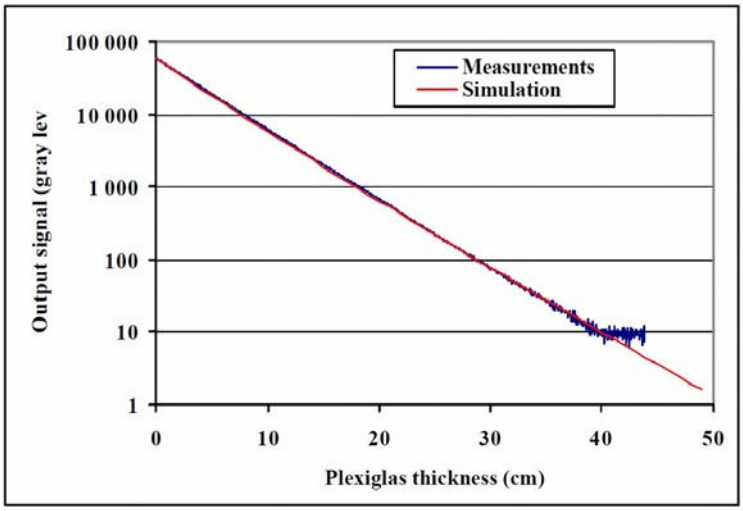

Figure 58: Measured standard deviation of gray level to thickness.

The figure 59 shows the measured standard deviation of the output signal. The red line is the standard deviation corresponding to a Poisson law according behavior. There is a rather good agreement at high signal level or low attenuation. The discrepancy occurs beyond 30 cm of the material.

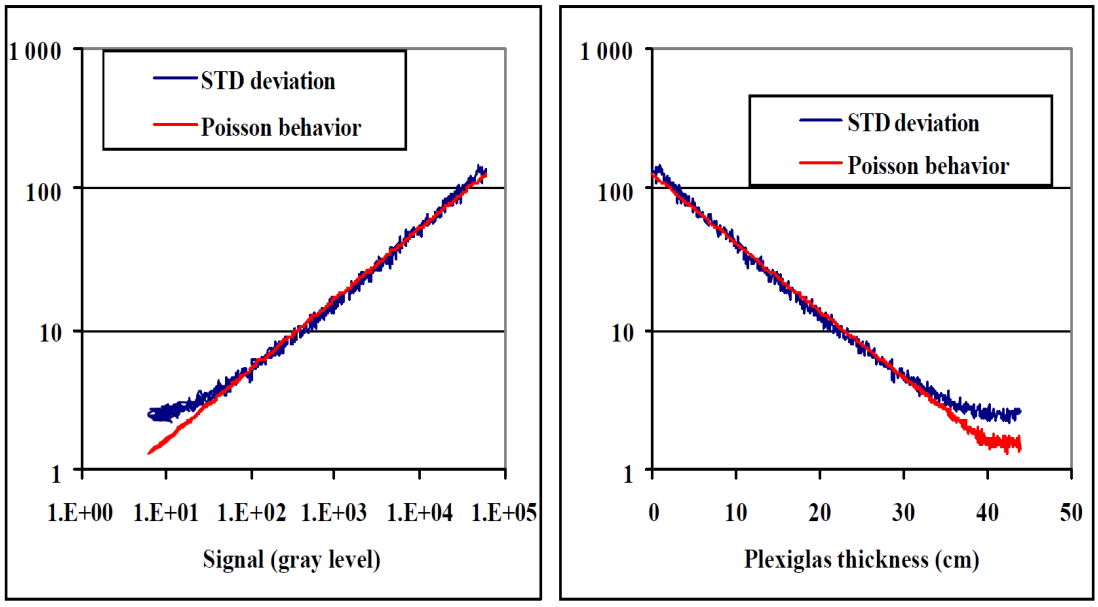

Figure 59: Signal Standard deviation by output signal and thickness
Left) Standard deviation (gray level) function of the output signal.
Right) Standard deviation (gray level) function of the material thickness

4.3.3 Modulation Transfer Function (MTF) And Detection Quantum Efficiency (DQE)

The modulation transfer functions (MTF) and the detection quantum efficiency have been measured both along the horizontal and the vertical directions. Along the horizontal direction both results are related to the performance of the detector, while the other direction, the results are related to the alignment of the collimations including the tube focal spot of the scanning system. The measurements have been done with a 70 kV X-ray spectrum, and 2.5 mm aluminum filtration, using a narrow slit (10μm) at angle (2°) with the plane orthogonal to the axis under study. The incident flux, inferior to 100 kHz by channel, is set so that measurements are not biased by the space charge phenomenon. The detector gain effect has been taken into account. The figures 60 and 61 show the comparison between the horizontal and the vertical direction.

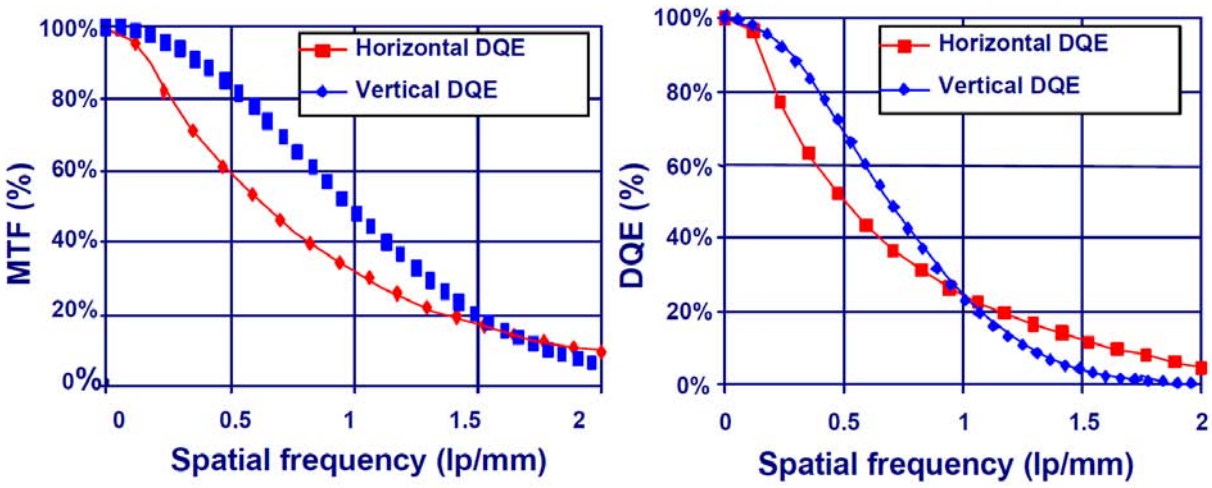

Figure 60: Comparison between the horizontal and the vertical direction.
a) MTF, 70 kV, 2.5 mm aluminum b) DQE, 70 kV, 2.5 mm aluminum

In ionization chamber operation the difference between simulation and measurement value remains on the average less than 10%. This finding favors the simulation model to account for the processes leading to MTF and DQE. The loss under the detector gain effect is due to the broadening of the impulse response with the detector gain.

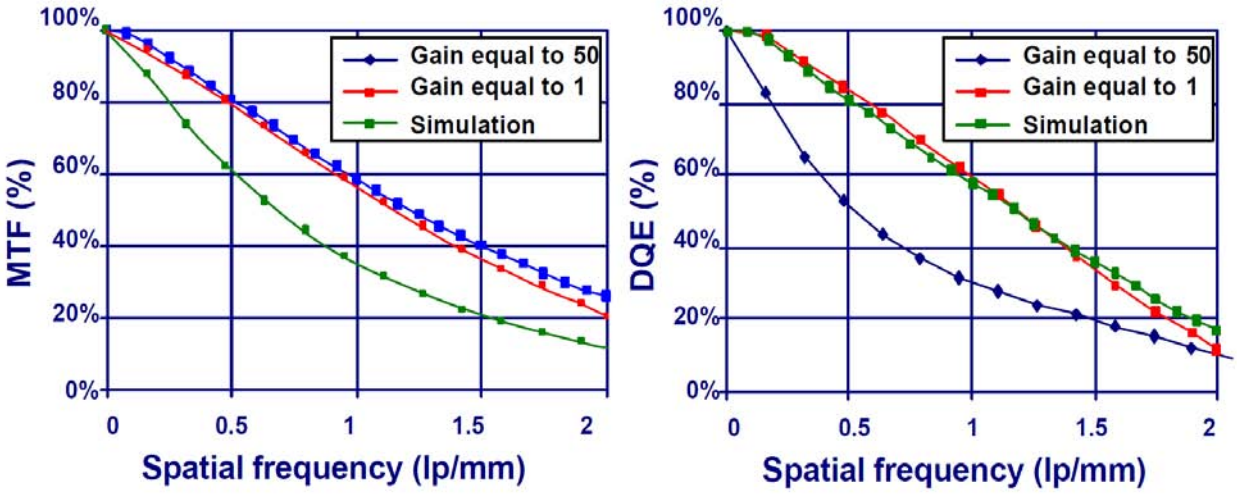

Figure 61: Horizontal modulation transfer function.
a) MTF, 70 kV, 2.5 mm aluminum and b) DQE, 70 kV, 2.5 mm aluminum

The summary of different MTF values obtained at 1 and 2 lp/mm frequency is compiled in table 50.below

MTF values obtained at 1 lp/mm and 2 lp/mm		
	1 lp/mm	**2 lp/mm**
Horizontal MTF (Simulation)	58 %	26 %
Measured horizontal MTF @Gain =1	57 %	20 %
Measured horizontal MTF @Gain = 50	35 %	12 %
Measured horizontal MTF @RQA5 & Gain = 50	32 %	5 %
Measured vertical MTF @RQA5 & Gain = 50	48 %	9 %

Table 50: MTF values obtained at 1 lp/mm and 2 lp/mm frequencies

4.3.4 Detector Output Signal

The electronic output signal is another source of noise that contributes to the total MTF of an imaging system. Several repeated measurements were done to assess these sources of noise

4.3.4.1 Output signal average and profile

The detector signal on the pixel i receiving N_i photons, during the acquisition time Δt is ex-

pressed as following:

$$S_i (N, kV, HT) = \varepsilon(kV) \times N_i (kV) \times \langle p \rangle \times M_i (HT)$$

Whereis the conversion efficiency, <p> is the average produced charge (primary electrons) per event and Mi (HT) is the internal gain of the detector. The internal gain of the detector is adjusted via the high voltage power supply. It is not constant along the pixels.

The figure 62 shows the output signal average for each pixel when the detector is irradiated by a 80 kV X-ray beam at 3 different applied high voltage. The average was calculated on 500 measurements. As it can be seen, signal level depends on the applied high voltage and the profile shows a non flat shape. This is mainly due to the internal gain of the detector which is not constant in addition to the electronic channel gain dispersion that is shown in figure 63.

The high frequency signal variations that are well seen in figure 63 are mainly due to the statistical nature of the radiation.

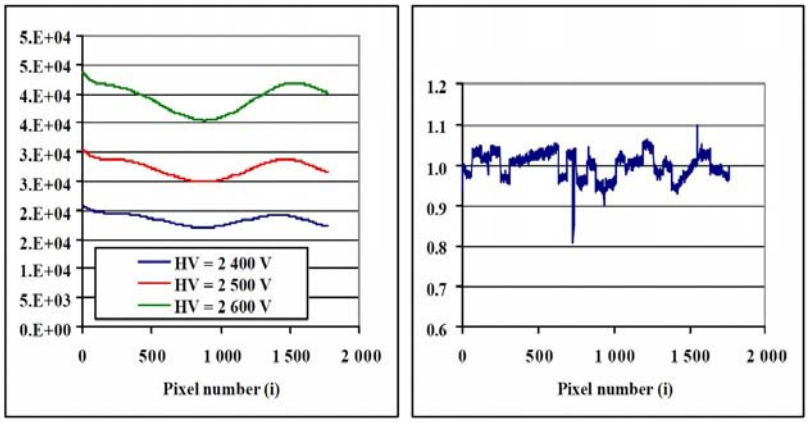

Figure 62: Output signal average per pixel at different voltages

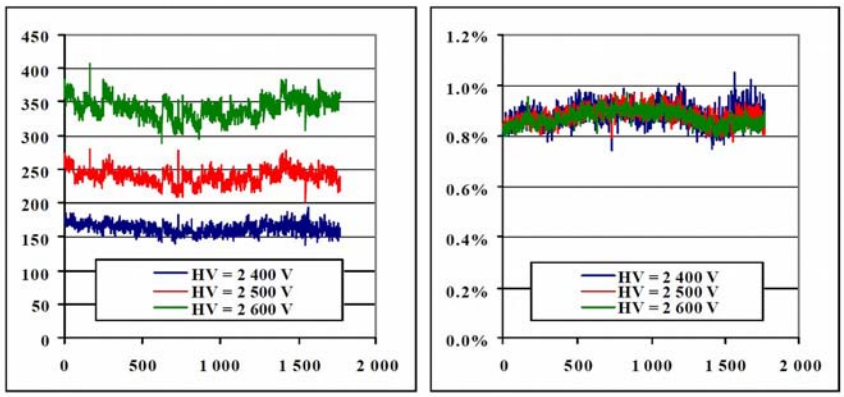

Figure 63: Output signal level profile, fluctuations by kilovoltage and channel gain
Left) Repeated measures for each pixel showing fluctuations by kilovoltage
Right) Repeated measures by electronic channel gain dispersion

4.3.5 Signal Profile and Image Corrections

The profile dispersion of the detector chain are linear and can be easily corrected by calibration. The figure 64 shows an example of image correction. Image ripple can be seen as ti depends from quantum noise, electronic noise and mechanical vibration, that may be attenuated by image post-processing and noise removal. Under clinical operation noise and are present that is quite noticeable if a magnification is applied (figure 65)

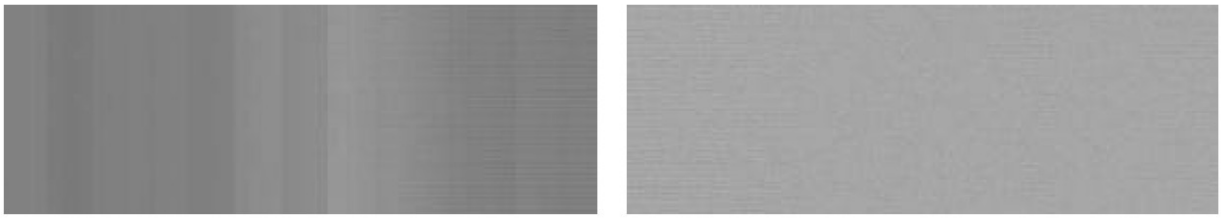

Figure 64: Vertical stripes depending from channel gain

a) Raw image. Vertical stripes depending from channel gain can be seen in the raw image that may be removed by calibration. Horizontal ripple is also present.
b) Corrected image. Some horizontal ripple can be noticed in the corrected image

Figure 65. Visible ripple and noise in EOS images .

Left) 58-year-old male with a large chest mass. Markers are centered in the image
Right) Close up view. The markers shape a 4 x 4 pixels square area
Noise and ripple generate a pattern like small squares

4.4 EOS analysis of chest images

At the end of the experimental period 40 patients were examined as initially planned. All 40 underwent an EOS chest x-ray exam immediately after their clinically scheduled DX chest x-ray exam. Nevertheless, 3 three were excluded, leaving 37 comparative cases in our series as their 3 sets of DX images were unavailable at the time of image quality assessment (they were unavailable at the local PACS). Therefore, the results presented here encompasses the 37 remaining patients.

This set of 37 patients ended the experiment had 4 images (2 EOS + 2 DX) that were scored independently by 4 radiologists. The scores of four reading were aggregated per each criteria providing 148 data points per individual criteria, modality and projection.

37 patients were over the minimum sample size calculated for paired t test was previously calculated. For a power of 90%, with a 5% alpha error, a 0,3 foreseen difference of population mean, and 0.5 SD in paired response differences, the required number of cases was 32.

Three analytic tests have been applied to all score groups. Wilcoxon's signed ranks test, a test for matched pairs, has been used to compare the significance of the differences between modalities. Kendall's Tau (τ) Rank Correlation has been used to test for independence between both modalities scores. The Berry-Mielke Universal R coefficient, equivalent to a linearly weighted kappa statistic, has been applied to assess agreement between observers.

Each item has been scored following and ordinal scale from 1 to 5 as:

1: Not seen: The image does not depict this structure or criteria.

2: Poor: the image allows to barely assess the evaluated structure or criteria.

3: Good: the image allows an adequate assessment the evaluated structure or criteria

4: Very Good: the image allows an excellent assessment of the evaluated structure or criteria.

5: Outstanding: the image quality allows to depict with outstanding resolution or contrast the evaluated structure or criteria.

The results of each image quality item are presented in the next 10 subheadings (for the ten quality criteria presented as comparative sets). Results for each item are grouped as

comparative PA/AP EOS versus DX results, and Lateral EOS versus Lateral DX results. Box and whisker graphics associate both PA and Lateral representations for both modalities.

As a reminder, this is the ordered list of the assessed criteria:

	AP/PA Projection	LAT Projection
1	Performed at peak of inspiration, except for suspected foreign body aspiration	Performed at the peak of inspiration
2	Reproduction of the thorax without rotation and tilting	True lateral projection
3	Reproduction of the chest must extend from just above the apices of the lungs to T12/L1.	Reproduction of the chest must extend from just above the apices of the lungs to T12/L1.
4	Reproduction of the vascular pattern in central 2/3 of the lungs	Reproduction of the hilar vessels
5	Reproduction of fine interstitial structures in the 1/3 periphery of the lungs	Reproduction of fine interstitial structures in the 1/3 periphery of the lungs (Retro-sternal space)
6	Reproduction of fissures major and fissure minor	Reproduction of fissures major and fissure minor
7	Reproduction of the trachea and the proximal bronchi	Visualization of the trachea from the apices of the lungs down to and including the main bronchi.
8	Visually sharp reproduction of the diaphragm and costophrenic angles	Visually sharp reproduction of the whole of both domes of the diaphragm
9	Reproduction of the spine and paraspinal structures and visualization of the retrocardiac lung and the mediastinum.	Reproduction of the sternum and the thoracic spine
10	Reproduction of the soft tissues and fat pads.	Reproduction of the soft tissues and fat pads.

4.4.1 Quality Assessment. Criteria 1. Inspiration. Performed at the peak of inspiration, except for suspected foreign body aspiration

4.4.1.1 Descriptive Statistics.

The table below display the relevant statistics for the assessment criteria, for both modalities and views.

Quality criteria 1. Inspiration. EOS and DX scores (PA & Lateral)											
Scores	Median	Mean	Geometric mean	Standard deviation	95% CL of mean Lower to Upper	Standard error of mean	Range	Maximum	Upper quartile	Lower quartile	Minimum
EOS_1 (PA)	**4**	**3.71**	3.66	0.55	3.62 to 3.80	0.05	3	5	4	3	2
DX_1 (PA)	**4**	3.50	3.43	0.66	3.39 to 3.61	0.05	4	5	4	3	1
EOS_1L (Lat)	**4**	**3.58**	3.53	0.55	3.49 to 3.67	0.05	3	5	4	3	2
DX_1L (Lat)	**3**	3.24	3.18	0.61	3.14 to 3.34	0.05	4	5	4	3	1
	37 Patients; 4 observers; 148 independent observations; Valid n: 147										

Table 51. Quality criteria 1: Inspiration. EOS vs. DX (PA & Lateral)
EOS and DX, as overall results for Posterior-anterior (PA) and lateral (L) projections.

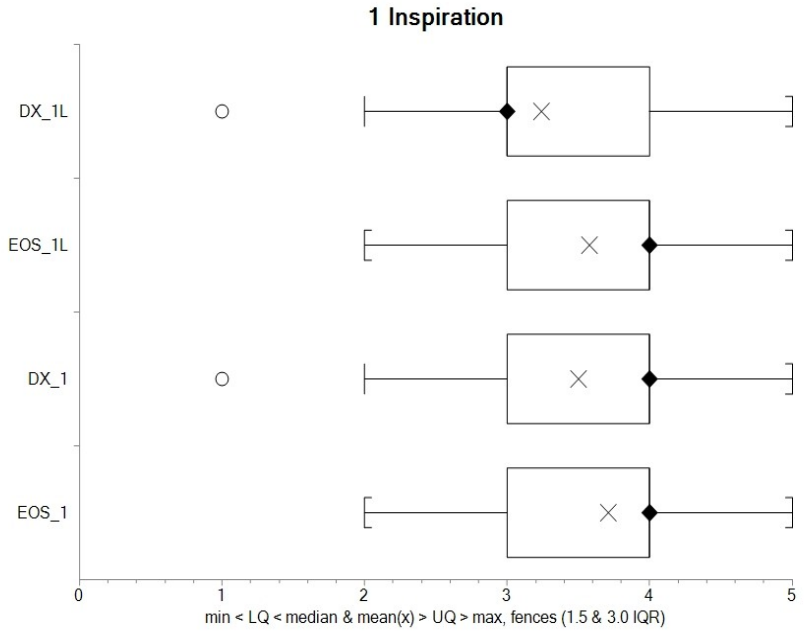

Figure 66: Quality criteria 1: Inspiration. Box and whisker plot.
EOS and DX results for Posterior-anterior (_nn) and lateral (_nnL) projections

4.4.1.2 Criteria 1: inspiration. Significance of the difference of Medians

Quality Criteria 1. Inspiration. EOS - DX scores (PA & Lateral)					
Projection view	Median difference	95% CI	P values		
			Lower side	Upper side	Two sided
PA-AP	**0**	0 to 0.5	> 0.9999	**< 0.0001**	**P = 0.0002**
Lat	**0.5**	0 to 0.5	> 0.9999	**< 0.0001**	**P = 0.0002**

Table 52. Quality criteria 1: Inspiration. PA and Lat. Wilcoxon's signed ranks tests.

Results were statistically significant, with no differences in PA-AP median, but with a small positive difference for EOS in lateral projection and for both confidence intervals.

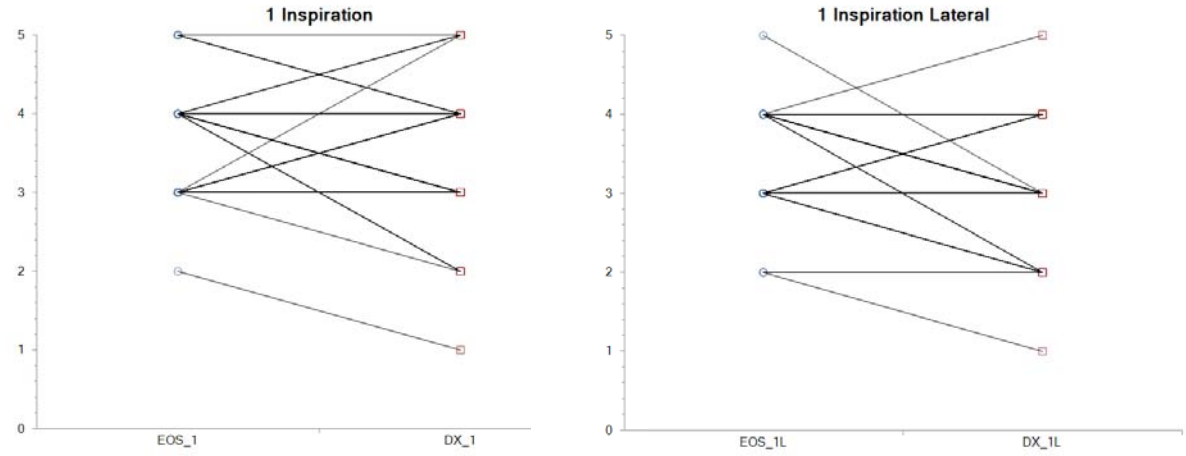

Figure 67. Quality criteria 1: Inspiration. Ladder Plots PA and lateral

EOS and DX results for Posterior-anterior (_nn) and lateral (_nnL) projections
Ladder plots suggest a rather good correlation between both modalities and projections but with a small advantage for EOS

4.4.1.3 Criteria 1: inspiration. Independence Test

Quality Criteria 1. Inspiration. EOS vs. DX correlation Kendall's Tau_b					
Projection view	r_τ (Tau_b)	95% CI	Approximate tests (adjusted for ties)		
			Lower side	Upper side	Two sided
PA-AP	**0.408446**	0.3290 to 0.4878	> 0.9999	**< 0.0001**	**P = 0.0001**
Lat	**0.392888**	0.3159 to 0.4697	> 0.9999	**< 0.0001**	**P = 0.0001**

Table 53. Quality criteria 1: Inspiration. EOS vs. DX correlation (Kendall's correlation).

Results are statistically significant, There is a moderate positive correlation.

4.4.1.4 Criteria 1: inspiration. Interobserver Agreement (Universal R)

Quality Criteria 1. Inspiration. Interobserver Universal Agreement R		
Projection	**R**	**P value**
AP EOS	**0.206971**	**P < 0.0001**
PA DX	**0.115691**	**0.0046**
Lat EOS	0.251868	**< 0.0001**
Lat DX	**0.108172**	**0.0073**

Table 54. Quality criteria 1: Inspiration. EOS and DX Interobserver Agreement R

4.4.2 Criteria 2: Rotation. Reproduction of the thorax without rotation and tilting, and true lateral projection

4.4.2.1 Descriptive Statistics.

The table below display the relevant statistics for the assessment criteria, for both modalities and views.

Quality criteria 2. Rotation. EOS and DX scores (PA & Lateral)											
Scores	**Median**	**Mean**	**Geometric mean**	**Standard deviation**	**95% CL of mean Lower to Upper**	**Standard error of mean**	**Range**	**Maximum**	**Upper quartile**	**Lower quartile**	**Minimum**
EOS_2 (PA)	**4**	3.47	3.41	0.59	3.37 to 3.57	0.05	2	4	4	3	2
DX_2 (PA)	**4**	**3.63**	3.59	0.54	3.54 to 3.72	0.04	3	5	4	3	2
EOS_2L (lat)	**4**	3.51	3.45	0.61	3.41 to 3.61	0.05	2	4	4	3	2
DX_2L (lat)	**4**	**3.61**	3.57	0.54	3.52 to 3.70	0.04	3	5	4	3	2
	37 Patients; 4 observers; 148 independent observations; Valid n: 147										

Table 55. Quality criteria 2: Rotation. EOS vs. DX (PA & Lateral)
EOS and DX, as overall results for Posterior-anterior (PA) and lateral (L) projections.

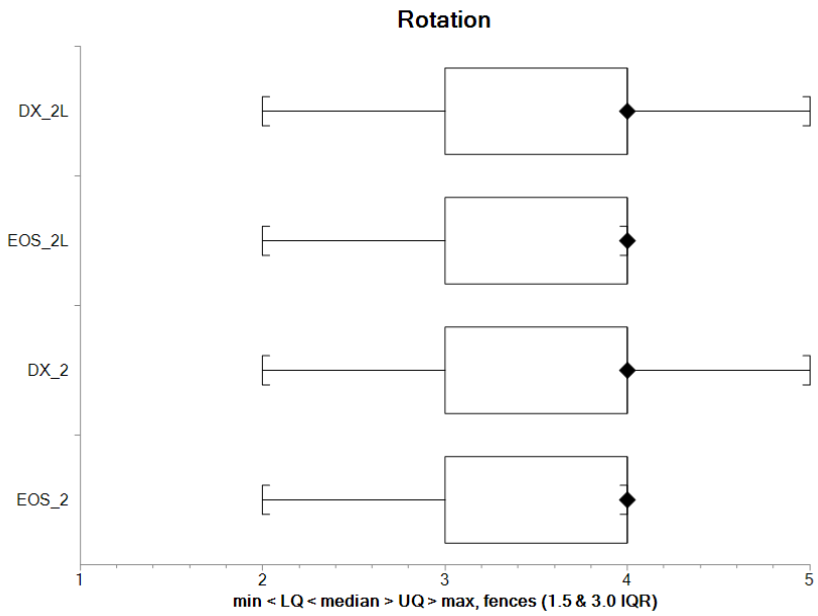

Figure 68: Quality criteria 2: Rotation. Box and whisker plot.
EOS and DX results for Posterior-anterior (_nn) and lateral (_nnL) projections

4.4.2.2 Criteria 2: Rotation. Significance of the difference of Medians

Quality criteria 2: Rotation. EOS - DX scores (PA & Lateral)					
Projection view	**Median difference**	**95% CI**	**P values**		
			Lower side	**Upper side**	**Two sided**
PA-AP	**0**	0 to 0.0	**0.0008**	0.09996	**0.0016**
Lat	**0**	0 to 0.0	> 0.0413	< 0.9963	0.0826

Table 56. Quality criteria 2: Rotation: PA and Lat. Wilcoxon's signed ranks tests.

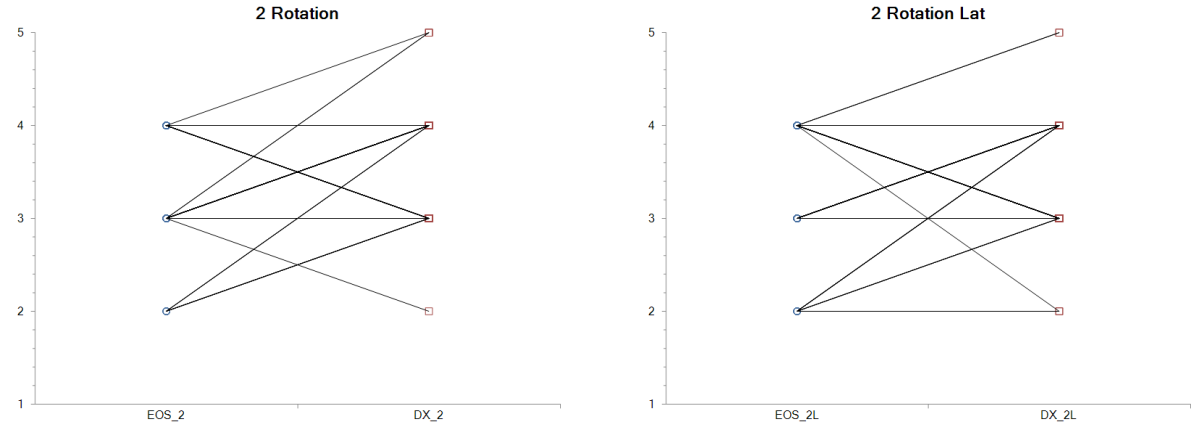

Figure 69. Quality criteria 2: Rotation. Ladder Plots PA and lateral
EOS and DX results for Posterior-anterior (_nn) and lateral (_nnL) projections

Ladder plot display inferior values for EOS than for DX

4.4.2.3 Quality criteria 2: Rotation. Independence Test

Quality criteria 2: Rotation. EOS vs. DX correlation Kendall's Tau_b					
Projection view	**r_τ (Tau_b)**	**95% CI**	**Approximate tests (adjusted for ties)**		
			Lower side	**Upper side**	**Two sided**
PA-AP	**0.482275**	0.4079 to 0.5566	> 0.9999	**< 0.0001**	**< 0.0001**
Lat	**0.356352**	0.2751 to 0.4375	> 0.9999	**< 0.0001**	**< 0.0001**

Table 57. Quality criteria 2: Rotation. EOS vs. DX correlation
(Kendall's correlation).

4.4.2.4 Quality criteria 2: Rotation. Interobserver Agreement (Universal R)

Quality Criteria 2: Rotation. Interobserver Universal Agreement R		
Projection	**R**	**P value**
AP EOS	0.058131	0.0672
PA DX	0.031084	0.2105
Lat EOS	0.034313	0.1345
Lat DX	**0.099471**	**0.0093**

Table 58. Quality criteria 2: Rotation. EOS and DX
Interobserver Agreement R

4.4.3 Criteria 3: Anatomic Coverage. Reproduction of the chest must extend from just above the apices of the lungs to T12/L1

4.4.3.1 Descriptive Statistics.

The table below display the relevant statistics for the assessment criteria, for both modalities and views.

Quality Criteria 3: Anatomic Coverage. EOS and DX scores (PA & Lateral)											
Scores	Median	Mean	Geometric mean	Standard deviation	95% CL of mean Lower to Upper	Standard error of mean	Range	Maximum	Upper quartile	Lower quartile	Minimum
EOS_3 (PA)	**4**	**3.75**	3.70	0.55	3.66 to 3.84	0.05	2	4	4	4	2
DX_3 (PA)	**4**	3.74	3.70	0.49	3.66 to 3.82	0.04	2	5	4	3	3
EOS_3L (lat)	**4**	**3.72**	3.68	0.51	3.63 to 3.80	0.04	2	4	4	3	2
DX_3L (lat)	**4**	3.49	3.44	0.57	3.40 to 3.58	0.05	3	5	4	3	2
	37 Patients; 4 observers; 148 independent observations; Valid n: 147										

Table 59. Quality criteria 3: Anatomic Coverage. EOS vs. DX (PA & Lateral)
EOS and DX, as overall results for Posterior-anterior (PA) and lateral (L) projections.

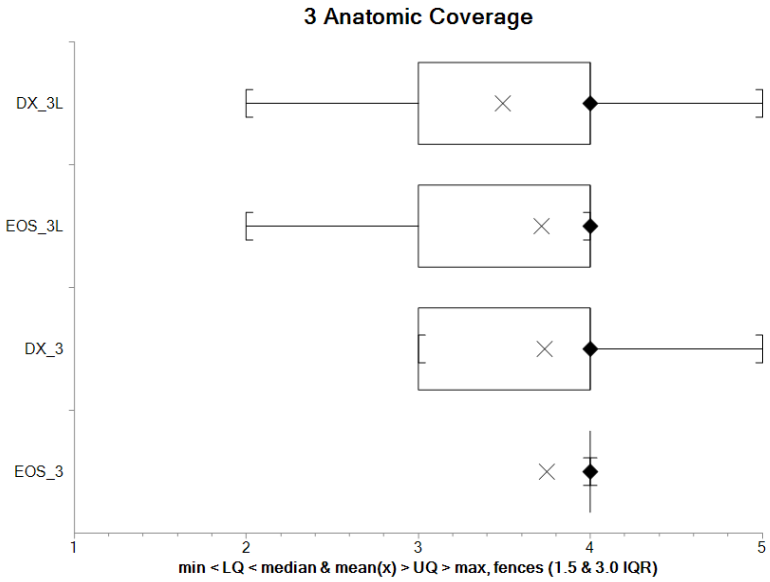

Figure 70: Quality criteria 3: Anatomic Coverage. Box and whisker plot.
EOS and DX results for Posterior-anterior (_nn) and lateral (_nnL) projections

4.4.3.2 Criteria 3: Anatomic Coverage. Significance of the difference of Medians

Quality criteria 3: Anatomic Coverage. EOS - DX scores (PA & Lateral)					
Projection view	Median difference	95% CI	P values		
			Lower side	Upper side	Two sided
PA-AP	**0**	0 to 0.0	0.5075	0.4026	0.8052
Lat	**0**	0 to 0.5	0.9996	**0.0004**	**0.0009**

Table 60. Quality criteria 3: Anatomic Coverage: PA and Lat.
Wilcoxon's signed ranks tests.

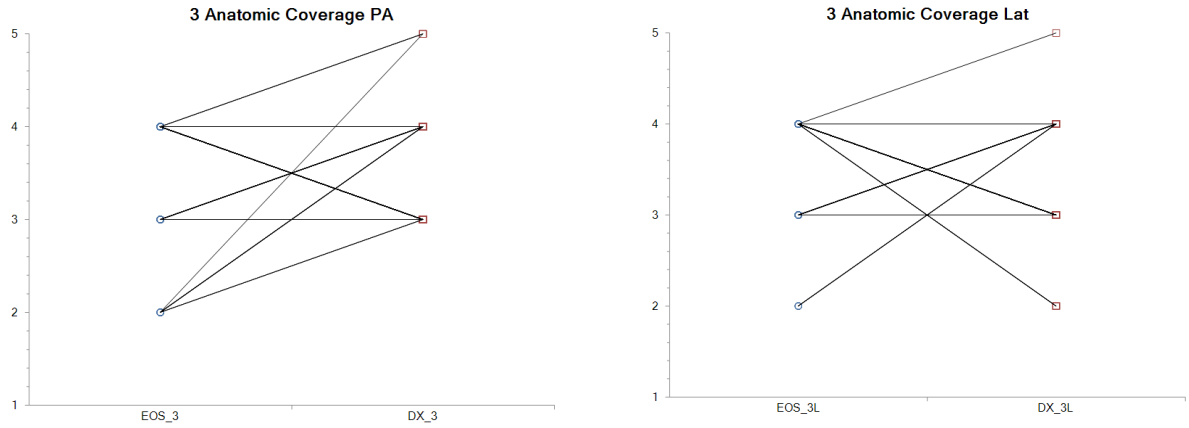

Figure 71. Quality criteria 3: Anatomic Coverage. Ladder Plots PA and lateral
EOS and DX results for Posterior-anterior (_nn) and lateral (_nnL) projections

4.4.3.3 Quality criteria 3: Anatomic Coverage. Independence Test

Quality criteria 3: Anatomic Coverage. EOS vs. DX correlation Kendall's Tau_b					
Projection view	r_τ (Tau_b)	95% CI	Approximate tests (adjusted for ties)		
			Lower side	Upper side	Two sided
PA-AP	**0.174255**	0.1025 to 0.2459	0.9849	**0.0151**	**0.0303**
Lat	**0.059358**	-0.0143 to 0.1330	0.7673	0.2327	0.4655

Table 61. Quality criteria 3: Anatomic Coverage. EOS vs. DX correlation
(Kendall's correlation).

4.4.3.4 Quality criteria 3: Anatomic Coverage. Interobserver Agreement (Universal R)

Quality criteria 3: Anatomic Coverage. Interobserver Universal Agreement R		
Projection	**R**	**P value**
AP EOS	**0.12929**	**0.0082**
PA DX	0.02029	0.2772
Lat EOS	**0.13322**	**0.0182**
Lat DX	0.06026	0.8667

Table 62. Quality criteria 3: Anatomic Coverage. EOS and DX
Interobserver Agreement R

4.4.4 Criteria 4: Vascular Pattern. Reproduction of the vascular pattern in central 2/3 of the lungs. Reproduction of the hilar vessels.

4.4.4.1 Descriptive Statistics.

The table below display the relevant statistics for the assessment criteria, for both modalities and views.

Quality Criteria 4: Vascular Pattern. EOS and DX scores (PA & Lateral)											
Scores	**Median**	**Mean**	**Geometric mean**	**Standard deviation**	**95% CL of mean Lower to Upper**	**Standard error of mean**	**Range**	**Maximum**	**Upper quartile**	**Lower quartile**	**Minimum**
EOS_4 (PA)	**4**	**3.73**	3.69	0.49	3.65 to 3.81	0.04	3	5	4	3	2
DX_4 (PA)	**4**	3.64	3.59	0.55	3.55 to 3.72	0.05	3	5	4	3	2
EOS_4L (lat)	**3**	3.34	3.29	0.58	3.25 to 3.44	0.05	2	4	4	3	2
DX_4L (lat)	**4**	**3.56**	3.52	0.54	3.47 to 3.65	0.04	3	5	4	3	2
	37 Patients; 4 observers; 148 independent observations; Valid n: 147										

Table 63. Quality Criteria 4: Vascular Pattern. EOS vs. DX (PA & Lateral)
EOS and DX, as overall results for Posterior-anterior (PA) and lateral (L) projections.

Figure 72: Quality Criteria 4: Vascular Pattern. Box and whisker plot.

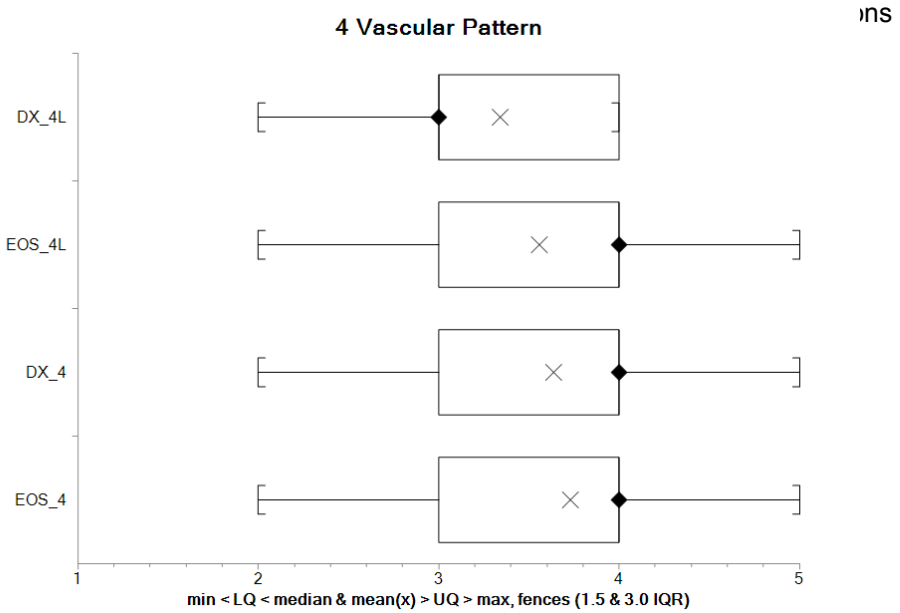

4.4.4.2 *Criteria 4: Vascular Pattern. Significance of the difference of Medians*

Quality Criteria 4: Vascular Pattern. EOS - DX scores (PA & Lateral)					
Projection view	**Median difference**	**95% CI**	**P values**		
			Lower side	**Upper side**	**Two sided**
PA-AP	**0**	0 to 0.0	0.5075	0.4026	0.8052
Lat	**0**	0 to 0.5	>0.9999	**0.0001**	**0.0003**

Table 64. Quality criteria 3: Anatomic Coverage: PA and Lat.
Wilcoxon's signed ranks tests.

No statistically significant differences of medians were found. A small positive difference in 95% confidence interval may be detected for EOS lateral view.

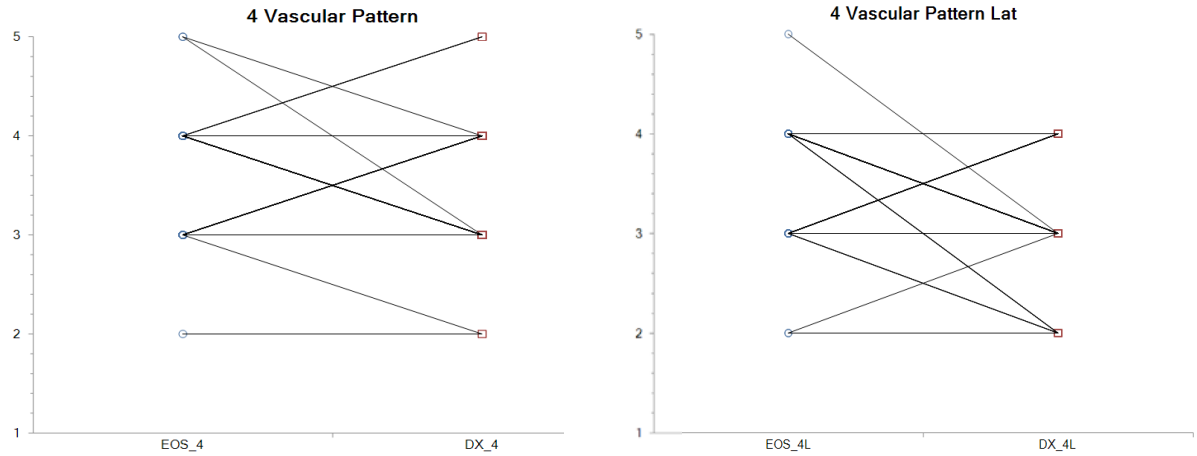

Figure 73. Quality Criteria 4: Vascular Pattern. Ladder Plots PA and lateral
EOS and DX results for Posterior-anterior (_nn) and lateral (_nnL) projections

4.4.4.3 Quality criteria 4: Vascular Pattern. Independence Test

Criteria 4: Vascular Pattern. EOS vs. DX correlation Kendall's Tau_b					
Projection view	**r_τ (Tau_b)**	**95% CI**	**Approximate tests (adjusted for ties)**		
			Lower side	**Upper side**	**Two sided**
PA-AP	**0.247802**	0.1686 to 0.3269	0.9989	**0.0011**	**0.0021**
Lat	**0.183464**	0.0994 to 0.2674	0.9885	**0.0115**	0.4655

Table 65. Criteria 4: Vascular Pattern. EOS vs. DX correlation (Kendall's correlation).

A weak significant correlation is present between both modalities for their PA views

4.4.4.4 Criteria 4: Vascular Pattern. Interobserver Agreement (Universal R)

Criteria 4: Vascular Pattern. Interobserver Universal Agreement R		
Projection	**R**	**P value**
AP EOS	0.03152	0.2608
PA DX	-0.01605	0.6474
Lat EOS	**0.15102**	**0.0015**
Lat DX	0.04091	0.1939

Table 66. Criteria 4: Vascular Pattern. EOS and DX Interobserver Agreement (Universal R)

Weak but statistically significant agreement was present only for EOS lateral view.

4.4.5 Criteria 5: Fine Interstitial Structures. Reproduction of fine interstitial structures in the 1/3 periphery of the lungs. Including retrosternal space

4.4.5.1 Descriptive Statistics.

The table below display the relevant statistics for the assessment criteria, for both modalities and views.

Quality Criteria 5: Fine Interstitial Structures. EOS and DX scores (PA & Lateral)											
Scores	Median	Mean	Geometric mean	Standard deviation	95% CL of mean Lower to Upper	Standard error of mean	Range	Maximum	Upper quartile	Lower quartile	Minimum
EOS_5 (PA)	**3**	2.74	2.60	0.79	2.61 to 2.87	0.06	3	4	3	2	1
DX_5 (PA)	**3**	**2.89**	2.77	0.74	2.77 to 3.01	0.06	3	4	3	3	1
EOS_5L (lat)	**3**	**2.89**	2.73	0.83	2.75 to 3.03	0.07	3	4	3	3	1
DX_5L (lat)	**3**	2.84	2.72	0.79	2.71 to 2.97	0.06	3	4	3	2	1
	37 Patients; 4 observers; 148 independent observations; Valid n: 147										

Table 67. Quality Criteria 5: Fine Interstitial Structures. EOS vs. DX (PA & Lateral)
EOS and DX, as overall results for Posterior-anterior (PA) and lateral (L) projections.

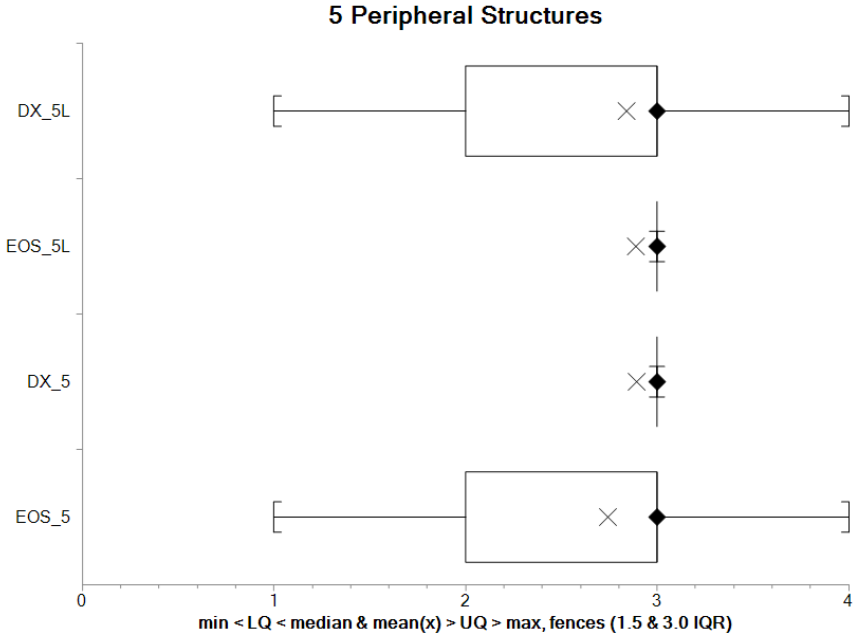

Figure 74: Quality Criteria 5: Fine Interstitial Structures. Box and whisker plot.
EOS and DX results for Posterior-anterior (_nn) and lateral (_nnL) projections

4.4.5.2 Quality Criteria 5: Fine Interstitial Structures.. Significance of the difference of Medians

Quality Criteria 5: Fine Interstitial Structures. EOS - DX scores (PA & Lateral)					
Projection view	Median difference	95% CI	P values		
			Lower side	Upper side	Two sided
PA-AP	**0**	-0.5 to 0	0.5075	0.4026	0.8052
Lat	**0**	0 to 0.0	>0.9999	**0.0001**	**0.0003**

Table 68. Quality Criteria 5: Fine Interstitial Structures. PA and Lat. Wilcoxon's signed

No statistically significant differences were found

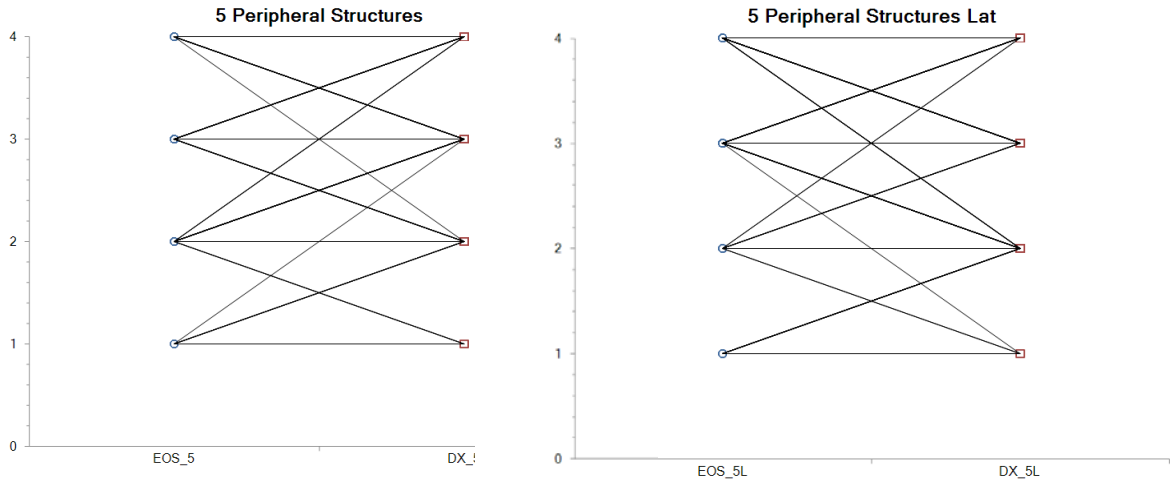

Figure 75. Quality Criteria 5: Fine Interstitial Structures. Ladder Plots PA and lateral

EOS and DX results for Posterior-anterior (_nn) and lateral (_nnL) projections

4.4.5.3 Quality Criteria 5: Fine Interstitial Structures. Independence Test

Quality Criteria 5: Fine Interstitial Structures. EOS vs. DX correlation Kendall's Tau_b					
Projection view	r_τ (Tau_b)	95% CI	Approximate tests (adjusted for ties)		
			Lower side	Upper side	Two sided
PA-AP	**0.456168**	0.3690 to 0.5433	> 0.9999	**< 0.0001**	**< 0.0001**
Lat	**0.398905**	0.3056 to 0.4922	> 0.9999	**< 0.0001**	**< 0.0001**

Table 69. Quality Criteria 5: Fine Interstitial Structures.. EOS vs. DX correlation (Kendall's correlation).

Statistically significant correlation was present for both views

4.4.5.4 Quality Criteria 5: Fine Interstitial Structures. Interobserver Agreement (Universal R)

Quality Criteria 5: Fine Interstitial Structures. Interobserver Universal Agreement R		
Projection	**R**	**P value**
AP EOS	-0,007744	0,6394
PA DX	-0,009898	0.64
Lat EOS	0,006711	0,3653
Lat DX	0,053043	0,0153

Table 70. Quality Criteria 5: Fine Interstitial Structures. EOS and DX Interobserver Agreement Universal R

Poor agreement was present just for lateral DX view statistically significant

4.4.6 Criteria 6: Fissures. Reproduction of fissures major and fissure minor.

4.4.6.1 Descriptive Statistics.

The table below display the relevant statistics for the assessment criteria, for both modalities and views.

Quality Criteria 6: Fissures. EOS and DX scores (PA & Lateral)											
Scores	**Median**	**Mean**	**Geometric mean**	**Standard deviation**	**95% CL of mean Lower to Upper**	**Standard error of mean**	**Range**	**Maximum**	**Upper quartile**	**Lower quartile**	**Minimum**
EOS_6 (PA)	**2**	1.99	1.81	0.85	1.85 to 2.13	0.07	3	4	3	1	1
DX_6 (PA)	**2**	**2.25**	2.03	0.95	2.10 to 2.40	0.08	3	4	3	1.5	1
EOS_6L (lat)	**3**	**2.81**	2.63	0.93	2.66 to 2.97	0.08	3	4	4	2	1
DX_6L (lat)	**3**	2.71	2.58	0.80	2.58 to 2.84	0.07	4	5	3	2	1
	37 Patients; 4 observers; 148 independent observations; Valid n: 147										

Table 71. Quality Criteria 6: Fissures. EOS vs. DX (PA & Lateral)
EOS and DX, as overall results for Posterior-anterior (PA) and lateral (L) projections.

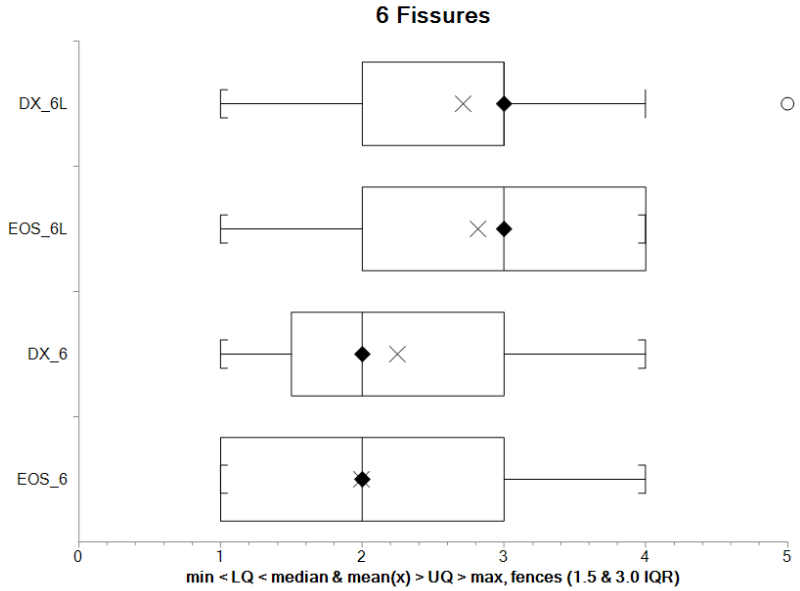

Figure 76: Quality Criteria 6: Fissures. Box and whisker plot.
EOS and DX results for Posterior-anterior (_nn) and lateral (_nnL) projections

4.4.6.2 Quality Criteria 6: Fissures. Significance of the difference of Medians

Quality Criteria 6: Fissures. EOS - DX scores (PA & Lateral)					
Projection view	**Median difference**	**95% CI**	**P values**		
			Lower side	**Upper side**	**Two sided**
PA-AP	**0**	-0.5 to 0	**0.0031**	0.9969	**0.0062**
Lat	**0**	0 to 0.5	0.9151	0.0923	0.1846

Table 72. Quality Criteria 6: Fissures. PA and Lat. Wilcoxon's signed ranks tests.

No statistically significant differences in medians were found. A small difference was detected in the 95% CI with postero-anterior DX median over EOS.

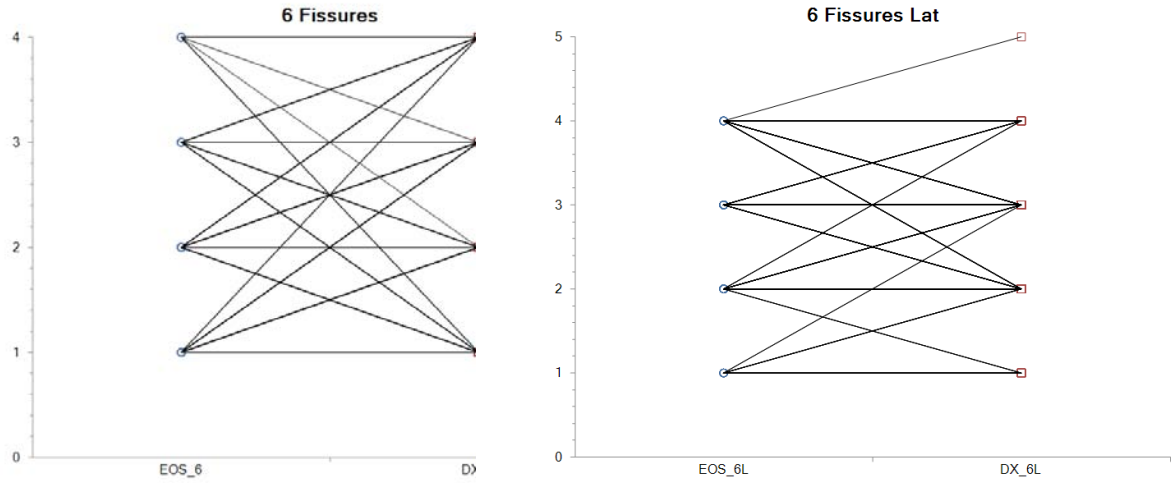

Figure 77. Quality Criteria 6: Fissures. Ladder Plots PA and lateral
EOS and DX results for Posterior-anterior (_nn) and lateral (_nnL) projections

4.4.6.3 Quality Criteria 6: Fissures. Independence Test

Quality Criteria 6: Fissures. EOS vs. DX correlation Kendall's Tau_b					
Projection view	**r_τ (Tau_b)**	**95% CI**	**Approximate tests (adjusted for ties)**		
			Lower side	**Upper side**	**Two sided**
PA-AP	**0.263618**	0.1564 to 0.3709	0.9999	0.0001	0.0002
Lat	**0.326519**	0.2290 to 0.4240	> 0.9999	< 0.0001	< 0.0001

Table 73. Quality Criteria 6: Fissures EOS vs. DX correlation (Kendall's correlation). Statistically significant correlation is present with both views,

4.4.6.4 Quality Criteria 6: Fissures Interobserver Agreement (Universal R)

Quality Criteria 6: Fissures. Interobserver Universal Agreement R		
Projection	**R**	**P value**
AP EOS	**0.210351**	**< 0.0001**
PA DX	**0.223776**	**< 0.0001**
Lat EOS	0.052382	0.0705
Lat DX	**0.072394**	**0.0383**

Table 74. Quality Criteria 6: Fissures. EOS and DX Interobserver Agreement Universal R

Weak agreement was present for PA/AP views and lateral DX view.

4.4.7 Criteria 7: Trachea and Bronchi. Reproduction of the trachea and the proximal bronchi. Visualization of the trachea from the apices of the lungs down to and including the main bronchi..

4.4.7.1 Descriptive Statistics.

The table below display the relevant statistics for the assessment criteria, for both modalities and views.

Quality Criteria 7: Trachea and Bronchi. EOS and DX scores (PA & Lateral)											
Scores	Median	Mean	Geometric mean	Standard deviation	95% CL of mean Lower to Upper	Standard error of mean	Range	Maximum	Upper quartile	Lower quartile	Minimum
EOS_7 (PA)	**4**	**3.81**	3.75	0.60	3.71 to 3.91	0.05	4	5	4	4	1
DX_7 (PA)	3	3.21	3.17	0.52	3.12 to 3.29	0.04	3	5	3.5	3	2
EOS_7L (lat)	**4**	**3.60**	3.55	0.62	3.50 to 3.70	0.05	3	5	4	3	2
DX_7L (lat)	3	3.38	3.32	0.60	3.29 to 3.48	0.05	4	5	4	3	1
	37 Patients; 4 observers; 148 independent observations; Valid n: 147										

Table 75. Quality Criteria 7: Trachea and Bronchi. EOS vs. DX (PA & Lateral)
EOS and DX, as overall results for Posterior-anterior (PA) and lateral (L) projections.

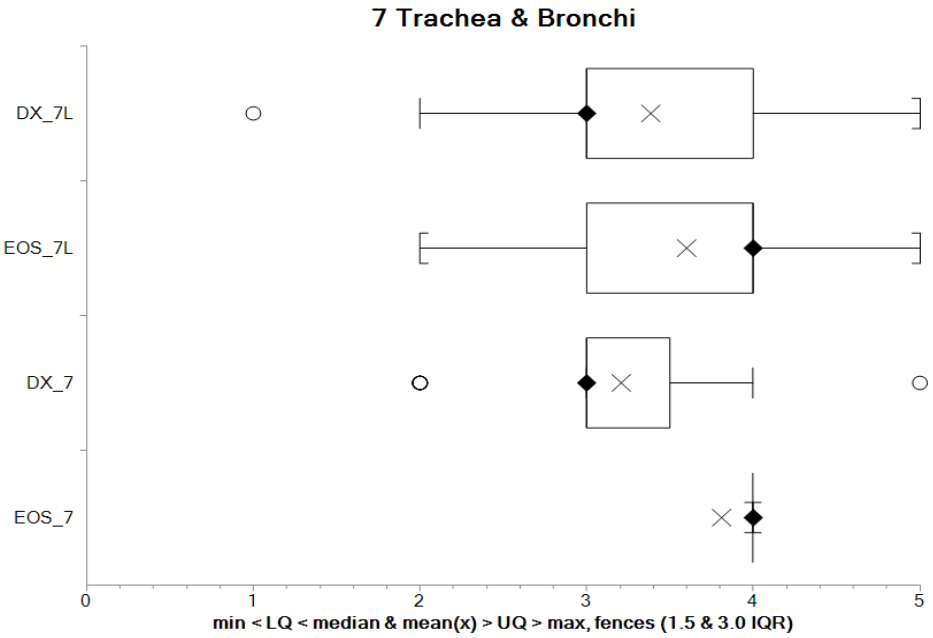

Figure 78: Quality Criteria 7: Trachea and Bronchi. Box and whisker plot.
EOS and DX results for Posterior-anterior (_nn) and lateral (_nnL) projections

4.4.7.2 Quality Criteria 7: Trachea and Bronchi. Significance of the difference of Medians

Quality Criteria 7: Trachea and Bronchi. EOS - DX scores (PA & Lateral)					
Projection view	Median difference	95% CI	P values		
			Lower side	Upper side	Two sided
PA-AP	**0.5**	0.5 to 0.5	> 0.9990	< 0.0001	**< 0.0001**
Lat	**0**	0 to 0.5	0.9996	0.0006	**0.0012**

Table 76. Quality Criteria 7: Trachea and Bronchi. PA and Lat.
Wilcoxon's signed ranks tests.

A small but statistically significant differences of medians is present of 0.5 of EOS over DX. No statistically significant differences of medians are present between EOS and DX in lateral view

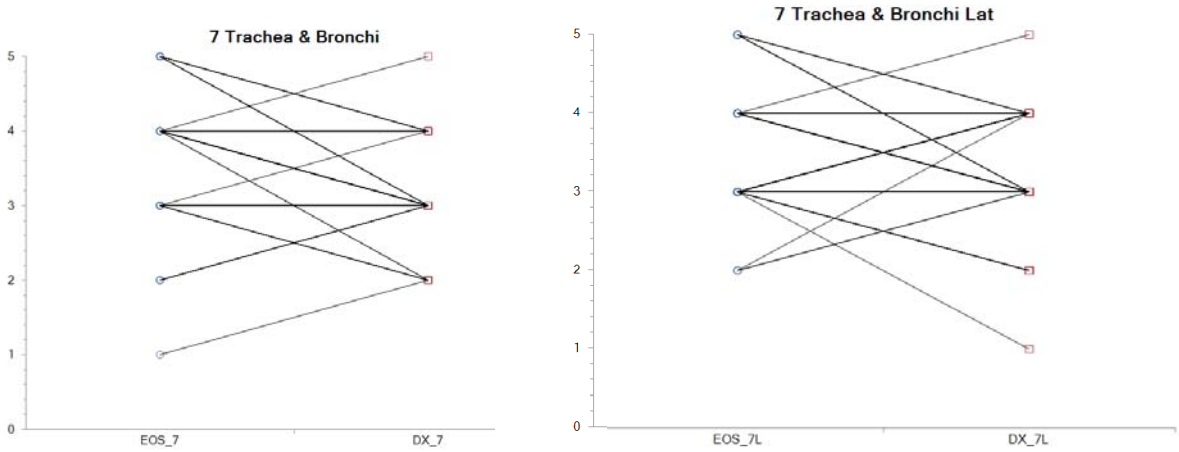

Figure 79. Quality Criteria 7: Trachea and Bronchi. Ladder Plots PA and lateral
EOS and DX results for Posterior-anterior (_nn) and lateral (_nnL) projections

4.4.7.3 Quality Criteria 7: Trachea and Bronchi. Independence Test

Quality Criteria 7: Trachea and Bronchi. EOS vs. DX correlation Kendall's Tau_b					
Projection view	r_τ (Tau_b)	95% CI	Approximate tests (adjusted for ties)		
			Lower side	Upper side	Two sided
PA-AP	**0.323166**	0.2593 to 0.3870	> 0.9999	**< 0.0001**	**< 0.0001**
Lat	**0.199175**	0.1153 to 0.2831	0.994	**0.006**	**0.012**

Table 77. Quality Criteria 7: Trachea and Bronchi. EOS vs. DX correlation

(Kendall's correlation).

A statistically significant is present for both views

4.4.7.4 Quality Criteria 7: Trachea and Bronchi. Interobserver Agreement (Universal R)

Quality Criteria 7: Trachea and Bronchi. Interobserver Universal Agreement R		
Projection	**R**	**P value**
AP EOS	**0.280019**	**< 0.0001**
PA DX	**0,114386**	**0.022**
Lat EOS	**0.219531**	**0.0015**
Lat DX	0.052439	0.1633

Table 78. Quality Criteria 7: Trachea and Bronchi. EOS and DX Interobserver Agreement Universal R

There is weak but significant agreement for both PA/AP view and EOS Lateral view

4.4.8 Criteria 8: Diaphragms. Visually sharp reproduction of the diaphragm and costophrenic angles, and the whole of both domes of the diaphragm.

4.4.8.1 Descriptive Statistics.

The table below display the relevant statistics for the assessment criteria, for both modalities and views.

Quality Criteria 8: Diaphragms. EOS and DX scores (PA & Lateral)											
Scores	**Median**	**Mean**	**Geometric mean**	**Standard deviation**	**95% CL of mean Lower to Upper**	**Standard error of mean**	**Range**	**Maximum**	**Upper quartile**	**Lower quartile**	**Minimum**
EOS_8 (PA)	**4**	**3.51**	3.44	0.68	3.40 to 3.62	0.06	3	5	4	3	2
DX_8 (PA)	**4**	3.44	3.36	0.69	3.33 to 3.55	0.06	4	5	4	3	1
EOS_8L (lat)	**3**	**3.32**	3.26	0.61	3.22 to 3.42	0.05	2	4	4	3	2
DX_8L (lat)	**3**	3.29	3.23	0.62	3.19 to 3.40	0.05	3	5	4	3	2
	37 Patients; 4 observers; 148 independent observations; Valid n: 147										

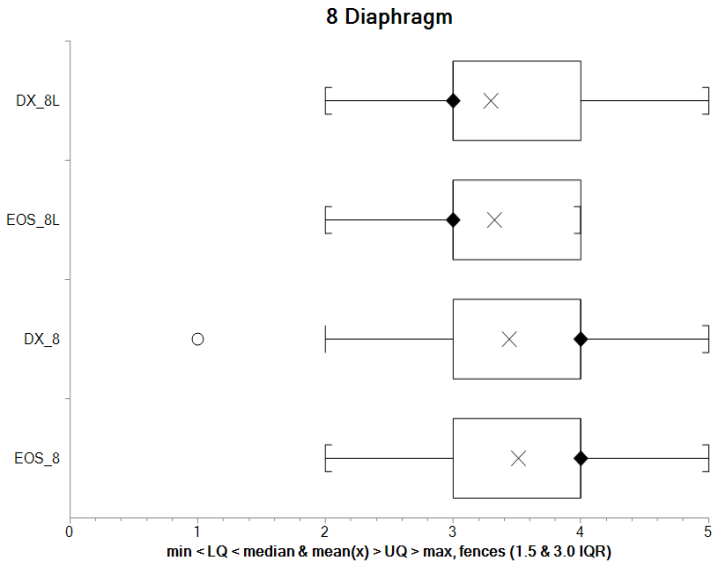

Figure 80: Quality Criteria 8: Diaphragms. Box and whisker plot.
EOS and DX results for Posterior-anterior (_nn) and lateral (_nnL) projections

Table 79. Quality Criteria 8: Diaphragms. EOS vs. DX (PA & Lateral)
EOS and DX, as overall results for Posterior-anterior (PA) and lateral (L) projections.

4.4.8.2 Quality Criteria 8: Diaphragms. Significance of the difference of Medians

Quality Criteria 8: Diaphragms. EOS - DX scores (PA & Lateral)					
Projection view	**Median difference**	**95% CI**	**P values**		
			Lower side	**Upper side**	**Two sided**
PA-AP	**0**	0 to 0.0	0.9138	0.0899	0.1798
Lat	**0 to 0.5**	0 to 0.5	0.7678	0.2578	0.5156

Table 80. Quality Criteria 8: Diaphragms. PA and Lat.
Wilcoxon's signed ranks tests.

No statistically significant differences of medians were present between EOS and DX

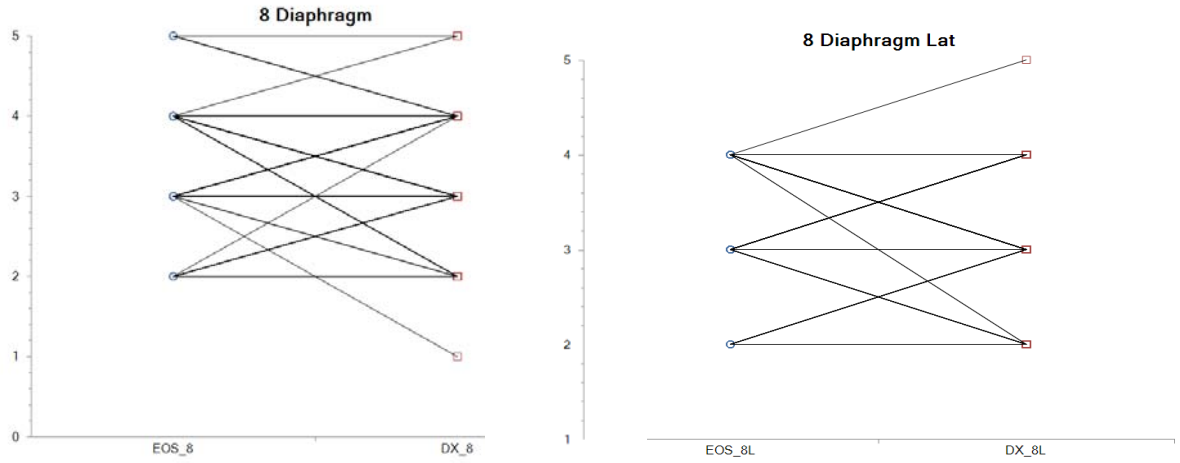

Figure 81. Quality Criteria 8: Diaphragms. Ladder Plots PA and lateral
EOS and DX results for Posterior-anterior (_nn) and lateral (_nnL) projections

Ladder plots show horizontal correspondence of most values in PA.

4.4.8.3 Quality Criteria 8: Diaphragms. Independence Test

Quality Criteria 8: Diaphragms. EOS vs. DX correlation Kendall's Tau_b					
Projection view	**r_τ (Tau_b)**	**95% CI**	**Approximate tests (adjusted for ties)**		
			Lower side	**Upper side**	**Two sided**
PA-AP	**0.436551**	0.3519 to 0.5211	0.994	**0.006**	**0.012**
Lat	**0.356839**	0.2736 to 0.4400	< 0.9999	**< 0.0001**	**< 0.0001**

Table 81. Quality Criteria 8: Diaphragms. EOS vs. DX correlation
(Kendall's correlation).

Statistically significant correlation is present for both views

4.4.8.4 Quality Criteria 8: Diaphragms. Interobserver Agreement (Universal R)

Quality Criteria 8: Diaphragms. Interobserver Universal Agreement R		
Projection	**R**	**P value**
AP EOS	0,121626	**< 0,0001**
PA DX	0,193965	**< 0,0001**
Lat EOS	0,068226	**0.0155**
Lat DX	0,170283	**< 0,0001**

Table 82. Quality Criteria 8: Diaphragms. EOS and DX Interobserver Agreement
Universal R

Weak statistically significant agreement is present for all 4 views

4.4.9 Criteria 9: Mediastinum and Spine.

Reproduction of the spine and paraspinal structures, visualization of the retrocardiac lung, mediastinum, sternum and the thoracic spine

4.4.9.1 Descriptive Statistics.

The table below display the relevant statistics for the assessment criteria, for both modalities and views.

Quality Criteria 9: Mediastinum and Spine. EOS and DX scores (PA & Lateral)											
Scores	Median	Mean	Geometric mean	Standard deviation	95% CL of mean Lower to Upper	Standard error of mean	Range	Maximum	Upper quartile	Lower quartile	Minimum
EOS_9 (PA)	**4**	**3.73**	3.69	0.49	3.65 to 3.81	0.04	3	5	4	3	2
DX_9 (PA)	**4**	3.64	3.59	0.55	3.55 to 3.72	0.05	3	5	4	3	2
EOS_9L (lat)	**4**	**3.56**	3.52	0.54	3.47 to 3.65	0.04	3	5	4	3	2
DX_9L (lat)	**3**	3.34	3.29	0.58	3.25 to 3.44	0.05	2	4	4	3	2
	37 Patients; 4 observers; 148 independent observations; Valid n: 147										

Table 83. Quality Criteria 9: Mediastinum and Spine. EOS vs. DX (PA & Lateral)
EOS and DX, as overall results for Posterior-anterior (PA) and lateral (L) projections.
EOS median were higher than DX on both view.

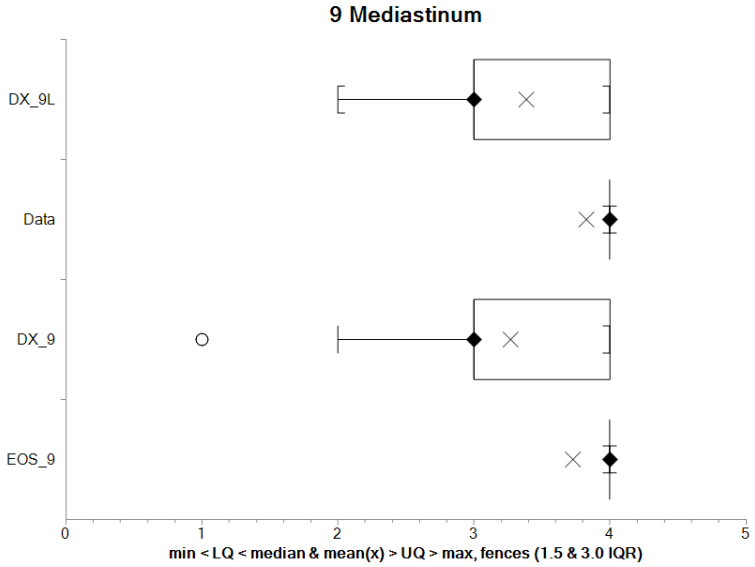

Figure 82: Quality Criteria 9: Mediastinum and Spine. Box and whisker plot.
EOS and DX results for Posterior-anterior (_nn) and lateral (_nnL) projections

4.4.9.2 Quality Criteria 9: Mediastinum and Spine. Significance of the difference of Medians

Quality Criteria 9: Mediastinum and Spine.EOS - DX scores (PA & Lateral)					
Projection view	Median difference	95% CI	P values		
			Lower side	Upper side	Two sided
PA-AP	**0.5**	0.5 to 0.5	>0.9999	**0.0001**	**< 0.0001**
Lat	**0.5**	0.5 to 0.5	>0.9999	**< 0.0001**	**< 0.0001**

Table 84. Quality Criteria 9: Mediastinum and Spine. PA and Lat.
Wilcoxon's signed ranks tests.

Both median differences for EOS were positive with statistical significance

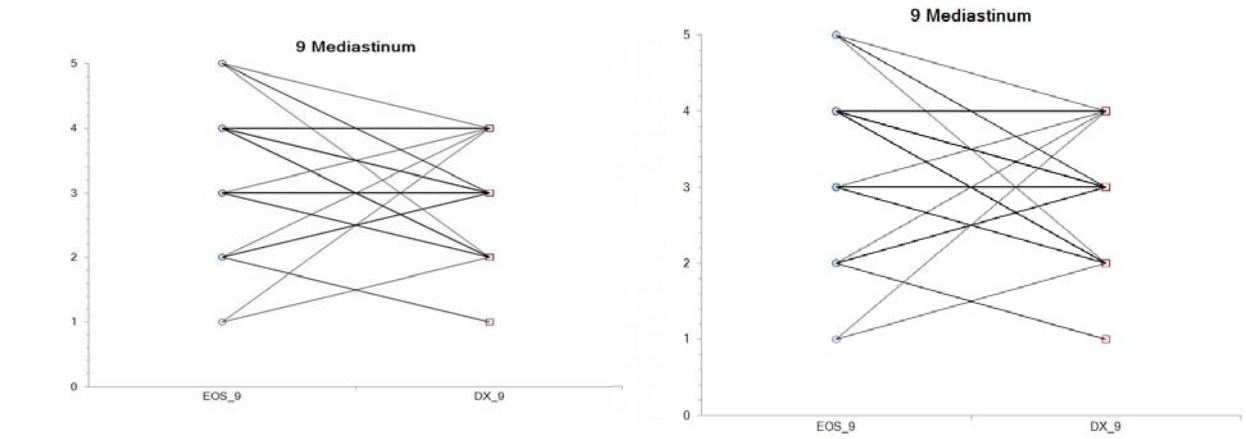

EOS and DX results for Posterior-anterior (_nn) and lateral (_nnL) projections

Ladder plots suggest a little advantage of EOS over DX for both views

4.4.9.3 Quality Criteria 9: Mediastinum and Spine. Independence Test

Quality Criteria 9: Mediastinum and Spine. EOS vs. DX correlation Kendall's Tau_b					
Projection view	r_τ (Tau_b)	95% CI	Approximate tests (adjusted for ties)		
			Lower side	Upper side	Two sided
PA-AP	**0.263675**	0.1875 to 0.3398	0.9997	**0.0003**	**0.0005**
Lat	**0.220146**	0.1527 to 0.2876	0.9969	**0.0031**	**0.0063**

Table 85. Quality Criteria 9: Mediastinum and Spine. EOS vs. DX correlation (Kendall's correlation).

A statistically significant correlation is present for both views

4.4.9.4 Quality Criteria 9: Mediastinum and Spine. Interobserver Agreement (Universal R)

Quality Criteria 9: Mediastinum and Spine. Interobserver Universal Agreement R		
Projection	**R**	**P value**
AP EOS	0,226322	**< 0,0001**
PA DX	0,101835	**0,0049**
Lat EOS	0,094054	**0,0552**
Lat DX	0,07235	**0,0197**

Table 86. Quality Criteria 9: Mediastinum and Spine. EOS and DX
Interobserver Agreement Universal R

A poor but statistically significant interobserver agreement was found for all 4 sets.

4.4.10 Criteria 10: Soft Tissues. Reproduction of the soft tissues and fat pads.

4.4.10.1 Descriptive Statistics.

The table below display the relevant statistics for the assessment criteria, for both modalities and views.

Quality Criteria 10: Soft Tissues. EOS and DX scores (PA & Lateral)											
Scores	**Median**	**Mean**	**Geometric mean**	**Standard deviation**	**95% CL of mean Lower to Upper**	**Standard error of mean**	**Range**	**Maximum**	**Upper quartile**	**Lower quartile**	**Minimum**
EOS_10 (PA)	**4**	**3.90**	3.83	0.63	3.80 to 4.00	0.05	4	5	4	4	1
DX_10 (PA)	**4**	3.55	3.51	0.53	3.46 to 3.63	0.04	2	4	4	3	2
EOS_10L (lat)	**4**	**3.44**	3.33	0.75	3.32 to 3.57	0.06	4	5	4	3	1
DX_10L (lat)	**3**	3.20	3.09	0.77	3.07 to 3.32	0.06	3	4	4	3	1
	37 Patients; 4 observers; 148 independent observations; Valid n: 147										

Table 87. Quality Criteria 10: Soft Tissues. EOS vs. DX (PA & Lateral)
EOS and DX, as overall results for Posterior-anterior (PA) and lateral (L) projections.

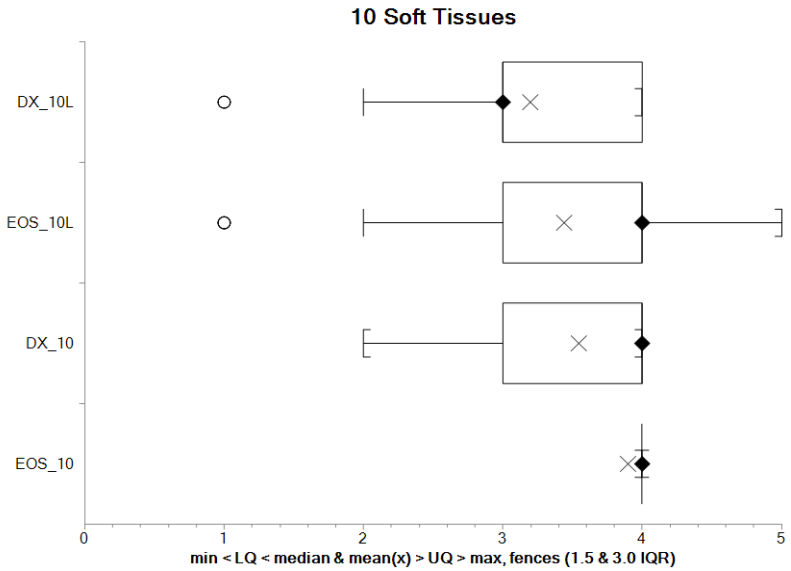

Figure 84: Quality Criteria 10: Soft Tissues. Vascular Pattern. Box and whisker plot.

EOS and DX results for Posterior-anterior (_nn) and lateral (_nnL) projections

EOS lateral views had statistically significant higher median scores

4.4.10.2 Quality Criteria 10: Soft Tissues. Significance of the difference of Medians

Quality Criteria 10: Soft Tissues. EOS - DX scores (PA & Lateral)					
Projection view	**Median difference**	**95% CI**	**P values**		
			Lower side	**Upper side**	**Two sided**
PA-AP	**0.5**	0 to 0.5	0.5075	0.4026	0.8052
Lat	**0**	0 to 0.5	>0.9999	**< 0.0001**	**0.0001**

Table 88. Quality Criteria 10: Soft Tissues: PA and Lat.
Wilcoxon's signed ranks tests.

There is no statistically significant difference of medians. A small difference can be detected for the 95% confidence interval in lateral view can be detected for EOS.

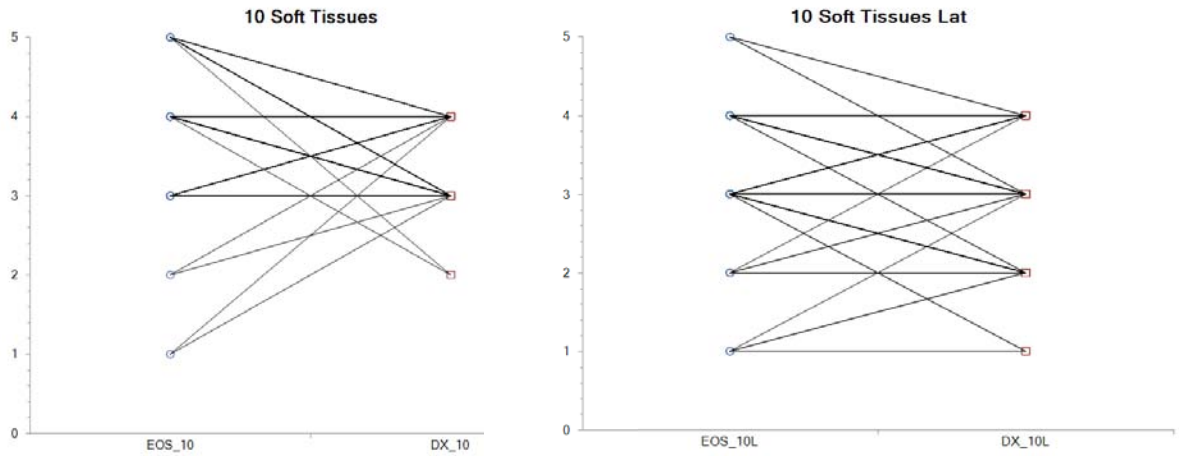

Figure 85. Quality Criteria 10: Soft Tissues. Ladder Plots PA and lateral
EOS and DX results for Posterior-anterior (_nn) and lateral (_nnL) projections

Ladder plots show a little advantage of EOS over DX scores

4.4.10.3 Quality Criteria 10: Soft Tissues. Independence Test

Quality Criteria 10: Soft Tissues. EOS vs. DX correlation Kendall's Tau_b					
Projection view	**r_τ (Tau_b)**	**95% CI**	**Approximate tests (adjusted for ties)**		
			Lower side	**Upper side**	**Two sided**
PA-AP	**-0.032292**	0.1686 to 0.3269	0.3414	0.6585	0.6831
Lat	**0.503365**	0.4269 to 0.5798	0.9999	**< 0.0001**	**< 0.0001**

Table 89. Quality Criteria 10: Soft Tissues. EOS vs DX correlation
(Kendall's correlation).

A positive correlation was present between both lateral projections.

4.4.10.4 Quality Criteria 10: Soft Tissues. Interobserver Agreement (Universal R)

Quality Criteria 10: Soft Tissues. Interobserver Universal Agreement R		
Projection	**R**	**P value**
AP EOS	0.108331	0.0021
PA DX	-0.01605	0,2224
Lat EOS	0,018087	0.2224
Lat DX	-0,00995	0,671

Table 90. Quality Criteria 10: Soft Tissues. EOS and DX
Interobserver Agreement Universal R

A poor statistically significant Interobserver agreement was present only for EOS AP view. The other three grups ob observation displayed no agreement with very low scores..

4.5 Imaging findings

Several typical imaging obtained from the subjects of experimental EOS are presented as samples to show the relevant image findings presented in the statistical analysis. A few examples of the image quality group with serendipitous findings (see table 21) are also shown

4.5.1.1 EOS Images and Findings

EOS images look 'different' than common projection radiography images: the thorax has an unusual thinner shape, and the EOS wider latitude allows displaying densities from the soft tissues to the spine behind the mediastinum.

The shape of the thorax in EOS corresponds to the real size without geometric distortion: EOS images have real size 1:1 square pixels. The original vertical scan plane is perpendicular, orthogonal to the spine without any magnification, and the transverse diameter that had the geometric magnification caused by the fan-shaped x-ray beam has been corrected. Vertebral bodies look 'squared' and the intervertebral disk spaces are parallel to the beam. In normally acquired chest x-ray, magnification and deformation is present and uncorrected in both planes by a conic projection, but this is seen as the 'normal' shape for every radiologist. Magnification correction is calculated for an average position and size of a patient, with a minification corrective factor. Thin patients, or those positioned backwards, with less geometric magnifications as they are closer to the detector, may result with in relatively inferior transverse diameters than obese patients. This thin shaped thorax can be seen as in figures 86 and 87 of the same patient. As EOS has a wide latitude, fat soft tissues planes and their interfaces are better depicted, mediastinal and the density of thick and dense areas, as diaphragmatic domes, does not hide posterior structures.

Figures 88 to 91 illustrate the most relevant features and differences observed on the EOS vs DX image quality analysis.

The shape and width of the DX and EOS histograms (figure 92) describes visually fundamentals about latitude, postprocessing and noise suppression.

Figure 93 depicts the lack of motion blur in a fast moving object as a hearth valve in EOS. This is related to the short line scan time in EOS:

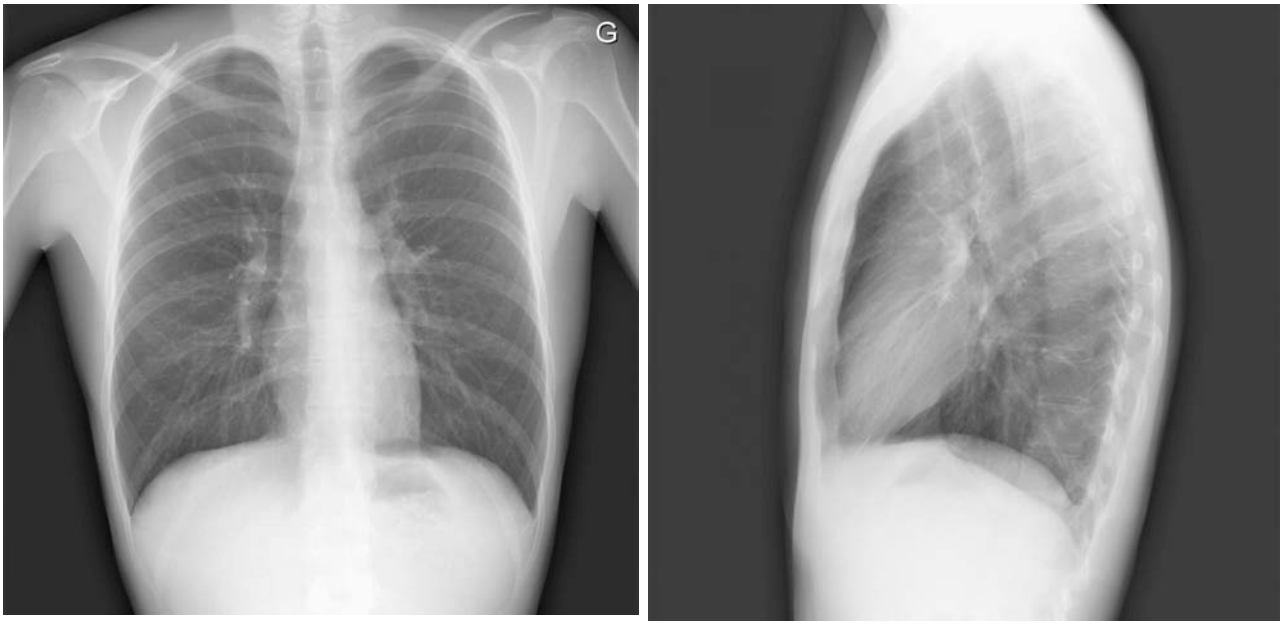

Figure 86. 19-year-old. Female Digital Radiography (DR).

- This is the usual shape of the thorax on projection radiography considered the 'normal shape', but has a conical projection deformation. Uncorrected 'normal' radiography
- Collimation / patient position are unretouched. No collimation was applied as in most DX patients.

Figure 87. 19-year-old Female. EOS acquired radiography.

- This is the orthogonal projection of thorax, but its looks unusual. It has a 1:1 projection ratio, with corrected transverse magnification.
- Collimation / patient position are unretouched. Vertical collimation was applied.
- The wider latitude of EOS can be promptly appreciated, and may have been a source of reading bias: the spine is visible in both views, and the diaphragms allow to the see the posterior costophrenic sulcus.
- Patient positioning needs training, as there is no close contact with the detector.

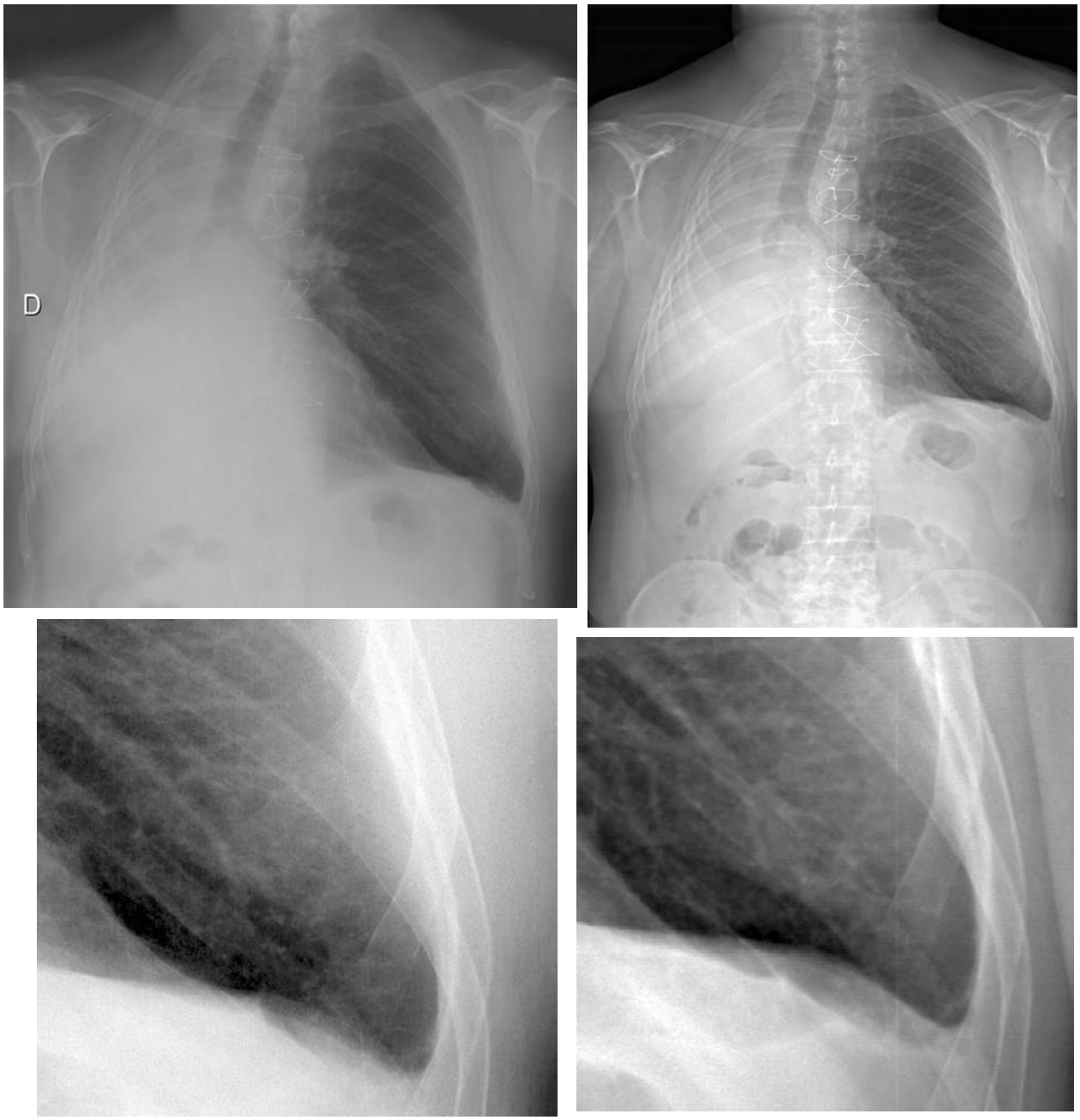

Figure 88. 71-year-old male. Right pneumonectomy. Left: DR; Right: EOS image

- EOS shows structures behind de diaphragmatic domes and mediastinum.
- The trachea and the main right cut-off bronchus are better seen by EOS.
- At the left base, peripheral Interstitial structures are better depicted by DX.
- Bone margins are well seen by both modalities
- Dense foreign bodies, steel sternotomy sutures, are better seen by EOS
- The inferior limit of the examination area has been set too low in EOS, up to L5

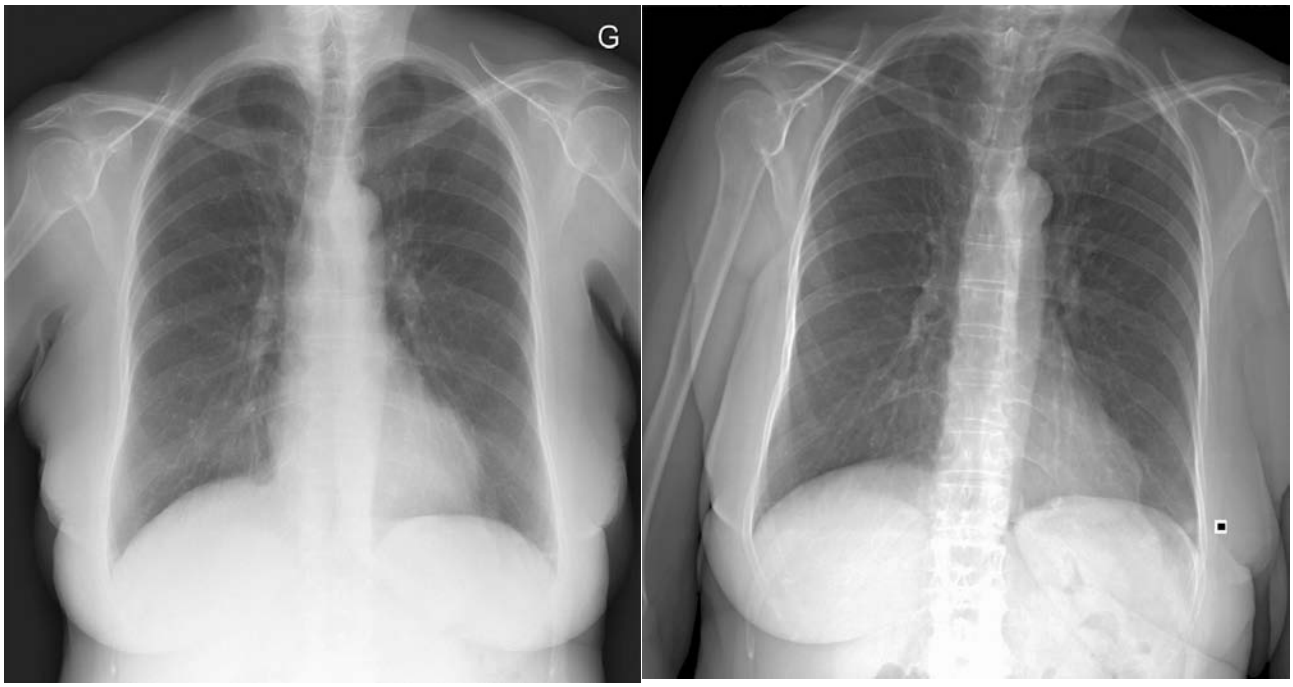

Figure 89.75-year-old female. Lung metastases. Left: DR image. Right: EOS image.

- A small nodule (< 10 mm.) is present at the left costophrenic angle.
- It can be better identified by EOS (Dot marker in EOS).
- The patient position is slightly bent to the left, only in EOS, so it's not a real scoliotic curve. In the EOS prototype the patients had no contact with the detector or other support, standing in the center of the gantry.

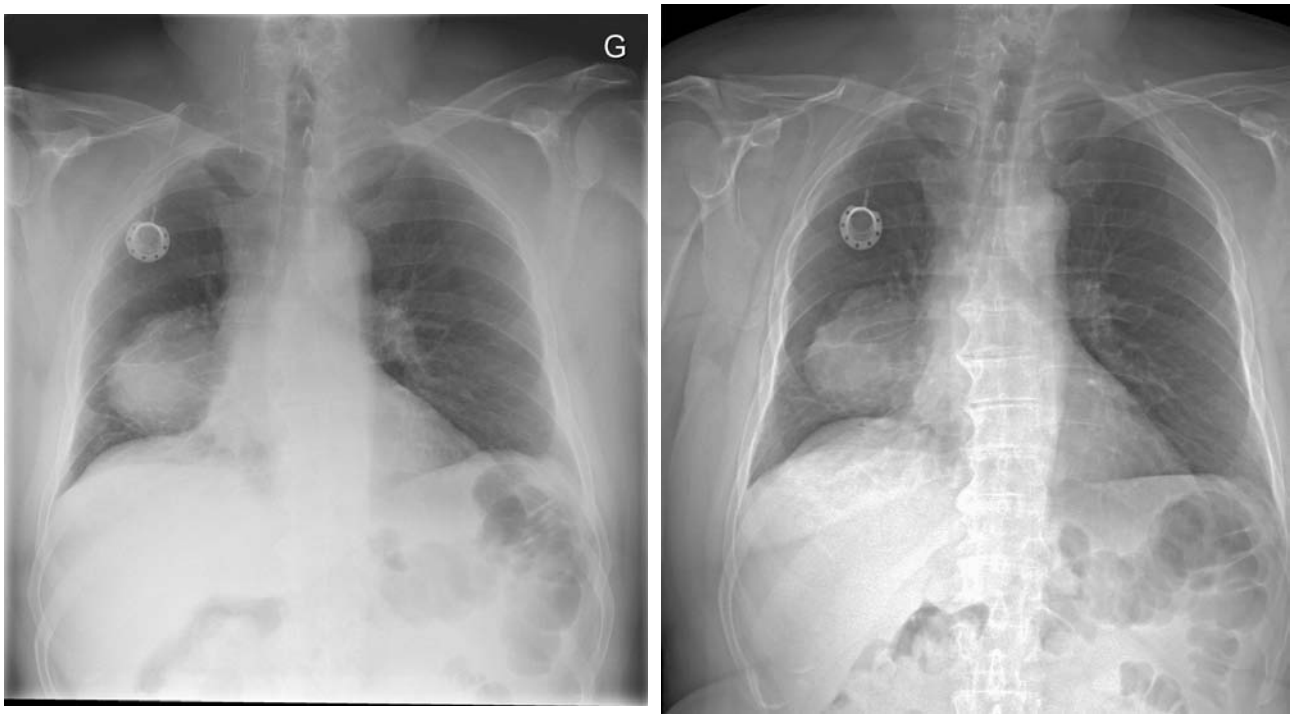

Figure 90.58-year-old male. Lung carcinoma. Left: DR and Right: EOS image.

- A large nodule, fissures and fine linear pleural images or discoid atelectasis can be seen by both modalities.
- The fine interstitial texture at the left lower lobe is best seen by DR
- The venous catheter is better depicted by EOS than by DR

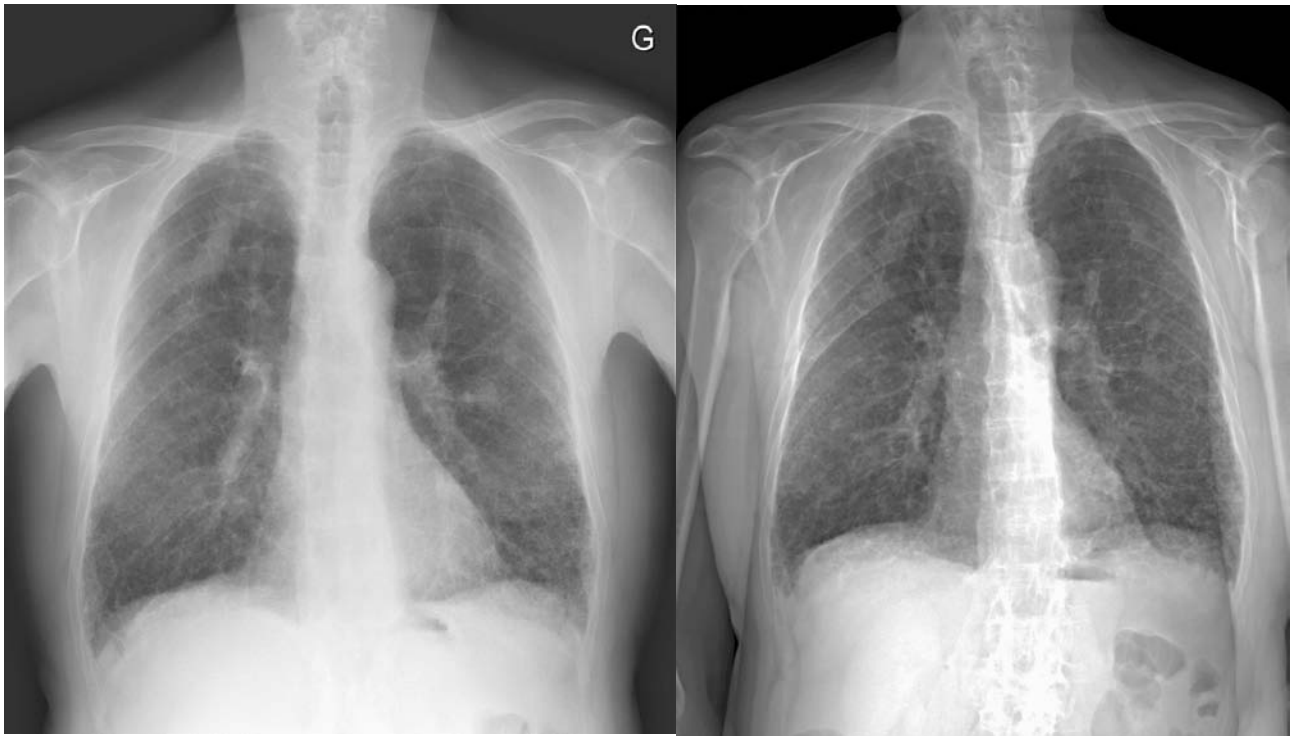

Figure 91.69-year-old Female. Interstitial lung disease. Left: DR ; Right: EOS image.

- The diffuse interstitial fine pattern and nodules is better demonstrated by DX).

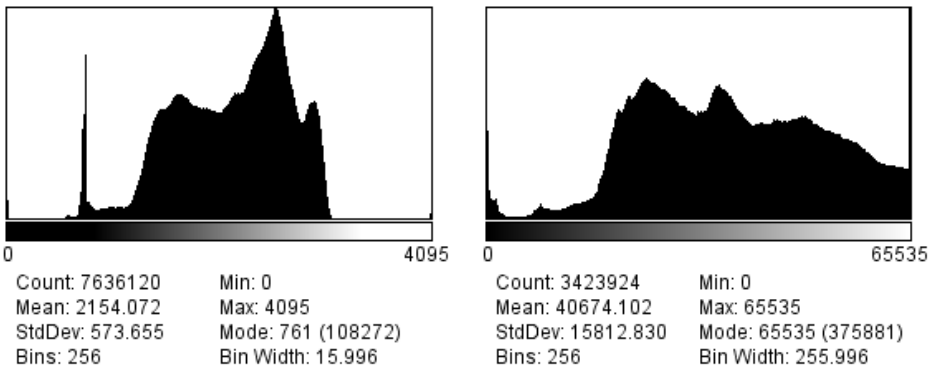

Figure 92. Typical histograms for DX (left) and EOS (right) images

- DX has several filters applied, enhancing resolution and suppressing noise
- EOS has its full 65535 values while DR 4095 has a cut-off in gray-levels

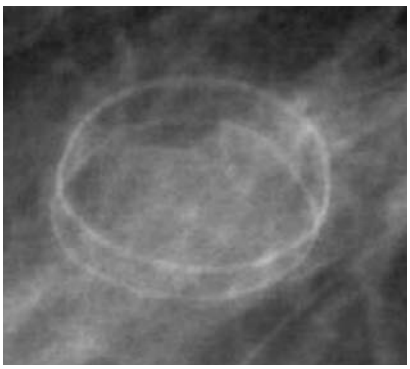

Figure 93. EOS lateral view. Mitral valve prosthesis

- A subtle wavy pattern can be noticed along the twin contours of the valve ring, caused by the line delay, and cardiac movement along the time of the EOS linear scan. It distorts the valve less than expected.
- The two mobile discs are not imaged as they were by DR

5 Discussion

5.1 Clinical feasibility

The EOS prototype has been able to used in a clinical environment, generating good quality images, and fulfilling European Quality Guidelines for chest radiography, and complying with adult reference doses. In the current study.(310,383,384,390,391)

Few examinations were repeated after incorrect centering. This is caused because the patient is not in contact with a detector surface as in planar radiography but standing (or seating) in the middle of an open vertical gantry. In two patient scan span was set too short and required a new acquisition The EOS repeat rate was 13.5%, but concentrating most incidences in the first half of the experimental period, so centering issues were reduced in cooperative adult patient Reported repeat rates for digital modalities are up to 13.3% for installed DR systems (392) No motion artifacts were detected in EOS chest exams, as has been reported in other EOS settings. (46)

The acquisitions were performed in AP view, because it was the standard position for spine acquisition and because it was may allow better communication with the patients, but this position results in up to 8 times higher radiation dose to the breasts and up 4 times higher radiation dose to the thyroid. It is feasible to place the patient in PA rather than AP in EOS examinations as this has proved that does not compromise image quality,.(349)

5.2 EOS Dose

Assessment was performed following CEC quality criteria of diagnostic radiographic images and patient exposure trial (393). On the 18 TLD measures done during DR and EOS exam for the frontal and lateral views quality collected data was insufficient. Only 2 PA and 12 lateral DX examination TLDs had collected evaluable doses. The rest had doses below the minimal evaluable measurement threshold. Thus, we had too few TLD values of the frontal views to provide significant results. However, lateral TLD measurements are shown in the results table below to give an idea of the dose ratio between the two modalities. The number of final analyzable TLD measurements was insufficient to provide a good analysis of the dosimetric ratio between the two modalities with this method. However, the calculation of the kerma free in air (entrance dose without backscatter) for the both modalities allows us to compare them for the two incidences.

Concerning the front view, the mean dose received at the entrance of the patient was 4.5

times superior when the EOS system was used than when the DR system was used. For the lateral view this mean ratio was 1.8. The entrance dose was significantly superior with the EOS device for the two incidences. This can be explained by the fact that acquisition parameters were set automatically on the EOS device according to 3 main morphotypes, whereas for the DR device an automatic cell managed the necessary dose for each case. So the dose received during the DR exam was the minimal dose needed to obtain a correct radiograph according to the settings of the automatic cell. For the EOS device this optimization was not implemented yet, and it is possible that the acquisition parameters set was over what they should have been to obtain an equivalent image quality.

The table below compares the values found from the two modalities evaluated with the EC diagnostic reference levels for chest imaging defined from the third quartile of European surveys. A supplement of approximately 30% should be added to the entrance doses (free in air) calculated in our study compared with the entrance surface doses which take into account the backscattering.

	EOS		**DR**		**EC**
Doses in mGy	**Mean Entrance Dose free in air**	**Entrance Surface Dose**	**Mean Entrance Dose free in air**	**Entrance Surface Dose**	**Reference Dose (mGy)**
Front view	**0.22** (min= 0.16 – max=0.35)	**0.29** (min= 0.21 – max=0.45)	**0.05** (min= 0.02 – max= 0.14)	**0.07** (min= 0.03 – max=0.18)	**0.3**
Lateral View	**0.31** (min= 0.18 – max= 0.41)	**0.40** (min= 0.23 – max=0.53)	**0.17** (min= 0.05 – max= 0.77)	**0.22** (min= 0.07 – max=1)	**1.5**

Table 91: Measured doses with EOS, DX, and EC reference entrance doses

Once this comparison to the EC reference level done, we can estimate that the entrance dose obtained for EOS the lateral view was at less 3 time lower than the EC reference level. However, considering the frontal view the EOS entrance surface dose was much to the reference level dose. This dose is in the range of current EOS spine dose. (344)

The EOS prototype was engaged in a continuous development. Further assessment on the same EOS prototype performed in Montreal already found a lower ESD of 0.09 mGy per view (330)

Current reported EOS spine doses are 0.069 mSv for the PA projection and 0.1, with an air kerma of 0.18 and 0.33 mGy for PA and lateral views. (349)

Dose Reference Levels (DRL) are recommendations taken from the value of the third quartile of a European dose study, but they nowadays fall over the operative doses of all

normally operated current systems.(394)Additional DRL standard are required for pediatric patients, differentiating the segments of age/body size (395). Prematures are a special subgroup subject to repeated studies at neonatal intensive care units (NICU). As it happens in any x-ray exam broad intercentre differences are present also for chest examinations. (383,396–398)

5.3 Detector Performance

5.3.1 Collimation. EOS Dose utilization factor. EOS Tube tilting

Horizontal collimation is fixed in the EOS prototype bearing to a large exposure area. Nevertheless, vertical collimation has been better in the EOS than in the DR group. In the DR group most patients were done without collimation adjustment: The horizontal field size for DR was less than EOS not by active collimation but for the physical detector size (43:45 cm).

Poor horizontal collimation is not a real problem for a slot scan device as EOS; behaving differently of full-field radiography systems it has much less scatter radiation. In EOS, the beam is orthogonal to the detector in the vertical and should adjusted to cover the exit skin contacting the detector, while its horizontal plane is conic segment. In opposition, DR is a full-field system where the conic x-ray beam irradiates a somewhat smaller entry skin area but opens the cone towards the detector. This may justify part of the over-coverage, but it has systematic, in the vast majority of cases, and should be attributed to the poor exam procedure. Poor collimation is a common problem in radiography conveying unnecessary exposure out off the area under examination, adding unnecessary exposure, increasing blur, and reducing image quality. (399–401)

The system performance is based on the spatial resolution, the dose utilization factor and the detected dose. A narrow detector collimator (Cd) results in a better spatial resolution, but lowering of the dose utilization factor and consequently of the detected dose. The detected dose will be in proportion to the object collimator opening Co. Besides, it will depend on the angle function F (angle), relating the x-ray photon flux to the direction of emission. Detected intensity is a function of tube angle and object and detector collimator opening configurations.

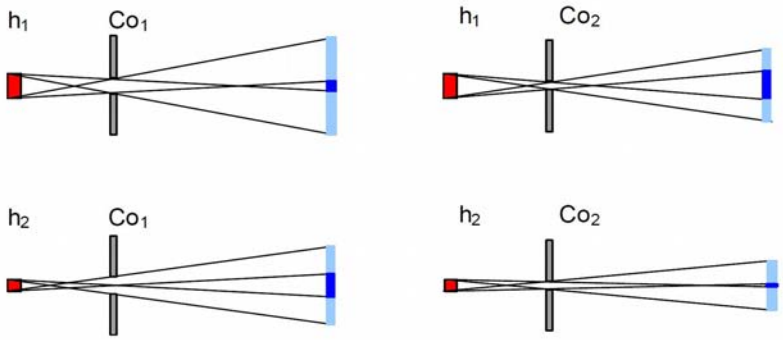

Figure 94: Effect of reducing the focus size and fore collimation gap.
The combination of a small focal spot with a narrow collimation gap generates less undesired penumbra.

To minimize the ripple in EOS and prevent already known alignment and vibration problems, the collimation at the exit of the x-ray tube is set to produce a larger illumination area than the actual detector slit width. Unfortunately, this has a dramatic effect on the DQE since a relatively large portion of photons contribute to the dose without participating in image formation. (330,331)

Anode heel effect is a consequence of the angled anode surface facing the output window. The X-beam is inhomogeneous along the anode surface, being attenuated by the anode material itself. The x-ray beam is less intense in the anode side than at the cathode side. The range of intensity depends on the manufacture but for normal medical applications can be less than between 85 to 104%, and can be noticed while making use of lateral portions of the X-ray beam in full field radiography, when collimators are full open. This asymmetry may be applied when body thickness is of different thickness along the field, as in lumbar spine imaging, where the image should be done with the cathode side oriented to the more think lumbar area. The opposite should be done for full-length lower limbs' radiography, where the thick part is the upper side of the legs. In small images, or collimated beams, the heel effect is less noticeable.(10,14,402–404)

EOS needs a high output X-ray tube, high thermal capacity, but needs a small focal size. This apparent reduced focus size may be achieved by a small negative tilting of the x-ray tube (towards the anode side), but it may compromise x-ray output as described. The apparent size of the focal spot is a function of the tube tilting as follows:

$$h = \sin(\varphi - \alpha)/\sin(\varphi) * [0°\text{focal spot size}]$$

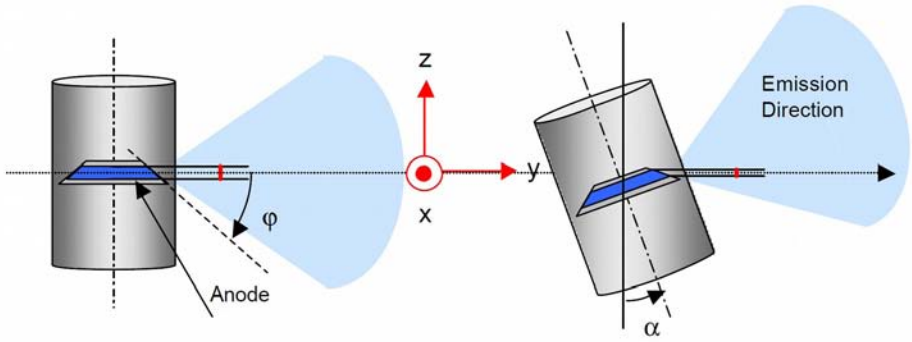

Figure 95: Effect of X-ray tube tilting on focal spot size

The negative tilting reduces the focal spot, but the heel effect makes that the x-ray output has less intensity linked to the degree of tilting and the absorption of some of the x-ray photons by the anode target itself.

Several test were done by the EOS team, with a final focal spot size and collimation providing the best balance on the largest fraction of the usable dose.

Table. Collimation and tilting configurations						
Config.	**Angle**	**Co**	**Cd**	**Fraction of useful dose**	**Detected intensity**	**Quality factor (UA)**
(1)	***5.0 °***	***500 µm***	***500 µm***	34.7%	0.75	0.26
(2)	6.5 °	250 µm	500 µm	57.1%	0.45	0.25
(3)	7.0 °	250 µm	250 µm	33.3%	0.23	0.08

Table 92. Collimation and x-ray tube tilting configurations: 5º with 500 µm selected.

Configuration with narrow detector collimator opening (250 µm) looks very beneficial as regards spatial resolution but remains the least effective as regards the dose utilization factor and above all the detected intensity. Configurations tested and selected are presented in the Table 92. Experimentation demonstrated that the 250 µm object collimator opening (2 and 3 test configurations) makes x-rays detection highly sensitive to minor focus deviations on the anode track, resulting in low quality radiological images.

The research done later on this same EOS prototype in Montreal (CA) showed worst performance of the detector, that was attributed to beam misalignment between the focus, collimators, and detector. These problems were already observed along the experimental phase, after the EOS prototype was disassembled in Paris, transported to Brussels and reassembled to run spine and chest experiments. The re-calibration procedure was prolonged, generating a project delay that even forced to cancel the already scheduled additional transportation and experimentation in Barcelona. The transportation and reassem-

bling of the prototype in Montreal may well have contributed to additional misalignment. The effective spatial resolution was found in Montreal to be 1.5 lp/mm at 20%. and 1 lp/mm at 40%, less than was tested in the original installation in Paris. Simulations have also confirmed that resolution in the scan direction could be greatly improved by using a tighter collimation, that will require a X.ray tube capable of higher load. (331)

The presence or absence of noise can be traced visually as graininess in homogeneous areas as adipose soft tissues or air background. It can also be described by variability of density values in otherwise uniform black/air areas of the image. Noise can suppressed by image filtering. In the EOS prototype no post-processing was applied for noise suppression. In addition, edge enhancement filters may have been applied contributing to improve the perceived spatial resolution. The effect of noise suppression can be seen in figure 96.

The DR modality, as all commercial imaging systems, has several proprietary image processing automatic methods automatically applied to all images, that clean noise and enhance borders.The comparative images presented in figure 96.shows the degree of noise that can be suppressed in a DR flat panel. (75)

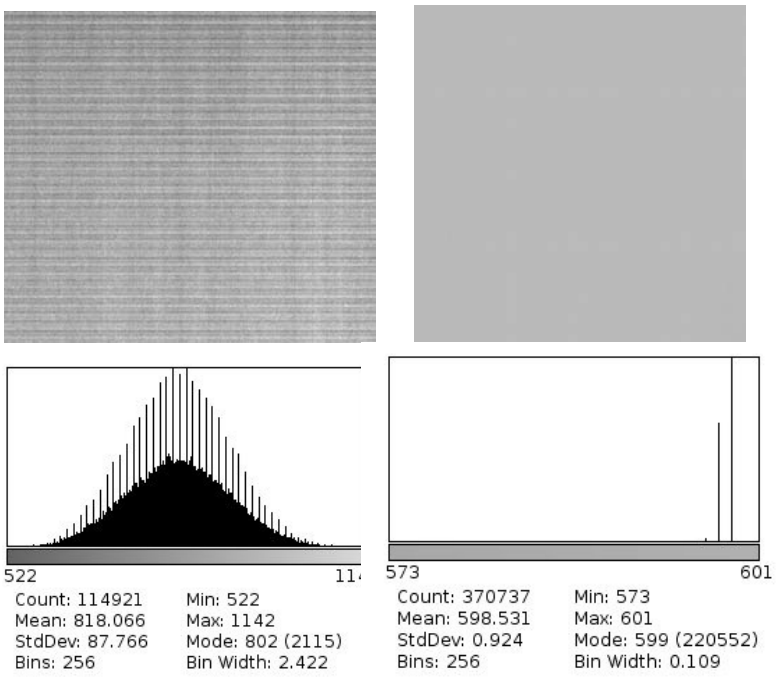

Figure 96. Background 'black' image and their histograms for EOS and DX.
Left) EOS image shows a normally distributed of noise: 10,7%. horizontal ripple lines and vertical channel noise can be noticed.
Right) DX image hasn't significant noise. < 2% level

EOS has undergone several improvements since the prototype trial period, and its dose

efficiency has improved, with its effective resolution is brought down to 193 µm by 185 µm for the frontal view and to 179 µm by 185 µm in the lateral view. The dynamic range has been reduce by a half to over 30,000. (285,330,331,344,348)

5.4 Image quality assessment

The methodology used was similar to other contemporary studies (234,405), Based on European guidelines in image quality (310,383,393) and CE criteria (384,393). Visual grading studies are considered as solid as free-response forced error (FFE) experiments. FFE and ROC analysis are methods suited to compare known lesions resolution between different imaging methods. (75,406–408)

An abstract of image quality results comparing both modalities is presented in table 93

- EOS has higher scores in 14 of 20 scores, where 7 are statistically significant
- DX has higher scores in 6 of 20 scores, where 2 are statistically significant

Quality Criteria : Aggregated Results							
	Median/95% CI		**Correlation**		**Agreement**		
Scored Item	**AP**	**LAT**	**AP**	**LAT**	**AP**	**LAT**	
1 Inspiration	EOS	**EOS**	yes	yes	poor	poor	
2 Rotation	DX	DX	yes	yes	-	poor	
3 Anatomic coverage	EOS	**EOS**	yes	-	poor	poor	
4 Vascular pattern	EOS	DX	yes	yes	-	poor	
5 Fine interstitial	DX	**EOS**	yes	yes	-	poor	
6 Fissures	**DX**	EOS	yes	yes	fair	poor	
7 Trachea and bronchi	**EOS**	**EOS**	yes	yes	fair	fair	
8 Spine and mediastinum	EOS	EOS	yes	yes	poor	poor	
9 Mediastinum	**EOS**	**EOS**	yes	yes	fair	poor	
10 Soft Tissues	EOS	**DX**	-	yes	poor	-	

Table 93. Aggregated Image Quality Results. Best scores
EOS and DX, significant results for Posterior-anterior (PA) and lateral (L) projections.
Bold text marks statistically significant results.

EOS account for an advantage in positive scores, but detected differences are very small, with confidence intervals for differences of medians of 0, and with 95% confidence intervals from 0 to 0.5. So it can be said that for the both views, image quality proposed by the two devices was approximately equivalent.

5.4.1 Interobserver agreement.

The image quality study considered the assessment of interobserver agreement. Intraob-

server agreement was set out of the scope of the assessment of the EOS prototype as only a reading session per reader was scheduled along the short experimental chest phase. No training session was undergone by the 4 observers, who worked independently in three different hospitals. These two factors that may contributed to the poor overall inter-observer agreement.

A shortcoming of the reading sessions was that Image masking, as hiding large parts of the image by an opaque mask, was not performed. EOS, as happens in other comparative imaging modalities studies, has image characteristics that can be identified as being from a certain origin, so readers may be able to recognize the modality of origin and may have a biased score, as it has been reported by Tingberg. (409) Masking was not feasible in this study, as general aspects of the complete image should be reviewed.

Reading sessions were performed with optimum reading room lighting of approximately 50–80 lux, under a dark room condition (1 lux) but this settings are considered to not affect the reading detection ability. (410) Readers were invited to use any routine workstation tool while reviewing the sets of images (75,408,411–413)

Nevertheless, detected score differences are very small, with confidence intervals for differences of medians of 0 in most scores, and a few of 95% confidence intervals from 0 to 0.5. So it can be said that for the both views, image quality proposed by the two devices was approximately equivalent.

Interobserver agreement was poor as it happens when non-parametric, categorical, image quality scores are assessed. The Universal R agreement behaves as a weighted Kappa when data are at least ordinal as in this study. Interobserver and intraobserver agreement between EOS and radiography results are better when simple parametric data, as angles or pelvic measurements, were assessed (366).

5.5 Conventional Wide Latitude Chest imaging techniques

5.6 Screen-film derived imaging

Screen film was the traditional method of chest imaging but it does not have an adequate dynamic range for representing the density values between the lung parenchima, soft tissues and denser mediastinal or the lung superimposed to dense diaphragmatic domes adequately. Asymmetrical dual speed intensifying screen where the last and best approach by conventional screen-film systems but where replaced by digital modalities, namely CR.

The details of conventional screen-film imaging of the chest, that was the reference technique till the advent of current flat panel detectors, has been described extensively in the literature and will not be discussed specifically in this work. It will be referenced when it accounts to be relevant along the different sections discussing digital modalities. Nevertheless, three less common techniques addressing the challenges of imaging the chest are presented: high kilovoltage, slot imaging, and beam equalization.

5.6.1 High Kilovoltage Techniques

The wide differences on densities between the mediastinum and lung fields have been a challenge for chest radiography. Beam equalization, discussed later, was the most successful approach, but high kilovoltage techniques were also used in several recognized imaging centers.

High kilovoltages between 240 kVp and 350 kVp where used 50 years-ago looking for advantages in visualization over conventional radiography techniques, as the visual wide latitude, unattainable at that moment by means of the available screen-films combinations. Using high kVp, chest radiography was improved by more uniform bone visibility that overlapped the lungs, better visualization of soft tissues, areas, better mediastinum penetration and depth resolution, better visual response by a flattened gray-scale (achieving 20:1 light intensities range). Applied to a series of 16000 patients, radiation dose was 1/3 of the 120 standard kVp and the retake rate was lower. The advantages of high kilovoltage where better visualization of pulmonary nodules, airways, interstitial and alveolar disease, and dense areas as infra-diaphragmatic areas, or obese patients. Among the disadvantage were increased quantum mottle, loss of calcium visibility, general loss of bone texture as rib detail, and low visibility of catheters. (414,415)

5.6.2 Slot imaging of the chest

To reduce scatter anti-scatter grids have been used for its advantages of simplicity and effectiveness, but theses grids attenuates a substantial fraction of the primary x-rays by as much as 30– 50%, resulting in a significant loss of information and an increase of relative noise level in the image. Therefore, to compensate for the attenuation of primary x-rays by a grid, the entrance exposure must be increased to preserve the quantum noise level. Slot-scan methods have been an alternative by using a collimated narrow fan beam to scan the patient. Research has shown that when a proper slot width is selected, the image contrast-to-noise ratios (CNRs) from the slot-scan technique are better than those from conventional full-field radiography with an anti-scatter grid. The second issue that has been long recognized is that low x-ray photon flux in heavily attenuating regions results in

a poorer image signal-to-noise ratio (SNR), leading to degraded visualization of low-contrast objects. The technical limitation in conventional chest radiography arises from the wide variation in patient thickness between various body parts, while exposures are routinely made to optimize the contrast in the lung areas. This leads to the exposures in areas such as retrocardium, mediastinum and subdiaphragmatic areas falling outside the useful exposure range for conventional SF radiography (31,51,416–420)

This approach is what the analyzed EOS device is applying, but using a narrower collimation than in any previous modality (0.5 mm).

5.6.3 AMBER

AMBER was a scanning slit chest device manufactured by Kodak in Oldelft, Netherlands that solved several of the issues of dose and image resolution by sequentially scanning the chest by a quickly equalized X-ray beam. Equalization was achieved by a linear array of ionization chambers behind the patient that modulate the x-ray exposure along the full chest acquisition. Their typical working parameters were 117 kVp and 280 mAs for PA examinations and 140 kVp for lateral examinations, with an entrance skin dose by TLD of 0.16 mSv (0.088 to 0.260 mSv), (231).

AMBER was found to give the best image quality followed by computed radiography and conventional film-screen radiography (421,231,422–424)

This technology vanished by 1997 (last FDA application form) when the progress of computed radiography and DR flat panels in addition to the requirement of digital images for PACS. Olfel-Digidelca started manufacturing CCD -slot based s-ray systems in 1998: Digidelca-C and Digidelca-M, that finally became Thorascan, a linear CCD scanning described later.

5.7 Chest Digital Imaging Modalities

5.7.1 Computed radiography

Computed radiography, storage phosphor imaging, is still the most used digital radiography technology. Delivering resolutions between 2,5 to 5 lp/mm it allows the practice of chest x-ray examinations in any x-ray device originally manufactured for legacy screen-film cassettes. Conventional radiology has been replaced in developed countries by digital radiology modalities, more frequently by CR it is able to provide equivalent or better image quality. (215,239,217,425,426,249,250)

Image quality studies have proven image quality equal or better to asymmetrical screen-

film systems that were considered superior to standard screen-film combinations

Comparative dose evaluation studies shows that the EOS scanner delivers 6 to 9 times less entrance dose than a CR system when applied to comparative full spine studies. (344). A study reported a mean entrance surface radiation dose for the postero-anterior spine and lateral spine acquisitions of 0.23 and 0.37 mGy, respectively, with EOS, compared with 1.2 and 2.3 mGy, respectively, for CR, resulting in a 5- to 6-fold reduction of radiation dose. (347)

Comparative dose studies between EOS and CR in chest applications are not available.

While storage phosphors introduced approximately twenty-five years ago is still widely used, it is being replaced by flat panel systems in most hospital applications in western countries as DR is able to provide better quality, less dose and high thoughput. (425,427–431)

5.7.2 Digital Radiography

Digital radiography (DR) refers nowadays almost exclusively to amorphous-silicon flat-panel detectors, as selenium detectors have a marginal market penetration in spite of they feature several physical advantages. DR flat-panel are manufactured with pixel pitches ranging from 70 to 200 µm, with resolutions of 150-100 µm for general or chest applications (4-5 lp/mm), and with mammography applications using the lower end of this range. DR has a high detective quantum efficiency of approximately 65% that exceeds that of screen-film (24%) and storage phosphor systems (35%, 21% for HR systems). (71,251,275,432)

In terms of dose and image quality on digital amorphous-silicon flat-panel detector for routine chest radiography, at the Ghent University (BE) with the same device model (Siemens Thorax FD), the doses were lower for the flat-panel system than the conventional system in both views. For the PA, the ESD was 66.8 µGy versus 199.0 µGy. For the lateral view, the skin dose was 346.7 µGy for the flat-panel system (aSi+CsI) and 1,286 µGy on the Thoramat (Selenium) unit (234,405). Another group at University of Heidelberg (DE) reach the conclusion that dose measurements with a chest phantom also showed a dose reduction of approximately 50% with the digital radiography system compared with the film-screen radiography system. The image quality and the visibility of all but one anatomic structure of the images obtained with the digital flat-panel detector system were rated significantly superior (377) Dose reductions with the same flat panel where also reported by a research done the University Hospital in Regensburg (DE) (375)

The main departmental advantages of DR are its high throughput, as cassette and film handling are absent, and high reliability as they lack moving parts. DR detectors have better resolution than CR, and its linear response is better at low dose than both CR or selenium detectors. The flat-panel detector has diagnostic performance superior to that of conventional screen-film and storage-phosphor radiography also in skeletal applications for detecting small artificial bone lesions at standard or reduced exposure settings, thus It allows reducing exposure by 50% but obtaining diagnostic results comparable to conventional speed class 400 screen-film systems. The image quality of CR is similar to that of DR only at high dose levels; Image quality of DR proved to be superior to CR, in particular for low contrast details and if dose is reduced. The image quality and visibility of anatomic structures on the images obtained by the flat-panel detector system were perceived as equal or superior to the images from conventional film-screen chest radiography. (232,234,379,405,433–436)

Comparative dose studies between EOS and DR in chest applications are not available. Few comparisons are available between DX and EOS devices in other. Full-length lower limb radiographs and whole spine radiographs of a standard digital radiography system were compared with radiographs of a biplanar X-ray system by Dietrich (2013); The standard digital radiography system has the same detector than in this work. Dose for EOS was the 40% of the dose delivered by the DR system (158.4±103.8 cGy*cm^2 vs. 392.2±231.7 cGy*cm^2), and the examination time for 2 views of the spine was significantly shorter (-30%). (437)

For clinical radiology practice, it is important the examination time as it may limit the throughput of any examination room; the median time of examination of the chest was 18 minutes, 8 minutes and 6 minutes for conventional S/F radiography, CR and DR respectively. This reduction ratio happens in most anatomic regions with few variations: the median time of examination for ankle radiographs were 22 minutes, 7 minutes and 5 minutes for conventional S/F, CR and DR respectively. An additional 30% time can be saved by integrating the radiology information system (RIS), PACS with the worklist at the modality. (221,248,392,438,439)

Images the digital selenium chest system provides better visualization of most anatomic structures than the phosphor system. Lateral images show an almost equal preference. Digital radiography (DR) based on a flat-panel detector technology is progressively replacing conventional screen-film system and computed Radiography radiographic (CR).

Reasons for that are the continuously improved detective or dose efficiency of the detector

systems and an improved image processing. The new direct detector systems have the largest potential for dose reduction while storage phosphor and selenium radiographs are usually obtained with a dose comparable to that of a 400 speed system.

The diagnostic performance of the new large-area silicon flat-panel detector is equivalent or superior to that of the conventional screen-film system for clinical chest imaging and can replace conventional radiography systems. This new technology offers transmission and storage possibilities inherent to digital radiology that would facilitate daily practice and reduce the initial high costs in the long-term.

The introduction of digital flat-panel radiography systems based on amorphous silicon and cesium iodide have been an important step forward in chest imaging that offers improved image quality combined with a significant reduction in the patient radiation dose.

Nevertheless, DX detector presents a narrow range of densities, not only respect the 65500 gray-levels of EOS, but by the design of the Trixell 4600 detectors with 16000 gray-levels. It may be theorized that is being done as noise suppression.

Considering its advantages in image quality, dose, and clinical performance, DR systems are considered the gold standard for radiographic exams.

5.7.3 Linear CCD scanning - Thorascan

This modality is the evolution of the electromechanical slot-devices manufactured by Delf-Kodak described previously. It is manufactured since 2000, by Nucletron-Delf Imaging, but the first unit was not installed until 2002 at the Bronovo Hospital (The Hague, the Netherlands). The technology is based in slot x-ray scanning. A 10 mm-thick fan-shaped x-ray beam performs a linear scan of the chest, mechanically paired with a linear detector, an array of 8 CCDs. The detector has a thallium-doped cesium iodide scintillator with a thickness of 0.5 mm used to convert the x-ray image into visible light with fiber-optic coupling. The system delivers a resolution of 162x162 µm, 2736x2736 pixels, over an area of 44x44 cm, with a modulation transfer function (MTF) at 15%, 3.2 line pairs/mm, and detective quantum efficiency (DQE) of 60%. It provides a high-resolution mode 162x81 µm, with a MTF at 5% and 5 line pairs/mm. The local exposure time is of 20 msec avoiding movement blur. The system requires two x-ray expositions, a downward pre-scan where the detector measures the transmission through the chest, and an upward actual acquisition that lasts 1.2 sec. The system provided a comparable performance and visibility index to other contemporary digital systems but with a higher dose (Thorascan 8 to 9.8 mGy (133 kVp), Siemens FD 3.2 mGy, GE Xqi: 6.2 mGy, and Agfa CR: 6.8 mGy). (55,44,440,425)

As in the case of EOS, the system does not require a grid. When compared to a full filed x-ray system with a high efficiency grid, the scatter fractions with the slot detector is reduced from 70%-80% at the level of the mediastinum to 30%-40%, and in the lung fields from 40%-45% to 13%. The scatter in the full-field system may reach 86%-91% at the denser mediastinal or subdiaphragmatic areas. So, the reduction of scatter with the slot system was between the 47% and 57% at 120kVp. The anti-scatter grid is a 13:1, focused at 180 cm, with 78 lines per centimeter of 20 μm lead strips, and aluminum interspace (Mitaya Manufacturing, Tokyo, Japan). The measured dose in this study also showed a small advantage of full field flat panel device in front of the CCD (0.017 mSv vs .028 mSv in PA, 0.038 mSv vs. 0.068 in lateral views. (441)

Another low-dose linear CCD scanning device is Lodox Statscan (Lodox, Sandton, South Africa), initially intended for full body skeletal trauma surveys. The system is a C-arm that slides along the examination stretcher at 138 mm/sec that is also able to perform standing studies in children. The lineal detector is composed for up to 5800 elements of 60μm, that be combined to provide resolutions between 1.6 and 4.1 lp/mm. Chest exams can be completed with 0.26 mGy (72% of the conventional dose), but while the mean digital dose (skeletal) was 0.33 mGy. The system allows full body pediatric studies with 0.061 mGy or 0.039 mGy with added aluminum filtration. These reported dose levels were close to those of the EOS prototype. Recent publications describe further successful applications of Lodox devices in ventriculo-peritoneal shunts follow-up, vascular studies, foreign body assessment, and children tuberculosis screening. (442–446)

5.7.4 Selenium Digital Scan equalization

The Imaging Physics department of the University of Texas have developed a slot scan digital radiography (SEDR) prototype implemented with an commercial amorphous selenium full field flat-panel .as a detector (DirectRay, Hologic, Inc., Newark, DE). The detector is exposed sequentially to narrow fan beam width of 1.61 cm at the image plane, and 0.2 sec per scan line. A computer-controlled scanning fore-collimator system was mounted at the output of the x-ray tube to generate a narrow fan-shape beam (3.58 mm). Several iterations of the design have been done that have tested with phantoms. On of them added modulation requires a pre-scan image acquisition and has modulation only for 7 channel, but they have announced a new prototype with 24 channels. (272,420,447,448)

5.7.5 Other Micromegas Detectors in Medicine

Several multiwire ionization chamber detectors, with similar internal configuration to the EOS Micromegas prototype, both with micro-wires or with printed strips, have been de-

signed for intended applications medical field (54,326,449–45). At least one of these devices has been reported in routine clinical use in chest imaging as a low-dose screening diagnosis tool for tuberculosis screening (450). The miniaturization of the Micromegas concept to the size of integrated CMOS microchips; as the successive generations of multipixel (“Medipix, Timepix and Medipix3”) has opened new lines in radiation, particles and medical research. These small devices have several characteristic for X-ray imaging: energy discrimination, noiseless digital integration (photon counting), high frame rate, high detection efficiency at low energies (5–15kV), being able to respond to a single photon and with a virtually unlimited dynamic range. Medipix3 is being already used in micro-CT devices as MARS, (60-120 kVp, 20-350 μA, helical scan) where it provides submillimeter spatial resolution (110 μm pixel pitch) and spectral resolution for atomic characterization, allowing in vivo images with anatomic and molecular quantification (MARS Bioimaging Ltd, Christchurch, New Zealand). The next step, edgeless microchips that can be tiled together as detector panels without gaps, are already tested. Therefore, the development large full-field radiography gas-based detectors can be foreseen. (314,451–456)

6 Conclusions

6.1 EOS usage in a clinical setting

The system showed a reliable mechanical movement and a linear response over the range of exposures intended to be used in diagnostic imaging. In 4 of 37 cases a lateral cut-off caused by incorrect standing positioning at the center of the examination area; three patients required a repeated acquisition for technical reasons. In all patients, images conveyed the major landmarks and were usable. No blurring or motion artifacts, more susceptible to occur in scanning slit devices, were detected.

6.2 Assessment of Dose delivered to patients

Radiation dose with the EOS prototype, that only had a reduced of fixed exposure settings and was not optimized for chest imaging, conveyed a dose superior to dedicated chest DR flat panel system, with automated exposure (0.22 vs 0.05 mGy for PA; 0.41 vs 0.24 mGy for lateral projection). However, the radiation dose calculated with the EOS device was below to the EC reference level for frontal and lateral chest imaging (0.3 and 1.5 mGy).

6.3 Detector Performance

The measured DQE and MTF (< 1.5 lp/mm) values of the EOS system are lower than the nominal and expected value (2.5 lp/mm), and is less than the nominal and measured values of flat panel digital systems (3-4 lp/mm). The DQE and MTF estimation of large area detectors is often conducted without any antiscatter grid. This leads to performances that are better than those that would be obtained in a clinical context where such a grid is used most of the time. However, EOS' wide latitude (65500 gray-levels), scatter-free acquisition, and derived improved contrast resolution, allows EOS to maintain a comparable performance to DX in image quality scores. The resolution was shown to be dependent on beam quality in the horizontal direction but almost unaffected in the vertical direction. The scanning slit geometry of the EOS system has been a very efficient way to deal with diffused radiation but may lead to other problems. Ripple and quantum noise, tied to a low SNR, are present in EOS images and have not suppressed by image post-processing, as in DX; ripple may be attenuated by controlling vibration resonances and by normalizing each line. Vertical line artifacts require a better control of noisy channels. To improve image quality, the noise level should be reduced to an optimum value.

6.4 Image Quality Assessment

Both modalities are able to comply with European Standards for chest image quality. The overall results in image quality confer to EOS a small, but statistically significant, advantage over DX, even most median values are the same. This advantage appears can be found the mean values and 95% CI of the medians more than in median differences.

EOS outperforms DX in most items (14:6 items), but more in the lateral view. EOS scores with statistically significant results in: Inspiration lateral, anatomic coverage lateral, interstitium lateral, trachea and bronchi in both views, and mediastinum in both views. DX outperforms EOS in fissures postero-anterior, soft issues lateral.

Interobserver agreement has been poor for most scored items reflecting the difficulties of subjective visual quality grading. Nevertheless, the score differences were small and all scores indicated that all images were clinically usable. Correlation between matched pairs was present, suggesting than the poor observed agreement was related to the subjective personal scoring scales of each rater. Further interobserver and intraobserver agreement should be assessed in the future.

Further research will be required to assess the performance and quality assessment if new optimized dose parameters were applied.

6.5 A preliminary assessment of pathologies

In the reduced set of patients with known lung pathologies, EOS has been able to render representative sample of chest lesions as pulmonary masses, alveolar densities, thin linear densities, interstitial disease, thickened septa, pleural lines, normal or thickened fissures, or lung metastatic nodules, with morphology and detail comparable to those provided by the state-of the-art DX system.

Further investigation should be done to verify the diagnostic performance of EOS in the diagnostic of chest diseases.

This initial study on the EOS prototype concludes that this imaging modality, originally intended for low-dose skeletal imaging, complies the minimum requirements and has the potential to include in its applications chest x-ray imaging. Nevertheless, additional dose reduction is required to compete with current dose levels of flat panels detectors. This improved EOS device with better MTF and lower dose will require further assessment.

7 Bibliography

1. Biospace Instruments S.A., Cyberqual S.R.L., Hôpital Saint-Vincent-de-Paul, Institut Català de la Salut, Sogameca, Université Libre de Bruxelles. EOS Project - G6RD-CT-2001-00614 - Low dose x-ray diagnostic imaging: a new modality for planar and three dimensional applications in rheumatology, orthopaedics and chest radiography (EOS) - FP5-GROWTH [Internet]. Paris (F); 2002 Jan. Available from: http://cordis.europa.eu/project/rcn/60155_en.html
2. Charpak G, Bouclier R, Bressani T, Favier J, Zupančič Č. The use of multiwire proportional counters to select and localize charged particles. Nucl Instrum Methods. 1968;62(3):262–8.
3. Charpak G. L'évolution des détecteurs de particules en physique des hautes énergies. J Phys Colloq. 1973;34(C10):C10–73 – C10–82.
4. Kalifa G, Charpak Y, Maccia C, Fery-Lemonnier E, Bloch J, Boussard JM, et al. Evaluation of a new low-dose digital x-ray device: first dosimetric and clinical results in children. Pediatr Radiol. 1998;28(7):557–61.
5. Charpak G. Particle detectors and society. Eur Phys J C - Part Fields. 2004;34(1):77–83.
6. The Nobel Prize in Physics 1992 [Internet]. 2012 [cited 2012 Oct 26]. Available from: http://www.nobelprize.org/nobel_prizes/physics/laureates/1992/index.html
7. Suzuki F, Fukami T, Tsuji A, Takagi K, Matsuda M. Discrepancies of MRI findings between recumbent and upright positions in atlantoaxial lesion. Report of two cases. Eur Spine J. 2008;17(Suppl 2):304–7.
8. Mauch F, Jung C, Huth J, Bauer G. Changes in the lumbar spine of athletes from supine to the true-standing position in magnetic resonance imaging. Spine. 2010;35(9):1002–7.
9. Tarantino U, Fanucci E, Iundusi R, Celi M, Altobelli S, Gasbarra E, et al. Lumbar spine MRI in upright position for diagnosing acute and chronic low back pain: statistical analysis of morphological changes. J Orthop Traumatol Off J Ital Soc Orthop Traumatol. 2013;14(1):15–22.
10. Curry TS, Dowdey JE, Murry RC. Christensen's Introduction to the physics of diagnostic radiology. 3rd ed. Philadelphia: Lea & Febiger; 1984.
11. Wilhelm Conrad Röntgen - Biographical [Internet]. [cited 2015 Oct 28]. Available from: http://www.nobelprize.org/nobel_prizes/physics/laureates/1901/rontgen-bio.html
12. X-Rays — Report of the Surgeon-General United States Navy — Medical Notes. Boston Med Surg J. 1896;134(7):174–8.
13. Greene R. Fleischner Lecture. Imaging the respiratory system in the first few years after discovery of the X-ray: contributions of Francis H. Williams, M.D. Am J Roentgenol. 1992;159(1):1–7.
14. Sprawls P. Physical principles of medical imaging [Internet]. 2nd ed. Gaithersburg (USA): Wolters Kluwer Aspen; 1993 [cited 2015 Oct 10]. Available from: http://www.sprawls.org/ppmi2/
15. Suetens P. Fundamentals of medical imaging. Second Edition. New York, USA: Cambridge University Press; 2002.
16. BIPM - Ionizing Radiation: Measurement units [Internet]. BIPMorg Bur. Int. Poids Mes. [cited 2015 Jul 12]. Available from: http://www.bipm.org/metrology/ionizing-radiation/units.html
17. ISO 4037-1:1996 - X and gamma reference radiation for calibrating dosemeters and doserate meters and for determining their response as a function of photon energy -- Part 1: Radiation characteristics and production methods [Internet]. ISO Intl. Standard Organization; 1996 [cited 2015 Jul 13]. Available from: http://www.iso.org/iso/catalogue_detail.htm?csnumber=20781
18. ISO 4037-4:2004 - X and gamma reference radiation for calibrating dosemeters and doserate meters and for determining their response as a function of photon energy -- Part 4: Calibration of area and personal dosemeters in low energy X reference radiation fields [Internet]. ISO Intl. Standard Organization; 2004 [cited 2015 Jul 13]. Available from: http://www.iso.org/iso/catalogue_detail.htm?csnumber=32192
19. Sechopoulos I, Suryanarayanan S, Vedantham S, D'Orsi C, Karellas A. Computation of the glandular radiation dose in digital tomosynthesis of the breast. Med Phys. 2007;34(1):221–32.

20. Morin LRM, Berroir A. Calculation of x-ray single scattering in diagnostic radiology. Phys Med Biol. 1983;28(7):789.
21. Hajdok G, Yao J, Battista JJ, Cunningham IA. Signal and noise transfer properties of photoelectric interactions in diagnostic x-ray imaging detectors. Med Phys. 2006;33(10):3601–20.
22. Neitzel U, Maack I, Günther-Kohfahl S. Image quality of a digital chest radiography system based on a selenium detector. Med Phys. 1994;21(4):509–16.
23. Liu X, Shaw CC. Rejection and redistribution of scattered radiation in Scan Equalization Digital Radiography (SEDR): simulation with spot images. Med Phys. 2007;34(7):2718–29.
24. Lo WY, Hornof WJ, Zwingenberger AL, Robertson ID. Multiscale Image Processing and Antiscatter Grids in Digital Radiography. Vet Radiol Ultrasound. 2009;50(6):569–76.
25. Barnes GT. Contrast and scatter in x-ray imaging. Radiogr Rev Publ Radiol Soc N Am Inc. 1991;11(2):307–23.
26. Gelfand M. Dosimetry of FDG PET/CT and other molecular imaging applications in pediatric patients. Pediatr Radiol. 2009;39(0):46–56.
27. Bailey DL, Townsend DW, Valk PE, Maisey MN. Positron Emission Tomography [Internet]. 2005 [cited 2009 Nov 29]. Available from: http://dx.doi.org/10.1007/b136169
28. Frush DP, Huda W, editors. From Invisible to Visible— The Science and Practice of X-ray Imaging and Radiation Dose Optimization. 2006 Syllabus Physics: Oak Brokk, IL, EEUUA: RSNA, Radiological Society of North America; 2006.
29. Kanal KM, Krupinski E, Berns EA, Geiser WR, Karellas A, Mainiero MB, et al. ACR–AAPM–SIIM Practice Guideline for Determinants of Image Quality in Digital Mammography. J Digit Imaging. 2013;26(1):10–25.
30. Miettunen R, Korhola O, Savikurki S. The scatter-to-primary ratio as a function of varying X-ray absorption measured by computed radiography. Eur J Radiol. 1991;13(2):156–9.
31. Miettunen RH, Korhola OA. The effect of scatter reduction on the signal-to-noise ratio in computed radiography. Eur J Radiol. 1991;12(3):167–70.
32. Miettunen R, Korhola O, Bondestam S, Standertskjöld-Nordenstam C-G, Lamminen A, Somer K, et al. Combination of multiple pencil-beam imaging to computed storage phosphor radiography: a new method. Eur J Radiol. 1991;12(3):161–6.
33. Don S, MacDougall R, Strauss K, Moore QT, Goske MJ, Cohen M, et al. Image Gently Campaign Back to Basics Initiative: Ten Steps to Help Manage Radiation Dose in Pediatric Digital Radiography. Am J Roentgenol. 2013;200(5):W431–6.
34. Knight SP. A paediatric X-ray exposure chart. J Med Radiat Sci. 2014;61(3):191–201.
35. Willis CE. Strategies for dose reduction in ordinary radiographic examinations using CR and DR. Pediatr Radiol. 2004;34(S3):S196–200.
36. Guo H, Liu W-Y, He X-Y, Zhou X-S, Zeng Q-L, Li B-Y. Optimizing Imaging Quality and Radiation Dose by the Age-Dependent Setting of Tube Voltage in Pediatric Chest Digital Radiography. Korean J Radiol. 2013;14(1):126.
37. Gould RG, Hale J. Control of scattered radiation by air gap techniques: applications to chest radiography. Am J Roentgenol Radium Ther Nucl Med. 1974;122(1):109–18.
38. Sorenson JA, Floch J. Scatter rejection by air gaps: An empirical model. Med Phys. 1985;12(3):308–16.
39. Shah GA, Hassam G, Newman DL. The effectiveness of antiscatter techniques. Radiography. 1996;2(3):191–7.
40. Neitzel U. Grids or air gaps for scatter reduction in digital radiography: A model calculation. Med Phys. 1992;19(2):475–81.
41. Niklason LT, Sorenson JA, Nelson JA. Scattered radiation in chest radiography. Med Phys. 1981;8(5):677–81.
42. Båth M, Sund P, Månsson LG. Evaluation of the imaging properties of two generations of a CCD-based system for digital chest radiography. Med Phys. 2002;29(10):2286–97.
43. Sorenson JA, Nelson JA, Niklason LT, Jacobsen SC. Rotating disk device for slit radiography of the

chest. Radiology. 1980;134(1):227–31.

44. Kroft LJM, Geleijns J, Mertens BJA, Veldkamp WJH, Zonderland HM, de Roos A. Digital Slot-Scan Charge-coupled Device Radiography versus AMBER and Bucky Screen-Film Radiography for Detection of Simulated Nodules and Interstitial Disease in a Chest Phantom. Radiology. 2004;231(1):156–63.
45. Hejazi S, Trauernicht DP. System considerations in CCD-based x-ray imaging for digital chest radiography and digital mammography. Med Phys. 1997;24(2):287–97.
46. Blumer SL, Dinan D, Grissom LE. Benefits and unexpected artifacts of biplanar digital slot-scanning imaging in children. Pediatr Radiol. 2014;44(7):871–82.
47. Barnes GT, Wu X, Sanders PC. Scanning slit chest radiography: a practical and efficient scatter control design. Radiology. 1994;190(2):525–8.
48. Plenkovich D, Kruger RA, Sorenson JA. Electronic scanning-slit fluorography: Design and performance of a prototype unit. Med Phys. 1987;14(1):49–55.
49. Vlasbloem H, Kool LJ. AMBER: a scanning multiple-beam equalization system for chest radiography. Radiology. 1988;169(1):29–34.
50. Veldkamp WJH, Kroft LJM, Mertens BJA, Geleijns J. Digital Slot-Scan Charge-coupled Device Radiography versus AMBER and Bucky Screen-Film Radiography: Comparison of Image Quality in a Phantom Study. Radiology. 2005;235(3):857–66.
51. Barnes GT, Cleare HM, Brezovich IA. Reduction of scatter in diagnostic radiology by means of a scanning multiple slit assembly. Radiology. 1976;120(3):691–4.
52. Shikhaliev PM, Xu T, Le H, Molloi S. Scanning-slit photon counting x-ray imaging system using a microchannel plate detector. Med Phys. 2004;31(5):1061–71.
53. Speidel MA, Wilfley BP, Star-Lack JM, Heanue JA, Lysel MSV. Scanning-beam digital x-ray (SBDX) technology for interventional and diagnostic cardiac angiography. Med Phys. 2006;33(8):2714–27.
54. Babichev EA, Baru SE, Groshev VR, Khabakhpashev AG, Leonov VV, Neustroev VA, et al. The new effective detector for digital scanning radiography. Nucl Instrum Methods Phys Res Sect Accel Spectrometers Detect Assoc Equip. 2003;513(1–2):57–60.
55. Veldkamp WJH, Kroft LJM, Geleijns J. Dose and perceived image quality in chest radiography. Eur J Radiol. 2009;72(2):209–17.
56. Kroft LJM, Veldkamp WJH, Mertens BJA, van Delft J-PA, Geleijns J. Dose reduction in digital chest radiography and perceived image quality. 2007 [cited 2012 Nov 9]; Available from: http://bjr.birjournals.org/content/80/960/984.abstract
57. Samei E, Ranger NT, Dobbins JT, Ravin CE. Effective dose efficiency: an application-specific metric of quality and dose for digital radiography. Phys Med Biol. 2011;56(16):5099–118.
58. Gray J, Taylor K, Hobbs B. Detection accuracy in chest radiography. Am J Roentgenol. 1978;131(2):247–53.
59. Wesenberg RL, Amundson GM. Fluoroscopy in children: low-exposure technology. Radiology. 1984;153(1):243–7.
60. Ranger NT, Samei E, Iii JTD, Ravin CE. Measurement of the detective quantum efficiency in digital detectors consistent with the IEC 62220-1 standard: Practical considerations regarding the choice of filter material. Med Phys. 2005;32(7):2305–11.
61. Overdick M. Detectors for X-ray Imaging and Computed Tomography. Chapter 4. In: Spekowius G, Wendler T, editors. Adv Health Care Technol Care Shap Future Med [Internet]. Dordrecht: Kluwer Academic Publishers; 2006 [cited 2011 Apr 19]. p. 49–64. Available from: http://www.springerlink.com/content/m74k8523422466x5/
62. Huda W, Abrahams RB. Radiographic Techniques, Contrast, and Noise in X-Ray Imaging. Am J Roentgenol. 2015;204(2):W126–31.
63. Huda W, Rill LN, Bruner AP. Relative speeds of Kodak computed radiography phosphors and screen-film systems. Med Phys. 1997;24(10):1621–8.
64. Shepard SJ, Wang J, Flynn M, Gingold E, Goldman L, Krugh K, et al. An exposure indicator for digital radiography: AAPM Task Group 116 (Executive Summary). Med Phys. 2009;36(7):2898–914.

65. Giger ML, Doi K. Investigation of basic imaging properties in digital radiography. I. Modulation transfer function. Med Phys. 1984;11(3):287–95.

66. Schueler BA. Clinical applications of basic x-ray physics principles. RadioGraphics. 1998;18(3):731–44.

67. Fujita H, Giger ML, Doi K. Investigation of basic imaging properties in digital radiography. 12. Effect of matrix configuration on spatial resolution. Med Phys. 1988;15(3):384–90.

68. Iii JTD. Effects of undersampling on the proper interpretation of modulation transfer function, noise power spectra, and noise equivalent quanta of digital imaging systems. Med Phys. 1995;22(2):171–81.

69. Cowen AR, Kengyelics SM, Davies AG. Solid-state, flat-panel, digital radiography detectors and their physical imaging characteristics. Clin Radiol. 2008;63(5):487–98.

70. Kuhls-Gilcrist A, Jain A, Bednarek DR, Hoffmann KR, Rudin S. Accurate MTF measurement in digital radiography using noise response. Med Phys. 2010;37(2):724–35.

71. Yaffe MJ, Rowlands JA. X-ray detectors for digital radiography. Phys Med Biol. 1997;42(1):1.

72. Ritman EL. Small-animal CT - Its Difference from, and Impact on, Clinical CT. Nucl Instrum Methods Phys Res Sect Accel Spectrometers Detect Assoc Equip. 2007;580(2):968–70.

73. Ritman EL. Vision 20/20: increased image resolution versus reduced radiation exposure. Med Phys. 2008;35(6):2502–12.

74. Kheddache S, Månsson L., Angelhed J., Denbratt L, Gottfridsson B, Schlossman D. Effects of optimization and image processing in digital chest radiography: An ROC study with an anthropomorphic phantom. Eur J Radiol. 1991;13(2):143–50.

75. Kheddache S, Denbratt L, Angelhed JE. Digital chest radiography — optimizing image processing parameters for the visibility of chest lesions and anatomy. Eur J Radiol. 1996;22(3):241–5.

76. Seco J, Clasie B, Partridge M. Review on the characteristics of radiation detectors for dosimetry and imaging. Phys Med Biol. 2014;59(20):R303–47.

77. Sankaranarayanan K, Wassom JS. Reflections on the impact of advances in the assessment of genetic risks of exposure to ionizing radiation on international radiation protection recommendations between the mid-1950s and the present. Mutat Res. 2008;658(1-2):1–27.

78. Boice JD, Land CE, Shore RE, Norman JE, Tokunaga M. Risk of Breast Cancer Following Low-Dose Radiation Exposure. Radiology. 1979;131(3):589–97.

79. Yoshimoto Y, Kato H, Schull W. Risk of cancer among children exposed in utero to a-bomb radiations, 1950-84. The Lancet. 1988;332(8612):665–9.

80. Hall EJ. Is there a place for quantitative risk assessment? J Radiol Prot. 2009;29(2A):A171.

81. Hall E. Lessons we have learned from our children: cancer risks from diagnostic radiology. Pediatr Radiol. 2002;32(10):700–6.

82. de González AB, Darby S. Risk of cancer from diagnostic X-rays: estimates for the UK and 14 other countries. The Lancet. 2004;363(9406):345–51.

83. Einstein AJ. Beyond the bombs: cancer risks of low-dose medical radiation. The Lancet. 2012;380(9840):455–7.

84. Pearce MS, Salotti JA, Little MP, McHugh K, Lee C, Kim KP, et al. Radiation exposure from CT scans in childhood and subsequent risk of leukaemia and brain tumours: a retrospective cohort study. The Lancet. 2012;380(9840):499–505.

85. National Research Council (U.S.), Committee to Assess Health Risks from Exposure to Low Level of Ionizing Radiation. Health risks from exposure to low levels of ionizing radiation BEIR VII, Phase 2 [Internet]. Washington, D.C.: National Academies Press; 2006 [cited 2015 Oct 29]. Available from: http://www.nap.edu/read/11340/chapter/1

86. Brenner DJ. Should we be concerned about the rapid increase in CT usage? Rev Environ Health. 2010;25(1):63–8.

87. Brenner DJ. What we know and what we don't know about cancer risks associated with radiation doses from radiological imaging. Br J Radiol. 2013;20130629.

88. Parry RA, Glaze SA, Archer BR. Typical Patient Radiation Doses in Diagnostic Radiology - The AAPM/RSNA Physics Tutorial for Residents. Radiographics. 1999;19(5):1289–302.

89. Sodhi KS, Lee EY. What all physicians should know about the potential radiation risk that computed tomography poses for paediatric patients. Acta Paediatr. 2014;n/a – n/a.

90. Mullenders L, Atkinson M, Paretzke H, Sabatier L, Bouffler S. Assessing cancer risks of low-dose radiation. Nat Rev Cancer. 2009;9(8):596–604.

91. Morgan RH, Gehret JC. The radiant energy received by patients in diagnostic x-ray practice. Am J Roentgenol. 1966;97(3):793–810.

92. Kumamoto Y. Population Doses, Excess Deaths and Loss of Life Expectancy from Mass Chest X-ray Examinations in Japan - 1980. Health Phys July 1985. 1985;49(1):37–48.

93. Huda W, Sandison GA, Palser RF, Savoie D. Radiation doses and detriment from chest X-ray examinations. Phys Med Biol. 1989;34(10):1477.

94. Hart D, Wall BF. UK population dose from medical X-ray examinations. Eur J Radiol. 2004;50(3):285–91.

95. Scanff P, Donadieu J, Pirard P, Aubert B. Population exposure to ionizing radiation from medical examinations in France. Br J Radiol. 2008;81(963):204–13.

96. Samara ET, Aroua A, Bochud FO, Ott B, Theiler T, Treier R, et al. Exposure of the Swiss population by medical x-rays: 2008 review. Health Phys. 2012;102(3):263–70.

97. Zenone F, Aimonetto S, Catuzzo P, Peruzzo Cornetto A, Marchisio P, Natrella M, et al. Effective dose delivered by conventional radiology to Aosta Valley population between 2002 and 2009. Br J Radiol. 2012;85(1015):e330–8.

98. Grazia Andreassi M, Sagliano I, Cioppa A, Manfredi S, Picano E. Chronic low-dose radiation exposure from interventional cardiology procedures induces chromosomal abnormalities in originally genetically identical twins. Int J Cardiol. 2007;118(1):130–1.

99. Walsh L, Shore R, Auvinen A, Jung T, Wakeford R. Risks from CT scans-what do recent studies tell us? J Radiol Prot Off J Soc Radiol Prot. 2014;34(1):E1.

100. Frazier TH, Richardson JB, Fabre VC, Callen JP. Fluoroscopy-Induced Chronic Radiation Skin Injury: A Disease Perhaps Often Overlooked. Arch Dermatol. 2007;143(5):637–40.

101. Frush DP. Review of radiation issues for computed tomography. Semin Ultrasound CT MR. 2004;25(1):17–24.

102. Pearce MS, Salotti JA, McHugh K, Metcalf W, Kim KP, Craft AW, et al. CT scans in young people in Northern England: trends and patterns 1993-2002. Pediatr Radiol [Internet]. 2011 [cited 2011 Jun 3]; Available from: http://www.ncbi.nlm.nih.gov/pubmed/21594548

103. Smith-Bindman R, Lipson J, Marcus R, Kim K-P, Mahesh M, Gould R, et al. Radiation Dose Associated With Common Computed Tomography Examinations and the Associated Lifetime Attributable Risk of Cancer. Arch Intern Med. 2009;169(22):2078–86.

104. Larkin CJ, Workman A, Wright RER, Tham TCK. Radiation doses to patients during ERCP. Gastrointest Endosc. 2001;53(2):161–4.

105. Storm ES, Miller DL, Hoover LJ, Georgia JD, Bivens T. Radiation doses from venous access procedures. Radiology. 2006;238(3):1044–50.

106. Morrell RE, Rogers AT, Jobling JC, Shakespeare KE. Barium enema: use of increased copper filtration to optimize dose and image quality. Br J Radiol. 2004;77(914):116–22.

107. Berner K, Båth M, Jonasson P, Cappelen-Smith J, Fogelstam P, Söderberg J. Dose optimisation of double-contrast barium enema examinations. Radiat Prot Dosimetry. 2010;139(1-3):388–92.

108. Kalra MK, Singh S, Blake MA. CT of the Urinary Tract: Turning Attention to Radiation Dose. Radiol Clin North Am. 2008;46(1):1–9.

109. Sodickson A, Baeyens PF, Andriole KP, Prevedello LM, Nawfel RD, Hanson R, et al. Recurrent CT, Cumulative Radiation Exposure, and Associated Radiation-induced Cancer Risks from CT of Adults1. Radiology. 2009;251(1):175–84.

110. Zondervan RL, Hahn PF, Sadow CA, Liu B, Lee SI. Frequent Body CT Scanning of Young Adults: Indications, Outcomes, and Risk for Radiation-Induced Cancer. J Am Coll Radiol. 2011;8(7):501–7.

111. OECD. Computed tomography (CT) exams [Internet]. OECD Publishing; 2015 Jan. Available from: http://www.oecd-ilibrary.org/social-issues-migration-health/computed-tomography-ct-

exams/indicator/english_3c994537-en

112. OECD, European Union. Health at a Glance: Europe 2010 [Internet]. OECD Publishing; 2010 [cited 2015 Oct 29]. Available from: http://www.oecd-ilibrary.org/social-issues-migration-health/health-at-a-glance-europe-2010_health_glance-2010-en
113. Muhogora WE, Ahmed NA, Beganovic A, Benider A, Ciraj-Bjelac O, Gershan V, et al. Patient doses in CT Examinations in 18 countries: initial results from international atomic energy agency projects. Radiat Prot Dosimetry. 2009;136(2):118–26.
114. Richards PJBs, George J, Metelko MF, Brown MF. Spine Computed Tomography Doses and Cancer Induction. Spine Febr 15 2010. 2010;35(4):430–3.
115. National Council Radiation Protection and Measurements (NCRP). Radiation protection in Pediatric Radiology. Report No. 68. Bethesda: NCRP; 1981.
116. Webster E. Garland Lecture. On the question of cancer induction by small X-ray doses. Am J Roentgenol. 1981;137(4):647–66.
117. Brenner DJ, Doll R, Goodhead DT, Hall EJ, Land CE, Little JB, et al. Cancer risks attributable to low doses of ionizing radiation: Assessing what we really know. Proc Natl Acad Sci U S A. 2003;100(24):13761–6.
118. European Communities, editor. New Insights in Radiation Risk and Basic Safety Standards - EU Scientific Seminar 2006 - Radiation Protection 145 [Internet]. European Commission; 2006. Available from: http://ec.europa.eu/energy/nuclear/radiation_protection/doc/publication/125.pdf
119. European Communities. European Guidance on Estimating Population Doses from Medical X-Ray Procedures. RADIATION PROTECTION N° 154 [Internet]. Dir.-Gen. Energy Transp. Dir. H — Nucl. Energy Unit H4 — Radiat. Prot. 2008 [cited 2009 Nov 16]. Available from: http://ec.europa.eu/energy/nuclear/radiation_protection/doc/publication/154.zip
120. ICRP Internation Commision Radiological Protection. The Biological Basis for Dose Limitation in the Skin - ICRP Publication 59. Ann ICRP [Internet]. 1992 [cited 2015 Oct 31];22(2). Available from: http://www.icrp.org/publication.asp?id=ICRP%20Publication%2059
121. IRCP. Avoidance of radiation injuries from medical interventional procedures - ICRP Publication 85. Ann ICRP. 2000;30(2):7.
122. Theodorakou C, Horrocks JA. A study on radiation doses and irradiated areas in cerebral embolisation. Br J Radiol. 2003;76(908):546–52.
123. Sankaranarayanan K. Estimation of the hereditary risks of exposure to ionizing radiation: history, current status, and emerging perspectives. Health Phys. 2001;80(4):363–9.
124. ICRP Internation Commision Radiological Protection, SEPR Sociedad Española de Protección Radiológica. The 2007 Recommendations of the International Commission on Radiological Protection (Spanish version) [Internet]. Madrid: Senda Editorial S.A; 2007. Available from: http://www.icrp.org/publication.asp?id=ICRP%20Publication%20103
125. Preston RJ, Jr JDB, Brill AB, Chakraborty R, Conolly R, Hoffman FO, et al. Uncertainties in estimating health risks associated with exposure to ionising radiation. J Radiol Prot. 2013;33(3):573.
126. Doll SR. Effects of small doses of ionising radiation. J Radiol Prot. 1998;18(3):163.
127. Jolly D, Meyer J. A brief review of radiation hormesis. Australas Phys Eng Sci Med Support Australas Coll Phys Sci Med Australas Assoc Phys Sci Med. 2009;32(4):180–7.
128. Ulsh BA. The New Radiobiology: Returning to Our Roots. Dose-Response. 2012;10(4):593–609.
129. Pace N, Ricci L, Negrini S. A comparison approach to explain risks related to X-ray imaging for scoliosis, 2012 SOSORT award winner. Scoliosis. 2013;8(1):1–7.
130. Tubiana M, Aurengo A, Averbeck D, Masse R. Recent reports on the effect of low doses of ionizing radiation and its dose–effect relationship. Radiat Environ Biophys. 2006;44(4):245–51.
131. Tubiana M, Aurengo A, Averbeck D, Masse R. The debate on the use of linear no threshold for assessing the effects of low doses. J Radiol Prot Off J Soc Radiol Prot. 2006;26(3):317–24.
132. Tubiana M, Feinendegen LE, Yang C, Kaminski JM. The Linear No-Threshold Relationship Is Inconsistent with Radiation Biologic and Experimental Data1. Radiology. 2009;251(1):13–22.
133. Richardson DB, Cardis E, Daniels RD, Gillies M, O'Hagan JA, Hamra GB, et al. Risk of cancer from

occupational exposure to ionising radiation: retrospective cohort study of workers in France, the United Kingdom, and the United States (INWORKS). BMJ. 2015;351:h5359.

134. Kleinerman R. Cancer risks following diagnostic and therapeutic radiation exposure in children. Pediatr Radiol. 2006;36(0):121–5.
135. Vock P, Wolf R. Dose Optimization and Reduction in CT of Children. Radiat Dose Adult Pediatr Multidetector Comput Tomogr [Internet]. 2007 [cited 2009 Nov 23]. p. 223–36. Available from: http://dx.doi.org/10.1007/978-3-540-68575-3_15
136. Lucaya J, Piqueras J, García-Peña P, Enríquez G, García-Macías M, Sotil J. Low-dose high-resolution CT of the chest in children and young adults: dose, cooperation, artifact incidence, and image quality. AJR Am J Roentgenol. 2000;175(4):985–92.
137. Yakoumakis E, Kostopoulou H, Makri T, Dimitriadis A, Georgiou E, Tsalafoutas I. Estimation of radiation dose and risk to children undergoing cardiac catheterization for the treatment of a congenital heart disease using Monte Carlo simulations. Pediatr Radiol. 2013;43(3):339–46.
138. IAEA - International Atomic Energy Agency. Children - Radiation Protection of Patients (RPOP) [Internet]. 2013 [cited 2015 Nov 1]. Available from: https://rpop.iaea.org/RPOP/RPoP/Content/SpecialGroups/2_Children/index.htm
139. Miglioretti DL, Johnson E, Williams A, Greenlee RT, Weinmann S, Solberg LI, et al. Pediatric Computed Tomography and Associated Radiation Exposure and Estimated Cancer Risk. JAMA Pediatr. 2013;167(8):700–7.
140. McHugh K. Ct Scanning in Children and Risk of Cancer: What Three Large-Scale Studies Have Demonstrated. Radiat Prot Dosimetry. 2015;ncv118.
141. ICRP, Internation Commision Radiological Protection. Pregnancy and medical radiation. ICRP Publication 84 [Internet]. Pergamon : Elsevier Science; 2000. Available from: http://www.icrp.org/publication.asp?id=ICRP%20Publication%2084
142. IAEA - International Atomic Energy Agency. Pregnancy and Radiation Protection in Diagnostic Radiology [Internet]. IAEA - Int. At. Energy Agency. 2013 [cited 2015 Nov 1]. Available from: https://rpop.iaea.org/RPOP/RPoP/Content/SpecialGroups/1_PregnantWomen/Pregnancyandradiology.htm
143. European Communities, editor. Effects of in utero exposure to ionising radiation during the early phases of pregnancy. 2002.
144. Damilakis J, Perisinakis K, Prassopoulos P, Dimovasili E, Varveris H, Gourtsoyiannis N. Conceptus radiation dose and risk from chest screen-film radiography. Eur Radiol. 2003;13(2):406–12.
145. Hurwitz LM, Yoshizumi T, Reiman RE, Goodman PC, Paulson EK, Frush DP, et al. Radiation Dose to the Fetus from Body MDCT During Early Gestation. Am J Roentgenol. 2006;186(3):871–6.
146. McCollough CH, Schueler BA, Atwell TD, Braun NN, Regner DM, Brown DL, et al. Radiation Exposure and Pregnancy: When Should We Be Concerned? Radiographics. 2007;27(4):909–17.
147. Patel SJ, Reede DL, Katz DS, Subramaniam R, Amorosa JK. Imaging the Pregnant Patient for Nonobstetric Conditions: Algorithms and Radiation Dose Considerations. Radiographics. 2007;27(6):1705–22.
148. Ratnapalan S, Bentur Y, Koren G. Doctor, will that x-ray harm my unborn child? CMAJ. 2008;179(12):1293–6.
149. Kufe DW, Holland JF, Frei E, American Cancer Society. Holland Frei cancer medicine. Hamilton, Ont.; Lewiston, NY [distributor]: BC Decker; 2006.
150. Fuchs B, Valenzuela RG, Petersen IA, Arndt CA, Sim FH. Ewing's sarcoma and the development of secondary malignancies. Clin Orthop. 2003;(415):82–9.
151. Löbrich M, Rief N, Kühne M, Heckmann M, Fleckenstein J, Rübe C, et al. In vivo formation and repair of DNA double-strand breaks after computed tomography examinations. Proc Natl Acad Sci U S A. 2005;102(25):8984–9.
152. Strzelczyk J, Potter W, Zdrojewicz Z. Rad-by-Rad (Bit-by-Bit): Triumph of Evidence Over Activities Fostering Fear of Radiogenic Cancers at Low Doses. Dose-Response. 2007;5(4):275–83.
153. Tucker JD. Low-dose ionizing radiation and chromosome translocations: a review of the major considerations for human biological dosimetry. Mutat Res. 2008;659(3):211–20.

154. Fachin AL, Mello SS, Sandrin-Garcia P, Junta CM, Ghilardi-Netto T, Donadi EA, et al. Gene Expression Profiles in Radiation Workers Occupationally Exposed to Ionizing Radiation. J Radiat Res (Tokyo). 2009;50(1):61–71.

155. Martínez A, Coleman M, Romero-Talamás CA, Frias S. An assessment of immediate DNA damage to occupationally exposed workers to low dose ionizing radiation by using the comet assay. Rev Investig Clínica Organo Hosp Enfermedades Nutr. 2010;62(1):23–30.

156. Pinto MMP de L, Santos NFG, Amaral A. Current status of biodosimetry based on standard cytogenetic methods. Radiat Environ Biophys. 2010;49(4):567–81.

157. Geisel D, Zimmermann E, Rief M, Greupner J, Laule M, Knebel F, et al. DNA double-strand breaks as potential indicators for the biological effects of ionising radiation exposure from cardiac CT and conventional coronary angiography: a randomised, controlled study. Eur Radiol. 2012;22(8):1641–50.

158. Manning G, Rothkamm K. Deoxyribonucleic acid damage-associated biomarkers of ionising radiation: current status and future relevance for radiology and radiotherapy. Br J Radiol [Internet]. 2013 [cited 2015 Jul 17];86(1027). Available from: http://www.ncbi.nlm.nih.gov/pmc/articles/PMC3700735/

159. Li M, Cui F, Cheng Y, Sun D, Zhou P, Min R. Changes in the adhesion and migration ability of peripheral blood cells: potential biomarkers indicating exposure dose. Health Phys. 2014;107(3):242–7.

160. Vellingiri B, Shanmugam S, Subramaniam MD, Balasubramanian B, Meyyazhagan A, Alagamuthu K, et al. Cytogenetic endpoints and Xenobiotic gene polymorphism in lymphocytes of hospital workers chronically exposed to ionizing radiation in Cardiology, Radiology and Orthopedic Laboratories. Ecotoxicol Environ Saf. 2014;100:266–74.

161. Cho MS, Lee JK, Bae KS, Han E-A, Jang SJ, Ha W-H, et al. Retrospective biodosimetry using translocation frequency in a stable cell of occupationally exposed to ionizing radiation. J Radiat Res (Tokyo). 2015;56(4):709–16.

162. Piechowiak EI, Peter J-FW, Kleb B, Klose KJ, Heverhagen JT. Intravenous Iodinated Contrast Agents Amplify DNA Radiation Damage at CT. Radiology. 2015;275(3):692–7.

163. Shahid S, Mahmood N, Chaudhry MN, Sheikh S, Ahmad N. Mutations of the human interferon alpha-2b (hIFN-α2b) gene in occupationally protracted low dose radiation exposed personnel. Cytokine. 2015;73(1):181–9.

164. Amis Jr ES, Butler PF, Applegate KE, Birnbaum SB, Brateman LF, Hevezi JM, et al. American College of Radiology White Paper on Radiation Dose in Medicine. J Am Coll Radiol. 2007;4(5):272–84.

165. Strauss KJ. Developing patient-specific dose protocols for a CT scanner and exam using diagnostic reference levels. Pediatr Radiol. 2014;44(3):479–88.

166. Keen JD. Is This Appropriate: Will CT Take My Life? Am J Roentgenol. 2011;196(2):W217–W217.

167. Vano E, Gonzalez L. Patient Dosimetry and Reference Doses: Practical Considerations. Radiat Prot Dosim. 2000;90(1-2):85–8.

168. Ogunseyinde AO, Adeniran SAM, Obed RI, Akinlade BI, Ogundare FO. Comparison of entrance surface doses of some X ray examinations with CEC reference doses. Radiat Prot Dosimetry. 2002;98(2):231–4.

169. Hart D, Hillier MC, Wall BF. National reference doses for common radiographic, fluoroscopic and dental X-ray examinations in the UK. Br J Radiol. 2009;82(973):1–12.

170. Treier R, Aroua A, Verdun FR, Samara E, Stuessi A, Trueb PR. Patient doses in CT examinations in Switzerland: implementation of national diagnostic reference levels. Radiat Prot Dosimetry. 2010;142(2-4):244–54.

171. Kalra MK, Sodickson AD, Mayo-Smith WW. CT Radiation: Key Concepts for Gentle and Wise Use. RadioGraphics. 2015;35(6):1706–21.

172. Alpert HR, Hillman BJ. Quality and variability in diagnostic radiology. J Am Coll Radiol. 2004;1(2):127–32.

173. NEXT 2001 Protocol for Adult Chest Radiography - NEXT [Internet]. www.crcpd.org. 2002 [cited 2014 May 10]. Available from: http://www.crcpd.org/Pubs/NEXT.aspx

174. NEXT 1998 Pediatric Chest Protocol [Internet]. www.crcpd.org. 2004 [cited 2014 May 10]. Available from: http://www.crcpd.org/Pubs/NEXT.aspx

175. Whaley JS, Pressman BD, Wilson JR, Bravo L, Sehnert WJ, Foos DH. Investigation of the Variability in

the Assessment of Digital Chest X-ray Image Quality. J Digit Imaging Off J Soc Comput Appl Radiol. 2012;

176. Gibson DJ, Davidson RA. Exposure Creep in Computed Radiography: A Longitudinal Study. Acad Radiol. 2012;19(4):458–62.
177. Schaefer-Prokop C, Neitzel U, Venema HW, Uffmann M, Prokop M. Digital chest radiography: an update on modern technology, dose containment and control of image quality. Eur Radiol. 2008;18(9):1818–30.
178. Butler ML, Rainford L, Last J, Brennan PC. Are exposure index values consistent in clinical practice? A multi-manufacturer investigation. Radiat Prot Dosimetry. 2010;139(1-3):371–4.
179. imagegently > Home [Internet]. [cited 2015 Nov 1]. Available from: http://imagegently.org/
180. Goske MJ, Charkot E, Herrmann T, John SD, Mills TT, Morrison G, et al. Image Gently: Challenges for radiologic technologists when performing digital radiography in children. Pediatr Radiol. 2011;41(5):611–9.
181. ACR, RSNA, ASRT, AAPM. Image Wisely - Radiation Safety in Adult Medical Imaging [Internet]. Image Wisely. 2011 [cited 2015 Nov 1]. Available from: http://imagewisely.org/
182. Fairbank J. Historical perspective: William Adams, the forward bending test, and the spine of Gideon Algernon Mantell. Spine. 2004;29(17):1953–5.
183. Kim H, Kim HS, Moon ES, Yoon C-S, Chung T-S, Song H-T, et al. Scoliosis imaging: what radiologists should know. Radiogr Rev Publ Radiol Soc N Am Inc. 2010;30(7):1823–42.
184. Stokes IA. Three-dimensional terminology of spinal deformity. A report presented to the Scoliosis Research Society by the Scoliosis Research Society Working Group on 3-D terminology of spinal deformity. Spine. 1994;19(2):236–48.
185. Almén AJ, Mattsson S. Dose distribution at radiographic examination of the spine in pediatric radiology. Spine. 1996;21(6):750–6.
186. Nash CL Jr, Gregg EC, Brown RH, Pillai K. Risks of exposure to X-rays in patients undergoing long-term treatment for scoliosis. J Bone Joint Surg Am. 1979;61(3):371–4.
187. Hallén S, Martling K, Mattsson S. Dosimetry at X Ray Examinations of Scoliosis. Radiat Prot Dosimetry. 1992;43(1-4):49–54.
188. Arlet V, Reddi V. Adolescent Idiopathic Scoliosis. Neurosurg Clin N Am. 2007;18(2):255–9.
189. Cannon TA, Neto NA, Kelly DM, Warner WC Jr, Sawyer JR. Characterization of Radiation Exposure in Early-Onset Scoliosis Patients Treated With the Vertical Expandable Prosthetic Titanium Rib (VEPTR). J Pediatr Orthop. 2013;
190. Presciutti SM, Karukanda T, Lee M. Management decisions for adolescent idiopathic scoliosis significantly affect patient radiation exposure. Spine J Off J North Am Spine Soc. 2014;14(9):1984–90.
191. Enríquez G, Piqueras J, Catalá A, Oliva G, Ruiz A, Ribas M, et al. Optimización del estudio radiológico de la escoliosis. Med Clin (Barc). 2014;143(Supl.1):62–7.
192. Levy AR, Goldberg MS, Hanley JA, Mayo NE, Poitras B. Projecting the lifetime risk of cancer from exposure to diagnostic ionizing radiation for adolescent idiopathic scoliosis. Health Phys. 1994;66(6):621–33.
193. Morin Doody M, Lonstein JE, Stovall M, Hacker DG, Luckyanov N, Land CE. Breast cancer mortality after diagnostic radiography: findings from the U.S. Scoliosis Cohort Study. Spine. 2000;25(16):2052–63.
194. Ronckers CM, Doody MM, Lonstein JE, Stovall M, Land CE. Multiple diagnostic X-rays for spine deformities and risk of breast cancer. Cancer Epidemiol Biomark Prev Publ Am Assoc Cancer Res Cosponsored Am Soc Prev Oncol. 2008;17(3):605–13.
195. Ronckers CM, Land CE, Miller JS, Stovall M, Lonstein JE, Doody MM. Cancer mortality among women frequently exposed to radiographic examinations for spinal disorders. Radiat Res. 2010;174(1):83–90.
196. Geijer H, Beckman K-W, Jonsson B, Andersson T, Persliden J. Digital Radiography of Scoliosis with a Scanning Method: Initial Evaluation. Radiology. 2001;218(2):402–10.
197. Geijer H, Verdonck B, Beckman K-W, Andersson T, Persliden J. Digital radiography of scoliosis with a scanning method: radiation dose optimization. Eur Radiol. 2003;13(3):543–51.

198. Schaefer J, Kluba T, Niemeyer T, Hahnfeldt T, Vonthein R, Kottke R, et al. [Comparison of conventional full spine radiographs and fluoroscopic scanning method in young patients with idiopathic scoliosis]. RöFo Fortschritte Auf Dem Geb Röntgenstrahlen Nukl. 2005;177(8):1110–5.

199. Abul-Kasim K, Overgaard A, Maly P, Ohlin A, Gunnarsson M, Sundgren PC. Low-dose helical computed tomography (CT) in the perioperative workup of adolescent idiopathic scoliosis. Eur Radiol. 2009;19(3):610–8.

200. Kalra MK, Quick P, Singh S, Sandborg M, Persson A. Whole spine CT for evaluation of scoliosis in children: feasibility of sub-milliSievert scanning protocol. Acta Radiol Stockh Swed 1987. 2013;54(2):226–30.

201. Chu WCW, Wong MS, Chau WW, Lam TP, Ng KW, Lam WWM, et al. Curve correction effect of rigid spinal orthosis in different recumbent positions in adolescent idiopathic scoliosis (AIS): a pilot MRI study. Prosthet Orthot Int. 2006;30(2):136–44.

202. Wessberg P, Danielson BI, Willén J. Comparison of Cobb angles in idiopathic scoliosis on standing radiographs and supine axially loaded MRI. Spine. 2006;31(26):3039–44.

203. Diefenbach C, Lonner BS, Auerbach JD, Bharucha N, Dean LE. Is radiation-free diagnostic monitoring of adolescent idiopathic scoliosis feasible using upright positional magnetic resonance imaging? Spine. 2013;38(7):576–80.

204. Osibote OA, de Azevedo ACP. Estimation of adult patient doses for common diagnostic X-ray examinations in Rio de Janeiro, Brazil. Phys Med. 2008;24(1):21–8.

205. ACR Routine Admission and Preoperative Chest Radiography.

206. Radiografia de tòrax en el diagnòstic de la bronquiolitis en població pediàtrica. Essencial. Generalitat de Catalunya [Internet]. [cited 2015 Nov 4]. Available from: http://essencialsalut.gencat.cat/ca/detalls/Article/radiografia_torax_bronquiolitis_pediatria#FW_bloc_1e6954f1-214f-11e4-ac19-005056924a59_6

207. Radiografia de tòrax en el diagnòstic de l'asma en població pediàtrica. Essencial. Generalitat de Catalunya [Internet]. [cited 2015 Nov 4]. Available from: http://essencialsalut.gencat.cat/ca/detalls/Article/radiografia_torax_pediatrica

208. Bush A, Fleming L. Diagnosis and management of asthma in children. BMJ. 2015;350:h996.

209. Schuh S, Lalani A, Allen U, Manson D, Babyn P, Stephens D, et al. Evaluation of the utility of radiography in acute bronchiolitis. J Pediatr. 2007;150(4):429–33.

210. Oba Y, Zaza T. Abandoning daily routine chest radiography in the intensive care unit: meta-analysis. Radiology. 2010;255(2):386–95.

211. Ziegler K, Feeney JM, Desai C, Sharpio D, Marshall WT, Twohig M. Retrospective review of the use and costs of routine chest x rays in a trauma setting. J Trauma Manag Outcomes. 2013;7(1):2.

212. Tesic MM, Mattson RA, Barnes GT, Sones RA, Stickney JB. Digital radiography of the chest: design features and considerations for a prototype unit. Radiology. 1983;148(1):259–64.

213. Månsson LG, Kheddache S, Schlossman D, Börjesson J, Håkansson E, Mattsson S, et al. Digital Chest Radiography with a Large Image Intensifier. Evaluation of diagnostic performance and patient exposure. Acta Radiol. 1989;30(4):337–42.

214. Sonoda M, Takano M, Miyahara J, Kato H. Computed radiography utilizing scanning laser stimulated luminescence. Radiology. 1983;148(3):833–8.

215. Fuhrman C, Gur D, Good B, Rockette H, Cooperstein L, Feist J. Storage phosphor radiographs vs conventional films: interpreters' perceptions of diagnostic quality. Am J Roentgenol. 1988;150(5):1011–4.

216. Fujita H, Ueda K, Morishita J, Fujikawa T, Ohtsuka A, Sai T. Basic imaging properties of a computed radiographic system with photostimulable phosphors. Med Phys. 1989;16(1):52–9.

217. MacMahon H, Sanada S, Doi K, Giger M, Xu XW, Yin FF, et al. Direct comparison of conventional and computed radiography with a dual-image recording technique. Radiogr Rev Publ Radiol Soc N Am Inc. 1991;11(2):259–68.

218. Broderick NJ, Long B, Dreesen RG, Cohen MD, Cory DA, Katz BP, et al. Phosphor plate computed radiography: Response to variation in mAs at fixed kVp in an animal model. Potential role in neonatal imaging. Clin Radiol. 1993;47(1):39–45.

219. Anthony Seibert J, Shelton DK, Moore EH. Computed radiography x-ray exposure trends. Acad Radiol. 1995;2(12):1167.

220. Bragg DG, Murray KA, Tripp D. Experiences with computed radiography: can we afford the cost? AJR Am J Roentgenol. 1997;169(4):935–41.

221. Andriole KP. Productivity and Cost Assessment of Computed Radiography, Digital Radiography, and Screen-Film for Outpatient Chest Examinations. J Digit Imaging. 2002;15(3):161–9.

222. Kheddache S, Thilander-Klang A, Lanhede B, Månsson LG, Bjurstam N, Ackerholm P, et al. Storage phosphor and film-screen mammography: performance with different mammographic techniques. Eur Radiol. 1999;9(4):591–7.

223. Dhawan AP, Huang HK, Kim, Dae-Shik. Principles and advanced methods in medical imaging and image analysis [Internet]. 1st ed. Singapore; Hackensack, NJ: World Scientific; 2008 [cited 2013 Nov 11]. Available from: http://site.ebrary.com/id/10255579

224. Freiherr G. Digital Radiography - Battle of the detectors [Internet]. www.Diagnosticimaging.com. 2008 [cited 2014 May 10]. Available from: http://www.diagnosticimaging.com/dimag/legacy/DR/battle.html

225. Lança L, Silva A. Digital radiography detectors – A technical overview: Part 1. Radiography. 2009;15(1):58–62.

226. Lança L, Silva A. Digital radiography detectors – A technical overview: Part 2. Radiography. 2009;15(2):134–8.

227. Kump K, Grantors P, Pla F, Gobert P. Digital X-ray detector technology. RBM-News. 1998;20(9):221–6.

228. Spahn M. Flat detectors and their clinical applications. Eur Radiol. 2005;15(9):1934–47.

229. Kim H, Cunningham IA, Yin Z, Cho G. On the Development of Digital Radiography Detectors : A Review. Intl J Precis Eng Manuf. 2008;9(4):86–100.

230. Chotas HG, Dobbins JT, Ravin CE. Principles of Digital Radiography with Large-Area, Electronically Readable Detectors: A Review of the Basics. Radiology. 1999;210(3):595–9.

231. Marshall NW, Faulkner K, Busch HP, Marsh DM, Pfenning H. An investigation into the radiation dose associated with different imaging systems for chest radiology. Br J Radiol. 1994;67(796):353–9.

232. Strotzer M, Volk M, Reiser M, Lenhart M, Manke C, Gmeinwieser J, et al. Chest Radiography With a Large-Area Detector Based on Cesium-Iodide/Amorphous-Silicon Technology: Image Quality and Dose Requirement in Comparison With an Asymmetric Screen-Film System. J Thorac Imaging July 2000. 2000;15(3):157–61.

233. Rill LN, Brateman L, Arreola M. Evaluating radiographic parameters for mobile chest computed radiography: phantoms, image quality and effective dose. Med Phys. 2003;30(10):2727–35.

234. Bacher K, Smeets P, Vereecken L, Hauwere AD, Duyck P, Man RD, et al. Image Quality and Radiation Dose on Digital Chest Imaging: Comparison of Amorphous Silicon and Amorphous Selenium Flat-Panel Systems. Am J Roentgenol. 2006;187(3):630–7.

235. Prato A, Ropolo R, Fava C. Digital chest radiography system with amorphous selenium flat-panel detectors: Qualitative and dosimetric comparison with a dedicated film-screen system. Radiol Med (Torino). 2005;110(5-6):561–73.

236. Veldkamp WJH, Kroft LJM, Boot MV, Mertens BJA, Geleijns J. Contrast-detail evaluation and dose assessment of eight digital chest radiography systems in clinical practice. Eur Radiol. 2006;16(2):333–41.

237. Grieser T, Baldauf AQ, Ludwig K. Radiation Dose Reduction in Scoliosis Patients: Low-Dose Full-Spine Radiography with Digital Flat Panel Detector and Image Stitching System. Rofo-Fortschritte Auf Dem Geb Rontgenstrahlen Bildgeb Verfahr. 2011;183(7):645–9.

238. von Seggern H, Hesse S, Zimmermann J, Appleby GA, Meng X, Fasel C, et al. New synthesis of high-quality storage phosphors. Radiat Meas. 2010;45(3–6):478–84.

239. Kogutt M, Jones J, Perkins D. Low-dose digital computed radiography in pediatric chest imaging. Am J Roentgenol. 1988;151(4):775–9.

240. Cowen AR, Workman A, Price JS. Physical aspects of photostimulable phosphor computed radiography. Br J Radiol. 1993;66(784):332–45.

241. Aldrich J, Duran E, Dunlop P, Mayo J. Optimization of Dose and Image Quality for Computed

Radiography and Digital Radiography. J Digit Imaging. 2006;19(2):126–31.

242. Sanchez Jacob R, Vano-Galvan E, Vano E, Gomez Ruiz N, Fernandez Soto J, Martinez Barrio D, et al. Optimising the Use of Computed Radiography in Pediatric Chest Imaging. J Digit Imaging. 2009;22(2):104–13.
243. Huda W, Slone RM, Belden CJ, Williams JL, Cumming WA, Palmer CK. Mottle on computed radiographs of the chest in pediatric patients. Radiology. 1996;199(1):249–52.
244. Thomas MA, Rowberg AH, Langer SG, Kim Y. Interactive Image Enhancement of CR and DR Images. J Digit Imaging. 2004;17(3):189–95.
245. Tylén U. Stimulable phosphor plates in chest radiology. Eur Radiol. 1997;7(3):S83–6.
246. Rapp-Bernhardt U, Bernhardt TM, Lenzen H, Esseling R, Roehl FW, Schiborr M, et al. Experimental Evaluation of a Portable Indirect Flat-Panel Detector for the Pediatric Chest: Comparison with Storage Phosphor Radiography at Different Exposures by Using a Chest Phantom. Radiology. 2005;237(2):485–91.
247. Kelsey CA, Jr FAM, Sullivan LM. Radiation dose and image quality of double-loaded cassettes. Med Phys. 1996;23(2):239–40.
248. Lehnert T, Naguib NN, Ackermann H, Schomerus C, Jacobi V, Balzer JO, et al. Novel, portable, cassette-sized, and wireless flat-panel digital radiography system: initial workflow results versus computed radiography. AJR Am J Roentgenol. 2011;196(6):1368–71.
249. Leblans P, Struye L, Willems P. A new needle-crystalline computed radiography detector. J Digit Imaging. 2000;13(Suppl 1):117–20.
250. Berger-Kulemann V, Pötter-Lang S, Gruber M, Berger R, Vonbank K, Weber M, et al. Needle image plates compared to conventional CR in chest radiography: Is dose reduction possible? Eur J Radiol [Internet]. 2012 [cited 2012 Oct 26]; Available from: http://www.sciencedirect.com/science/article/pii/S0720048X11006048
251. Seibert JA. Advances in Computed Radiography: Dual-Side Readout. J Am Coll Radiol. 2010;7(2):154–7.
252. Carlander A, Hansson J, Söderberg J, Steneryd K, Båth M. The effect of radiation dose reduction on clinical image quality in chest radiography of premature neonates using a dual-side readout technique computed radiography system. Radiat Prot Dosimetry. 2010;139(1-3):275–80.
253. Cohen M, Corea D, Wanner M, Karmazyn B, Gunderman R, Applegate K, et al. Evaluation of a New Phosphor Plate Technology for Neonatal Portable Chest Radiographs. Acad Radiol. 2011;18(2):197–8.
254. International Commission on Radiological Protection. Managing Patient Dose in Digital Radiology - ICRP Publication 93. ICRP. 2004;34(1):1–71.
255. Neofotistou V, Tsapaki V, Kottou S, Schreiner-Karoussou A, Vano E. Does digital imaging decrease patient dose? A pilot study and review of the literature. Radiat Prot Dosimetry. 2005;117(1-3):204–10.
256. Seibert JA. Digital radiography: image quality and radiation dose. Health Phys. 2008;95(5):586–98.
257. Thakur Y, Bjarnason TA, Hammerstrom K, Marchinkow L, Koch T, Aldrich JE. Assessment of patient doses in CR examinations throughout a large health region. J Digit Imaging Off J Soc Comput Appl Radiol. 2012;25(1):189–95.
258. Kasap SO, Rowlands JA. Direct-conversion flat-panel X-ray image detectors. Circuits Devices Syst IEE Proc -. 2002;149(2):85–96.
259. Samei E, Flynn MJ. An experimental comparison of detector performance for direct and indirect digital radiography systems. Med Phys. 2003;30(4):608–22.
260. Boag JW. Xeroradiography. Phys Med Biol. 1973;18(1):3–37.
261. Que W, Rowlands JA. X-ray imaging using amorphous selenium: Inherent spatial resolution. Med Phys. 1995;22(4):365–74.
262. Floyd CE, Baker JA, Chotas HG, Delong DM, Ravin CE. Selenium-based digital radiography of the chest: radiologists' preference compared with film-screen radiographs. Am J Roentgenol. 1995;165(6):1353–8.
263. van Heesewijk HP, Neitzel U, van der Graaf Y, de Valois JC, Feldberg MA. Digital chest imaging with a selenium detector: comparison with conventional radiography for visualization of specific anatomic

regions of the chest. AJR Am J Roentgenol. 1995;165(3):535–40.

264. Woodard PK, Slone RM, Gierada DS, Reiker GG, Pilgram TK, Jost RG. Chest radiography: depiction of normal anatomy and pathologic structures with selenium-based digital radiography versus conventional screen-film radiography. Radiology. 1997;203(1):197–201.
265. Goo JM, Im JG, Kim JH, Seo JB, Kim TS, Shine SJ, et al. Digital chest radiography with a selenium-based flat-panel detector versus a storage phosphor system: comparison of soft-copy images. AJR Am J Roentgenol. 2000;175(4):1013–8.
266. Awai K, Komi M, Hori S. Selenium-based digital radiography versus high-resolution storage phosphor radiography in the detection of solitary pulmonary nodules without calcification: receiver operating characteristic curve analysis. AJR Am J Roentgenol. 2001;177(5):1141–4.
267. Beute GH, Flynn MJ, Eyler WR, Samei E, Spizarny DL, Zylak CJ. Chest radiographic image quality: comparison of asymmetric screen-film, digital storage phosphor, and digital selenium drum systems--preliminary study. Radiographics. 1998;18:745–54.
268. Abbene L, Gerardi G, Principato F, Del Sordo S, Ienzi R, Raso G. High-rate x-ray spectroscopy in mammography with a CdTe detector: a digital pulse processing approach. Med Phys. 2010;37(12):6147–56.
269. van Heesewijk HP, van der Graaf Y, de Valois JC, Feldberg MA. Effects of dose reduction on digital chest imaging using a selenium detector: a study of detecting simulated diffuse interstitial pulmonary disease. Am J Roentgenol. 1996;167(2):403–8.
270. Borasi G, Nitrosi A, Ferrari P, Tassoni D. On site evaluation of three flat panel detectors for digital radiography. Med Phys. 2003;30(7):1719–31.
271. Lehnert T, Wohlers J, Streng W, Manegold K, Wetter A, Jacobi V, et al. [Variation in X-ray dose quantity using an amorphous selenium based flat-panel detector -- a study on the dose reduction rate up to the limit of diagnostical utilization]. RöFo Fortschritte Auf Dem Geb Röntgenstrahlen Nukl. 2006;178(3):278–86.
272. Liu X, Lai C-J, Chen L, Han T, Zhong Y, Shen Y, et al. Scan equalization digital radiography (SEDR) implemented with an amorphous selenium flat-panel detector: initial experience. Phys Med Biol. 2009;54(22):6959–78.
273. Chaussat C, Chabbal J, Ducourant T, Spinnler V, Vieux G, Neyret R. New CsI/a-Si 17“ x 17” x-ray flat-panel detector provides superior detectivity and immediate direct digital output for general radiography systems. Proc SPIE. 1998;3336:45–56.
274. Hamers S, Freyschmidt J, Neitzel U. Digital radiography with a large-scale electronic flat-panel detector vs screen-film radiography: observer preference in clinical skeletal diagnostics. Eur Radiol. 2001;11(9):1753–9.
275. Völk M, Strotzer M, Gmeinwieser J, Alexander J, Fründ R, Seitz J, et al. Flat-panel x-ray detector using amorphous silicon technology. Reduced radiation dose for the detection of foreign bodies. Invest Radiol. 1997;32(7):373–7.
276. Chotas HG, Ravin CE. Digital chest radiography with a solid-state flat-panel x-ray detector: contrast-detail evaluation with processed images printed on film hard copy. Radiology. 2001;218(3):679–82.
277. Metz et al._2005_Chest Radiography with a Digital Flat-Panel Detect.pdf.
278. Granfors PR, Albagli D. Scintillator-based flat-panel x-ray imaging detectors. J Soc Inf Disp. 2009;17(6):535–42.
279. Davies AG, Cowen AR, Kengyelics SM, Moore J, Sivananthan MU. Do flat detector cardiac X-ray systems convey advantages over image-intensifier-based systems? Study comparing X-ray dose and image quality. Eur Radiol. 2006;17(7):1787–94.
280. Krug KB, Stutzer H, Girnus R, Zahringer M, Gossmann A, Winnekendonk G, et al. Image Quality of Digital Direct Flat-Panel Mammography Versus an Analog Screen-Film Technique Using a Phantom Model. Am J Roentgenol. 2007;188(2):399–407.
281. Baldelli P, Phelan N, Egan G. Investigation of the effect of anode/filter materials on the dose and image quality of a digital mammography system based on an amorphous selenium flat panel detector. Br J Radiol. 2010;83(988):290–5.
282. Rivetti S, Lanconelli N, Campanini R, Bertolini M, Borasi G, Nitrosi A, et al. Comparison of different commercial FFDM units by means of physical characterization and contrast-detail analysis. Med Phys.

2006;33(11):4198–209.

283. Siewerdsen JH, Antonuk LE, El-Mohri Y, Yorkston J, Huang W, Boudry JM, et al. Empirical and theoretical investigation of the noise performance of indirect detection, active matrix flat-panel imagers (AMFPIs) for diagnostic radiology. Med Phys. 1997;24(1):71–89.
284. Zhao W, Rowlands JA. Digital radiology using active matrix readout of amorphous selenium: Theoretical analysis of detective quantum efficiency. Med Phys. 1997;24(12):1819–33.
285. Kunitomo H, Ichikawa K, Higashide R, Ohashi K. Physical Image Properties of Digital Radiography Systems in Low Dose Range. Jpn J Radiol Technol. 2012;68(8):961–9.
286. Walz-Flannigan A, Magnuson D, Erickson D, Schueler B. Artifacts in Digital Radiography. Am J Roentgenol. 2012;198(1):156–61.
287. Willis CE, Vinogradskiy YY, Lofton BK, White RA. Gain and offset calibration reduces variation in exposure-dependent SNR among systems with identical digital flat-panel detectors. Med Phys. 2011;38(7):4422–9.
288. Bogaert E, Bacher K, Lapere R, Thierens H. Does digital flat detector technology tip the scale towards better image quality or reduced patient dose in interventional cardiology? Eur J Radiol. 2009;72(2):348–53.
289. Geijer H. Radiation dose and image quality in diagnostic radiology. Optimization of the dose-image quality relationship with clinical experience from scoliosis radiography, coronary intervention and a flat-panel digital detector. Acta Radiol Suppl. 2002;43(427):1–43.
290. Granfors PR, Aufrichtig R, Possin GE, Giambattista BW, Huang ZS, Liu J, et al. Performance of a 41 x 41 cm2 amorphous silicon flat panel x-ray detector designed for angiographic and R&F imaging applications. Med Phys. 2003;30(10):2715–26.
291. Jaffray DA, Siewerdsen JH. Cone-beam computed tomography with a flat-panel imager: initial performance characterization. Med Phys. 2000;27(6):1311–23.
292. Miracle AC, Mukherji SK. Conebeam CT of the head and neck, part 1: physical principles. AJNR Am J Neuroradiol. 2009;30(6):1088–95.
293. Tacher V, Radaelli A, Lin M, Geschwind J-F. How I do it: Cone-beam CT during transarterial chemoembolization for liver cancer. Radiology. 2015;274(2):320–34.
294. Dobbins JT, Godfrey DJ. Digital x-ray tomosynthesis: current state of the art and clinical potential. Phys Med Biol. 2003;48(19):R65–106.
295. Andersson I, Ikeda D, Zackrisson S, Ruschin M, Svahn T, Timberg P, et al. Breast tomosynthesis and digital mammography: a comparison of breast cancer visibility and BIRADS classification in a population of cancers with subtle mammographic findings. Eur Radiol. 2008;18(12):2817–25.
296. Vikgren J, Zachrisson S, Svalkvist A, Johnsson ÅA, Boijsen M, Flinck A, et al. Comparison of Chest Tomosynthesis and Chest Radiography for Detection of Pulmonary Nodules: Human Observer Study of Clinical Cases1. Radiology. 2008;249(3):1034–41.
297. Dobbins III JT, McAdams HP. Chest tomosynthesis: Technical principles and clinical update. Eur J Radiol. 2009;72(2):244–51.
298. Fischbach F, Freund T, Röttgen R, Engert U, Felix R, Ricke J. Dual-energy chest radiography with a flat-panel digital detector: revealing calcified chest abnormalities. AJR Am J Roentgenol. 2003;181(6):1519–24.
299. Szucs-Farkas Z, Patak MA, Yuksel-Hatz S, Ruder T, Vock P. Single-exposure dual-energy subtraction chest radiography: Detection of pulmonary nodules and masses in clinical practice. Eur Radiol. 2008;18(1):24–31.
300. Shkumat NA, Siewerdsen JH, Dhanantwari AC, Williams DB, Richard S, Paul NS, et al. Optimization of image acquisition techniques for dual-energy imaging of the chest. Med Phys. 2007;34(10):3904–15.
301. The Council of the European Union. Council Directive 97/43/Euratom of 30 June 1997 on health protection of individuals against the dangers of ionizing radiation in relation to medical exposure, and repealing Directive 84/466/Euratom [Internet]. EUR-Lex - 31997L0043 - EN Jul 9, 1997 p. p.0022–7. Available from: http://eur-lex.europa.eu/legal-content/AUTO/?uri=CELEX:31997L0043&qid=1447326754883&rid=1
302. European Communities, editor. Implementation of the “Medical Exposure Directive” (97/43/Euratom).

Proceedings of the international workshop held in Madrid, on 27 April 1998 - Radiation Protection 102 [Internet]. European Commission; 1998. Available from: http://ec.europa.eu/energy/nuclear/radiation_protection/doc/publication/102_en.pdf

303. Schulte E-H, European Union, Euratom. Optimisation of protection in the medical uses of radiation. Luxembourg: EUR-OP; 2002.

304. Vano E. ICRP recommendations on “Managing patient dose in digital radiology.” Radiat Prot Dosimetry. 2005;114(1-3):126–30.

305. ICRP Publication 113 Education and Training in Radiological Protection for Diagnostic and Interventional Procedures. Ann ICRP. 2009;39(5):5–6.

306. Khong P-L, Ringertz H, Donoghue V, Frush D, Rehani M, Appelgate K, et al. ICRP PUBLICATION 121: Radiological Protection in Paediatric Diagnostic and Interventional Radiology. Ann ICRP. 2013;42(2):1–63.

307. European Communities, editor. Referral Guidelines For Imaging - Update 2003 - Radiation Protection 118 [Internet]. Directorate-General for Energy and Transpor Directorate H — Nuclear Energy Unit H.4 — Radiation Protection; 2007 [cited 2009 Nov 16]. Available from: http://ec.europa.eu/energy/nuclear/radiation_protection/doc/publication/118.zip

308. European Communities, editor. Guía de Indicaciones para la Correcta Solicitud de Pruebas de Diagnóstico por Imagen - Proteccion Radiologica 118 [Internet]. Directorate-General for Energy and Transpor Directorate H — Nuclear Energy Unit H.4 — Radiation Protection; 2007 [cited 2009 Nov 16]. Available from: http://ec.europa.eu/energy/nuclear/radiation_protection/doc/publication/118.zip

309. Société Française de Radiologie. Guide du Bon Usage - SFR.FR [Internet]. [cited 2014 Sep 9]. Available from: http://gbu.radiologie.fr/

310. Carmichael JH., European Union, European Commission, Directorate-General XII - Science R and D. European guidelines on quality criteria for diagnostic radiographic images - EUR 16260 [Internet]. 1st ed. Luxembourg: EUR-OP; 1996. Available from: http://bookshop.europa.eu/en/european-guidelines-on-quality-criteria-for-diagnostic-radiographic-images-pbCGNA16260/

311. Vañó E, Guibelalde E, Morillo A, Alvarez-Pedrosa CS, Fernández JM. Evaluation of the European image quality criteria for chest examinations. Br J Radiol. 1995;68(816):1349–55.

312. Charpak, Georges, Sauli, F. High Accuracy, Two-Dimensional Read-Out in Multiwire Proportional Chambers [Internet]. European Organization for Nuclear Research, Geneva (Switzerland), editor. CERN--73-4 ACC0406; 1973 [cited 2014 May 7]. Available from: http://www.osti.gov/cgi-bin/rd_accomplishments/display_biblio.cgi?id=ACC0406&numPages=16&fp=N

313. Charpak, Georges. Evolution of Some Particle Detectors Based On the Discharge in Gases [Internet]. European Organization for Nuclear Research, Geneva (Switzerland), editor. CERN - CERN--69-29 UI: ACC0406; 1969 [cited 2014 May 7]. Available from: http://www.osti.gov/cgi-bin/rd_accomplishments/display_biblio.cgi?id=ACC0405&numPages=20&fp=N

314. Heuer R. Particle physics: a valuable driver of innovation in medicine | CERN [Internet]. CERN. 2014 [cited 2014 May 7]. Available from: http://home.web.cern.ch/cern-people/opinion/2012/12/particle-physics-valuable-driver-innovation-medicine

315. Martínez-Dávalos A, Speller RD, Miller DJ, Shekhtman LI, Baru SE, Khabakhpashev AG, et al. Evaluation of a low-dose digital X-ray system with improved spatial resolution. Nucl Instrum Methods Phys Res Sect Accel Spectrometers Detect Assoc Equip. 1994;348(2–3):241–4.

316. Rao DV, Goodwin PN, Khalil FL. 165Er: an “ideal” radionuclide for imaging with pressurized multiwire proportional gamma cameras. J Nucl Med Off Publ Soc Nucl Med. 1974;15(11):1008–10.

317. Christie PF, Mathieson E, Evans KD. An X-ray imaging proportional chamber incorporating a radial field drift chamber. J Phys [E]. 1976;9(8):673.

318. Lacy JL, LeBlanc AD, Babich JW, Bungo MW, Latson LA, Lewis RM, et al. A gamma camera for medical applications, using a multiwire proportional counter. J Nucl Med Off Publ Soc Nucl Med. 1984;25(9):1003–12.

319. Baru SE, Proviz GI, Savinov GA, Sidorov VA, Khabakhpashev AG, Shekhtman LI, et al. Two-coordinate X-ray detector. Nucl Instrum Methods Phys Res. 1983;208(1-3):445–7.

320. Baru SE, Khabakhpashev AG, Makarov IR, Savinov GA, Shekhtman LI, Sidorov VA. Digital x-ray imaging installation for medical diagnostics. Nucl Instrum Methods Phys Res Sect Accel Spectrometers

Detect Assoc Equip. 1985;238(1):165–9.

321. Baru SE, Khabakhpashev AG, Shekhtman LI. Multiwire proportional chamber for a digital radiographic installation. Nucl Instrum Methods Phys Res Sect Accel Spectrometers Detect Assoc Equip. 1989;283(3):431–5.

322. Giomataris Y, Rebourgeard P, Robert JP, Charpak G. MICROMEGAS: a high-granularity position-sensitive gaseous detector for high particle-flux environments. Nucl Instrum Methods Phys Res Sect Accel Spectrometers Detect Assoc Equip. 1996;376(1):29–35.

323. Babichev EA, Baru SE, Khabakhpashev AG, Kolachev GM, Savinov GA, Shekhtman KI, et al. Digital radiographic scanning installation with multiwire proportional chamber. Nucl Instrum Methods Phys Res Sect Accel Spectrometers Detect Assoc Equip. 1991;310(1–2):449–54.

324. Martinez-Davalos A, Speller RD, Horrocks JA, Miller DJ, Baru SE, Khabakhpashov AG, et al. Evaluation of a new low-dose digital X-ray system. Phys Med Biol. 1993;38(10):1419.

325. Babichev EA, Baru SE, Khabakhpashev AG, Kolachev GM, Neustroev VV, Pestov YN, et al. High pressure multiwire proportional and gas microstrip chambers for medical radiology. Nucl Instrum Methods Phys Res Sect Accel Spectrometers Detect Assoc Equip. 1995;360(1–2):271–6.

326. Baru SE, Aulchenko VM, Babichev EA, Dubrovin MS, Groshev VR, Khabakhpashev AG, et al. X-ray detectors based on multiwire proportional chambers. Nucl Instrum Methods Phys Res Sect Accel Spectrometers Detect Assoc Equip. 1997;392(1-3):12–7.

327. Babichev EA, Baru SE, Groshev VR, Khabakhpashev AG, Porosev VV, Savinov GA, et al. Photon counting and integrating analog gaseous detectors for digital scanning radiography. Nucl Instrum Methods Phys Res Sect Accel Spectrometers Detect Assoc Equip. 1998;419(2–3):290–4.

328. Baru SE, Khabakhpashev AG, Shekhtman LI. A low-dose x-ray imaging device. Eur J Phys. 1998;19(6):475–83.

329. Sushkov A, Andreev V, Camenen Y, Pochelon A, Klimanov I, Scarabosio A, et al. High-resolution multiwire proportional soft x-ray diagnostic measurements on TCV. Rev Sci Instrum. 2008;79(2 Pt 1):023506.

330. Després P, Beaudoin G, Gravel P, Guise JA de. Physical characteristics of a low-dose gas microstrip detector for orthopedic x-ray imaging. Med Phys. 2005;32(4):1193–204.

331. Després P, Beaudoin G, Gravel P, A. de Guise J. Evaluation of a full-scale gas microstrip detector for low-dose X-ray imaging. Nucl Instrum Methods Phys Res Sect Accel Spectrometers Detect Assoc Equip. 2005;536(1–2):52–60.

332. Hayakawa Y, Maeda Y. Microstrip Gas Chamber for X-Rays and Neutrons. Jpn J Appl Phys. 1996;35(1B):L123.

333. Kunn F, Abbon P, Ball J, Bedfer Y, Bernet C, Delagnes E, et al. The gaseous microstrip detector micromegas for the COMPASS experiment at CERN. Nucl Phys A. 2003;721(0):C1087–90.

334. Berger, M.J., Hubbell, J.H., Seltzer, S.M., Chang, J., Coursey, J.S., Sukumar, R., Zucker, D.S., and Olsen, K., National Institute of Standards and Technology (U.S.), Physics Laboratory (U.S.). XCOM photon cross sections database (version 1.5). [Internet]. Gaithersburg, Md, USA: NIST, Physics Laboratory; 2010 [cited 2015 Oct 28]. Available from: http://physics.nist.gov/xcom

335. Desprès P. Évaluation d'un détecteur gazeux à micropistes pour la radiologie et applications en imagerie multi-énergie. [[Montréal]]: Université de Montréal; 2004.

336. Dorion I, Le Bras A, Pomero V, Campana S, Teysseyre S, Meynadier M, et al. Rhumatologie et orthopédie : apport d'une nouvelle modalité d'imagerie radiologique tridimensionnelle multi-énergie, faible dose, et haute résolution à l'imagerie du système ostéo-articulaire. ITBM-RBM. 2004;25(5):274–9.

337. Rehel J-L, Beauvais-March H, Kalifa G, Aubert B. Evaluation dosimetrique comparative en radiologie pediatrique de l'installation EOS (BIO-SPACE) et d'une installation conventionnelle. J Radiol. 2004;85(9):1459.

338. Dubousset J, Charpak G, Dorion I, Skalli W, Lavaste F, Deguise J, et al. A new 2D and 3D imaging approach to musculoskeletal physiology and pathology with low-dose radiation and the standing position: the EOS system. Bull Académie Natl Médecine. 2005;189(2):287–97; discussion 297–300.

339. Dubousset J, Charpak G, Skalli W, Kalifa G, Lazennec J-Y. Système EOS : la radiographie de la tête aux pieds face et profil simultanés à très basses doses de radiations: Un nouveau regard pour

l'orthopédie. Rev Chir Orthopédique Réparatrice Appar Mot. 2007;93(6, Supplement 1):141–3.

340. Gorincour G, Barrau K, Waultier S, Viehweger E, Paris M, Jouve JL, et al. Radiographie des scolioses : dosimétrie comparée entre la technique conventionnelle et la fluorographie numérique. J Radiol. 2007;88(3, Part 1):361–6.
341. Dubois J, Deschênes S, Charron G, Beaudoin G, Miron MC, Labelle H, et al. Evaluation dosimetrique d'un nouveau systeme radiographique a basse irradiation. J Radiol. 2008;89(10):1224.
342. Dubousset J, Charpak G, Skalli W, de Guise J, Kalifa G, Wicart P. Modélisation vertébrale et squelettique par le système EOS. Arch Pédiatrie. 2008;15(5):665–6.
343. Alison M, Azoulay R, Tilea B, Grandjean S, Lefevre T, Achour I, et al. Evaluation de la productivite du systeme de radiologie ultra-basse dose (EOS) en pediatrie. J Radiol. 2009;90(10):1428.
344. Deschênes S, Charron G, Beaudoin G, Labelle H, Dubois J, Miron M-C, et al. Diagnostic imaging of spinal deformities: reducing patients radiation dose with a new slot-scanning X-ray imager. Spine. 2010;35(9):989–94.
345. McKenna C, Wade R, Faria R, Yang H, Stirk L, Gummerson N, et al. EOS 2D/3D X-ray imaging system: a systematic review and economic evaluation. Health Technol Assess Winch Engl. 2012;16(14):1–188.
346. Faria R, McKenna C, Wade R, Yang H, Woolacott N, Sculpher M. The EOS 2D/3D X-ray imaging system: A cost-effectiveness analysis quantifying the health benefits from reduced radiation exposure. Eur J Radiol. 2013;82(8):e342–9.
347. Wade R, Yang H, McKenna C, Faria R, Gummerson N, Woolacott N. A systematic review of the clinical effectiveness of EOS 2D/3D X-ray imaging system. Eur Spine J. 2013;22(2):296–304.
348. Damet J, Fournier P, Monnin P, Sans-Merce M, Ceroni D, Zand T, et al. Occupational and patient exposure as well as image quality for full spine examinations with the EOS imaging system. Med Phys. 2014;41(6):063901.
349. Luo TD, Stans AA, Schueler BA, Larson AN. Cumulative Radiation Exposure With EOS Imaging Compared With Standard Spine Radiographs. Spine Deform. 2015;3(2):144–50.
350. Le Bras A, Laporte S, Bousson V, Mitton D, De Guise J., Laredo J., et al. Personalised 3D reconstruction of proximal femur from low-dose digital biplanar radiographs. Int Congr Ser. 2003;1256:214–9.
351. Dumas R, Aissaoui R, Mitton D, Skalli W, de Guise J. Determination of personalized inertial parameters of lower limb by biplanar low-dose radiography. Int Congr Ser. 2004;1268:19–24.
352. Skalli W, Mitton D, de Guise J, Dubousset J. The EOS system: New perspectives for musculoskeletal biomechanics. J Biomech. 2006;39, Supplement 1(0):S460.
353. Schlatterer B, Suedhoff I, Bonnet X, Catonne Y, Maestro M, Skalli W. Analyse 3D par radiographie biplanaire basse dose EOS® des alignements osseux et prothétiques lors de la pose d'une PTG. Incertitude des repères mis en place. Rev Chir Orthopédique Traumatol. 2009;95(1):2–11.
354. Schlatterer B, Suedhoff I, Bonnet X, Catonne Y, Maestro M, Skalli W. Skeletal landmarks for TKR implantations: Evaluation of their accuracy using EOS imaging acquisition system. Orthop Traumatol Surg Res. 2009;95(1):2–11.
355. Azmy C, Guérard S, Bonnet X, Gabrielli F, Skalli W. Apport du système EOS® dans l'analyse expérimentale de la cinématique fémoropatellaire : évaluation de l'incertitude. Rev Chir Orthopédique Traumatol. 2010;96(1):23–32.
356. Husson J-L, Mallet J-F, Parent H, Cavagna R, Vital J-M, Blamoutier A, et al. The lumbar-pelvic-femoral complex: applications in spinal imbalance. Orthop Traumatol Surg Res. 2010;96(4, Supplement):S1–9.
357. Ohl X, Stanchina C, Billuart F, Skalli W. Shoulder bony landmarks location using the EOS® low-dose stereoradiography system: a reproducibility study. Surg Radiol Anat. 2010;32(2):153–8.
358. Sabourin M, Jolivet E, Miladi L, Wicart P, Rampal V, Skalli W. Three-dimensional stereoradiographic modeling of rib cage before and after spinal growing rod procedures in early-onset scoliosis. Clin Biomech. 2010;25(4):284–91.
359. Illés T, Tunyogi-Csapó M, Somoskeöy S. Breakthrough in three-dimensional scoliosis diagnosis: significance of horizontal plane view and vertebra vectors. Eur Spine J. 2011;20(1):135–43.
360. Lazennec J-Y, Brusson A, Rousseau M-A. Hip–spine relations and sagittal balance clinical

consequences. Eur Spine J. 2011;20(5):686–98.

361. Lazennec J-Y, Rangel A, Baudoin A, Skalli W, Catonne Y, Rousseau M-A. The EOS imaging system for understanding a patellofemoral disorder following THR. Orthop Traumatol Surg Res. 2011;97(1):98–101.
362. Lazennec JY, Rousseau MA, Rangel A, Gorin M, Belicourt C, Brusson A, et al. Pelvis and total hip arthroplasty acetabular component orientations in sitting and standing positions: Measurements reproductibility with EOS imaging system versus conventional radiographies. Orthop Traumatol Surg Res. 2011;97(4):373–80.
363. Rousseau M-A, Laporte S, Dufour T, Steib J-P, Lazennec J-Y, Skalli W. Three-dimensional assessment of the intervertebral kinematics after Mobi-C total disc replacement at the cervical spine in vivo using the EOS stereoradiography system. SAS J. 2011;5(3):63–8.
364. Guenoun B, Zadegan F, Aim F, Hannouche D, Nizard R. Reliability of a new method for lower-extremity measurements based on stereoradiographic three-dimensional reconstruction. Orthop Traumatol Surg Res. 2012;98(5):506–13.
365. Thepaut M, Leboucher J, Tissot V, Lempereur M, Remy-Neris O, Stindel E, et al. Measurement of femoral torsion using the EOS system: Validity, reliability, and perspectives for children and adults with cerebral palsy. Ann Phys Rehabil Med. 2012;55, Supplement 1(0):e222.
366. Bittersohl B, Freitas J, Zaps D, Schmitz MR, Bomar JD, Muhamad AR, et al. EOS imaging of the human pelvis: reliability, validity, and controlled comparison with radiography. J Bone Joint Surg Am. 2013;95(9):e581–9.
367. Boutry N, Dutouquet B, Leleu X, Vieillard M-H, Duhamel A, Cotten A. Low-dose biplanar skeletal survey versus digital skeletal survey in multiple myeloma. Eur Radiol. 2013;23(8):2236–45.
368. Ilharreborde B, Dubousset J, Skalli W, Mazda K. Spinal penetration index assessment in adolescent idiopathic scoliosis using EOS low-dose biplanar stereoradiography. Eur Spine J. 2013;22(11):2438–44.
369. Moura DC, Boisvert J, Barbosa JG, Labelle H, Tavares JMRS. Fast 3D reconstruction of the spine from biplanar radiographs using a deformable articulated model. Med Eng Phys. 2011;33(8):924–33.
370. Moura DC, Barbosa JG. Real-scale 3D models of the scoliotic spine from biplanar radiography without calibration objects. Comput Med Imaging Graph. 2014;38(7):580–5.
371. Harvey P. ExifTool v.9.61 [Internet]. Kingston, Ontario, Canada: Queen's University - Particle Astrophysics; 2014. Available from: http://owl.phy.queensu.ca/~phil/exiftool/
372. Schneider CA, Rasband WS, Eliceiri KW. NIH Image to ImageJ: 25 years of image analysis. Nat Methods. 2012;9(7):671–5.
373. Schindelin J, Rueden CT, Hiner MC, Eliceiri KW. The ImageJ ecosystem: An open platform for biomedical image analysis. Mol Reprod Dev. 2015;82(7-8):518–29.
374. Rasband W. ImageJ v1.50a [Internet]. National Institutes of Health, USA; 2014 [cited 2014 Jun 20]. Available from: http://imagej.nih.gov/ij
375. Strotzer M, Völk M, Fründ R, Hamer O, Zorger N, Feuerbach S. Routine Chest Radiography Using a Flat-Panel Detector Image Quality at Standard Detector Dose and 33% Dose Reduction. Am J Roentgenol. 2002;178(1):169–71.
376. Compagnone G. Radiation Doses to Patients Using Computed Radiography, Direct Digital Radiography, and Screen-Film Radiography. In: Hayat MA, editor. Gen Methods Overv Lung Carcinoma Prostate Carcinoma [Internet]. Dordrecht: Springer Netherlands; 2008 [cited 2013 Jan 5]. p. 109–28. Available from: http://www.springerlink.com/content/w6260536544k0063/abstract/
377. Fink C, Hallscheidt PJ, Noeldge G, Kampschulte A, Radeleff B, Hosch WP, et al. Clinical comparative study with a large-area amorphous silicon flat-panel detector: image quality and visibility of anatomic structures on chest radiography. AJR Am J Roentgenol. 2002;178(2):481–6.
378. Bacher K, Smeets P, De Hauwere A, Voet T, Duyck P, Verstraete K, et al. Image quality performance of liquid crystal display systems: Influence of display resolution, magnification and window settings on contrast-detail detection. Eur J Radiol. 2006;58(3):471–9.
379. Ganten M, Radeleff B, Kampschulte A, Daniels MD, Kauffmann GW, Hansmann J. Comparing Image Quality of Flat-Panel Chest Radiography with Storage Phosphor Radiography and Film-Screen Radiography. Am J Roentgenol. 2003;181(1):171–6.

380. Kroft LJM, Veldkamp WJH, Mertens BJA, van Delft JPA, Geleijns J. Detection of Simulated Nodules on Clinical Radiographs: Dose Reduction at Digital Posteroanterior Chest Radiography. Radiology. 2006;241(2):392–8.

381. Siemens AG, Medical Solutions. AXIOM Aristos® VB10 Dicom conformance statement - Rev. 2.0 [Internet]. Siemens AG; 2004 [cited 2015 Oct 10]. Available from: http://www.healthcare.siemens.com/siemens_hwem-hwem_ssxa_websites-context-root/wcm/idc/groups/public/@global/@services/documents/download/mdaw/mtiz/~edisp/aristos_dicomconformancestatement-00074233.pdf

382. Seibert JA, Morin RL. The standardized exposure index for digital radiography: an opportunity for optimization of radiation dose to the pediatric population. Pediatr Radiol. 2011;41(5):573–81.

383. Kohn MM, European Commission, Directorate-General XII S Research, and Development. European guidelines on quality criteria for diagnostic radiographic images in paediatrics [Internet]. Luxembourg: Office for Official Publications of the European Communities; 1996. Available from: http://bookshop.europa.eu/en/european-guidelines-on-quality-criteria-for-diagnostic-radiographic-images-in-paediatrics-pbCGNA16261/

384. Maccia C, Moores BM, Wall BF. The 1991 CEC trial on quality criteria for diagnostic radiographic images: detailed results and findings. Luxembourg: Office for Official Publications of the European Communities; 1997.

385. Altman DG. Practical statistics for medical research. Boca Raton, Fla: Chapman & Hall/CRC; 1999.

386. Norman GR, Streiner DL. Biostatistics: the bare essentials. St. Louis: Mosby; 1994.

387. Berry KJ, Johnston JE, Mielke PW. Weighted kappa for multiple raters. Percept Mot Skills. 2008;107(3):837–48.

388. Altman DG. Practical statistics for medical research. 1st ed. Boca Raton, Fla, USA: Chapman & Hall/CRC; 1991.

389. StatsDirect statistical software [Internet]. Altrincham, Cheshire WA14 4QA, UK: StatsDirect Ltd; 2015 [cited 2015 Oct 9]. Available from: http://www.statsdirect.com/

390. European Communities, editor. Guidelines on education and training in radiation protection for medical exposures - Radiation Protection 116 [Internet]. European Commission; 2000. Available from: http://ec.europa.eu/energy/nuclear/radiation_protection/doc/publication/116.pdf

391. European Communities, editor. Guidance on diagnostic reference levels (DRLs) for medical exposures - Radiation Protection 109 [Internet]. European Commission; 1999. Available from: http://ec.europa.eu/energy/nuclear/radiation_protection/doc/publication/109_en.pdf

392. Fintelmann F, Pulli B, Abedi-Tari F, Trombley M, Shore M-T, Shepard J-A, et al. Repeat rates in digital chest radiography and strategies for improvement. J Thorac Imaging. 2012;27(3):148–51.

393. Maccia C, Commission of the European Communities, Directorate-General for Science R and Development. CEC quality criteria for diagnostic radiographic images and patient exposure trial. Commission of the European Communities; 1990.

394. Chateil J-F, Aubert B, Brisse H. Ordre de grandeur des doses délivrées en radiodiagnostic. J Radiol. 2010;91(11, Part 2):1192–200.

395. Chateil J-F, Durand C, Diard F. Radiographie normale de face et de profil du thorax chez l'enfant. EMC - Radiol. 2005;2(6):587–616.

396. Olgar T, Onal E, Bor D, Okumus N, Atalay Y, Turkyilmaz C, et al. Radiation Exposure to Premature Infants in a Neonatal Intensive Care Unit in Turkey. Korean J Radiol. 2008;9(5):416–9.

397. Smans K, Struelens L, Smet M, Bosmans H, Vanhavere F. Patient dose in neonatal units. Radiat Prot Dosimetry. 2008;131(1):143–7.

398. Dabin J, Struelens L, Vanhavere F. Radiation dose to premature new-borns in the Belgian neonatal intensive care units. Radiat Prot Dosimetry. 2014;158(1):28–35.

399. Datz H, Ben-Shlomo A, Bader D, Sadetzki S, Juster-Reicher A, Marks K, et al. The additional dose to radiosensitive organs caused by using under-collimated X-ray beams in neonatal intensive care radiography. Radiat Prot Dosim. 2008;130(4):518–24.

400. Kalin AG. Gonadal shielding and collimation information for pelvic radiography in podiatric practice. J Am Podiatry Assoc. 1976;66(1):1–14.

401. Zetterberg LG, Espeland A. Lumbar spine radiography -- poor collimation practices after implementation of digital technology. Br J Radiol. 2011;84(1002):566–9.

402. Whitley AS, Clark KC. Clark's positioning in radiography. 12th ed. London; New York, NY: Hodder Arnold ; Distributed in the U.S. of America by Oxford University Press; 2005.

403. Fung K, Gilboy W. "Anode heel effect" on patient dose in lumbar spine radiography. Br J Radiol. 2000;73(869):531–6.

404. Dong X, Niu T, Jia X, Zhu L. Relationship between x-ray illumination field size and flat field intensity and its impacts on x-ray imaging. Med Phys. 2012;39(10):5901–9.

405. Bacher K, Smeets P, Bonnarens K, De Hauwere A, Verstraete K, Thierens H. Dose reduction in patients undergoing chest imaging: digital amorphous silicon flat-panel detector radiography versus conventional film-screen radiography and phosphor-based computed radiography. AJR Am J Roentgenol. 2003;181(4):923–9.

406. Tingberg A, Herrmann C, Lanhede B, Alm_ A, J.Besjakov, Mattsson S, et al. Comparison of Two Methods for Evaluation of the Image Quality of Lumbar Spine Radiographs. 2000 [cited 2013 Jan 5]; Available from: http://rpd.oxfordjournals.org/content/90/1-2/165.abstract

407. Redlich U, Hoeschen C, Doehring W. Assessment and optimisation of the image quality of chest-radiography systems. Radiat Prot Dosimetry. 2005;114(1-3):264–8.

408. Sund P, Båth M, Kheddache S, Månsson LG. Comparison of visual grading analysis and determination of detective quantum efficiency for evaluating system performance in digital chest radiography. Eur Radiol. 2004;14(1):48–58.

409. Tingberg A, Eriksson F, Medin J, Besjakov J, Båth M, Håkansson M, et al. Inter-observer variation in masked and unmasked images for quality evaluation of clinical radiographs. Radiat Prot Dosimetry. 2005;114(1-3):62–8.

410. Pollard BJ, Chawla AS, Delong DM, Hashimoto N, Samei E. Object detectability at increased ambient lighting conditions. Med Phys. 2008;35(6):2204–13.

411. Kheddache S, Månsson LG, Angelhed JE, Denbratt L, Gottfridson B, Schlossman D. Digital chest radiography: should images be presented in negative or positive mode? Eur J Radiol. 1991;13(2):151–5.

412. Krupinski EA, Williams MB, Andriole K, Strauss KJ, Applegate K, Wyatt M, et al. Digital Radiography Image Quality: Image Processing and Display. J Am Coll Radiol. 2007;4(6):389–400.

413. Andriole KP, Gould RG, Webb WR. Finding-specific display presets for computed radiography soft-copy reading. J Digit Imaging. 1999;12(Suppl 1):3–5.

414. Proto A, Lane E. 350 kVp chest radiography: review and comparison with 120 kVp. Am J Roentgenol. 1978;130(5):859–66.

415. Tabrisky J, Herman M, Torrance D, Hieshima G. Mobile 240 kVp phototimed chest radiography. Am J Roentgenol. 1980;135(2):295–300.

416. Jaffe C, Webster EW. Radiographic contrast improvement by means of slit radiography. Radiology. 1975;116(3):631–5.

417. Barnes GT, Brezovich IA, Witten DM. Scanning multiple slit assembly: a practical and efficient device to reduce scatter. Am J Roentgenol. 1977;129(3):497–501.

418. Plewes DB, Wandtke JC. A scanning equalization system for improved chest radiography. Radiology. 1982;142(3):765–8.

419. Plewes DB, Vogelstein E. A scanning system for chest radiography with regional exposure control: Practical implementation. Med Phys. 1983;10(5):655–63.

420. Liu X, Shaw CC, Lai C-J, Wang T. Comparison of scatter rejection and low-contrast performance of scan equalization digital radiography (SEDR), slot-scan digital radiography, and full-field digital radiography systems for chest phantom imaging. Med Phys. 2011;38(1):23–33.

421. Wandtke JC, Plewes DB. Improved chest disease detection with scanning equalization radiography. AJR Am J Roentgenol. 1985;145(5):979–83.

422. Axelsson B, Forsberg H, Hansson B, Haverling M. Multiple-beam equalization radiography in chest radiology. Image quality and radiation dose considerations. Acta Radiol. 1991;32(1):12–7.

423. Aarts NJM, Oestmann JW, Schultze Kool LJ. Visualization of basal pleural space and lung with advanced multiple beam equalization radiography (AMBER). Eur J Radiol. 1993;16(2):138–42.

424. Chotas HG, Floyd CE Jr, Ravin CE. Film-based chest radiography: AMBER vs asymmetric screen-film systems. AJR Am J Roentgenol. 1993;161(4):743–7.

425. Pascoal A, Lawinski CP, Mackenzie A, Tabakov S, Lewis CA. Chest radiography: a comparison of image quality and effective dose using four digital systems. 2005 [cited 2013 Jan 6]; Available from: http://rpd.oxfordjournals.org/content/114/1-3/273.abstract?sid=7e49a2a2-e118-4b51-b9c4-5fc2fc451b83

426. Peer S, Neitzel U, Giacomuzzi SM, Peer R, Gassner E, Steingruber I, et al. Comparison of low-contrast detail perception on storage phosphor radiographs and digital flat panel detector images. IEEE Trans Med Imaging. 2001;20(3):239–42.

427. McEntee M, Frawley H, Brennan PC. A comparison of low contrast performance for amorphous Silicon/caesium iodide direct radiography with a computed radiography: A contrast detail phantom study. Radiography. 2007;13(2):89–94.

428. Liu X, Shaw CC. A-Si:H/CsI(Tl) flat-panel versus computed radiography for chest imaging applications: image quality metrics measurement. Med Phys. 2004;31(1):98–110.

429. Compagnone G, Baleni MC, Pagan L, Calzolaio FL, Barozzi L, Bergamini C. Comparison of radiation doses to patients undergoing standard radiographic examinations with conventional screen-film radiography, computed radiography and direct digital radiography. Br J Radiol. 2006;79(947):899–904.

430. Hamer O, Volk M, Zorger N, Feuerbach S, Strotzer M. Amorphous Silicon, Flat-Panel, X-Ray Detector Versus Storage Phosphor-Based Computed Radiography: Contrast-Detail Phantom Study at Different Tube Voltages and Detector Entrance Doses. Investig Radiol April 2003. 2003;38(4):212–20.

431. Nagatani Y, Nitta N, Ikeda M, Kitahara H, Otani H, Seko A, et al. Ability of chest X-ray to detect faint shadows documented as ground-glass attenuation in images of computed tomography: A comparison between flat-panel detector radiography and film-screen radiography. Pediatr Neoplasms Abdomen. 2010;75(3):384–90.

432. Kotter E, Langer M. Digital radiography with large-area flat-panel detectors. Eur Radiol. 2002;12(10):2562–70.

433. Ludwig K, Schülke C, Diederich S, Wormanns D, Lenzen H, Bernhardt TM, et al. Detection of subtle undisplaced rib fractures in a porcine model: radiation dose requirement--digital flat-panel versus screen-film and storage-phosphor systems. Radiology. 2003;227(1):163–8.

434. Metz S, Damoser P, Hollweck R, Roggel R, Engelke C, Woertler K, et al. Chest Radiography with a Digital Flat-Panel Detector: Experimental Receiver Operating Characteristic Analysis1. Radiat Prot Dosim. 2005;114(1-3):273–7.

435. Gruber M, Uffmann M, Weber M, Prokop M, Balassy C, Schaefer-Prokop C. Direct detector radiography versus dual reading computed radiography: feasibility of dose reduction in chest radiography. Eur Radiol. 2006;16(7):1544–50.

436. Uffmann M, Neitzel U, Prokop M, Kabalan N, Weber M, Herold CJ, et al. Flat-panel-detector chest radiography: effect of tube voltage on image quality. Radiology. 2005;235(2):642–50.

437. Dietrich TJ, Pfirrmann CWA, Schwab A, Pankalla K, Buck FM. Comparison of radiation dose, workflow, patient comfort and financial break-even of standard digital radiography and a novel biplanar low-dose X-ray system for upright full-length lower limb and whole spine radiography. Skeletal Radiol. 2013;42(7):959–67.

438. May GA, Deer DD, Dackiewicz D. Impact of digital radiography on clinical workflow. J Digit Imaging. 2000;13(Suppl 1):76–8.

439. Andriole KP, Luth DM, Gould RG. Workflow assessment of digital versus computed radiography and screen-film in the outpatient environment. J Digit Imaging. 2002;15 Suppl 1:124–6.

440. Samei E, Saunders RS, Lo JY, Dobbins JT 3rd, Jesneck JL, Floyd CE, et al. Fundamental imaging characteristics of a slot-scan digital chest radiographic system. Med Phys. 2004;31(9):2687–98.

441. Samei E, Lo JY, Yoshizumi TT, Jesneck JL, Dobbins JT, Floyd CE, et al. Comparative Scatter and Dose Performance of Slot-Scan and Full-Field Digital Chest Radiography Systems1. Radiology. 2005;235(3):940–9.

442. Beningfield S, Potgieter H, Nicol A, van As S, Bowie G, Hering E, et al. Report on a new type of trauma

full-body digital X-ray machine. Emerg Radiol. 2003;10(1):23–9.

443. Maree GJ, Irving BJ, Hering ER. Paediatric dose measurement in a full-body digital radiography unit. Pediatr Radiol. 2007;37(10):990–7.

444. Mantokoudis G, Hegner S, Dubach P, Bonel HM, Senn P, Caversaccio MD, et al. How reliable and safe is full-body low-dose radiography (LODOX Statscan) in detecting foreign bodies ingested by adults? Emerg Med J [Internet]. 2012 [cited 2012 Nov 9]; Available from: http://emj.bmj.com/content/early/2012/07/24/emermed-2011-200911

445. Whiley SP, Mantokoudis G, Ott D, Zimmerman H, Exadaktylos AK. A Review of Full-Body Radiography in Nontraumatic Emergency Medicine. Emerg Med Int [Internet]. 2012;2012. Available from: http://www.ncbi.nlm.nih.gov/pmc/articles/PMC3517877/

446. Perks TD, Dendere R, Irving B, Hartley T, Scholtz P, Lawson A, et al. Filtration to reduce paediatric dose for a linear slot-scanning digital x-ray machine. Radiat Prot Dosimetry. 2014;

447. Liu XM, Shaw CC, Altunbas MC, Wang TP. An alternate line erasure and readout (ALER) method for implementing slot-scan imaging technique with a flat-panel detector - Initial experiences. Ieee Trans Med Imaging. 2006;25(4):496–502.

448. Liu X, Lai C-J, Whitman GJ, Geiser WR, Shen Y, Yi Y, et al. Effects of exposure equalization on image signal-to-noise ratios in digital mammography: A simulation study with an anthropomorphic breast phantom. Med Phys. 2011;38(12):6489–501.

449. Babichev EA, Baru SE, Neustroev VA, Porosev VV, Savinov GA, Sidorov VA, et al. [Digital X-ray apparatus 'Sibir''. Measurement of the value of a signal]. Med Tekh. 2001;(5):3–7.

450. Baru SE, Ukraintsev IG. [Industrial production of the LDRD 'Siberia-N' digital radiographic devices]. Med Tekh. 2004;(1):38–9.

451. Titov M. New developments and future perspectives of gaseous detectors. Nucl Instrum Methods Phys Res Sect Accel Spectrometers Detect Assoc Equip. 2007;581(1–2):25–37.

452. Krejci F, Jakubek J, Dammer J, Vavrik D. Enhancement of spatial resolution of roentgenographic methods. Nucl Instrum Methods Phys Res Sect Accel Spectrometers Detect Assoc Equip. 2009;607(1):208–11.

453. Ballabriga R, Campbell M, Heijne E, Llopart X, Tlustos L, Wong W. Medipix3: A 64 k pixel detector readout chip working in single photon counting mode with improved spectrometric performance. Nucl Instrum Methods Phys Res Sect Accel Spectrometers Detect Assoc Equip. 2011;633, Supplement 1:S15–8.

454. Bosma MJ, Visser J, Evrard O, Moor PD, Munck KD, Tezcan DS, et al. Edgeless silicon sensors for Medipix-based large-area X-ray imaging detectors. J Instrum. 2011;6(01):C01035.

455. Yu H, Xu Q, He P, Bennett J, Amir R, Dobbs B, et al. Medipix-based Spectral Micro-CT. CT Li Lun Yu Ying Yong Yan Jiu. 2012;21(4):583.

456. He P, Yu H, Bennett J, Ronaldson P, Zainon R, Butler A, et al. Energy-discriminative performance of a spectral micro-CT system. J X-Ray Sci Technol. 2013;21(3):335–45.

457. Rowlands JA, Zhao W, Blevis IM, Waechter DF, Huang Z. Flat-panel digital radiology with amorphous selenium and active-matrix readout. RadioGraphics. 1997;17(3):753–60.

458. Amzallag-Bellenger E, Uyttenhove F, Nectoux É, Moraux A, Bigot J, Herbaux B, et al. Idiopathic scoliosis in children and adolescents: assessment with a biplanar X-ray device. Insights Imaging. 2014;5(5):571–83.

8 List of Figures

Figure number:

9 List of Tables

Table number:

10 Annex

10.1 EOS Acquisition Software Console

The software at the EOS prototype provided an interface to control the start and end of the linear acquisition scan, controls the X-ray tube scanning parameters, and provides a work-list interface for image identification, acquisition, storage and transmission.

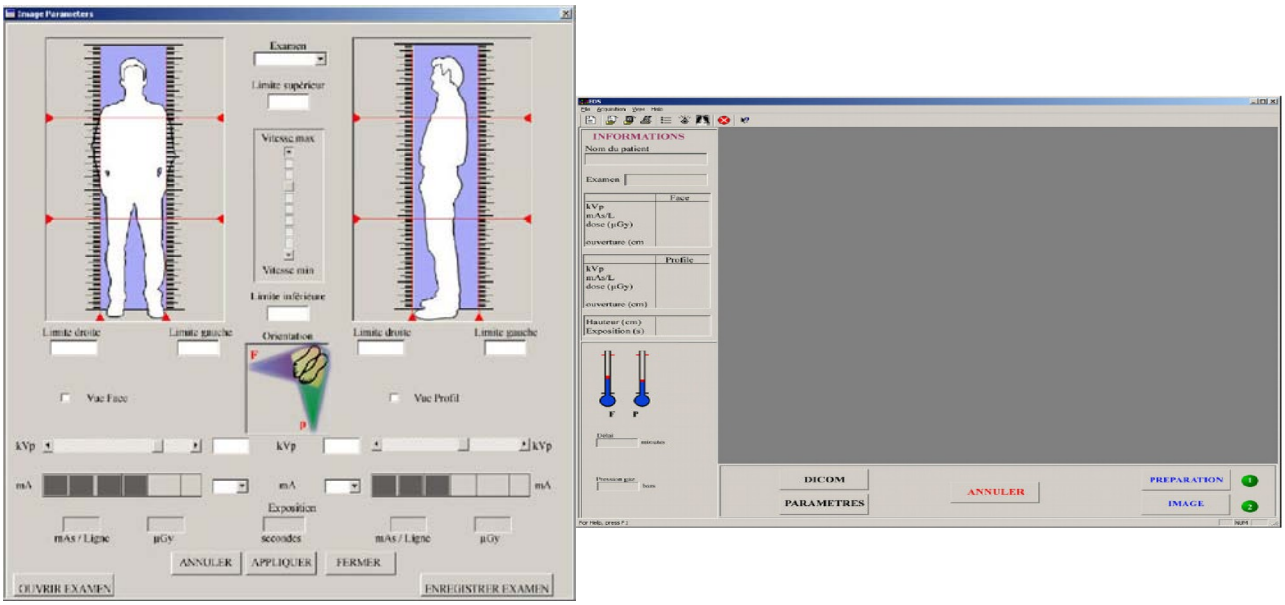

Figure 97: Main control window at operator's console of the EOS 1 prototype (2005)